UNIVERSIDADE FEDERAL DE SANTA CATARINA CAMPUS UNIVERSITÁRIO - TRINDADE
PROGRAMA DE PÓS-GRADUAÇÃO EM ENGENHARIA QUÍMICA

UNIVERSIDAD DE MÁLAGA
FACULTAD DE CIENCIAS
DEPARTAMENTO DE QUÍMICA INORGÁNICA, CRISTALOGRAFÍA Y MINERALOGÍA

Mariana Schneider

Innovative Geopolymer/Zeolite Composites Fabricated by Electrospinning and 3D Printing for CO_2 Capture and Separation Applications

Florianópolis
2025

Mariana Schneider

Innovative Geopolymer/Zeolite Composites Fabricated by Electrospinning and 3D Printing for CO_2 Capture and Separation Applications

Doctoral Thesis submitted to the Postgraduate Program in Chemical Engineering (PósENQ) at the Federal University of Santa Catarina (UFSC) to obtain a degree of Doctor in Chemical Engineering and to the Universidad de Málaga as a requirement to obtain the PhD Degree in Chemistry, Chemical Technology, Materials and Nanotechnology.

Advisors:
Prof. Regina de F. M. Moreira, Dra. (UFSC)
Prof. M. Olga Guerrero-Pérez, Dra. (UMA)

Co-advisor:
Prof. Dachamir Hotza, Dr. (UFSC)

Tutor
Prof. Enrique Rodríguez-Castellón, Dr. (UMA)

Florianópolis
2026

Mariana Schneider

Compósitos Inovadores de Geopolímero/Zeólita Fabricados por Eletrofiação e Impressão 3D para Aplicações em Captura e Separação de CO_2

Tese de doutorado submetida ao Programa de Pós-Graduação em Engenharia Química (PósENQ) da Universidade Federal de Santa Catarina (UFSC) para obtenção do título de Doutora em Engenharia Química em regime de cotutela com a Universidade de Málaga para obtenção do título de Doutora em Química, Tecnologia Química, Materiais e Nanotecnologia.

Orientadoras:
Prof. Regina de F. M. Moreira, Dra. (UFSC)
Prof. M. Olga Guerrero-Pérez, Dra. (UMA)

Coorientador:
Prof. Dachamir Hotza, Dr. (UFSC)

Tutor
Prof. Enrique Rodríguez-Castellón, Dr. (UMA)

Florianópolis
2026

Mariana Schneider

Innovadores Compuestos de Geopolímero/Zeolita Fabricados Mediante Electrohilado e Impresión 3D para Aplicaciones de Captura y Separación De CO_2

Tesis doctoral presentada al Programa de Posgrado en Ingeniería Química (PósENQ) de la Universidad Federal de Santa Catarina (UFSC) para obtener el título de Doctor en Ingeniería Química y a la Universidad de Málaga como requisito para obtener el grado de Doctor en Química, Tecnología Química, Materiales y Nanotecnología.

Directoras: Prof. Regina de F. M. Moreira, Dra. (UFSC)
Prof. M. Olga Guerrero-Pérez, Dra. (UMA)

Codirector:
Prof. Dachamir Hotza, Dr. (UFSC)

Tutor
Prof. Enrique Rodríguez-Castellón, Dr. (UMA)

Florianópolis

2026

AUTORA: Mariana Schneider

https://orcid.org/0000-0002-9670-4322

EDITA: Publicaciones y Divulgación Científica. Universidad de Málaga

DECLARACIÓN DE AUTORÍA Y ORIGINALIDAD DE LA TESIS PRESENTADA PARA OBTENER EL TÍTULO DE DOCTOR

Dña MARIANA SCHNEIDER
Estudiante del programa de doctorado en QUÍMICA Y TECNOLOGÍAS QUÍMICAS, MATERIALES Y NANOTECNOLOGÍA de la Universidad de Málaga, autor/a de la tesis, presentada para la obtención del título de doctor por la Universidad de Málaga, titulada: INNOVATIVE GEOPOLYMER/ZEOLITE COMPOSITES FABRICATED BY ELECTROSPINNING AND 3D PRINTING FOR CO_2 CAPTURE AND SEPARATION APPLICATIONS

Realizada bajo la tutorización de ENRIQUE RODRÍGUEZ-CASTELLÓN, codirección de DACHAMIR HOTZA y dirección de MARIA OLGA GUERRERO-PÉREZ Y REGINA DE FATIMA PERALTA MUNIZ MOREIRA (si tuviera varios directores deberá hacer constar el nombre de todos)

DECLARO QUE:

La tesis presentada es una obra original que no infringe los derechos de propiedad intelectual ni los derechos de propiedad industrial u otros, conforme al ordenamiento jurídico vigente (Real Decreto Legislativo 1/1996, de 12 de abril, por el que se aprueba el texto refundido de la Ley de Propiedad Intelectual, regularizando, aclarando y armonizando las disposiciones legales vigentes sobre la materia), modificado por la Ley 2/2019, de 1 de marzo.

Igualmente asumo, ante a la Universidad de Málaga y ante cualquier otra instancia, la responsabilidad que pudiera derivarse en caso de plagio de contenidos en la tesis presentada, conforme al ordenamiento jurídico vigente.

En Málaga, a 26 de febrero de 2026.

Fdo.: MARIANA SCHNEIDER Doctoranda	Fdo.: ENRIQUE RODRÍGUEZ-CASTELLÓN Tutor
Fdo.: Mª OLGA GUERRERO-PÉREZ Directora de tesis	Fdo.: REGINA DE FÁTIMA P. M. MOREIRA Directora de tesis
Fdo.: DACHAMIR HOTZA Codirector de tesis	

CERTIFICACIÓN DE DIRECCIÓN DE LA TESIS DOCTORAL

Dra. Regina de Fátima Peralta Muniz Moreira, Profesora titular de la Universidad Federal de Santa Catarina, en calidad de Directora de la tesis doctoral realizada por **Mariana Schneider**, titulada:

"Innovative Geopolymer/Zeolite Composites Fabricated by Electrospinning and 3D Printing for CO_2 Capture and Separation Applications"

INFORMA:

1. Que la mencionada tesis ha sido realizada íntegramente por la doctoranda bajo mi dirección.
2. Que las publicaciones en coautoría que la avalan no han sido utilizadas en ninguna tesis doctoral anterior.

Y para que así conste, y a los efectos oportunos, firmo el presente informe en Florianópolis, a 26 de febrero de 2026.

_____

Regina de Fátima Peralta Muniz Moreira
Profesora titular
Universidad Federal de Santa Catarina

CERTIFICACIÓN DE DIRECCIÓN DE LA TESIS DOCTORAL

Dra. M. Olga Guerrero-Pérez, Catedrática de la Universidad de Málaga, en calidad de Directora de la tesis doctoral realizada por **Mariana Schneider**, titulada:

"Innovative Geopolymer/Zeolite Composites Fabricated by Electrospinning and 3D Printing for CO_2 Capture and Separation Applications"

INFORMA:

1. Que la mencionada tesis ha sido realizada íntegramente por la doctoranda bajo mi dirección.
2. Que las publicaciones en coautoría que la avalan no han sido utilizadas en ninguna tesis doctoral anterior.

Y para que así conste, y a los efectos oportunos, firmo el presente informe en Málaga, a 26 de febrero de 2026.

_____

M. Olga Guerrero-Pérez
Catedrática
Universidad de Málaga

CERTIFICACIÓN DE CODIRECCIÓN DE LA TESIS DOCTORAL

Dr. Dachamir Hotza, Profesor titular de la Universidad Federal de Santa Catarina, en calidad de Codirector de la tesis doctoral realizada por **Mariana Schneider**, titulada:

"Innovative Geopolymer/Zeolite Composites Fabricated by Electrospinning and 3D Printing for CO_2 Capture and Separation Applications"

INFORMA:

1. Que la mencionada tesis ha sido realizada íntegramente por la doctoranda bajo mi codirección.
2. Que las publicaciones en coautoría que la avalan no han sido utilizadas en ninguna tesis doctoral anterior.

Y para que así conste, y a los efectos oportunos, firmo el presente informe en Florianópolis, a 26 de febrero de 2026.

_____

Dachamir Hotza
Profesor titular
Universidad Federal de Santa Catarina

CERTIFICACIÓN DE TUTORIZACIÓN DE LA TESIS DOCTORAL

Dr. Enrique Rodríguez-Castellón, Catedrático de la Universidad de Málaga, en calidad de Tutor de la tesis doctoral realizada por **Mariana Schneider,** titulada:

"Innovative Geopolymer/Zeolite Composites Fabricated by Electrospinning and 3D Printing for CO_2 Capture and Separation Applications"

INFORMA:

1. Que la mencionada tesis ha sido realizada íntegramente por la doctoranda bajo mi tutorización.
2. Que las publicaciones en coautoría que la avalan no han sido utilizadas en ninguna tesis doctoral anterior.

Y para que así conste, y a los efectos oportunos, firmo el presente informe en Málaga, a 26 de febrero de 2026.

_____

Enrique Rodrígues-Castellón
Catedrático
Universidad de Málaga

Ficha de identificação da obra elaborada pela autora, através do Programa de Geração Automática da Biblioteca Universitária da UFSC.

Schneider, Mariana
Innovative Geopolymer/Zeolite Composites Fabricated by Electrospinning and 3D Printing for CO2 Capture and Separation Applications / Mariana Schneider ; orientadora, Regina Moreira, orientadora, M. Olga Guerrero-Pérez, coorientador, Dachamir Hotza, coorientador, Enrique Castellón, 2026.
250 p.

Tese (doutorado) - Universidade Federal de Santa Catarina, Centro Tecnológico, Programa de Pós-Graduação em Engenharia Química, Florianópolis, 2026.

Inclui referências.

1. Engenharia Química. 2. Geopolymer/Zeolite composite. 3. CO2 Capture. 4. 3D printing. 5. Electrospinning. I. Moreira, Regina . II. Guerrero-Pérez, M. Olga III. Hotza, Dachamir . IV. Castellón, Enrique . V. Universidade Federal de Santa Catarina. Programa de Pós-Graduação em Engenharia Química. VI. Título.

Mariana Schneider

Innovative Geopolymer/Zeolite Composites Fabricated by Electrospinning and 3D Printing for CO_2 Capture and Separation Applications

The present work at the Doctorate qualification level was evaluated and approved by an examining board composed of the following members:

Prof. Moisés Bastos Neto, Dr.
Federal University of Ceará

Prof. Juan Antonio Cecilia Buenestado, Dr.
University of Málaga

Daniela Gier Della Rocca, Dr.
Federal University of Santa Catarina

Prof. Claudia Sayer, Dr.
Federal University of Santa Catarina

We certify that this is the original and final version of the final paper which was deemed appropriate to obtain the title of Doctor in Chemical Engineering.

_____

Prof. Agenor Furigo Jr, Dr. (PósENQ/UFSC Coordinator)

_____

Prof. Regina de Fátima Peralta Muniz Moreira, Dr. (PósENQ/UFSC Advisor)

Florianópolis, 2026.

ABSTRACT

The capture, storage, and use of greenhouse gases are crucial in combating global warming. CO_2 emissions can be captured and stored through processes like adsorption. However, relying solely on CO_2 storage is not a feasible strategy for reducing atmospheric CO_2 concentrations, due to the high investment costs currently presented and limited geological storage capacity. Therefore, it is essential to improve efficiency and reduce the costs of CO_2 capture and utilization processes. Zeolitic, geopolymeric, materials, or hybrid adsorbents are efficient in CO_2 capture since they can be used in CO_2 separation processes from exhaust, synthesis and flue gases. Additionally, the gas recovered from the adsorbent regeneration process through desorption, rich in CO_2, can be used in various processes, such as electro-, photo- or thermo-catalytic reduction. Despite promising results in carbon dioxide adsorption on geopolymer-based adsorbents, there is no consensus on the ideal formulation to achieve low-cost, high adsorptive capacity, and hierarchical porous materials suitable for both high and low temperatures. Additionally, adsorption must be reversible to enable the use of these materials in cyclic processes. Thus, this thesis aims to explore the potential of geopolymer/zeolite composites as a sustainable and innovative adsorbent to be applied in CO_2 capture and separation. To achieve this, phosphate mining tailing waste based geopolymers and geopolymer/zeolite13X composites materials were prepared. The composites materials were also manufactured by 3D printing, and electrospinning by adding polyvinyl alcohol. The characteristics of the materials were deeply investigated using different analytical techniques, such as X-Ray Fluorescence, X-Ray Diffraction, Fourier Transform Infrared Spectroscopy, scanning Electron Microscopy, Energy Dispersive X-ray Spectroscopy, X-ray Photoelectron Spectroscopy, Solid State Nuclear Magnetic Resonance, textural characteristics, and 3D X-ray microcomputed tomography. Kinetics and thermodynamics for CO_2 and nitrogen adsorption were studied at temperatures in the range of 30 to 100 °C at 1 bar using CO_2, CO, and H_2 pure gases. The best CO_2 adsorption capacity for the geopolymer was 2.24 mmol of CO_2/g, achieved with the sample cured at 80 °C and subjected to the submerged curing process for 30 days, highlighting the significance of the submerged curing process. For the geopolymer/zeolite13X composites, the incorporation of 30% (w/w) of zeolite to the composite yielded notable adsorption capacity at 30 ºC and 1 bar, achieving ~2.6 $mmol \cdot g^{-1}$, confirming the influence of high surface area and low porosity of the materials on the adsorption capacity, since it increases with the concentration of zeolite on the composite. Four polymeric membranes were developed by electrospinning; however, the concentration of adsorbent material (zeolite, geopolymer or composite) was very low compared to the amount commonly used in CO_2 adsorption, consequently, the best adsorption capacity, 0.62 mmol/g, was achieved with the MZ and MZ30 sample, at 30 °C and 1 bar. In addition, the 3D-printed geopolymer/zeolite composites showed stable structures and tunable porosity, with increased surface area as zeolite content increased, confirming their potential for practical CO_2 capture applications.

Keywords: Zeolite, Geopolymer, CO_2 Capture, 3D printing, Electrospinning.

RESUMO

A captura, armazenamento e utilização de gases de efeito estufa são cruciais no combate ao aquecimento global. As emissões de CO_2 podem ser capturadas e armazenadas por meio de processos como a adsorção. No entanto, apenas o armazenamento de CO_2 não é uma estratégia viável para reduzir as concentrações atmosféricas de CO_2, devido aos altos custos de investimento atualmente apresentados e à limitada capacidade de armazenamento geológico. Sendo assim, é essencial melhorar a eficiência e reduzir os custos dos processos de captura e utilização de CO_2. Materiais zeolíticos, geopoliméricos ou adsorventes híbridos são eficientes na captura de CO_2, pois podem ser utilizados em processos de separação de CO_2 de gases de síntese, exaustão e combustão. Além disso, o gás recuperado do processo de regeneração do adsorvente por dessorção, rico em CO_2, pode ser utilizado em diversos processos, como redução eletro, foto ou termo catalíticos. Apesar de resultados promissores na adsorção de CO_2 em adsorventes à base de geopolímeros, não há consenso sobre a formulação ideal para alcançar materiais de baixo custo, alta capacidade adsortiva e estrutura porosa hierárquica adequados para altas e baixas temperaturas. Além disso, a adsorção deve ser reversível para possibilitar o uso desses materiais em processos cíclicos. Dessa forma, a presente tese tem como objetivo explorar o potencial de compósitos de geopolímero/zeólita 13X como um adsorvente sustentável e inovador a ser aplicado na captura e separação de CO_2. Para isso, foram preparados geopolímeros à base de rejeitos de mineração de fosfato e materiais compósitos de geopolímero/zeólita 13X. Os materiais compósitos foram preparados utilizando impressão 3D e eletrofiação com adição de álcool poli vinílico. As características dos materiais foram investigadas por meio de diferentes técnicas analíticas, como Fluorescência de Raios-X, Difração de Raios-X, Espectroscopia no Infravermelho por Transformada de Fourier, Microscopia Eletrônica de Varredura, Espectroscopia de Energia Dispersiva de Raios-X, Espectroscopia de Fotoelétrons de Raios-X, Ressonância Magnética Nuclear em Estado Sólido, características texturais e tomografia micro computadorizada 3D Raio X. A cinética e a termodinâmica para a adsorção de CO_2 e nitrogênio foram estudadas em temperaturas na faixa de 30 a 100 °C a 1 bar usando gases puros de CO_2, CO e H_2. A melhor capacidade de adsorção de CO_2 para o geopolímero foi de 2,24 mmol/g, alcançada com a amostra curada a 80 °C e submetida um processo de cura submersa por 30 dias, destacando a importância do processo de cura submersa. Para os compósitos de geopolímero/zeólita 13X, a incorporação de 30% (m/m) de zeólita no compósito resultou em uma notável capacidade de adsorção de ~2,6 mmol/g a 30 °C e 1 bar, confirmando a influência da alta área superficial e baixa porosidade dos materiais na capacidade de adsorção, uma vez que esta aumenta com o aumento da concentração de zeólita no compósito. Quatro membranas poliméricas foram desenvolvidas por eletrofiação, no entanto, a concentração de material adsorvente (zeólita, geopolímero ou compósito) foi muito baixa em comparação com a quantidade comumente usada na adsorção de CO_2, resultando em uma baixa capacidade de adsorção, atingindo um máximo de 0,62 mmol/g, com as amostras MZ e MZ30, a 30 °C e 1 bar. Além disso, os compósitos de geopolímero/zeólita impressos em 3D apresentaram estruturas estáveis e porosidade ajustável, com aumento da área superficial à medida que o teor de zeólita aumentou, confirmando seu potencial para aplicações práticas na captura de CO_2.

Palavras-Chave: Zeólita, Geopolímero, Captura de CO_2, Impressão 3D, Eletrofiação.

RESUMEN

La captura, almacenamiento y utilización de gases de efecto invernadero son cruciales en la lucha contra el calentamiento global. Las emisiones de CO_2 pueden capturarse y almacenarse mediante procesos como la adsorción. Sin embargo, el almacenamiento de CO_2 por sí solo no es una estrategia viable para reducir las concentraciones atmosféricas de CO_2, debido a los altos costos de inversión actuales y a la limitada capacidad de almacenamiento geológico. Por lo tanto, es esencial mejorar la eficiencia y reducir los costos de los procesos de captura y utilización de CO_2. Los materiales zeolíticos, geopoliméricos o adsorbentes híbridos son eficientes en la captura de CO_2, ya que pueden utilizarse en procesos de separación de CO_2 de gases de escape, síntesis y combustión. Además, el gas recuperado del proceso de regeneración del adsorbente mediante desorción, rico en CO_2, puede utilizarse en diversos procesos, como reducción electro-, foto- o termo-catalítica. A pesar de los resultados prometedores en la adsorción de CO_2 en adsorbentes a base de geopolímeros, no existe consenso sobre la formulación ideal para lograr materiales de bajo costo, alta capacidad de adsorción y estructura porosa jerárquica adecuada para altas y bajas temperaturas. Además, la adsorción debe ser reversible para permitir el uso de estos materiales en procesos cíclicos. Por lo tanto, la presente tesis tiene como objetivo explorar el potencial de los compuestos de geopolímero/zeolita 13X como un adsorbente sostenible e innovador para su aplicación en la captura y separación de CO_2. Para ello, se prepararon geopolímeros a base de residuos de minería de fosfato y materiales compuestos de geopolímero/zeolita 13X. Los materiales compuestos se fabricaron utilizando impresión 3D y electrohilado con la adición de alcohol polivinílico. Las características de los materiales se investigaron mediante diferentes técnicas analíticas, como Fluorescencia de Rayos X, Difracción de Rayos X, Espectroscopia Infrarroja por Transformada de Fourier, Microscopía Electrónica de Barrido, Espectroscopia de Energía Dispersiva de Rayos X, Espectroscopia de Fotoelectrones de Rayos X, Resonancia Magnética Nuclear de Estado Sólido, características texturales y tomografía micro computada 3D de Rayos-X. La cinética y la termodinámica para la adsorción de CO_2 y nitrógeno se estudiaron en temperaturas en el rango de 30 a 100 °C a 1 bar utilizando gases puros de CO_2, CO y H_2. La mejor capacidad de adsorción de CO_2 para el geopolímero fue de 2,24 mmol/g, alcanzada con la muestra curada a 80 °C y mediante un proceso de curado sumergido durante 30 días, destacando la importancia del proceso de curado sumergido. Para los compuestos de geopolímero/zeolita 13X, la incorporación de un 30% (m/m) de zeolita en el compuesto resultó en una notable capacidad de adsorción de ~2,6 mmol/g a 30 °C y 1 bar, confirmando la influencia de la alta área superficial y baja porosidad de los materiales en la capacidad de adsorción, ya que esta aumenta con la concentración de zeolita en el compuesto. Además, se desarrollaron cuatro membranas poliméricas mediante electrohilado; sin embargo, la concentración de material adsorbente (zeolita, geopolímero o compuesto) fue muy baja en comparación con la cantidad comúnmente utilizada en la adsorción de CO_2, lo que resultó en una baja capacidad de adsorción, alcanzando un máximo de 0,62 mmol/g con las muestras MZ y MZ30, a 30 °C y 1 bar. Además, los compuestos de geopolímero/zeolita impresos en 3D mostraron estructuras estables y porosidad ajustable, con un aumento del área superficial a medida que aumentaba el contenido de zeolita, lo que confirma su potencial para aplicaciones prácticas en la captura de CO_2.

Palabras clave: Zeolita, Geopolímero, Captura de CO_2, Impresión 3D, Electrohilado.

RESUMO EXPANDIDO

INTRODUÇÃO

Os combustíveis fósseis têm sido a principal fonte de energia do mundo e espera-se que continuem desempenhando esse papel por várias décadas (Nasr et al., 2021). Sua queima é um dos principais fatores responsáveis pelas emissões de gases de efeito estufa, como metano (CH_4), óxido nitroso (N_2O) e dióxido de carbono (CO_2), que causam danos permanentes e irreversíveis ao sistema climático (Ahmed et al., 2020). Segundo Kazancoglu et al. (2021), as emissões de CO_2 contribuem para o aumento da temperatura média global, provocando a elevação do nível do mar, inundações e perda de biodiversidade (Liu et al., 2021). Embora duas estratégias principais tenham sido propostas para mitigar essas emissões —a substituição de fontes fósseis por energias renováveis e a captura de CO_2 diretamente da atmosfera ou de fontes industriais—, a primeira opção enfrenta importantes limitações técnicas e econômicas (Silveira, 2021). Por isso, a captura, o armazenamento e a utilização do CO_2 (CCU) são considerados uma alternativa fundamental no curto e médio prazo para reduzir a pegada de carbono (Candamano et al., 2022). Estima-se que até 90% das emissões de CO_2 possam ser capturadas após um processo de separação. No entanto, os altos custos de capital e as limitações de armazenamento têm impulsionado o desenvolvimento de tecnologias que permitam valorizar o CO_2 capturado, convertendo-o em produtos como metano, metanol ou éter dimetílico (Damideh et al., 2020; Candamano et al., 2022).

Recentemente, a adsorção tem ganhado destaque em relação a outras tecnologias de separação de CO_2, como a absorção com aminas, que requer o uso de solventes corrosivos, alto consumo energético e apresenta custos operacionais elevados. Em contraste, os processos de adsorção oferecem vantagens como menor demanda de energia, maior estabilidade, operação mais simples e o uso de materiais sólidos, não tóxicos e de baixo custo, especialmente quando derivados de resíduos industriais (Guerrero-Pérez, 2024). Nesse contexto, as zeólitas têm sido amplamente estudadas por sua estrutura cristalina e microporosa, alta área superficial, estabilidade térmica e elevada seletividade na adsorção. Além disso, podem ser sintetizadas a partir de aluminosilicatos ou resíduos como cinzas volantes, casca de arroz ou cinzas de carvão (Silveira, 2021). E nos últimos anos, o geopolímero tem ganhado interesse relevante em pesquisas, principalmente devido ao seu baixo custo e à síntese ecologicamente amigável. A matriz de geopolímero é predominantemente amorfa e formada por uma rede tridimensional de aluminossilicatos, geralmente ativada por uma solução alcalina (Davidovits, 1994; Candamano et al., 2022).

Além disso, adsorventes híbridos de geopolímero/zeólita também têm demonstrado eficiência na captura de CO_2 devido às suas propriedades adequadas de seletividade (Silveira, 2021). A resistência mecânica, a resistência química, a estabilidade térmica e o custo relativamente baixo de síntese são aspectos favoráveis ao uso desses materiais em processos de separação (Minelli et al., 2018). Além disso, a presença de mesoporos em materiais geopoliméricos/zeolíticos pode promover a rápida difusão de gases dentro dos poros, melhorando assim a eficiência de adsorção/dessorção de CO_2.

Uma forma de preparar materiais geopoliméricos é via impressão 3D, que permite produzir monólitos adequados para aplicação em colunas de leito fixo. No entanto, estudos atuais sobre impressão 3D de geopolímeros têm se concentrado no uso desses materiais como materiais de construção, que não exigem uma rede porosa controlada. Para a separação e captura de CO_2, é necessário desenvolver materiais com redes hierárquicas para obter alta seletividade e capacidade adsortiva (Souza, 2021). Assim, a preparação de geopolímeros porosos hierárquicos moldados como monólitos ou pellets geométricos seria útil para a separação cíclica

de gases por adsorção. Entretanto, até onde sabemos, monólitos compostos de zeólita/geopolímero ainda não foram desenvolvidos ou aplicados para separação de CO_2/H_2.

Além disso, compósitos de geopolímeros poderiam ser moldados utilizando a técnica de eletrofiação e o método sol-gel para produzir nanofibras elásticas e resistentes a altas temperaturas (Tang et al., 2022). A eletrofiação consiste na formação de fibras a partir de uma solução polimérica, ejetando-a de uma fina agulha entre dois eletrodos com cargas elétricas de polaridade oposta, um localizado na agulha e o outro em um coletor. O jato carregado da solução evapora durante o trajeto até o coletor, formando o arranjo de fibras não tecidas. Esse método pode ser utilizado para produzir a morfologia desejada, dependendo das propriedades da solução, como peso molecular do polímero, condutividade, tensão superficial e viscosidade. Parâmetros como a distância entre os eletrodos, a voltagem aplicada, a umidade, o fluxo volumétrico e o diâmetro da agulha podem ser ajustados para permitir a evaporação suficiente do solvente, evitando que as fibras derretam ou não sejam formadas (Haider, Haider e Kang, 2018). Portanto, a eletrofiação destaca-se como um método simples e econômico para produzir nanofibras, utilizando diversas fontes poliméricas (Yarin, Koombhongse e Reneker, 2001b, 2001a; Silva et al., 2021).

Considerando as lacunas de conhecimento relacionadas ao uso de materiais de baixo custo com porosidade hierárquica e o desafio de produzir materiais com alta capacidade de adsorção e seletividade, a presente tese visa desenvolver, via eletrofiação e impressão 3D, materiais compósitos de geopolímero e zeólita 13X com porosidade hierárquica com alto desempenho na captura de CO_2 em misturas binárias CO_2/N_2 a partir de gases de exaustão.

OBJETIVOS

O principal objetivo desta tese é explorar o potencial de geopolímeros à base de rejeitos da mineração de fosfato, zeólitas e materiais compósitos de geopólmero/zeólita com estrutura porosa hierárquica como adsorventes inovadores, sustentáveis, de baixo custo e facilmente escaláveis. Os materiais serão preparados por meio das técnicas de eletrofiação (electrospinning) e impressão 3D, com o objetivo de obter adsorventes seletivos para a separação de misturas binárias de CO_2/H_2.

METODOLOGIA

O processo utilizado para sintetizar as amostras de geopolímeros foi baseado em Minelli et al. (2016), Chen et al. (2020) e Freire et al. (2020; 2024), onde geopolímeros de baixo custo foram preparados substituindo parte do metacaulim (MK) por rejeito de mineração de fosfato (PW), e uma mistura de hidróxido de sódio e silicato de sódio como ativador alcalino. As razões molares para a síntese do geopolímero são $SiO_2:Al_2O_3 = 3{,}30$; $Na_2O:SiO_2 = 0{,}30$; $Na_2O:Al_2O_3 = 0{,}99$; e $H_2O:Na_2O = 12{,}00$, selecionadas com base em um estudo desenvolvido por Davidovits (1994).

Inicialmente, para sintetizar o metacaulim, o caulim foi primeiro calcinado a 900 ºC por 60 min. O geopolímero foi então preparado seguindo seis etapas: i) mistura dos dois componentes sólidos (MK 35% e PW 19%); ii) preparar o ativador alcalino, misturando NaOH (11%), silicato de sódio (SS, 13%) e água deionizada (DIW, 22%) a 800 rpm por 10 min em um agitador magnético; iii) preparação da suspensão adicionando os sólidos à solução ativadora alcalina e misturando por 15 min a 1500 rpm, em agitador mecânico; iv) moldar a pasta geopolimérica em forma cilíndrica, utilizando um molde de silicone de 2×4 cm; v) duas amostras foram preparadas e curadas em estufa (produtos químicos VENTI-line VWR) a 80 °C e 65 °C. O molde foi coberto com uma fita de alta temperatura para que a água evaporasse lentamente; vi) após a desmoldagem, parte das amostras foi submersa em água DIW para

remoção dos íons de sódio não reagidos, e a outra parte foi deixada para curar sem submersão, ambas as amostras foram deixadas em temperatura ambiente (25 ºC ± 2 ºC) por 30 dias. Por fim, o material submerso foi seco em estufa a 100 °C por 24 h. A composição das amostras é apresentada na Tabela 1. As amostras de geopolímero curadas a 65 ºC foram denominadas G65s e G65 para cura submersa e cura seca, respectivamente. Da mesma forma, as amostras curadas a 80 ºC foram denominadas G80s para a cura submersa e G80 para a cura a seco.

Para a preparação do compósito, o geopolímero foi sintetizado seguindo as etapas i, ii e iii descritas anteriormente, e durante o processo de mistura (iii), a zeólita foi hidratada e adicionada à pasta geopolimérica, mantendo a agitação. Após a agitação, os passos iv, v e vi foram seguidos, realizando o processo de cura a 65°C. Cinco amostras diferentes foram preparadas, com 0, 5, 10, 20 e 30% de zeólita.

A preparação da membrana eletrofiada foi baseada nos estudos conduzidos por Rad et al. (2014) e Asiri et al. (2021). A preparação da solução para eletrofiação foi realizada misturando 8% de álcool poli vinílico (PVA) e 1% de pó (zeólita, geopolímero, ou compósito com 20 e 30% de zeólita) em agitação magnética lenta com aquecimento a 80°C por 20 min. Então, DIW foi adicionada à mistura e a agitação foi mantida a 130°C por 2h.

Foi utilizado um electrospinning desenvolvido por Calzado-Delgado *et al*. (2022), a configuração experimental do equipamento consiste em uma fonte de alta voltagem, uma bomba de seringa, uma agulha de metal e um coletor de aterramento. A solução preparada foi carregada em uma seringa de plástico de 10 mL equipada com uma agulha de 22G. A eletrofiação da amostra foi realizada em um ambiente de temperatura ambiente, com uma distância de 14 cm entre a agulha e o coletor, com uma tensão de 8 kV e uma taxa de alimentação de 13 mL/h. As membranas eletrofiadas foram denominadas MZ (zeólita/PVA), MGP (geopolímero/PVA), MZ20 (geopolímero/zeólita20%/PVA) e MZ30 (geopolímero/zeólita30%/PVA).

Para a impressão 3D, o mesmo processo de síntese de geopolímero foi realizado, seguindo as etapas i, ii e iii descritas anteriormente, após a mistura, zeólita (5%, 20% e 40%) foi adicionada à mistura, que foi mantida em agitação por mais 30 min. Após a impressão, os passos iv, v e vi foram seguidos, os compósitos foram colocados em um vidro de relógio e fechados com uma fita de alta temperatura para que a água evaporasse lentamente e o processo de cura foi realizado a 80°C. Após o período de cura submersa, as amostras foram lixadas para obter as dimensões necessárias de 4 cm x 0,4 cm para análise em leito fixo. Três amostras diferentes foram preparadas. Os sistemas Free CAD e Slicer foram utilizados para o projeto das amostras, que apresentavam as dimensões de 4,5 x 2 x 1 cm, e a extrusão foi realizada utilizando um macarrão com diâmetro de 1,6 mm.

CARACTERIZAÇÃO

A caracterização dos materiais foi realizada por meio de Difração de raios-X (DRX), Microscopia eletrônica de varredura (MEV), Fluorescência de raios-X (FRX), Espectroscopia de infravermelho com transformada de Fourier (FTIR), Tomografia micro computadorizada 3D de raios-X (mCT), Ressonância magnética nuclear em estado sólido (RNM), Espectroscopia fotoeletrônica de raios-X (XPS), Termogravimetria (geopolímeros), área superficial, tamanho e volume de poros, e por fim, foram realizadas isotermas de adsorção para os gases CO_2, CO e H_2, com temperatura a 30, 50 e 100°C e pressão entre 0e 760 mmHg.

RESULTADOS E DISCUSSÃO

Influência da temperatura de cura na síntese de geopolímeros utilizando resíduo de mineração de fosfato para captura e separação de CO_2

Neste capítulo do estudo, foram sintetizadas quatro amostras de geopolímeros à base de resíduos de metacaulim-fosfato com composições idênticas. No entanto, parte do material foi curado a 65 °C e outra parte a 80 °C. Além disso, duas das amostras foram submetidas a um processo de cura submerso por 30 dias.

A composição química dos geopolímeros, analisada por meio FRX, apresentou sílica (SiO_2), alumina (Al_2O_3), oxido de sódio (Na_2O) e de ferro (Fe_2O_3) como principais componentes das amostras, e óxidos de titânio (TiO_2), cálcio (CaO) e fosforo (P_2O_5) em uma quantidade considerável. Em relação a temperatura de cura, as amostras não apresentaram diferença significativa, entretanto, as amostras sem cura submersa apresentaram maior quantidade de óxido de sódio, indicando a eficiência da cura submersa na extração de íons Na^+.

A densidade das amostras é muito semelhante, entretanto, as amostras submersas são um pouco menores, 2.400 g/cm³, do que as amostras sem cura submersa 2.450 g/cm³, o que pode estar relacionado à dissolução do sal não reagido. A densidade das amostras aumenta à medida que a área superficial (301, 187, 337, 154 m^2/g para G65s, G65, G80s e G80, respectivamente) e o volume total dos poros (0.131, 0.075, 0.133 e 0.053 cm³/g para G65s, G65, G80s e G80, respectivamente) diminuem, o que é esperado e concorda com os resultados obtidos por Candamano et al. (2022) para compósitos de zeólita e geopolímero. A distribuição de poros das amostras G65s, G80s e G65 apresentaram um pico amplo significativo em uma faixa de aproximadamente 35-83 Å, 37-81 Å e 40-73 Å, respectivamente, sendo que a amostra G80 apresentou uma quantidade muito baixa de poros. Isso sugere que as amostras de geopolímeros obtidas neste estudo possuem estruturas mesoporosas (Alothman, 2012; Thommes et al., 2015; Wang et al., 2025).

A cristalografia das quatro amostras é consideravelmente idêntica, indicando que o processo de geopolimerização ocorreu da mesma forma, independentemente da temperatura de cura aplicada. Nos difratogramas, observa-se um amplo pico na faixa de 15 a 40º, indicando a presença de fases amorfas de aluminossilicatos, o que é esperado, dado que o geopolímero é um material predominantemente amorfo. E duas fases cristalinas foram formadas: quartzo alfa (SiO2 ICSD 062406) e faujasita (Na5.12Al52.35Si139O362.88(OH)32H39.594 ICSD 024867). A presença de fases cristalinas em geopolímeros é reportada em muitos estudos na literatura, principalmente quando há cura térmica no processo de síntese. (Davidovits, 1994; Król, Minkiewicz & Mozgawa, 2016; He *et al.*, 2020). As imagens de MEV apresentaram a estrutura densa e homogênea das amostras, confirmando uma grande quantidade de oligômeros (Si-Al) no meio reacional, o que indica um alto grau de geopolimerização.

A análise de FTIR-ATR, como esperado, apresentou bandas características de aluminossilicatos, com bandas entre 4000 e 2600 cm^{-1}, atribuídas a vibrações dos grupos Si-OH, OH e Si-OH-Al e na faixa de 1300 to 900 cm^{-1}, relacionadas a vibrações do tipo Si-O-T, onde T pode ser Al ou Si (Kljajević *et al.*, 2017). Assim como na análise de XPS, que os espectros de alta resolução de Na *1s* apresentam um único pico em 1071,6 - 1072,4 eV, característico de Na^+ em aluminossilicato de sódio e os espectros de Si *2p* e Al *2p* têm um único pico em 102,4 - 102,6 e 74,2 - 74,4 eV, respectivamente. E os espectros de MAS-RMN de ^{27}Al e ^{29}Si das amostras são muito semelhantes para todas as amostras. Nos espetros de ^{27}Al apresentaram um pico correspondente ao alumínio tetraédrico Al(IV) e um pequeno pico relacionado ao Al(VI), alumínio octaédrico. A ausência de picos nítidos de alumínio octaédrico e penta-coordenado confirma que o processo de geopolimerização está completo (Nasab, Golestanifard & MacKenzie, 2014). Através dos espectros de ^{29}Si, é possível identificar os deslocamentos químicos dos diferentes ambientes Q4 do silício na estrutura. A presença desses

picos nas amostras confirma a presença de aluminossilicato, alternando entre tetraedros de sílica e alumina.

As amostras submersas apresentaram uma maior capacidade de adsorção de CO_2 do que as não-submersas, alcançando 2,25, 2,00, 1,43 e 0,88 mmol/g para as amostras G80s, G65s, G65 e G80, respectivamente. O mesmo ocorreu para a adsorção a 50 °C, onde a maior adsorção de gás, 1,85 mmol/g, foi obtida com a amostra G80s, seguida pela amostra G65s, com uma adsorção de 1,64 mmol/g. As amostras G65 e G80 apresentaram capacidade de adsorção de 0,93 e 0,60 mmol/g, respectivamente. Por fim, como esperado, a adsorção a 100 °C apresentou o mesmo padrão observado a 30 °C, mas com uma quantidade muito menor de CO_2 adsorvido. Novamente, a maior adsorção, de 1,11 mmol/g, foi alcançada com a amostra G80s, seguida pela amostra G65s, com 0,99 mmol/g, e as amostras G65 e G80 apresentaram capacidade de adsorção de 0,70 e 0,46 mmol/g, respectivamente. Seguindo um padrão expresso em estudos na literatura, a capacidade de adsorção diminui com o aumento da temperatura, confirmando que a captura de CO_2 ocorre por meio de adsorção física, envolvendo a estrutura de microporosa e a área superficial dos materiais (Wei et al., 2012; Chang et al., 2020; Freire, José e Moreira, 2022; Freire et al., 2024).

A adsorção de CO a 30 °C seguiu o mesmo padrão da adsorção de CO_2, mas com uma capacidade de adsorção baixa. As amostras G65s e G80s apresentaram capacidades de adsorção de 0,22 e 0,18 mmol/g, respectivamente, e as amostras G65 e G80 adsorveram 0,05 e 0,06 mmol/g, respectivamente. No entanto, para a adsorção de CO a 50 °C, as amostras não seguiram o mesmo padrão, a amostra G65s apresentou a maior adsorção, de 0,14 mmol/g, seguida pela amostra G80s, com capacidade de adsorção de 0,09 mmol/g. As amostras G65 e G80 apresentaram capacidade de adsorção de 0,02 e 0,03 mmol/g, respectivamente. Para a adsorção de CO a 100 °C, as amostras G80 e G80s não apresentaram adsorção significativa (abaixo de 0,001 mmol/g). As amostras G65s e G65 apresentaram uma adsorção um pouco maior, mas ainda muito baixa, com capacidades de 0,03 e 0,01 mmol/g, respectivamente. Diferentemente das outras amostras, a amostra G80s, a 50 °C, apresentou um pequeno ciclo de histerese, chamado de H4, onde o ramo de adsorção reflete uma mistura de isotermas Tipo I e II, caracterizadas por apresentarem a principal adsorção a baixas pressões relativas (P/P_0), o que está associado ao preenchimento de microporos. Os ciclos de histerese H4 são comumente observados em materiais como cristais de zeólita, zeólitas mesoporosas específicas e estruturas de carbono micro-mesoporoso (Thommes et al., 2015; Dantas et al., 2019; Pasabeyoglu et al., 2024).

Por fim, a capacidade de adsorção de H_2 a 30 °C foi muito baixa para todas as amostras. A quantidade adsorvida foi de 0,015 mmol/g para a amostra G65s, 0,008 mmol/g para a amostra G80s e 0,007 mmol/g para as amostras G65 e G80. A capacidade de adsorção a 50 e 100 °C foi insignificante, com todas as amostras apresentando uma quantidade adsorvida inferior a 0,006 mmol/g. As isotermas apresentaram uma ampla histerese, que, devido à adsorção muito baixa, foi considerada um comportamento pronunciado originado pelo equipamento. Até o momento, nenhum estudo foi encontrado na literatura sobre a capacidade de adsorção de geopolímeros para CO e H_2. No entanto, ao comparar com outros sólidos, como zeólitas, os valores obtidos para os geopolímeros neste estudo são significativamente mais baixos (Cui, Xing, et al., 2023; Streb & Mazzotti, 2021).

Os resultados confirmam a importância da cura submersa durante a síntese do geopolímero. Em relação à temperatura, o geopolímero curado a 80 °C apresentou maior capacidade de adsorção do que a amostra curada a 65 °C. No entanto, as características das duas amostras submersas são muito semelhantes. Assim, a única característica que parece influenciar diretamente a capacidade de adsorção é a área superficial e o tamanho dos poros, e, para todas

as amostras, a capacidade de adsorção aumentou à medida que a área superficial e o tamanho dos poros também aumentaram.

Síntese e caracterização de compósito de geopolímero/zeólita 13X para captura e separação de CO_2

Este capítulo da tese aborda a síntese e caracterização de compósitos de geopolímero com zeólita 13X, apresentando uma comparação dos resultados obtidos com os de geopolímero e zeólita 13X puros.

A composição química dos compósitos, amostras Z13X e GP, analisada por FRX, apresentou sílica (SiO_2), a alumina (Al_2O_3) e o óxido de sódio (Na_2O) como principais componentes das composições, e quantidade significativa de óxidos de magnésio (MgO) e ferro (Fe_2O_3) na amostra Z13X, e óxidos de ferro (Fe_2O_3), titânio (TiO_2), cálcio (CaO) e fosfato (P_2O_5) na amostra GP. E a s amostras dos compósitos, conforme esperado, apresentam, da mesma forma que os precursores, uma quantidade considerável de SiO_2, Al_2O_3, Na_2O e Fe_2O_3.

A densidade das amostras aumenta à medida que o volume total de poros diminui, o que é esperado e está de acordo com os resultados obtidos por Candamano et al. (2022) para compósitos de zeólita e geopolímero. O tamanho dos poros, o volume total de poros e a área de superfície do Z13x são superiores aos do GP, e nos compósitos, a área superficial aumenta à medida que o teor de zeólita aumenta, a área superficial da zeólita e do geopolímero 550 e 301 m^2/g e 340, 345, 405 e 438 m^2/g para os compósitos Z5, Z10, Z20 e Z30, respectivamente. As amostras de geopolímeros e compósitos apresentaram uma distribuição mesoporosa ampla na faixa de 60 e 55 Å, respectivamente, indicando uma estrutura mesoporosa mais uniforme que a da amostra de zeólita, que apresentou poucos poros em torno de 20 Å e uma ampla distribuição de poros entre 80 e 320 Å.

Através da análise de DRX foi possível identificar duas fases cristalinas em todas as amostras, quartzo (SiO_2 ICDD 01-086-1628) e Faujasita ($Na_2Al_2Si_{2.4}O_{8.8}\cdot 6.7H_2O$ – ICDD 00-012-0246), o geopolímero com picos de baixa intensidade, e nos compósitos a intensidade aumenta com o aumento de zeólita no material. Através da análise de MEV foi possível visualizar a forma amorfa do GP e cristalina da Z13X e nos compósitos é possível notar a estrutura densa do geopolímero e as estruturas cristalinas da zeólita com o aumento da mesma nas amostras.

A análise de FTIR-ATR, para todas as amostras, identificou bandas características de aluminossilicatos, entre 4000 e 2600 cm^{-1} (Si-OH, OH, Si-OH-Al) e 1300 a 900 cm^{-1} (Si-O-T, com T como Al ou Si) (Kljajević et al., 2017). Os espectros XPS de Na *1s*, Si *2p* e Al *2p* apresentaram picos em ~1072,3 eV, ~102,7 eV e ~74,4 eV, respectivamente, característicos de aluminossilicato de sódio. As amostras Z13X e compósitos também apresentaram Mg *1s*, com picos em ~1303,7 eV, atribuídos ao grupo Mg-O. Além disso, as amostras GP, Z20 e Z30 mostraram uma pequena quantidade de Fe *2p*, deconvoluída em duas contribuições: 711,4 e 712,0 eV, correspondentes ao grupo Fe(III) (~723,9 e ~725,2 eV), identificadas como transições por agitação de satélite $\pi \rightarrow \pi^*$. Os espectros de MAS-RMN de ^{27}Al e ^{29}Si são semelhantes para todas as amostras. Nos espetros de ^{27}Al apresentaram um pico correspondente ao alumínio tetraédrico Al(IV) e um pequeno pico relacionado ao Al(VI), alumínio octaédrico. A ausência de picos intensos de alumínio octaédrico e penta-coordenado confirma que o processo de geopolimerização está completo (Nasab, Golestanifard and MacKenzie, 2014). Através dos espectros de ^{29}Si, foram identificados deslocamentos químicos correspondentes a ambientes Q4 de silício, confirmando aluminossilicato com alternância entre tetraedros de sílica e alumina.

Nas isotermas de adsorção de CO_2 a 30 °C, a Z13X apresentou maior capacidade de adsorção (3,98 mmol/g), seguida das amostras Z3 0 e Z20 (2,58 e 2,57 mmol/g), GP e Z10

apresentaram similar capacidade de adsorção de 2,00 e 1.96 mmol/g, e o compósito Z5 apresentou menor capacidade adsortiva, de apenas 1,65 mmol/g. A capacidade de adsorção das amostras diminui com o aumento da temperatura, o que confirma que a adsorção acontece de forma física, e está relacionada à estrutura microporosa dos materiais (Wei et al., 2012; Chang et al., 2020; Freire et al., 2024). Por fim, a capacidade de adsorção de CO foi muito baixa em comparação à de CO_2. A 30 ºC, alcançou 0,57, 0,33, 0,25, 0,22, 0,16 e 0,16 mmol/g para as amostras Z13X, Z30, Z20, GP, Z10 e Z5, respectivamente. Para a adsorção de H_2 a 30 °C, todas as amostras apresentaram capacidade abaixo de 0,021. A capacidade de adsorção da amostra Z30 foi insignificante, próxima de 0,001 mmol/g.

Em síntese, os compósitos com maior quantidade de zeólita apresentaram os melhores resultados, o que era esperado, já que a zeólita possui maior capacidade de adsorção do que o geopolímero. As características das amostras de compósito são bastante semelhantes; entretanto, a única característica que parece influenciar a capacidade de adsorção é a área superficial, que aumenta com a adição de mais zeólita.

Compósito inovador de geopolímero/zeólita/PVA produzido por eletrofiação

Neste capítulo do estudo, foram desenvolvidas quatro amostras eletrofiadas, contendo geopolímero (MGP), zeólita 13X (MZ), e compósitos com 20 e 30 % de zeólita (Z20 e Z30).

A análise de DRX nas amostras MGP e MZ revelou pequenas esferas, onde a zeólita e o geopolímero estão encapsulados na membrana fibrosa de forma uniforme, sem conglomerados, como nas membranas de Zhang et al. (2021). A diferença entre os materiais é visível, o MGP tem esferas amorfas (~127,81), enquanto a MZ tem esferas (~88,23) mais uniformes e alongadas. A MZ20 apresenta mais esferas (~56,97) e poucos aglomerados, enquanto a MZ30 tem muitos aglomerados com esferas (~93,57).

A área superficial das amostras é muito baixa em comparação com algumas membranas eletrofiadas apresentadas na literatura e, até o momento, não foram encontrados estudos sobre compósitos de geopolímero/zeólita/PVA para uma melhor comparação (Schneider et al., 2024), a área superficial maior foi de 24,3 m^2/g, obtida com a amostra MZ30, seguida da MZ20 com 17,4 m^2/g, MGP com 11,6 m^2/g, e a menor área foi de 2,40 m^2/g, da MZ. As distribuições de poros das amostras MGP, MZ20 e MZ30 apresentaram uma ampla distribuição de mesoporos, com tamanhos de poros predominantes em aproximadamente 25 e 100 Å. A amostra MZ apresentou uma distribuição de poros muito baixa, sugerindo uma porosidade uniforme, com poucos poros em torno de 25 Å e uma ampla distribuição de mesoporos entre aproximadamente 70 e 230 Å. No geral, as amostras preparadas neste estudo exibem estruturas mesoporosa, conforme os achados de Wang et al. (2025).

Os espectros FTIR das amostras apresentaram semelhanças significativas, com bandas características do PVA. Além disso, apresenta vibrações Si–O–Si, bandas típicas de materiais zeolíticos. Os espectros XPS das amostras apresentam energias de ligação similares, com pequenas diferenças na intensidade dos picos, concentrações atômicas e pesos. As amostras não apresentaram aluminossilicatos na superfície, como esperado, devido à baixa concentração nas amostras, que estão recobertas por PDMS. A análise EDS também indica baixos teores de Si e Al.

Por fim, a capacidade de adsorção de CO_2 a 30 °C obtida pelas isotermas foi baixa em relação às amostras anteriores, sendo 0,62, 0,43, 0,21 e 0,62 mmol/g, para as amostras MZ, MGP, MZ20 e MZ30, respectivamente. Para CO e H_2, as amostras apresentaram uma capacidade de adsorção irrelevante, como esperado, já que o objetivo é utilizar o material para captura de CO_2.

Phosphate-waste based geopolymer/zeolite 13x composites manufactured by 3D printing for gas capture and separation

Este capítulo da tese aborda a síntese e caracterização de compósitos 3D de geopolímero com zeólita 13X (5%, 20 e 40%), e aplicação em coluna de adsorção de leito fixo.

A composição química dos compósitos, analisada por XRF, apresentou sílica (SiO_2), alumina (Al_2O_3) e óxido de sódio (Na_2O) como principais componentes. No entanto, foi observada uma quantidade considerável de óxido de ferro (Fe_2O_3) e titânio (TiO_2), além de pequenas quantidades de óxidos de cálcio (CaO) e fosfato (P_2O_5).

A área superficial aumenta à medida que o teor de zeólita aumenta e a densidade diminui, sendo 53, 203 e 374 m^2/g e 2,38, 2,27 e 2,18 g/cm^3 para C5, C20 e C40, respectivamente. Assim como para os outros materiais compósitos desenvolvidos neste estudo, as amostras apresentaram alta cristalinidade, mesmo o compósito com menor quantidade de zeólita (5 %). Os picos foram identificados como quartzo (SiO_2 ICDD 01-086-1628) e Faujasita ($Na_2Al_2Si_2.4O_8.8\cdot6.7H_2O$ – ICDD 00-012-0246). A principal diferença está na intensidade dos picos.

Através das imagens de MEV das amostras de compósitos foi possível observar a estrutura densa, homogênea e amorfa do geopolímero. À medida que a quantidade de zeólita no compósito aumenta, nota-se um aumento nos materiais cristalinos na amostra. Entretanto, diferente das amostras C20 e C40, a amostra C5 apresentou algumas fissuras, o que pode estar relacionado ao fato de a imagem ter sido tirada da área onde o material foi cortado, na superfície das amostras.

Os espectros de MAS-NMR de ^{27}Al das amostras são bastante semelhantes. Todas apresentaram um pico em aproximadamente 63 ppm, relacionado ao alumínio tetraédrico Al(IV) (Freire et al., 2024), e um pequeno pico em ~-20 ppm, referente ao alumínio octaédrico Al(VI). Esses picos estão associados à zeólita, conforme a análise de XRD, que indicou picos cristalinos relacionados à Faujasita. A ausência de picos nítidos de alumínio octaédrico e penta-coordenado confirma que o processo de geopolimerização foi concluído (Nasab, Golestanifard e MacKenzie, 2014). Os espectros de ^{29}Si de todas as amostras apresentam cinco picos significativos semelhantes, diferindo na intensidade dos picos conforme aumenta a concentração de zeólita. Os espectros identificam deslocamentos químicos dos diferentes ambientes de silício Q^4 na estrutura. A presença desses picos confirma a existência de aluminossilicatos, devido à alternância entre tetraedros de sílica e alumina (Gore et al., 2002).

A análise de FTIR-ATR confirma a presença de bandas características de materiais aluminossilicatos nas amostras. As bandas entre 4000 e 2600 cm^{-1}, atribuídas às vibrações de alongamento Si-OH, OH e Si-OH-Al, e entre 1200 e 900 cm^{-1} que corresponde ao alongamento assimétrico de estruturas do tipo Si-O-T, onde T é Si ou Al (Kljajević et al., 2017), bandas sobrepostas entre 1200 e 400 cm^{-1} são decorrentes das estruturas cristalinas e amorfas dos precursores Z13X e geopolímero, respectivamente (Minelli et al., 2018). Picos em ~980 cm^{-1} representam o alongamento simétrico das ligações Si-O e estão presentes nos espectros de todas as amostras (Papa et al., 2023). Bandas de 800 a 500 cm^{-1} são características de vibrações simétricas Si-O-Si, enquanto bandas entre 750 e 554 cm^{-1} correspondem a vibrações de materiais zeolíticos, neste caso, a Faujasita, tipo zeólita 13X (Jiménez, Lalangui, Guacho, Paucar et al., 2019).

A análise de XPS, realizada para determinar os estados químicos e a composição atômica da superfície das partículas das amostras, de forma geral, apresentou espectros muito semelhantes, já que todas são aluminossilicatos, com variações principalmente na intensidade dos picos, concentrações atômicas e peso. Os espectros XPS de Na 1*s*, Si 2*p* e Al 2*p*

apresentaram picos em ~1072,0 eV, ~102,1 eV e ~74,1 eV, respectivamente, característicos de aluminossilicato de sódio.

Por fim, os compósitos 3D mostraram boa estabilidade estrutural e porosidade ajustável, com aumento da área superficial conforme cresce o teor de zeólita. Essa combinação possibilita materiais eficientes e versáteis para captura e separação de CO_2, destacando o potencial da manufatura aditiva para produzir adsorventes sustentáveis e de baixo custo.

CONCLUSÃO

Para avaliar o impacto da temperatura de cura na síntese de geopolímeros, amostras à base de metacaulim e rejeitos de fosfato foram curadas a 65 e 80 ºC, com algumas submetidas a cura submersa por 28 dias. O FTIR e NMR indicaram material reativo significativo em todas as amostras. A capacidade de adsorção de CO_2 foi maior nas amostras submersas (2,24 e 2,00 mmol/g a 30 ºC para G80s e G65s) e diminuiu com o aumento da temperatura (1,42 e 0,88 mmol/g para G65 e G80).

Compósitos de geopolímero/zeólita apresentaram maior capacidade de adsorção em amostras com mais zeólita, atingindo 3,98 mmol/g para Z13X e 1,65 mmol/g para Z5. A baixa adsorção de CO e H_2 confirma o potencial dos compósitos para captura e separação de CO_2.

Na eletrofiação, quatro membranas poliméricas foram criadas e analisadas. A baixa concentração de aluminossilicatos resultou em baixa adsorção de CO_2 (0,62 a 0,21 mmol/g). Estudos adicionais são necessários para melhorar sua eficiência em captura de gases.

Além disso, os compósitos de geopolímero/zeólita impressos em 3D apresentaram estruturas estáveis e porosidade ajustável, com aumento da área superficial conforme o aumento do teor de zeólita, confirmando seu potencial para aplicações práticas na captura de CO_2.

Palavras-Chave: Zeólita, Geopolímero, Captura de CO_2, Impressão 3D, Eletrofiação.

RESUMEN AMPLIADO

INTRODUCIÓN

Los combustibles fósiles han sido la principal fuente de energía del mundo y se espera que sigan siéndolo durante varias décadas (Nasr et al., 2021). Su combustión es uno de los principales factores responsables de las emisiones de gases de efecto invernadero, como el metano (CH_4), óxido nitroso (N_2O) y dióxido de carbono (CO_2), que causan daños permanentes e irreversibles al sistema climático (Ahmed et al., 2020). Según Kazancoglu et al. (2021), las emisiones de CO_2 contribuyen al aumento de la temperatura media global, provocando el ascenso del nivel del mar, inundaciones y pérdida de biodiversidad (Liu et al., 2021). Aunque se han propuesto dos estrategias principales para mitigar estas emisiones —la sustitución de fuentes fósiles por energías renovables y la captura de CO_2 directamente de la atmósfera o de fuentes industriales—, la primera opción enfrenta importantes limitaciones técnicas y económicas (Silveira, 2021). Por ello, la captura, almacenamiento y utilización del CO_2 (CCU) se considera una alternativa clave a corto y medio plazo para reducir la huella de carbono (Candamano et al., 2022). Se estima que hasta el 90 % de las emisiones de CO_2 pueden ser capturadas tras un proceso de separación. No obstante, los elevados costes de capital y las limitaciones de almacenamiento han impulsado el desarrollo de tecnologías que permitan valorizar el CO_2 capturado, convirtiéndolo en productos como metano, metanol o éter dimetílico (Damideh et al., 2020; Candamano et al., 2022).

Recientemente, la adsorción ha ganado protagonismo frente a otras tecnologías de separación de CO_2, como la absorción con aminas, que requiere solventes corrosivos, un elevado consumo energético y presenta altos costes operativos. En contraste, los procesos de adsorción ofrecen ventajas como menor demanda energética, mayor estabilidad, operación más simple y el uso de materiales sólidos, no tóxicos y de bajo coste, especialmente si se derivan de residuos industriales (Guerrero-Pérez, 2024). En este contexto, las zeolitas han sido ampliamente estudiadas por su estructura microporosa y cristalina, alta área superficial, estabilidad térmica y elevada selectividad de adsorción. Además, pueden sintetizarse a partir de aluminosilicatos o residuos como cenizas volantes, cáscara de arroz o cenizas de carbón (Silveira, 2021). En los últimos años, el geopolímero ha ganado interés relevante en investigaciones, principalmente debido a su bajo costo y a la síntesis ecológicamente amigable. La matriz de geopolímero es predominantemente amorfa y está formada por una red tridimensional de aluminossilicatos, generalmente activada por una solución alcalina (Davidovits, 1994; Candamano et al., 2022).

Además, los adsorbentes híbridos de geopolímero/zeolita también han demostrado ser eficientes en la captura de CO_2 debido a sus propiedades adecuadas de selectividad (Silveira, 2021). La resistencia mecánica, la resistencia química, la estabilidad térmica y el bajo costo de síntesis son aspectos favorables para el uso de estos materiales en procesos de separación (Minelli et al., 2018). Además, la presencia de mesoporos en materiales geopoliméricos/zeolíticos puede promover la rápida difusión de gases dentro de los poros, mejorando así la eficiencia de adsorción/desorción de CO_2.

Una forma de preparar materiales geopoliméricos es mediante impresión 3D, lo que permite producir monolitos adecuados para aplicaciones en columnas de lecho fijo. Sin embargo, los estudios actuales sobre impresión 3D de geopolímeros se han centrado en el uso de estos materiales como materiales de construcción, que no requieren una red porosa controlada. Para la separación y captura de CO_2, es necesario desarrollar materiales con redes jerárquicas para obtener alta selectividad y capacidad de adsorción (Souza, 2021). Así, la preparación de geopolímeros porosos jerárquicos moldeados como monolitos o pellets

geométricos sería útil para la separación cíclica de gases por adsorción. No obstante, hasta donde sabemos, los monolitos compuestos de zeolita/geopolímero aún no se han desarrollado ni aplicado para la separación de CO_2/H_2.

Además, los compuestos de geopolímeros podrían moldearse utilizando la técnica de electrospinning y el método sol-gel para producir nanofibras elásticas y resistentes a altas temperaturas (Tang et al., 2022). El electrospinning consiste en la formación de fibras a partir de una solución polimérica, inyectándola desde una fina aguja entre dos electrodos con cargas eléctricas de polaridad opuesta, uno ubicado en la aguja y el otro en un colector. El chorro cargado de la solución se evapora durante su trayecto hasta el colector, formando el arreglo de fibras no tejidas. Este método puede utilizarse para producir la morfología deseada, dependiendo de las propiedades de la solución, como el peso molecular del polímero, conductividad, tensión superficial y viscosidad. Parámetros como la distancia entre los electrodos, el voltaje aplicado, la humedad, el flujo volumétrico y el diámetro de la aguja pueden ajustarse para permitir la evaporación suficiente del solvente, evitando que las fibras se derritan o no se formen (Haider, Haider y Kang, 2018). Por lo tanto, el electrospinning se destaca como un método simple y económico para producir nanofibras, utilizando diversas fuentes poliméricas (Yarin, Koombhongse y Reneker, 2001b, 2001a; Silva et al., 2021).

Considerando las brechas de conocimiento relacionadas con el uso de materiales de bajo costo con porosidad jerárquica y el desafío de producir materiales con alta capacidad de adsorción y selectividad, esta tesis tiene como objetivo desarrollar, mediante electrospinning e impresión 3D, materiales compuestos de geopolímero y zeolita 13X con porosidad jerárquica con alto desempeño en la captura de CO_2 en mezclas binarias CO_2/N_2 provenientes de gases de escape.

OBJETIVOS

El objetivo principal de esta tesis es explorar el potencial de geopolímeros elaborados a partir de residuos de minería de fosfato, zeolitas y materiales compuestos de geopolímero/zeolita con una estructura porosa jerárquica, como adsorbentes innovadores, sostenibles, de bajo costo y fácilmente escalables. Los materiales se prepararán mediante técnicas de electrospinning e impresión 3D, con el objetivo de obtener adsorbentes selectivos para la separación de mezclas binarias de CO_2/H_2.

METODOLOGÍA

El proceso utilizado para sintetizar las muestras de geopolímeros se basó en Minelli et al. (2016), Chen et al. (2020) y Freire et al. (2020; 2024), donde los geopolímeros de bajo costo fueron preparados reemplazando parte del metacaolín (MK) por desecho de minería de fosfato (PW), y una mezcla de hidróxido de sodio y silicato de sodio como activador alcalino. Las razones molares para la síntesis del geopolímero son SiO2:Al2O3 = 3,30; Na2O:SiO2 = 0,30; $Na_2O:Al_2O_3$ = 0,99; y $H_2O:Na_2O$ = 12,00, seleccionadas con base en un estudio desarrollado por Davidovits (1994).

Inicialmente, para sintetizar el metacaolín, el caolín se calcinó a 900 ºC por 60 minutos. El geopolímero se preparó entonces siguiendo seis etapas: i) mezcla de los dos componentes sólidos (MK 35% y PW 19%); ii) preparar el activador alcalino, mezclando NaOH (11%), silicato de sodio (SS, 13%) y agua desionizada (DIW, 22%) a 800 rpm por 10 minutos en un agitador magnético; iii) preparación de la suspensión añadiendo los sólidos a la solución activadora alcalina y mezclando durante 15 minutos a 1500 rpm, en un agitador mecánico; iv) moldear la pasta geopolimérica en forma cilíndrica, utilizando un molde de silicona de 2x4 cm; v) dos muestras se prepararon y curaron en estufa (productos químicos VENTI-line VWR) a 80

°C y 65 °C. El molde se cubrió con una cinta de alta temperatura para que el agua se evaporara lentamente; vi) después de desmoldar, parte de las muestras se sumergió en agua DIW para eliminar los iones de sodio no reaccionados, y otra parte se dajó para curar sin sumersión, ambas muestras se dejaron a temperatura ambiente (25 ºC ± 2 ºC) durante 30 días. Finalmente, el material sumergido se secó en estufa a 100 °C durante 24 horas. La composición de las muestras se presenta en la Tabla 1. Las muestras de geopolímero curadas a 65 °C se denominaron G65s y G65 para curado sumergido y seco, respectivamente. De manera similar, las muestras curadas a 80 °C se denominaron G80s para curado sumergido y G80 para curado seco.

Para la preparación del compuesto, el geopolímero se sintetizó siguiendo las etapas i, ii y iii descritas anteriormente, y durante el proceso de mezcla (iii), la zeolita se hidrató y añadió a la pasta geopolimérica, manteniendo la agitación. Después de la agitación, se siguieron los pasos iv, v y vi, realizando el proceso de curado a 65°C. Se prepararon cinco muestras diferentes, con 0, 5, 10, 20 e 30 % de zeolita.

La preparación de la membrana electrohilada se basó en los estudios realizados por Rad et al. (2014) y Asiri et al. (2021). La preparación de la solución para electrospinning se realizó mezclando 8% de alcohol polivinílico (PVA) y 1% de polvo (zeolita, geopolímero o compuesto con 20 y 30% de zeolita) en agitación magnética lenta con calentamiento a 80°C durante 20 min. Luego, se añadió DIW a la mezcla y la agitación se mantuvo a 130°C durante 2 horas. Se utilizó un Electrospinning desarrollado por Calzado-Delgado et al. (2022), cuya configuración experimental del equipo consiste en una fuente de alta tensión, una bomba de jeringa, una aguja de metal y un colector a tierra. La solución preparada se cargó en una jeringa de plástico de 10 mL equipada con una aguja de 22G. El electrospinning de la muestra se realizó en un ambiente a temperatura ambiente, con una distancia de 14 cm entre la aguja y el colector, con una tensión de 8 kV y una tasa de alimentación de 13 mL/h. Las membranas electrohiladas fueron denominadas MZ (zeolita/PVA), MGP (geopolímero/PVA), MZ20 (geopolímero/zeolita20%/PVA) y MZ30 (geopolímero/zeolita30%/PVA).

Para la impresión 3D, se realizó el mismo proceso de síntesis de geopolímero, siguiendo las etapas i, ii y iii descritas anteriormente. Después de la mezcla, se añadió zeolita (5%, 20% y 40%) a la mezcla, que se mantuvo en agitación durante 30 minutos adicionales. Tras la impresión, se siguieron los pasos iv, v y vi, los compuestos fueron colocados en un vidrio de reloj y cubiertos con una cinta de alta temperatura para que el agua se evaporara lentamente, y el proceso de curado se realizó a 80°C. Después del período de curado sumergido, las muestras fueron lijadas para obtener las dimensiones necesarias de 4 cm x 0,4 cm para el análisis en lecho fijo. Se prepararon tres muestras diferentes. Los sistemas Free CAD y Slicer se utilizaron para el diseño de las muestras, que presentaban dimensiones de 4,5 x 2 x 1 cm, y la extrusión se realizó utilizando un fideo con un diámetro de 1,6 mm.

CARACTERIZACIÓN

La caracterización de los materiales se realizó mediante Difracción de rayos X (DRX), Microscopía electrónica de barrido (MEB), Fluorescencia de rayos X (FRX), Espectroscopía de infrarrojo con transformada de Fourier (FTIR), Tomografía microcomputarizada (mCT) 3D de rayos X, Resonancia magnética nuclear de estado sólido (RMN), Espectroscopía fotoelectrónica de rayos X (XPS), Termogravimetría (geopolímeros), área superficial, tamaño y volumen de poros, y finalmente, se realizaron isotermas de adsorción para los gases CO_2, CO y H2, con temperaturas de 30, 50 y 100°C y presiones entre 0 y 760 mmHg.

RESULTADOS Y DISCUSION

Influencia de la temperatura de curado en la síntesis de geopolímeros utilizando residuos de minería de fosfato para la captura y separación de CO_2

En este capítulo del estudio, se sintetizaron cuatro muestras de geopolímeros a base de residuos de metacaolín-fosfato con composiciones idénticas. Sin embargo, parte del material se curó a 65 °C y otra parte a 80 °C. Además, dos de las muestras se sometieron a un proceso de curado sumergido durante 30 días.

La composición química de los geopolímeros, analizada mediante FRX, mostró que la sílice (SiO_2), alúmina (Al_2O_3), óxido de sodio (Na_2O) y óxido de hierro (Fe_2O_3) son los principales componentes de las muestras, con óxidos de titanio (TiO_2), calcio (CaO) y fósforo (P_2O_5) en cantidades considerables. Respecto a la temperatura de curado, las muestras no presentaron diferencias significativas; sin embargo, las muestras que no fueron curadas por inmersión presentaron una mayor cantidad de óxido de sodio, lo que indica que el curado sumergido es eficaz para eliminar iones Na^+.

La densidad de las muestras es muy similar; no obstante, las muestras sumergidas son ligeramente menos densas (2.40 g/cm³) que las muestras sin curado sumergido (2.45 g/cm³), lo que podría estar relacionado con la disolución de la sal no reaccionada. La densidad de las muestras aumenta a medida que disminuyen el área superficial (301, 187, 337, 154 m²/g para G65s, G65, G80s y G80, respectivamente) y el volumen total de poros (0,131, 0,075, 0,133 y 0,053 cm³/g para G65s, G65, G80s y G80, respectivamente), lo cual concuerda con los resultados obtenidos por Candamano et al. (2022) para compuestos de zeolita y geopolímero. La distribución de poros en las muestras G65s, G80s y G65 mostró un pico amplio significativo en un rango de aproximadamente 35-83 Å, 37-81 Å y 40-73 Å, respectivamente, mientras que la muestra G80 presentó una cantidad muy baja de poros. Esto sugiere que las muestras de geopolímeros obtenidas en este estudio tienen estructuras mesoporosa (Alothman, 2012; Thommes et al., 2015; Wang et al., 2025).

La cristalografía de las cuatro muestras es considerablemente idéntica, lo que indica que el proceso de geopolimerización ocurrió de manera uniforme, independientemente de la temperatura de curado aplicada. Los difratogramas muestran un pico amplio en el rango de 15 a 40°, indicando la presencia de fases amorfas de aluminosilicatos, lo que es esperado, dado que el geopolímero es un material predominantemente amorfo. Además, se formaron dos fases cristalinas: cuarzo alfa (SiO_2 ICSD 062406) y faujasita ($Na_{5.12}Al_{52.35}Si_{139}O_{362.88}(OH)_{32}H_{39.594}$ ICSD 024867). La presencia de fases cristalinas en geopolímeros se ha reporatdo en numerosos estudios, particularmente cuando se utiliza curado térmico en el proceso de síntesis (Davidovits, 1994; Król, Minkiewicz y Mozgawa, 2016; He et al., 2020).

Las imágenes SEM mostraron la estructura densa y homogénea de las muestras, confirmando una gran cantidad de oligómeros (Si-Al) en el medio de reacción, lo que indica un alto grado de geopolimerización.

El análisis FTIR-ATR mostró, como era esperado, bandas características de aluminosilicatos, con bandas entre 4000 y 2600 cm^{-1} atribuidas a vibraciones de los grupos Si-OH, OH y Si-OH-Al, y en el rango de 1300 a 900 cm^{-1}, relacionadas con vibraciones del tipo Si-O-T, donde T puede ser Al o Si (Kljajević et al., 2017). En el análisis XPS, los espectros de alta resolución de Na 1*s* presentaron un único pico en 1071,6-1072,4 eV, característico de Na^+ en aluminosilicatos de sodio; los espectros de Si 2p y Al 2p mostraron un único pico en 102,4-102,6 y 74,2-74,4 eV, respectivamente. Los espectros MAS-RMN de ^{27}Al y ^{29}Si de las muestras fueron muy similares. Los espectros de ^{27}Al mostraron un pico correspondiente al aluminio tetraédrico Al(IV) y un pequeño pico relacionado con el Al(VI), aluminio octaédrico. La ausencia de picos nítidos de aluminio octaédrico y pentacoordinado confirma que el proceso de geopolimerización está completo (Nasab, Golestanifard y MacKenzie, 2014). Los espectros de

^{29}Si permitieron identificar los desplazamientos químicos de los diferentes ambientes Q^4 del silicio en la estructura. La presencia de estos picos en las muestras confirma la existencia de aluminosilicatos, alternando entre tetraedros de sílice y alúmina.

Las muestras sumergidas mostraron una mayor capacidad de adsorción de CO_2 que las no sumergidas, alcanzando 2,25, 2,00, 1,43 y 0,88 mmol/g para las muestras G80s, G65s, G65 y G80, respectivamente. El mismo patrón se observó en la adsorción a 50 °C, donde la muestra G80s tuvo la mayor adsorción (1,85 mmol/g), seguida por G65s (1,64 mmol/g). Las muestras G65 y G80 mostraron capacidades de adsorción de 0,93 y 0,60 mmol/g, respectivamente. La adsorción a 100 °C presentó el mismo patrón observado a 30 °C, aunque con una cantidad menor de CO_2 adsorbido. Nuevamente, la mayor adsorción fue de 1,11 mmol/g para la muestra G80s, seguida por G65s con 0,99 mmol/g; G65 y G80 mostraron capacidades de adsorción de 0,70 y 0,46 mmol/g, respectivamente. Estos resultados confirman que la capacidad de adsorción disminuye con el aumento de la temperatura, lo cual concuerda con la literatura, indicando que la captura de CO_2 ocurre mediante adsorción física, relacionada con la estructura microporosa y el área superficial de los materiales (Wei et al., 2012; Chang et al., 2020; Freire, José y Moreira, 2022; Freire et al., 2024).

La adsorción de CO a 30 °C siguió el mismo patrón que la adsorción de CO_2, aunque con capacidades más bajas. G65s y G80s presentaron capacidades de adsorción de 0,22 y 0,18 mmol/g, respectivamente, mientras que G65 y G80 mostraron 0,05 y 0,06 mmol/g, respectivamente. Sin embargo, a 50 °C, el patrón fue diferente: G65s presentó la mayor adsorción (0,14 mmol/g), seguida de G80s (0,09 mmol/g), y G65 y G80 mostraron capacidades de 0,02 y 0,03 mmol/g, respectivamente. A 100 °C, las muestras G80 y G80s no presentaron adsorción significativa (menos de 0,001 mmol/g). Las muestras G65s y G65 mostraron capacidades algo mayores, pero aún muy bajas (0,03 y 0,01 mmol/g, respectivamente). La muestra G80s presentó un pequeño ciclo de histéresis H4 a 50 °C, típico de isotermas de Tipo I y II, asociadas con el llenado de microporos (Thommes et al., 2015; Dantas et al., 2019; Pasabeyoglu et al., 2024).

Finalmente, la capacidad de adsorción de H_2 a 30 °C fue muy baja para todas las muestras, con valores de 0,015 mmol/g para G65s, 0,008 mmol/g para G80s, y 0,007 mmol/g para G65 y G80. A 50 y 100 °C, las capacidades fueron insignificantes (menos de 0,006 mmol/g). Las isotermas presentaron una histéresis amplia, atribuida al comportamiento del equipo debido a la baja adsorción. Hasta ahora, no se han encontrado estudios en la literatura sobre la capacidad de adsorción de geopolímeros para CO y H_2. Comparados con otros sólidos como las zeolitas, los valores obtenidos para los geopolímeros son significativamente menores (Cui, Xing, et al., 2023; Streb & Mazzotti, 2021).

Los resultados destacan la importancia del curado sumergido durante la síntesis del geopolímero. En cuanto a la temperatura, los geopolímeros curados a 80 °C mostraron mayor capacidad de adsorción que los curados a 65 °C. Sin embargo, las características de las muestras sumergidas son muy similares. Por tanto, parece que el único factor que influye directamente en la capacidad de adsorción es el área superficial y el tamaño de los poros. En todas las muestras, la capacidad de adsorción aumentó con el incremento del área superficial y del tamaño de los poros.

Síntesis y caracterización de compuestos de geopolímero/zeolita 13X para captura y separación de CO_2

Este capítulo de la tesis aborda la síntesis y caracterización de compuestos de geopolímero con zeolita 13X, presentando una comparación de los resultados obtenidos con los del geopolímero y la zeolita 13X puros.

La composición química de los compuestos, muestras Z13X y GP, analizada mediante FRX, mostró sílice (SiO_2), alúmina (Al_2O_3) y óxido de sodio (Na_2O) como los principales componentes, y una cantidad significativa de óxidos de magnesio (MgO) y hierro (Fe_2O_3) en la muestra Z13X, así como óxidos de hierro (Fe_2O_3), titanio (TiO_2), calcio (CaO) y fosfato (P_2O_5) en la muestra GP. Como era de esperarse, las muestras de los compuestos presentaron una cantidad considerable de SiO_2, Al_2O_3, Na_2O y Fe_2O_3, similares a sus precursores.

La densidad de las muestras aumentó a medida que el volumen total de poros disminuyó, lo cual es consistente con los resultados obtenidos por Candamano et al. (2022) para compuestos de zeolita y geopolímero. El tamaño de los poros, el volumen total de poros y la superficie específica de Z13X son superiores a los de GP. En los compuestos, la superficie específica aumentó con el contenido de zeolita: 550 m^2/g para la zeolita, 301 m^2/g para el geopolímero, y 340, 345, 405 y 438 m^2/g para los compuestos Z5, Z10, Z20 y Z30, respectivamente. Las muestras de geopolímeros y compuestos presentaron una distribución mesoporosa uniforme en el rango de 60 y 55 Å, mientras que la muestra de zeolita mostró pocos poros en torno a 20 Å y una amplia distribución entre 80 y 320 Å.

El análisis de DRX identificó dos fases cristalinas en todas las muestras: cuarzo (SiO_2 ICDD 01-086-1628) y faujasita ($Na_2Al_2Si_{2.4}O_{8.8}\cdot 6.7H_2O$ – ICDD 00-012-0246). En el geopolímero, los picos eran de baja intensidad, mientras que, en los compuestos, la intensidad aumentó con la mayor proporción de zeolita. El análisis MEV mostró la estructura amorfa de GP, la estructura cristalina de Z13X y, en los compuestos, una estructura densa del geopolímero junto con estructuras cristalinas de la zeolita.

El análisis FTIR-ATR identificó bandas características de aluminosilicatos en todas las muestras, en el rango de 4000-2600 cm^{-1} (Si-OH, OH, Si-OH-Al) y 1300-900 cm^{-1} (Si-O-T, donde T puede ser Al o Si) (Kljajević et al., 2017). Los espectros XPS de Na 1*s*, Si 2*p* y Al 2*p* mostraron picos en ~1072,3 eV, ~102,7 eV y ~74,4 eV, respectivamente, característicos de aluminosilicatos de sodio. Las muestras Z13X y los compuestos también presentaron Mg 1*s* (~1303,7 eV), atribuibles al grupo Mg-O. GP, Z20 y Z30 exhibieron pequeñas cantidades de Fe 2p (~711,4 y ~712,0 eV), identificadas como transiciones por agitación satélite $\pi \rightarrow \pi^*$. Los espectros RMN de 27Al y 29Si mostraron picos correspondientes al aluminio tetraédrico Al(IV) y al silicio en ambientes Q4, confirmando la alternancia entre tetraedros de sílice y alúmina.

En las isotermas de adsorción de CO_2 a 30 ºC, Z13X mostró la mayor capacidad de adsorción (3,98 mmol/g), seguida por Z30 (2,58 mmol/g) y Z20 (2,57 mmol/g). GP y Z10 presentaron capacidades similares (2,00 y 1,96 mmol/g), mientras que Z5 mostró la menor capacidad (1,65 mmol/g). La capacidad de adsorción disminuyó con el aumento de la temperatura, confirmando un proceso de adsorción física relacionado con la estructura microporosa de los materiales (Wei et al., 2012; Chang et al., 2020; Freire et al., 2024).

La capacidad de adsorción de CO fue significativamente menor que la de CO_2. A 30 ºC, Z13X alcanzó 0,57 mmol/g, seguida por Z30 (0,33 mmol/g), Z20 (0,25 mmol/g), GP (0,22 mmol/g), Z10 y Z5 (ambos con 0,16 mmol/g). La capacidad de adsorción de H_2 fue baja para todas las muestras, con valores inferiores a 0,021 mmol/g a 30 °C.

En resumen, los compuestos con mayor contenido de zeolita presentaron mejores resultados, como era de esperarse, dado que la zeolita tiene una mayor capacidad de adsorción que el geopolímero. Las características de las muestras de compuestos son similares, y la superficie específica parece ser el factor clave que influye en la capacidad de adsorción, aumentando con el contenido de zeolita.

Compuesto innovador de geopolímero/zeolita/PVA producido mediante electrohilado

En este capítulo del estudio, se desarrollaron cuatro muestras electrohiladas, que contienen geopolímero (MGP), zeolita 13X (MZ) y compuestos con 20 y 30 % de zeolita (Z20 y Z30).

El análisis de DRX en las muestras MGP y MZ reveló pequeñas esferas, donde la zeolita y el geopolímero están encapsulados de manera uniforme en la membrana fibrosa, sin conglomerados, como en las membranas descritas por Zhang et al. (2021). La diferencia entre los materiales es evidente: MGP presenta esferas amorfas (~127,81), mientras que MZ tiene esferas (~88,23) más uniformes y alargadas. MZ20 muestra una mayor cantidad de esferas (~56,97) con pocos aglomerados, mientras que MZ30 presenta numerosos aglomerados con esferas (~93,57).

El área superficial de las muestras es muy baja en comparación con algunas membranas electrohiladas reportadas en la literatura, y hasta el momento no se han encontrado estudios sobre compuestos de geopolímero/zeolita/PVA para una mejor comparación (Schneider et al., 2024). La mayor área superficial fue de 24,3 m^2/g, obtenida con la muestra MZ30, seguida de MZ20 con 17,4 m^2/g, MGP con 11,6 m^2/g, y el área más baja fue de 2,4 m^2/g, correspondiente a MZ. Las distribuciones de poros en las muestras MGP, MZ20 y MZ30 presentaron una amplia distribución de mesoporos, con tamaños de poros predominantes alrededor de 25 y 100 Å. La muestra MZ mostró una distribución de poros muy baja, lo que sugiere una porosidad uniforme, con pocos poros alrededor de 25 Å y una amplia distribución de mesoporos entre aproximadamente 70 y 230 Å. En general, las muestras preparadas en este estudio presentan estructuras mesoporosa, en línea con los hallazgos de Wang et al. (2025).

Los espectros FTIR de las muestras mostraron similitudes significativas, con bandas características de PVA. Además, presentaron vibraciones Si–O–Si y bandas típicas de materiales zeolíticos. Los espectros XPS de las muestras indicaron energías de enlace similares, con pequeñas diferencias en la intensidad de los picos, las concentraciones atómicas y los pesos. Como era de esperarse, no se identificaron aluminosilicatos en la superficie, debido a la baja concentración en las muestras, que están recubiertas por PDMS. El análisis EDS también confirmó bajos contenidos de Si y Al en las muestras.

Finalmente, la capacidad de adsorción de CO_2 a 30 °C, obtenida mediante isotermas, fue baja en comparación con las muestras anteriores, siendo de 0,62, 0,43, 0,21 y 0,62 mmol/g para las muestras MZ, MGP, MZ20 y MZ30, respectivamente. Para CO y H_2, las muestras mostraron capacidades de adsorción irrelevantes, como era de esperarse, ya que el objetivo principal es la captura de CO_2.

Composites de geopolímeros/zeolita 13X fabricados a partir de residuos de fosfato mediante impresión 3D para la captura y separación de gases

Este capítulo de la tesis aborda la síntesis y caracterización de composites 3D de geopolímeros con zeolita 13X (5%, 20% y 40%), y su aplicación en columnas de adsorción de lecho fijo.

La composición química de los composites, analizada mediante XRF, mostró sílice (SiO_2), alúmina (Al_2O_3) y óxido de sodio (Na_2O) como componentes principales. No obstante, se observó una cantidad considerable de óxido de hierro (Fe_2O_3) y titanio (TiO_2), además de pequeñas cantidades de óxidos de calcio (CaO) y fosfato (P_2O_5).

El área superficial aumenta a medida que el contenido de zeolita incrementa y la densidad disminuye, siendo 53, 203 y 374 m^2/g y 2,38, 2,27 y 2,18 g/cm^3 para C5, C20 y C40, respectivamente. Al igual que en otros materiales compósitos desarrollados en este estudio, las muestras presentaron alta cristalinidad, incluso en el compositescon menor cantidad de zeolita (5%). Los picos cristalográficos fueron identificados como cuarzo (SiO_2 ICDD 01-086-1628) y

Faujasita ($Na_2Al_2Si_2.4O_8.8\cdot 6.7H_2O$ – ICDD 00-012-0246). La principal diferencia radica en la intensidad de los picos.

A través de las imágenes de SEM de las muestras de compósitos, fue posible observar la estructura densa, homogénea y amorfa del geopolímero. A medida que aumenta la cantidad de zeolita en el compósito, se observa un incremento en los materiales cristalinos de la muestra. Sin embargo, a diferencia de las muestras C20 y C40, la muestra C5 presentó algunas fisuras, posiblemente relacionadas con el hecho de que la imagen fue tomada en la zona donde se cortó el material, es decir, en la superficie de las muestras.

Los espectros de MAS-RMN de ^{27}Al de las muestras son bastante similares. Todas presentaron un pico en aproximadamente 63 ppm, relacionado con el aluminio tetraédrico Al(IV) (Freire et al., 2024), y un pequeño pico en ~-20 ppm, referente al aluminio octaédrico Al(VI). Estos picos están asociados a la zeolita, conforme al análisis de XRD, que indicó picos cristalinos relacionados con Faujasita. La ausencia de picos nítidos de aluminio octaédrico y penta-coordinado confirma que el proceso de geopolimerización se completó (Nasab, Golestanifard y MacKenzie, 2014). Los espectros de ^{29}Si de todas las muestras presentan cinco picos significativos similares, que difieren en intensidad conforme aumenta la concentración de zeolita. Estos espectros identifican desplazamientos químicos de los diferentes entornos de silicio Q^4 en la estructura. La presencia de estos picos confirma la existencia de aluminosilicatos, debido a la alternancia entre tetraedros de sílice y alúmina (Gore et al., 2002).

El análisis FTIR-ATR confirma la presencia de bandas características de materiales aluminosilicatos en las muestras. Las bandas entre 4000 y 2600 cm^{-1}, atribuidas a las vibraciones de estiramiento Si-OH, OH y Si-OH-Al, y entre 1200 y 900 cm^{-1}, correspondientes al estiramiento asimétrico de estructuras del tipo Si-O-T, donde T es Si o Al (Kljajević et al., 2017), presentan superposiciones entre 1200 y 400 cm^{-1} debidas a las estructuras cristalinas y amorfas de los precursores Z13X y geopolímero, respectivamente (Minelli et al., 2018). Picos a ~980 cm^{-1} representan el estiramiento simétrico de los enlaces Si-O y están presentes en los espectros de todas las muestras (Papa et al., 2023). Bandas entre 800 y 500 cm^{-1} son características de vibraciones simétricas Si-O-Si, mientras que bandas entre 750 y 554 cm^{-1} corresponden a vibraciones de materiales zeolíticos, en este caso, Faujasita, tipo zeolita 13X (Jiménez, Lalangui, Guacho, Paucar et al., 2019).

El análisis de XPS, realizado para determinar los estados químicos y la composición atómica de la superficie de las partículas de las muestras, en general, mostró espectros muy similares, ya que todas son aluminosilicatos, con variaciones principalmente en la intensidad de los picos, concentraciones atómicas y peso. Los espectros XPS de Na 1*s*, Si 2*p* y Al 2*p* presentaron picos en ~1072,0 eV, ~102,1 eV y ~74,1 eV, respectivamente, característicos del aluminosilicato de sodio.

En conclusión, los compuestos 3D mostraron buena estabilidad estructural y porosidad ajustable, con un aumento del área superficial conforme aumenta el contenido de zeolita. Esta combinación permite materiales eficientes y versátiles para la captura y separación de CO_2, destacando el potencial de la fabricación aditiva para producir adsorbentes sostenibles y de bajo costo.

CONCLUSIÓN

Para evaluar el impacto de la temperatura de curado en la síntesis de geopolímeros, se curaron muestras basadas en metacaolín y desechos de fosfato a 65 y 80 ºC, con algunas muestras sometidas a curado sumergido durante 28 días. Las técnicas de FTIR y MAS-NMR confirmaron la presencia de material reactivo significativo en todas las muestras analizadas. La capacidad de adsorción de CO_2 fue mayor en las muestras sometidas a curado sumergido (2,24

mmol/g y 2,00 mmol/g para G80s y G65s) en comparación con las curadas a temperaturas más altas (1,42 mmol/g y 0,88 mmol/g para G65 y G80).

Los compuestos de geopolímero/zeolita, por su parte, mostraron un desempeño superior, alcanzando una capacidad máxima de adsorción de 3,98 mmol/g para Z13X. Esto resalta el impacto positivo del contenido de zeolita en las propiedades de adsorción de los compuestos. La baja adsorción observada de CO y H_2 refuerza su idoneidad para aplicaciones de captura y separación de CO_2.

En el caso de las membranas poliméricas producidas por electrohilado, la baja adsorción de CO_2 (entre 0,62 mmol/g y 0,21 mmol/g) indica que se requieren esfuerzos adicionales para mejorar su eficiencia en la captura de gases.

Además, los compuestos de geopolímero/zeolita impresos en 3D mostraron estructuras estables y porosidad ajustable, con un aumento del área superficial conforme aumentaba el contenido de zeolita, lo que confirma su potencial para aplicaciones prácticas en la captura de CO_2.

Palabras clave: Zeolita, Geopolímero, Captura de CO_2, Impresión 3D, Electrohilado.

TABLE LIST

FIGURE LIST

EQUATIONS LIST

ABBREVIATIONS

3D – Three-dimensional

3DP – Three-dimensional printing

3DPG – Three-dimensional printed geopolymer

ANN - Aluminum nitrate nonahydrate

BWP – Brick waste powder

CAD – Computer-aided design

CAM – computer-aided manufacturing

CCS – Carbon capture and storage

CCU – CO_2 capture and utilization

DMF – n,n-dimethylformamide

DIW – Deionized water

EDS – Energy Dispersive Spectrometry

ESA – Electric swing adsorption

FID – Flame ionization detector

GF – Geopolymer foam

GP – Geopolymer

HTV – Hot vulcanizable silicon rubber

LDF – Linear Driving Force

LSR – Liquid silicon rubber

MK – Metakaolin

MTS – matching-to-sample

Na-PS – Sodium polysialate

PDMS – Polydimethylsiloxane

PLA – Polyvinyl alcohol

PU – Polyurethane

PVA – Polyvinyl alcohol

PVDF – Polyvinylidene fluoride

RH – Rice husk ash

RTV – Room temperature vulcanizable silicon rubber

SEM – Scanning electron microscopy

SS – Sodium silicate

SSS – Sodium silicate solution

TSA – Temperature swing adsorption

TEOS – Tetraethyl orthosilicate

TCD – Thermal conductivity detector

VA – Volcanic ash

SUMMARY

1 INTRODUCTION

The utilization of fossil fuels is one of the major contributors to greenhouse gas emissions, including methane (CH_4), nitrous oxide (N_2O), and carbon dioxide (CO_2), which cause permanent and irreversible damage to the climate system (Ahmed et al., 2020; Nasr et al., 2021). According to Kazancoglu et al. (2021), CO_2 emissions into the atmosphere contribute to the rise in global average temperatures, leading to severe consequences such as rising sea levels, floods, and biodiversity loss (Liu et al., 2021).

In recent years, significant efforts have been made to transition toward clean energy, especially in the European Union, which strongly supported the use of renewable sources (solar and wind) and promoted hydrogen as an energy carrier—produced via water electrolysis using renewable electricity. However, the high production, storage, and transport costs of green hydrogen have led to the cancellation of several industrial projects and a reassessment of the EU's original goals, as recent studies suggest that this technology may not become widely viable for decades (Guerrero-Pérez, 2024).

As a result, CO_2 has become the central focus of decarbonization strategies, particularly through technologies for its capture, storage, and conversion into value-added products. Among existing methods, amine-based absorption is the most widely used at industrial scale. However, it involves major drawbacks such as high regeneration energy demand, corrosiveness, and high operational costs. In contrast, adsorption using solid materials offers advantages like lower energy consumption, material stability, and the possibility of using low-cost, non-toxic, and sustainable resources (Guerrero-Pérez, 2024).

Therefore, alongside renewable energy development, CO_2 capture and utilization (CCU) technologies are essential to reduce the carbon footprint and combat climate change. These technologies not only prevent emissions but also enable the transformation of CO_2 into valuable chemicals, such as methane, methanol, or dimethyl ether (Candamano et al., 2022).

It is estimated that up to 90% of CO_2 emissions can be captured and stored after separation (Damideh et al., 2020). However, the high capital costs and limited storage options demand the development of effective, scalable, and economical solutions. This has stimulated the exploration of alternative solid adsorbents, especially those derived from waste materials, such as phosphate mining residues and natural zeolites, due to their properties and low environmental impact (Candamano et al., 2022).

Lately, there has been an increase in research into adsorbent materials applied in the adsorption of CO_2. In any macro scenario involving the post-treatment of CO_2, the steps of capture and separation are present, so it is crucial to continue improving efficiency and reducing costs. Among the available technologies for CO_2 separation—such as absorption, adsorption, cryogenic distillation, and membranes—adsorption has gained attention due to its lower regeneration energy requirements, simple operation, and the possibility of using non-toxic and low-cost solid materials derived from natural or waste sources (Guerrero-Pérez, 2024). Within the wide range of adsorbent materials being explored, zeolites have been extensively studied in CO_2 separation due to their crystalline and microporous structures, high surface area, thermal stability, and adsorption selectivity. Moreover, zeolites can be synthesized using aluminosilicates or industrial solid waste, like fly ash, rice husk ash, and coal ash (Silveira, 2021).

Zeolites are crystalline materials constructed by connected tetrahedra (TO_4: T = Si or Al), creating a network of well-defined channels and cavities with pore size at the molecular level. For CO_2 capture in large-scale, zeolites cannot be used in powder form, so their conformation into monoliths or structured pellets is necessary to avoid high-pressure drops in fixed bed adsorbers (Frontera *et al.*, 2013; Akhtar *et al.*, 2014; Mastropietro *et al.*, 2016). Some particular products such as monoliths or extruded pellets were proposed by adding bentonite, but a porous hierarchical structure is hardly obtained.

In addition, geopolymer has gained a relevant research interest in recent years, mainly due to its low-cost and eco-friendly synthesis. Geopolymers are aluminosilicate materials that contain a considerable amount of aluminum (Al) and silicon (Si) in amorphous form. They can be produced using different solid residue sources (slags, fly ash, red mug, phosphate, etc.) (Bong *et al.*, 2021). The geopolymer matrix is mainly amorphous and formed by a 3D network of aluminosilicates, overall activated by an alkaline solution (Davidovits, 1994; Candamano *et al.*, 2022). Moreover, the incorporation of other adsorbents (activated carbon, zeolites, etc.) in the geopolymeric matrixes allows the obtention of versatile and resistant materials different in composition (Zhong and Zhang, 2022) and porosity.

Hybrid geopolymer/zeolite adsorbents have also recently shown efficiency in CO_2 capture due to the suitable properties in selectivity to separate CO_2/CH_4 or CO_2/N_2 from flue gas (Silveira, 2021). Mechanical strength, chemical resistance, thermal stability, and relatively low cost of synthesis are favorable aspects of using these materials in separation

processes (Minelli *et al.*, 2018). Additionally, the presence of mesopores in geopolymeric/zeolitic materials can promote the rapid diffusion of gases within the pores, thus improve the efficiency of CO_2 adsorption/desorption.

One way to shape geopolymeric materials is 3D printing to produce monoliths suitable to be applied in a fixed bed column. Nevertheless, current 3D printing studies of geopolymers have focused on their use as a building material, which does not require a controlled porous network. For CO_2 separation and capture, it is required to develop materials with hierarchical network materials to obtain high selectivity and adsorptive capacity (Souza, 2021). Then, the preparation of hierarchical porous geopolymers shaped as monoliths or geometric pellets would be useful for cyclic gas separation by adsorption. However, to the best of our knowledge, zeolite/geopolymer composite monoliths have not been developed or applied to CO_2/N_2 separation.

Alternatively, geopolymer composites could be shaped using electrospinning and the sol-gel method to produce elastic and resistant nanofibers to high temperatures (Tang *et al.*, 2022). Electrospinning consists of forming fibers from a polymer solution, ejecting it from a fine spinneret between two electrodes bearing electrical charges of opposite polarity, one placed onto the spinneret and the other onto a collector. The charged solution jet evaporates during its travel towards the collector to form the nonwoven fibers' arrangement. This method can be used to produce the desirable morphology, depending on the solution properties such as polymer molecular weight, conductivity, surface tension, and viscosity. Some parameters such as the distance between electrodes, applied voltage, humidity, volumetric flow, and needle diameter can be adjusted to allow enough solvent evaporation, avoiding the fibers to melt, or not being formed (Haider, Haider and Kang, 2018). Therefore, electrospinning stands out as a simple and economical method to produce nanofibers, starting from several polymer sources (Yarin, Koombhongse and Reneker, 2001b, 2001a; Silva *et al.*, 2021) In both cases, 3DP and electrospinning, the challenge would be maintaining the hierarchical porosity and mechanical strength.

Considering the knowledge gaps related to the use of low-cost materials with hierarchical porosity and the challenge of producing materials with high adsorption capacity and selectivity. This thesis aims to selectively develop zeolite/geopolymer/PVA composite materials with hierarchical porosity with high performance in CO_2 capture in binary CO_2/N_2 mixtures from exhaust gases. These materials will be manufactured by 3D

printing or electrospinning, and their performance will be investigated in fixed bed columns.

1.1 OBJECTIVES

1.1.1 Main Objectives

The main objective of this thesis is to explore the potential of phosphate mining tailing-based geopolymers, zeolite, and geopolymer/zeolite composite materials with a hierarchical porous structure as innovative, sustainable, non-expensive, and easily scalable adsorbents. The materials will be prepared using electrospinning and 3D printing techniques, aiming to obtain selective adsorbents for the separation of binary CO_2/N_2 mixtures.

1.1.2 Specific Objectives

The following specific objectives are proposed to evaluate the study:

i. Develop a suitable formulation to produce geopolymeric materials by adding phosphate mining tailings with hierarchical porosity;
ii. Evaluate the most relevant properties of geopolymeric materials to be used in gases separation;
iii. Characterize the porous structures, highlighting the use of advanced techniques such as micro-computed tomography (m-CT), nuclear magnetic resonance of solids (NMR), and X-ray photoelectron spectroscopy (XPS).
iv. Evaluate the pure gases adsorption equilibrium and CO_2 selectivity of the materials along with the fit of isotherms to theoretical models.

1.1.3 Structure of this study

This thesis project is structured in 9 chapters, as presented in Figure 1:

Figure 1. Scheme of the structure of this thesis.

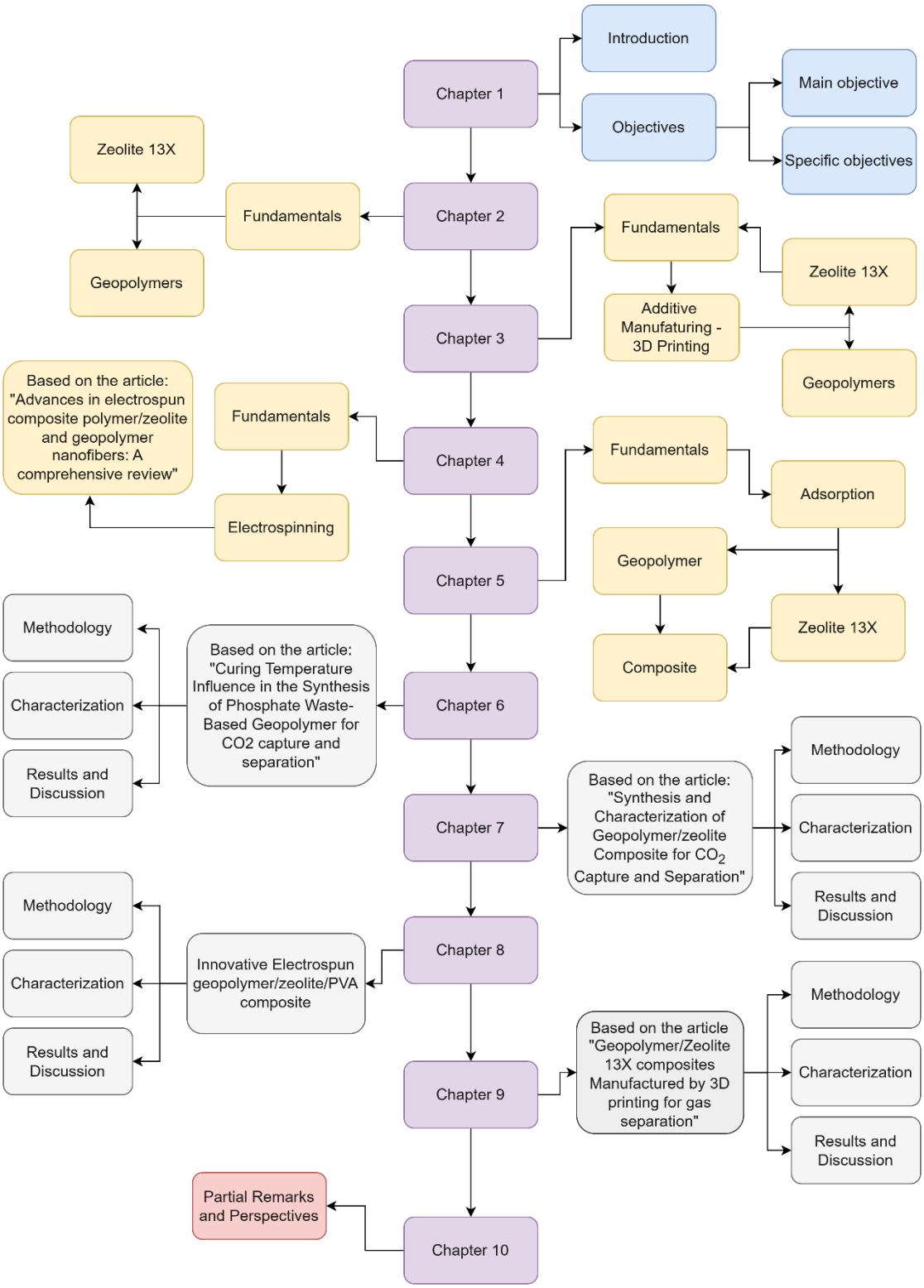

2 FUNDAMENTALS OF GEOPOLYMERS AND ZEOLITES

2.1 GEOPOLYMERS

Geopolymers are inorganic polymers, amorphous three-dimensional aluminosilicate, and ceramic-like properties materials that are produced and hardened at ambient temperature. The geopolymerization process is an exothermic phenomenon and occurs under highly alkaline conditions. Reactive aluminosilicates are rapidly dissolved, and free SiO_4^- and AlO_4^- tetrahedral units are released in the solution (Komnitsas, 2011; Silveira, 2021). The result of the polycondensation of monomers is called orthosialates, an abbreviation for silicon-oxo-aluminate (Pinto, 2006).

The tetrahedral units are alternatively linked to polymeric precursors by sharing oxygen atoms forming thus amorphous geopolymers. Positive ions such as K^+ or Na+ are present in framework cavities, to balance the negative charge. The main materials used in the manufacture of geopolymers are sodium polysialate (Na-PS), potassium polysialate (K-PS), sodium and potassium polysiloxosialate [(Na, K)-PSS], and potassium polysiloxosialate (K-PSS). The selection depends on the amount of SiO_2 monomers in the material (Pinto, 2006; Komnitsas, 2011).

Porous geopolymers have gained much attention due to the flexibility of the production processes and the diversity of their structural properties (Kovářík *et al.*, 2021). It is possible to control the porosity and morphology without compromising their essential mechanical resistance characteristics. This flexibility allows for their application across a wide range of fields. The performance of geopolymers as adsorbents can be improved, some works in literature enhanced the adsorption capacity by developing geopolymeric materials with a hierarchical porous structure or coating it with polysiloxanes (Bedarf *et al.*, 2021; Kovářík *et al.*, 2021).

2.1.1 Precursor materials

The materials used in geopolymer synthesis are rich in aluminosilicate including several inorganic wastes, such as civil construction waste, ground brick waste powder (Pasupathy, Ramakrishnan and Sanjayan, 2021), coconut ash (Hassan *et al.*, 2018), fly ash (Onutai *et al.*, 2016; Freire *et al.*, 2020), rice husk ash, mineral coal (Freire *et al.*, 2020), slag, pozzolan, clay, kaolinite (Pinto, 2006), and metakaolin (Okada *et al.*, 2011; Medpelli *et al.*, 2015; Papa *et al.*, 2016; Freire *et al.*, 2020; Kovářík *et al.*, 2021). These

materials present chemical and physical properties, like reactivity, composition, and particle size, which are ideal for the synthesis of geopolymers (Freire *et al.*, 2020). An alkaline activator, such as sodium hydroxide (NaOH), potassium hydroxide (KOH), sodium silicate (Na_2SiO_3), and potassium silicate (K_2SiO_3) (Assi *et al.*, 2020) is also used for geopolymerization reactions. Given the straightforward preparation and versatility of the precursors, it's unsurprising that geopolymerization has been regarded as an effective method for adding value to solid industrial residues. This process not only utilizes low-cost materials but also contributes to reducing the environmental impact of waste.

2.1.1.1 Metakaolin

Metakaolin (MK) is the most widely used raw material as an aluminosilicate source for obtaining geopolymers and zeolites. The synthesized geopolymer using MK as a precursor presents a suitable chemical composition, high purity, and excellent mechanical properties (Rowles and O'Connor, 2003; Freire *et al.*, 2020; Hodhod, Alharthy and Bakr, 2020) In kaolin, there are some secondary compounds present, including humusite, dickite, anatase, and quartz. However, Zibouche et al. (2009) studied the impact of these secondary compounds on the geopolymerization process and found that their presence, up to a concentration of 30 wt%, does not inhibit the geopolymerization process. The water loss of kaolinite occurs at 100°C, the dehydroxylation process occurs between 450 and 700°C, and metakaolin is obtained between 700 and 900°C (Zibouche *et al.*, 2009). Thus, metakaolin is obtained through calcination of kaolin, which is a clay mineral rich in kaolinite (Wan, Rao and Song, 2017). This occurs in a range between 450 and 900°C, when the dehydroxylation, as represented in Equation 1.

$$Al_2Si_2O_5(OH)_4 \xrightarrow[500 - 900°C]{} \underset{\text{Metakaolin}}{Al_2O_3 \cdot 2SiO_3} + 2H_2O \qquad (1)$$

2.1.1.2 Phosphate mine tailings

Phosphate mine tailings have led to storage challenges and environmental contamination, resulting in increased operational costs for industries. However, some solutions to these problems are being investigated. The utilization of these wastes in the synthesis of geopolymers is both environmentally and economic beneficial, as phosphate

waste contains significant fractions of Fe, PO_4^{3-}, SiO_2, and Al_2O_3 – key components for the geopolymerization process (Moukannaa *et al.*, 2018, 2019; Mabroum *et al.*, 2020; Idrissi *et al.*, 2021; Freire *et al.*, 2025).

2.1.1.3 Alkaline Activator

In the synthesis of geopolymers, the cation of the alkaline solution is crucial for achieving the charge balance of $Al(OH)_4^-$ within the pores of the geopolymeric paste. Therefore, selecting the right alkaline activator – options include potassium hydroxide, sodium hydroxide, silicate, fumed silica, and sodium silicate, either alone or in combination – is essential for the process (Rasaki *et al.*, 2019). Depending on the cation (Na^+, K^+, Li^+, and Ca^{+2}) employed to preserve the electrically neutral structure, the geopolymer will present a distinct microstructure and physicochemical characteristics (Silveira, 2021).

2.1.2 Cure

The curing process in geopolymeric materials is a key factor since the final properties depend on it. The curing process for geopolymers can be conducted under open or sealed conditions, as well as under dry, wet, thermal, or a combination of these conditions (Izquierdo *et al.*, 2010; Torgal and Jalali, 2010; Minelli *et al.*, 2016; Chen *et al.*, 2020; Silveira, 2021; Freire, 2022).

Due to the sensitivity of geopolymers to curing conditions, temperature, humidity, and aging time must be carefully selected to avoid incomplete reactions (Torgal and Jalali, 2010; Silveira, 2021). In their study, Izquierdo et al. (2010) examined the behavior of geopolymers cured in both open and sealed environments. They found that geopolymers cured in an open environment exhibited higher porosity. Additionally, the leaching rates of oxides were twice as high in open-cured geopolymers compared to those cured in sealed conditions. The physical properties of the open-cured geopolymers were also negatively affected due to the rapid evaporation of water, which interfered with the geopolymerization process.

Recently, several researchers have analyzed different forms and combinations of cure conditions, aiming to enhance the characteristics of geopolymers. There is general agreement that thermal curing speeds up the rate of geopolymerization by accelerating the dissolution of aluminosilicates (Minelli *et al.*, 2016; De Rossi *et al.*, 2018, 2020;

Freire, 2019, 2022; Chen *et al.*, 2020). Moreover, various scientists have investigated the curing of geopolymers at different temperatures, finding that curing at 60 and 80°C produced geopolymers with interesting physical and chemical properties, as well as significant textural features(Zhang *et al.*, 2014; Minelli *et al.*, 2016, 2018; Freire, 2019, 2022; Moukannaa *et al.*, 2019; Zribi, Samet and Baklouti, 2019; Freire *et al.*, 2020; Papa *et al.*, 2023)

2.1.3 Synthesis of geopolymers foams with hierarchical porosity

The geopolymerization process is an exothermic reaction that consists of three steps, dissolution and reorganization, condensation, and polymerization reactions, as seen in Figure 2. The dissolution (Fig. 2 a) and reorganization of aluminosilicate form several types of oligomers (Fig. 2 b), which connect and form large polymer chains (Fig. 2 c). As soon as the oligomers connect, the $^{-}$OH groups at the end of the chain meet and release water by sharing an oxygen atom (Singh and Middendorf, 2020).

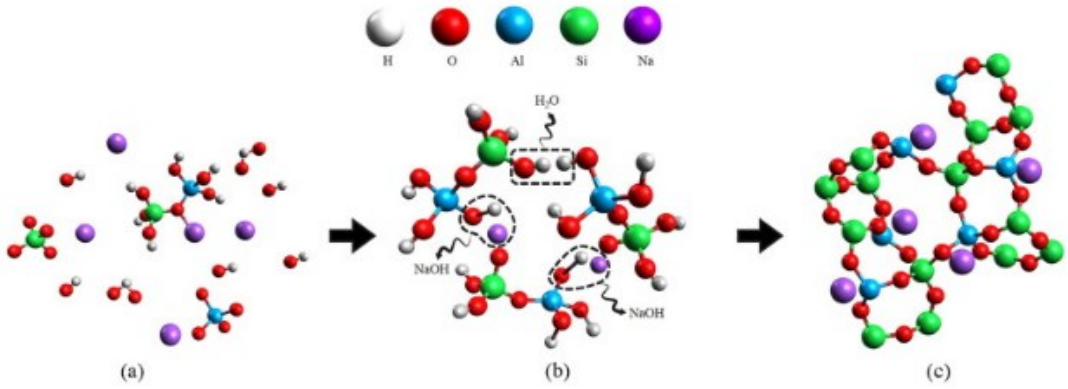

Figure 2. Illustration of the geopolymerization process, (a) reorganization of aluminosilicate, (b) gel formation from the condensation of oligomers, and (c) polymerization (Singh and Middendorf, 2020).

There are several methods to produce porous geopolymers, such as chemical foaming (Pasupathy, Ramakrishnan and Sanjayan, 2021), freeze-casting (Papa *et al.*, 2016), polymeric template (Kovářík *et al.*, 2021), microwave heating (Onutai *et al.*, 2016), reactive emulsion (Medpelli *et al.*, 2015), extrusion (Okada *et al.*, 2011), 3D printing (Panda *et al.*, 2017; Panda, Paul and Tan, 2017; Lim, Panda and Pham, 2018; Chougan *et al.*, 2020; Muthukrishnan, Ramakrishnan and Sanjayan, 2020, 2021; Bong *et al.*, 2021; Jin *et al.*, 2022), and electrospinning (Tang *et al.*, 2022). Geopolymer foams can be prepared by adding a foaming or a blowing agent to the geopolymer slurry and

exploiting any entrapped or generated evolving gases during the synthesis (Papa *et al.*, 2016).

In most of these methods, the initial preparations are very alike, using the mixing technique to produce the geopolymer slurry, where the main difference is in the forming method and the final cure for getting pores.

2.2 ZEOLITES

Zeolites are crystalline and hydrated aluminosilicates with regular pores, formed by basic structural units of the tetrahedral shape of Si and Al of the TO_4 type, where T is silicon or aluminum atoms, with exchangeable cations of alkali metals or alkaline earth metals electrostatically trapped into the pores, providing compensation for charges generated by the crystalline network. The TO_4 tetrahedrons are united to each other through the oxygen located at the vertices, thus originating the 3D crystalline networks. However, it is known that in addition to aluminosilicates, other materials may also have equivalent properties and structures, such as molecular sieves of aluminophosphates and silicoaluminophosphates, which are considered zeotypes (Chaves Lima *et al.*, 2019; Souza, 2021; Pérez-Botella, Valencia and Rey, 2022).

Moreover, in cases of a structure composed solely of silicon tetrahedra (SiO_4^{4-}), silica is formed. However, when Si^{4+} atoms are exchanged for Al^{3+} in the tetrahedron (AlO_4^{5-}), an aluminosilicate is obtained, characterized by charge disequilibrium, resulting in a zeolite with an anionic surface (Souza, 2021). In this case for each replaced Al atom, a positive charge is needed to maintain the neutral structure. For this, charge compensation is performed through interchangeable extra-structural cations, usually, Na^+, K^+, $Ca^{2+,}$ or Mg^{2+}, which are electrostatically bound to the crystalline structure of the zeolite, providing the property of ion exchange to the zeolite. Thus, the higher the Al/Si molar ratio, the greater the ion exchange capacity (Souza, 2021). Figure 3 is a representation of the tetrahedrons that form zeolites.

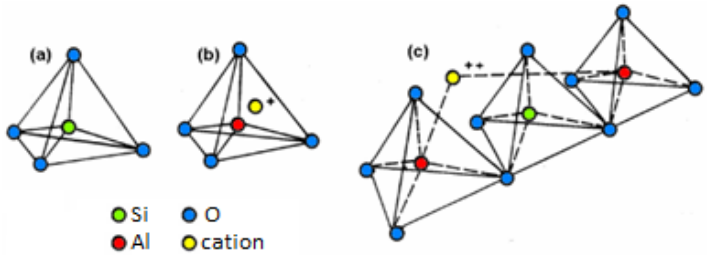

Figure 3. Basic structural units of zeolites, (a) tetrahedron with a Si atom at the center and O atoms at the vertices, (b) with an Al atom in the center bonded to a monovalent cation to

compensate for the charge difference between Si and Al. (c) A divalent atom balances the charges of two Al atoms separated by a Si atom (adapted from Vaclavik, 2010).

According to Byrappa & Yoshimura (2013), there are 250 distinct types of zeolites, including 46 natural varieties and 204 synthetic forms. A simplified structural representation of some zeolite types used industrially for catalysis is presented in Figure 4.

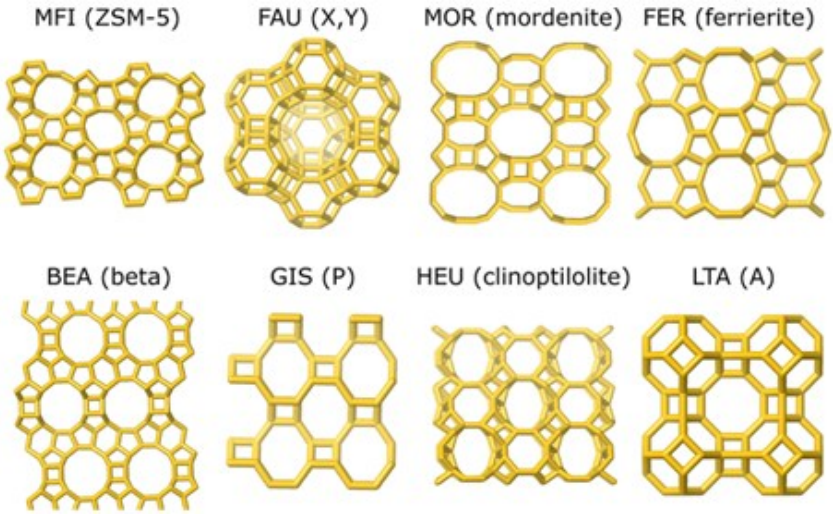

Figure 4. Front view of some zeolite's main pores representation. The official names are the three letters above the pictures and the common names are in parentheses (Pérez-Botella et al., 2022).

Figure 5 shows a representation of the structure of a FAU-type zeolite, with a three-dimensional layout of the true cell of the mineral, its chemical bonds, and the compensation of the anionic charges of the aluminum tetrahedrons.

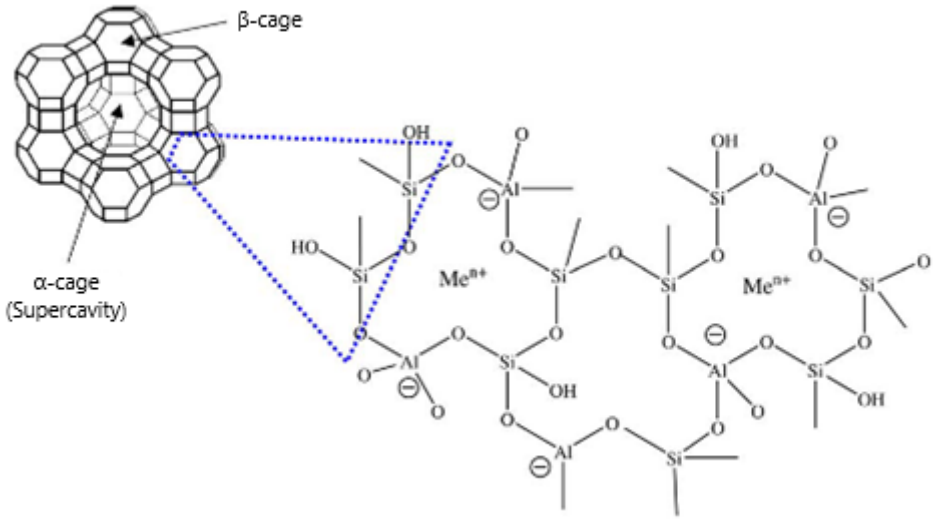

Figure 5. 2D and 3D concept of FAU-type zeolite (adapted from Valdés et al., 2006).

The union of basic tetrahedral structures, repeated in multiple ways, leads to the formation of diversified three-dimensional structures with channels and cavities with different dimensions. According to the IUPAC classification of materials by pore size, zeolites are microporous materials, and their micropores vary from small (< 4 Å), medium (4 - 6 Å), large (6 - 8 Å) to super large (8 - 20 Å), and this depends on the number of T-O-T bonds that form the pore, in other words, it depends on the number of oxygens that form the pore openings or rings (Luna and Schuchardt, 2001). The microporous structure allows mass transfer between the crystalline space and the external environment; however, this transfer is limited by the pore diameter of the zeolite structure. (Vaclavik, 2010).

The Faujasite-type zeolite (Linde 13X), also known as zeolite 13X, one of the objects of study of this research, has 3D pore structures linked by 12-ring openings, which lead to a larger cavity diameter of 12 Å, constrained by 10 sodalite cages in a hexagonal frame. The effective pore diameter in this type of zeolite is large at 7.4 Å (Khoramzadeh, Mofarahi and Lee, 2019).

Zeolites are widely discussed in literature, with theoretical basis and applications already consolidated in several areas. In chemistry, the zeolites can be used as **ion exchangers**, which was the first industrial application of zeolites, for water softening in laundry compositions, which is still widely applied; as **catalysts**, in a variety of industrial process, for example in oil refining and petrochemistry, and as **adsorbents**, due to characteristics like microporosity and regular pore size, selectivity, large adsorption

capacity, thermal stability, and relative low cost production (Pérez-Botella, Valencia and Rey, 2022). Overall, zeolites have shown significant efficacy in studies related to gas adsorption. Notably, certain types of zeolites are particularly relevant in industrial research and applications for gaseous adsorption processes, especially those involving carbon dioxide. For example, zeolite A, zeolite 13X, and zeolite beta are among the types that are highly valued for their performance in these applications. (Khoramzadeh, Mofarahi and Lee, 2019)

2.2.1 Synthesis of Zeolites

Zeolites are synthesized from saturated aqueous solutions, with defined composition, under predetermined temperature and pressure conditions. Thus, by varying the composition of the solution (or synthesis gel) and operating conditions, it is possible to synthesize zeolites with different structural characteristics and chemical compositions (Souza, 2021).

The primary method used in producing zeolites is the hydrothermal/hydrogel method. Moreover, it is the most suitable method for large-scale synthesis (Cundy and Cox, 2005; Mintova *et al.*, 2016; Souza, 2021; Pérez-Botella, Valencia and Rey, 2022). This method is performed as follows. First, the silicon and aluminum sources are mixed as structure-directing agents (organic or inorganic cations) with a mineralizing agent (OH^- or F^-) in an aqueous medium. So, the amorphous silicates and aluminates are dissolved through hydrolysis reactions in the alkaline medium, forming a hydrated gel with solubilized silicate anions and reactive aluminates. After that, the solution can be aged at room or higher temperature but lower than the crystallization temperature. Subsequently, the gel is crystalized through autoclave heating at varied temperatures, usually between 8 and 200 ºC, under autogenous pressure. In the process, the gel is separated into two phases, liquid and solid. The formation of crystals from the hydrated gel occurs in induction, nucleation, and crystal growth.

The induction process corresponds to mixing the two amorphous reagents until detecting crystalline cores is possible. Separating the amorphous phase into primary and secondary is possible at this stage. The primary consists of the initial products obtained by the hydrolysis and condensation of the reagents at the beginning of the mixture, which is considered a heterogeneous system where the reagents do not present a chemical equilibrium. The second stage represents an intermediate product of the synthesis, and it

is identified after the time passage or the heat application to the mixture containing the primary phase. This phase is characterized by the redistribution of the components formed in the prior phase until a preliminary equilibrium between the phases. Moreover, there is an increase in the ordering of intermediate aluminosilicates, but without establishing a repetitive crystalline structure. Figure 6 shows a diagram of the gel evolution in the two phases.

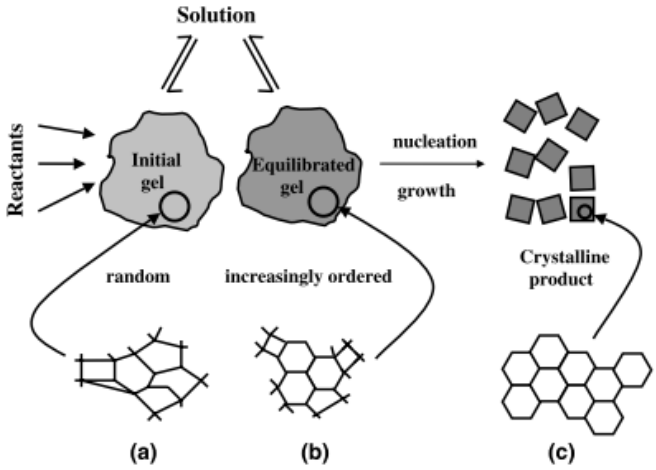

Figure 6. Evolution of the primary phase (a) through the secondary phase (b) to the crystalline zeolitic product (Cundy and Cox, 2005).

The nucleation step occurs with the development of the cores until they reach stability and sizes that favor their growth. Thus, the semi-ordered gel starts to form a crystalline structure, which can proceed to the growth process. At this step, the cations play a significant role in directing the structure to be arranged since the anions, aluminate, and silicate will configure the structure of the chains around the cations, determining the type of structure that will be formed. The nucleation rate is dependent on several parameters. However, the solution's supersaturation level, the medium's alkalinity, and the temperature are some of the most important.

Lastly, crystal growth occurs through mechanisms that include the transport processes of atoms or molecules. Initially, components are transported through a solution to the surface of the cores, where binding and diffusion take place. This movement is directed towards areas of higher fixation energy, often favoring corner sites. As a result, crystals with various three-dimensional geometric shapes are formed. It is worth highlighting that the three steps can occur simultaneously. One of the main factors in the process of core formation and subsequent crystal growth is the supersaturation condition of the solution. As the concentrations of Si and Al in the reactants decrease with the

process, the supersaturation approaches the equilibrium concentration, thus reducing the speed of core formation.

The crystallization from calcined kaolin is also a common process used in zeolite production (Luz, 1995). Briefly, in this process, the first stage consists of kaolin dehydration through calcination (500 - 600°C). Zeolites (type A) are formed without binder, where the pre-formed kaolin is converted "in situ" through a treatment with sodium hydroxide solution at 100°C. The synthesis reactions of zeolite "A" from kaolin occur as follows, where (a) is kaolin, (b) is metakaolin, and (c) is zeolite “A”:

$$(a)\ 2Al_2Si_2O_5(OH)_4 \rightarrow (b)\ 2Al_2Si_2O_7 + 4H_2O \rightarrow$$
$$6Al_2Si_2O_7 + 12NaOH + 21H_2O \rightarrow (c)\ Na_{12}(AlO_2)_{12}(SiO_2)_{12} \cdot 27H_2O$$

Structurally different zeolites, with distinct characteristics and properties, can be obtained by adjusting variables that participate in the synthesis process, such as the template (the molecule that defines the size of the cavities), temperature, pressure, concentration, crystallization time, pH, aluminum sources and silicon (Si/Al ratio) and cations (Vaclavik, 2010). Therefore, during the synthesis of the zeolite, aspects like the composition, temperature, and crystallization time can change the course of the process and thus result in different characteristics and properties of the final product (Souza, 2021).

3 ADDITIVE MANUFACTURING - 3D PRINTING

This chapter presents a review of the preparation of porous zeolite and geopolymer by 3D printing, including the characteristics and applications of the prepared materials.

3.1 GEOPOLYMER BY 3D PRINTING

Additive manufacturing, popularly known as 3D printing (3DP), has gained significant attention due to its ability to drive technological development as a sustainable, flexible, and customizable manufacturing scheme (Bedarf *et al.*, 2021).

3DP foaming refers to additive manufacturing that creates solid objects with cellular microstructure. The geometric complexity offered by 3DP enables the design of freeform building elements that are impossible or unfeasible to produce with other techniques (Labonnote *et al.*, 2016; Bedarf *et al.*, 2021).

To the best of our knowledge, no studies have been found on the application of 3D-printed geopolymers in carbon capture and utilization (CCU). Current research on 3D-printed geopolymers has primarily focused on their use as building materials. For their application as catalyst supports or adsorbents, a well-defined porous network is required. In this context, the direct 3DP approach faces a challenge. It needs to find the best slurry composition because the presence of mesopores in geopolymeric/zeolitic materials can promote a rapid diffusion of gases within the pores and thus improve the efficiency of CO_2 adsorption/desorption (Franchin and Colombo, 2015). However, the control of the rheology of the paste for shaping in 3D printing (3DP) has not been thoroughly investigated, especially when the goal is for the resulting material to possess specific physicochemical properties, density, and a cellular structure within the meso and macroporosity range. This is crucial for producing rigid foams from geopolymers.

Manufacturing 3DP foams encompasses a broad range of process technologies from which only a few are suitable for use on a large scale and with foam materials. Three processing candidates for a 3DP foam are extrusion-printing (Fig. 7a), spray-printing (Fig. 7b), and binder-jetting (Fig. 7c). (Bedarf *et al.*, 2021).

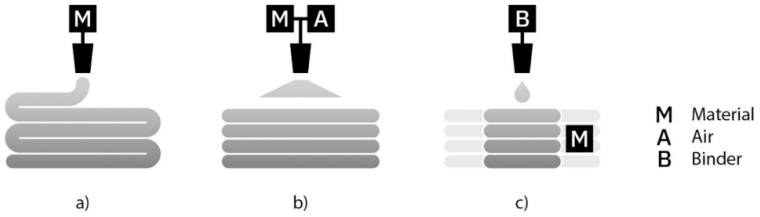

Figure 7. Schematic illustration of 3DP processes for manufacturing foams. a) extrusion, b) spray, c) binder-jetting (Bedarf et al., 2021).

Extrusion printing describes forcing material through a nozzle and depositing repeated layers of solidifying material until the three-dimensional object is created. This process can achieve high degrees of precision due to the control with nozzle diameters and resulting layer dimensions of up to 40 mm × 10 mm, and produced parts need little to no post-processing. Nevertheless, one disadvantage is that it limits the creation of overhang structures, which can only be overcome with additional printed support structures (Paolini, Kollmannsberger and Rank, 2019; Bedarf *et al.*, 2021).

The spraying technique involves distributing an atomized medium with compressed air in tiny droplets over an area. The most significant advantage of spray-based 3DP over other techniques is the production speed because the printing material is spread over a larger area. The main disadvantage is that it requires a high degree of precision, and the sprayed material is more challenging to control than extrusion-printed or binder-jetted substrates. Consequently, resulting print objects are either restricted to applications that require only poor surface quality or need to be post-processed on their later visible areas or precision interfaces (Bedarf *et al.*, 2021).

In the binder jetting process, bulk particles are evenly distributed onto a print bed and bound together by a binder to form the print object layer by layer. Nevertheless, as a disadvantage, it is much slower than traditional methods of mold fabrication. It adds value by enabling geometric features that improve the casting and cooling process. Furthermore, parts printed with this method possess inherently porous qualities depending on the binder infiltration into the particle bed. This happens due to the highest resolution details and geometric complexity for printed parts the method can achieve (Henke and Treml, 2013; Bedarf *et al.*, 2021).

Extrusion is the most studied printing process for porous geopolymer. This method is divided into four steps, mixing, pumping, extruding, and building, as presented in Figure 8. The mixed material is transferred to the extruder via the pumping system to

deposit the material layer by layer until the desired shape is achieved (Li, Wang and Ma, 2020; Zhong and Zhang, 2022).

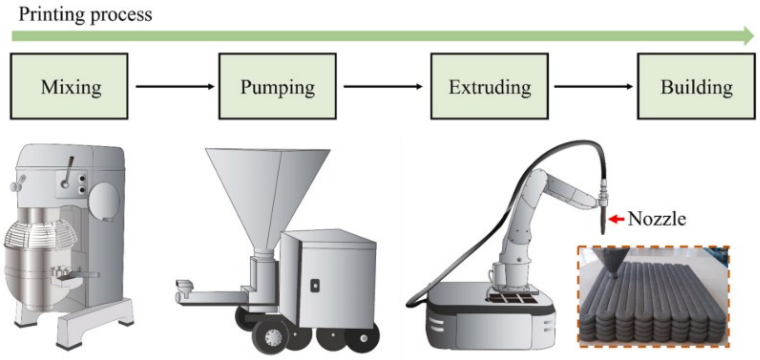

Figure 8. Scheme of extrusion-based printing steps (Zhong and Zhang, 2022).

For 3D printed geopolymers, distinct kinds of pumping systems have been used: grout pump (Panda *et al.*, 2017; Lim, Panda and Pham, 2018), PFT swing M pump (Bong *et al.*, 2021), and progressive cavity pump (Panda, Paul and Tan, 2017). However, some issues may occur between pumping and the material. For instance, it was found that polymer fibers with a long length may block the pump if the fibers are not well dispersed (Zhong and Zhang, 2022). Thus, the microwave heating method (Muthukrishnan, Ramakrishnan and Sanjayan, 2021), or auger extruder system (Chougan *et al.*, 2020) could be applied.

Zhong & Zhang (2022) recently reviewed 3DP studies for geopolymers. They concluded that to produce a paste with the characteristics suitable for printing, the most suitable binder is a combination of low calcium fly ash, ground granulated blast furnace slag, and fused silica. The alkaline activator should be the combination of NaOH + Na_2SiO_3, with a molar ratio SiO_2/Na_2O in the range of 0.5 – 2.0. Only fine aggregates with small sizes (<2 mm) should be used in 3D printing since materials with larger particle sizes are difficult to pass through the holes of the printing systems. Research on the development of hierarchical porous geopolymers shaped by 3D printing is limited, and it remains unclear which systems are fully compatible with geopolymer materials. It appears that these factors generally do not impact the printing process or the properties of the material, indicating that further research is necessary. Notably, no studies have been identified on the production of geopolymers with hierarchical porosity. Nevertheless, these are relevant techniques that could aid in developing a methodology to produce geopolymers with hierarchical porosity, aligning with the objectives of this project.

3.2 ZEOLITES MANUFACTURED BY 3D PRINTING

Unlike geopolymers, there have been studies on using 3D printing to create zeolites for CO_2 capture and separation. However, most of these studies focus on zeolite/polymer composites. Thakkar et al. (2016) prepared monoliths of zeolites by 3D printing for application in CO_2 removal from enclosed environments. The monoliths were prepared with powder zeolite 13X and 5A types (at 90 wt%), bentonite clay (7 wt%, as a binder), methylcellulose (2.0 wt%, as a plasticizing organic co-binder), and poly(vinyl) alcohol (PVA) (1.0 wt% as a co-binder). To prepare the materials, the components were first mixed until obtaining a homogeneous powder mixture, then distilled water was added to obtain a homogeneous aqueous viscous paste. To manufacture the material, the paste was loaded into a syringe attached to a nozzle 0.60 mm in diameter. Then, the paste was extruded through the moving nozzle in a Robocasting 3D printer. For printing the material, the product was designed by RoboCAD 4.2 software, which controlled the printer's motion. The paste was deposited in layers arranged perpendicular to each other, as presented in Figure 9, forming cylindrical zeolite monoliths with square channel structures with uniform channels. After printing the monoliths, they were first dried at room temperature and then dried in an oven at 100 ºC to remove the remaining water and avoid skin cracking. After that, the materials were calcined at 700 ºC for 2-4 h, aiming to decompose and remove methylcellulose and PVA.

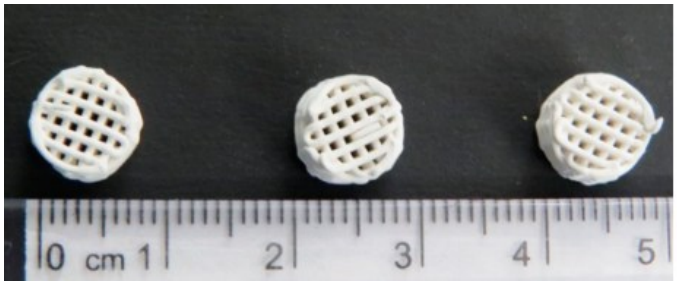

Figure 9. 3D printed zeolite monoliths prepared byThakkar et al. (2016).

Couck et al. (2017) prepared a ZSM-5 fiber monolith 3D printed for CO_2 separation. The monolith paste was made by mixing zeolite ZSM-5, with a mixed binder suspension containing colloidal silica and milled bentonite, aiming to improve the mechanical strength as compared to a single binder system. The silica was applied to help bind the zeolite and bentonite particles together, and the bentonite allowed to write the structures easily and without defects. The extrusion was carried out in a computer-

controlled machine, with a nozzle to extrude the paste layer-by-layer with the fibers perpendicular to each other. The monolith was printed at ambient temperature, a relative humidity of 80%, and the porosity between fibers was programmed to be 68%. When printing was completed, the monolith was dried in a controlled atmosphere, to prevent defects and cracks induced by fast loss of water from the structure. Finally, the material was calcined at ~550 ºC.

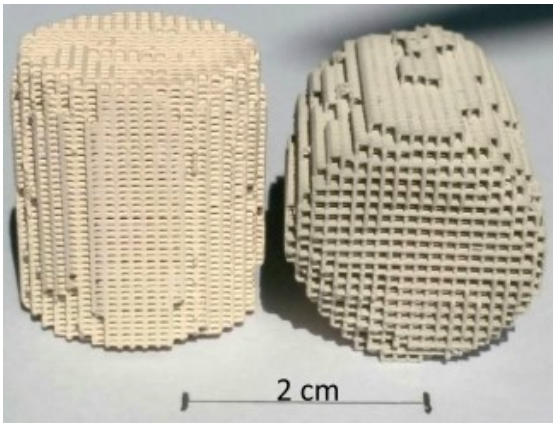

Figure 10. ZSM-5 fiber monolith 3D printed produced by Couck et al. (2017).

Thakkar et al. (2018) developed 3D poly(vinylpyrrolidone)/zeolite composites monoliths, using Torlon polymer and zeolite, for application in the removal of CO_2 from flue gas. The new material showed a significantly higher compressive strength than the material developed in the previous work, yet a considerably lower adsorption capacity. To prepare the samples, the zeolite (13 wt%) and poly(vinylpyrrolidone) (PVP) (3 wt%) were added to the N-methyl-2-pyrrolidone (NMP) (59 wt%)/water (7 wt%) and sonicated. The Torlon polymer solution was prepared by dissolving the polymer into a mixture of solvent and nonsolvent. Then, the dispersed zeolite mixture and Torlon polymer solution were mixed. So, the final dope was sealed in vials and kept on a roller for 3–4 days under continuous heating at 50 °C to completely dissolve the Torlon polymer and form the final print-ready paste. When the paste gets homogeneous, it was transferred into a tube which was tightened on a sample holder of Aluminum Prusa I3 A Pro 3D Printer. The slurry was deposited into a monolithic shape, using a 0.8-inch diameter nozzle. Aiming to obtain robust composites, after extruding one layer with cannels, they poured water dropwise with a syringe, to induce polymeric phase separation. After finishing the printing, the monoliths were submerged in deionized water to remove the NMP for 3 days, then they were solvent-exchanged by methanol for 9 days to remove the residual NMP, so the

monoliths were immersed in hexane to extract any remaining methanol. Finally, the monoliths were dried under vacuum. The monolith is presented in Figure 11.

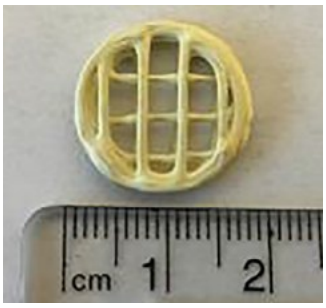

Figure 11. Torlon-zeolite monolith prepared by Thakkar et al. (2018)

An electrically conductive 3D-printed zeolite/activated carbon adsorbent monolith was developed by Regufe et al. (2019), for application in CO_2 capture by Electrical Swing Adsorption (ESA). For that, they used zeolite 13X type (9.1g), activated carbon (21.1g), and carboxymethylcellulose (CMC) (1.5g) as a binder. After mixing the powders, water was added drop by drop while mixing, until the mixture gets homogeneous. When the ink was finalized, the paste was added to a syringe and placed in a Discov3ry Extruder module to be printed. For printing, the ink was submitted to high pressure, to purge the system, and a conical polypropylene tip with a diameter of 0.84 mm was used to extrude. After printing, the monolith was dried at room temperature.

3D-printed hybrid zeolitic/carbonaceous electrically conductive adsorbent structures were produced by Mendes et al. (2021). The hybrid material, presented in Figure 12, was developed using zeolite 13X, graphite and bentonite as a binder (10% of the dry mixture). To prepare the paste, first the materials were mixed, then water was added and mixed under magnetic stirring. The designed monolithic structures were 3D printed using a direct ink writing printer developed in-house. After printing, the samples were dried in room conditions and then subjected to a pyrolysis step under nitrogen atmosphere with heating up to 823 K.

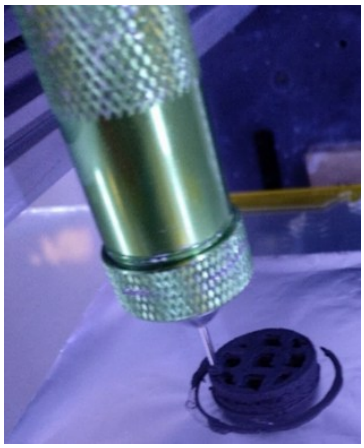

Figure 12. 3D-printed hybrid produced by Mendes et al. (2021).

Pereira et al. (2022) also developed monoliths by direct ink writing from zeolite 13X (47.5% m/m) and activated carbon (47.5% m/m) using CMC (5% m/m) as binder and plasticizer by direct ink writing. To prepare the paste, the two powders were mixed with the binder, and then distilled water was added to the mixture. To print, the ink was loaded in a 60 mL syringe, placed on a Discovery Extruder module, accoupled to an Ultimaker 2 + 3D-printer, and the syringe was connected to a conical nozzle with a diameter of 1.54 mm. The material was printed in a square-monolithic shape, and no thermal treatment was performed, to not deteriorate the activated carbon (Figure 13).

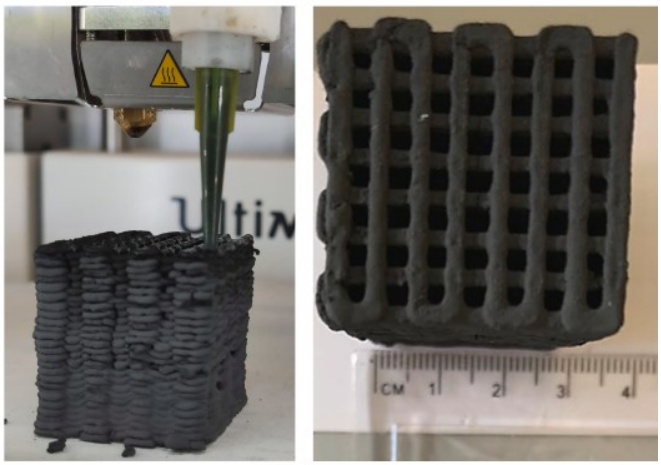

Figure 13. zeolite/activated carbon 3D printed monolith developed by Pereira et al. (2022).

Some characterization data of the materials reported in those studies are displayed in Table 1. The adsorption capacity in most cases can be related to the surface area of the material, the greater the surface area, the greater the adsorption capacity.

Table 1. Typical properties of zeolite produced by additive manufacture.

Sample	Surface area (m^2/g)	Pore volume (cm^3/g)	Compressive strength (MPa)	CO_2 Adsorption capacity (mmol/g)	Reference
13X (powder)	770	0.31	-	~5.01	Thakkar et al. (2016)
13X-R4	571	0.26	0.69	~4.49	
5A (powder)	705	0.29	-	~5.24	
5A-R4	543	0.25	0.35	~4.51	
ZSM-5-Powder	414	0.18	-	~2.05	Couck et al. (2017)
ZSM-5-monolith	305	0.32	-	~1.4	
13X-P	675	0.35	-	4.04	Thakkar et al. (2018)
T-13X	59	0.032	210	1.83	
5A-P	688	0.35	-	3.64	
T-5A	93	0.44	210	1.51	
Zeo powder	874	0.34	-	~5.4	Mendes et al. (2021)
Zeo-3D	632	0.26	-	~4.2	
Zeo-AC-3D	819	0.43	-	~3	
Zeo-G-3D	316	0.15	-	~1.8	

*Temperature between 25 ~ 30 ºC, and pressure of 1bar.

4 ELECTROSPUN COMPOSITE POLYMER/ZEOLITE AND GEOPOLYMER NANOFIBERS

This Chapter is adapted from a review paper entitled "Advances in electrospun composite polymer/zeolite and geopolymer nanofibers: A comprehensive review" published in *Separation and Purification Technology*[1]. It presents a review of zeolite/polymer and geopolymer preparation using the electrospinning technique, including the characteristics and applications of the prepared materials.

4.1 INTRODUCTION

Zeolitic materials have been extensively investigated during the last decades, and have theoretical foundations and consolidated applications in several areas of study. They are mainly used in adsorption, catalysis, and ion exchange. There are 250 different types of zeolites, 46 are natural, and 204 synthetic (Byrappa and Yoshimura, 2013; Souza, 2021). Some of the zeolite types have great importance in industrial studies and applications like separation processes, chemical synthesis, and sensor devices (Wong *et al.*, 2001). The precursor most used for zeolite synthesis is kaolin. Moreover, natural aluminosilicate minerals and industrial solid waste materials, including fly ash, metakaolin, coal gangue, rice husks, diatomite, and even geopolymers, have been investigated as viable sources of raw materials in the synthesis of zeolites (Su, Ma and Chuan, 2016; Freire *et al.*, 2020; Silveira, 2021; Oliveira *et al.*, 2023). These raw materials are typically combined with an alkaline activator, such as sodium silicate, sodium hydroxide, or potassium disilicate, to facilitate the zeolite synthesis process (Minelli *et al.*, 2018; Souza, 2021).

Geopolymers are amorphous three-dimensional aluminosilicate materials, classified as inorganic polymers that have ceramic-like properties and are produced and hardened at ambient temperature. Recently, the synthesis of geopolymeric materials has emerged as a promising way to recycle solid industrial byproducts due to their environmentally friendly attributes. This is particularly relevant for various waste streams, including debris from civil construction and powdered waste from ground bricks (Pasupathy, Ramakrishnan and Sanjayan, 2021), coconut ash (Hassan *et al.*, 2018), fly

[1] Schneider, M., Rodríguez-Castellón, E., Guerrero-Pérez, M. O., Hotza, D., De Noni, A., & de Fátima Peralta Muniz Moreira, R. (2024). Advances in electrospun composite polymer/zeolite and geopolymer nanofibers: A comprehensive review. *Separation and Purification Technology*, *340*, 126684. https://doi.org/10.1016/j.seppur.2024.126684

ash, rice husk ash, phosphate waste (Onutai *et al.*, 2016; Freire *et al.*, 2020), slag, pozzolan, clay, kaolinite (Pinto, 2006), and metakaolin/metakaolinite (Okada *et al.*, 2011; Medpelli *et al.*, 2015; Freire *et al.*, 2020; Kovářík *et al.*, 2021; Papa *et al.*, 2021). In addition, geopolymers offer diverse applications, including their use in thermal insulation (Minelli *et al.*, 2016), self-cleaning concrete cementation (Zailan *et al.*, 2016), CO_2 adsorption (Minelli *et al.*, 2016; Chen *et al.*, 2020; Freire, José and de Fátima Peralta Muniz Moreira, 2022), foam concrete (Pasupathy, Ramakrishnan and Sanjayan, 2021), ceramic foam (Kovářík *et al.*, 2021), arsenic removal from groundwater (Medpelli *et al.*, 2015), construction materials (Panda *et al.*, 2017; Bong *et al.*, 2021; Muthukrishnan, Ramakrishnan and Sanjayan, 2021).

Various methods are available for manufacturing such materials, with recent advances notably focusing on zeolitic composites and the preparation of geopolymeric materials. These methods include: 3-dimensional printing (Bong *et al.*, 2021), reactive emulsification (Medpelli *et al.*, 2015), extrusion (Okada *et al.*, 2011), polymeric molding (Kovářík *et al.*, 2021), microwave heating (Onutai *et al.*, 2016) for geopolymeric materials and 3-dimensional printing (Khalil, Hashaikeh and Hilal, 2021), heat mixing (Souza, 2021), co-extrusion (Etxeberria-Benavides *et al.*, 2020), and the phase-inversion technique (Haider, Haider and Kang, 2018) for zeolite/polymer composites.

A standout among these methods is the electrospinning technique, known for its simplicity and cost-effectiveness in producing nanofibers from various polymer sources. This technique consists of forming fibers from a polymer solution, ejecting them from a fine spinneret between two electrodes bearing electrical charges of opposite polarity, one placed on the spinneret and the other on a collector. The charged solution jet evaporates during its travel towards the collector to form the nonwoven fibers' arrangement (Yarin, Koombhongse and Reneker, 2001b; Silva *et al.*, 2021; Calzado-Delgado, Guerrero-Pérez and Yeung, 2022a).

The characteristics of the electrospinning solution, such as surface tension, electrical conductivity, volatility, and solvent viscosity, along with operational variables such as applied voltage; collector distance and solution flow rate, and environmental factors like humidity and temperature, can collectively influence the properties of the fibers. These factors highlight that by modifying fluid properties, it is possible to produce various types of fibers as needed (Yarin, Koombhongse and Reneker, 2001b, 2001a; Fu, Zhou and Wang, 2016).

Moreover, the diameter of the nanofibers can be changed by using different concentrations of solutions and electrical voltage. Thus, by adjusting the electrospinning, calcination settings, and precursor compositions, customized architectures may be created, such as hollow, porous, core-shell, and helical fibers (Zhang *et al.*, 2016; Xue *et al.*, 2019). Increasing viscosity tends to promote the formation of fibers by extending the electrospun fiber, while lower viscosity can result in the formation of beads rather than continuous fibers (Xue *et al.*, 2019). Furthermore, some parameters such as the distance between electrodes, applied voltage, humidity, volumetric flow, and needle diameter can be adjusted to allow sufficient solvent evaporation, preventing the fibers from melting, or even from being formed (Haider, Haider and Kang, 2018).

Despite being a relatively recent technique, there is a substantial body of literature that employs the electrospinning method to create diverse materials for use in a wide array of fields. For example, this method has been applied in the development of controlled-release vitamin C capsules (Calzado-Delgado, Guerrero-Pérez and Yeung, 2022b), and consumer products such as car filters, face masks, and water filter (Xue *et al.*, 2019), and some of the applications of zeolite/polymer and/or geopolymer/polymer composites studied in the literature are desalination (Sihombing *et al.*, 2022), filtration and dehumidification (Kang and Kang, 2016), medicine (Zhang *et al.*, 2021; Hu *et al.*, 2023; Mofarrah *et al.*, 2023) insecticide detection (Shan *et al.*, 2023), biofilms (Vergara-Figueroa *et al.*, 2020), catalysts (Guerrero-Pérez, 2021), and adsorption (Wu *et al.*, 2019), and more applications that will be presented below.

4.2 ADVANCES IN ELECTROSPINNING TECHNOLOGY

The first concept of electrospinning was designed in 1600 in a study by William Gilbert, in which he observed the formation of a cone-shaped water droplet in the presence of an electric field (Xue *et al.*, 2019). In 1747, an electrospray experiment was carried out by Abbe Nollet, and the work demonstrated that water could be sprayed as an aerosol when passing through an electrostatically charged vessel (Nollet, 1748). However, the behavior of the charged droplets was only systematically studied in 1882, by Lord Rayleigh, who theoretically estimated the number of charges that a droplet could carry before the liquid is ejected from a surface (Rayleigh, 1882).

The electrospinning technique can be viewed as a variation of electrospraying, as both methods rely on high voltage to expel liquid jets. However, the key distinction

between them hinges on the viscosity and viscoelasticity of the liquid used, as well as the behavior of the jet (Xue *et al.*, 2019). In electrospinning, the jet can be continuous, resulting in fiber production, while in electrospraying, the liquid jet breaks into droplets, forming particles (Figures 14 and 15). In 1902, John Cooley and Willian Morton patented the first two types of electrospinning equipment (Cooley, 1902; Morton, 1902). In 1934 and 1944, Anton Formhals patented an improved electrospinning device, which led to the commercialization of the equipment for textile fabrication (Formhals, 1934, 1944).

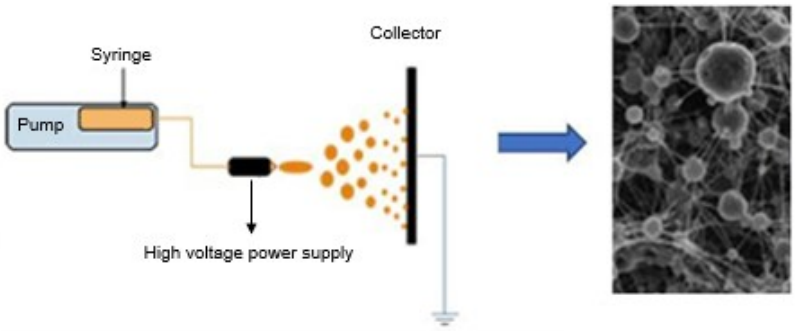

Figure 14. Schematic diagram of the electrospraying setup and SEM images of oil-loaded capsules (adapted from Rahmani-Manglano et al., 2024). Copyright © 2024 Nor E. Rahmani-Manglano, et al.

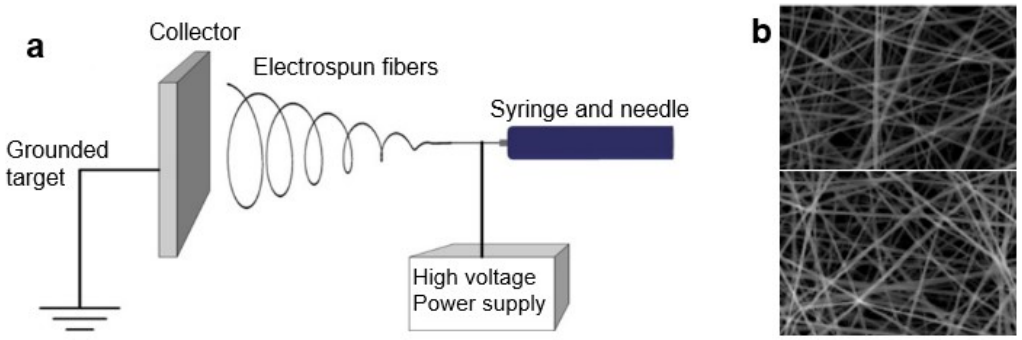

Figure 15. Schematic diagram of the electrospinning setup (a) and SEM images of electrospun lignin-zeolite nanofibers (b) (adapted from Bahi et al., 2017). Copyright © 2017 Addie Bahi, et al.

The use of electrospinning to produce nanofibers was first applied in 1938 when air filters were produced for capturing aerosol particles, and this work led to the manufacture of gas masks using nanofiber-based mats for smoke filters (Xue *et al.*, 2019). However, the understanding of the mechanics of electrospinning was developed only between 1964 and 1969, when Geoffrey Taylor published papers showing how to mathematically describe and model the change from a spherical to a conical shape of a

polymer solution or molten droplet under the influence of a strong electric field (Taylor, 1964, 1966, 1969).

Progress in electrospinning remained relatively dormant until between 1999 and 2001, when research groups collectively showed that various organic polymers could indeed be electrospun into nanofibers (Fong, Chun and Reneker, 1999; Reneker *et al.*, 2000; Hohman *et al.*, 2001; Shin *et al.*, 2001; Yarin, Koombhongse and Reneker, 2001a). It was during this period that multiple research teams revitalized the technique, thanks to the availability of electron microscopes capable of nanoscale observation (Xue *et al.*, 2019).

At the beginning of this century, electrospinning methods and equipment began to receive more attention and improvements. As has been established, the ability to introduce novel materials and formulations facilitates the production of composite and ceramic nanofibers, opening new avenues for applications in catalysis, energy conversion, harvesting, and storage. Moreover, the structure control and alignment of electrospun nanofibers were also studied, and methods for combining different properties such as size, structure, composition, morphology, porosity, and assembly of nanofibers were developed, increasing the range of applications (Xue *et al.*, 2019).

The electrospinning equipment consists of a syringe filled with a polymer solution, connected to a piston for controlled pressure and flow rate. The syringe needle, linked to an adjustable power supply, is set at a specific voltage. With a separation between the needle's nozzle and the collector, electrospinning employs electrical charge to draw fine fibers from solution droplets. High voltage induces charge, counteracting droplet surface tension, and creating a fine jet. The jet diameter decreases as it reaches the collection target for nanofibers (Huang *et al.*, 2003). The production of nanofibers with diversified compositions, structures (hollow fibers, porous, core-shell, helical fibers, etc), and properties was recently revised by (Xue *et al.*, 2019). However, the addition of porous materials enables new applications for these materials, since it explores adsorptive and catalytic properties.

Figure 16 illustrates a typical example of electrospun nanofibers that were produced by the physical cross-linking of poly(3,4-ethylenedioxythiophene) (PEDOT) and poly(styrenesulfonate) (PSS) by Mg^{2+} ions for the improvement of viscoelasticity, and a photograph of the nanofibers during the electrospinning process.

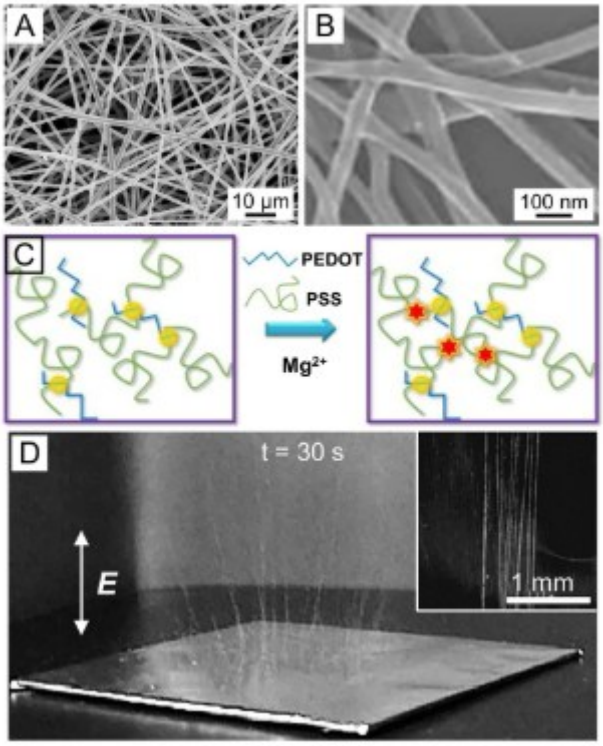

Figure 16. SEM images of the electrospun nanofiber (A and B), schema of the physical cross-linking of PEDOT and PSS by Mg^{2+} (C), and a photograph of the nanofibers during the electrospinning process (D) (Xue *et al.*, 2019)

A recent development has brought forth a highly adaptable x-y-z electrospinning apparatus for nanofiber synthesis. This innovative equipment has been characterized as a versatile system designed for the large-area, high-precision deposition, writing, and printing of electrospun nanofibers, and it essentially functions like a 3D printer (Calzado-Delgado, Guerrero-Pérez and Yeung, 2022a). Figure 17 provides a visual representation of this apparatus, highlighting its capacity for precise, rapid, and independent x-y-z movement.

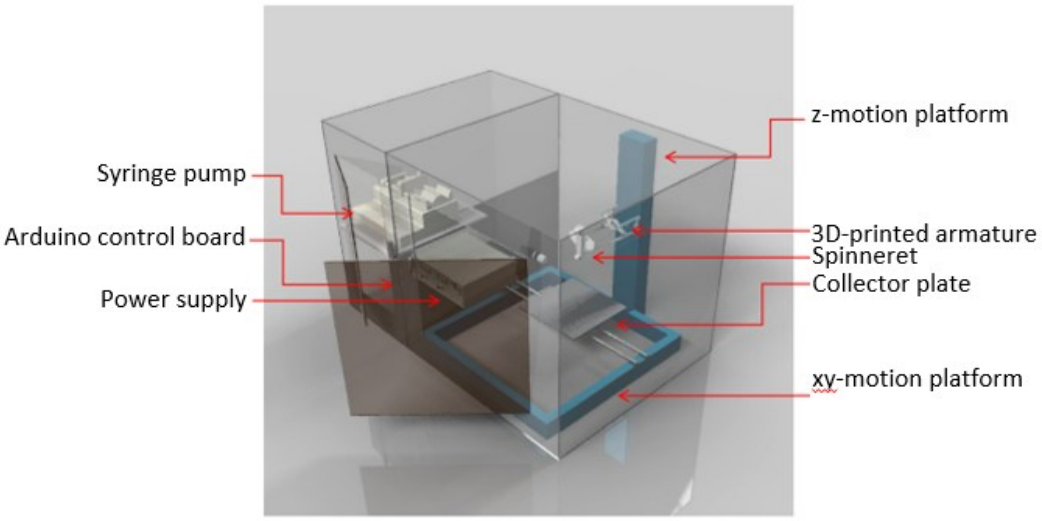

Figure 17. Illustration of an x–y–z electrospinning device (Calzado-Delgado, Guerrero-Pérez and Yeung, 2022a).

Furthermore, the device incorporates precise control over the electric field, ensuring not only the controlled fiber deposition but also the regulation of fiber diameter and size. These attributes contribute to making the final material highly reproducible, a valuable feature for industrial-scale production (Calzado-Delgado, Guerrero-Pérez and Yeung, 2022a). Finally, Figure 18 illustrates the difference between the membrane obtained through a traditional and using the x–y–z electrospinning device, both carried out with the same solution, and parameters, at 0.1 mL/h flow; 7.3 kV, and spinneret height (z) of 11 cm (Calzado-Delgado, Guerrero-Pérez and Yeung, 2022a). The fundamentals and parameters most used to produce zeolite/polymer, and geopolymer/polymer membranes are discussed in the following sections.

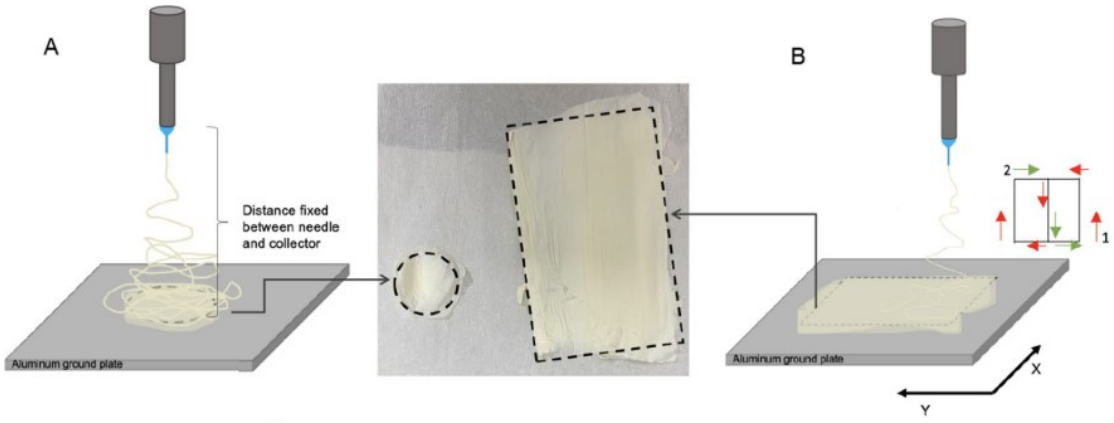

Figure 18. Illustration of the membranes obtained through (A) the conventional and (B) the x–y–z electrospinning device (Calzado-Delgado, Guerrero-Pérez and Yeung, 2022a).

4.3 ZEOLITES IN ELECTROSPUN COMPOSITES

Zeolites have firmly established themselves as a prominent subject in the literature, with a focus on both their synthesis and diverse applications. The synthesis of zeolites typically involves using well-defined saturated aqueous solutions, within specific compositions and under controlled temperature and pressure conditions. Consequently, manipulating the composition and operational parameters of the synthesis gel allows producing zeolites with varying structural features and chemical compositions. The hydrothermal/hydrogel method remains the primary technique used in the production of zeolites. Furthermore, it is the most suitable method for large-scale synthesis (Cundy and Cox, 2005; Anis *et al.*, 2016; Souza, 2021). Alternative methods for producing zeolite/polymer composites are 3-dimensional printing (Khalil, Hashaikeh and Hilal, 2021), heat mixing (Souza, 2021), co-extrusion (Etxeberria-Benavides *et al.*, 2020), and the phase-inversion technique (Luz, 1995).

Shaping zeolites through electrospinning is a relatively emerging field, with limited literature dedicated to the production of zeolite/polymer composites. This is because polymers are the predominant base for materials obtained via electrospinning. Furthermore, in some instances, zeolites are not the primary component but rather serve as an integral part of the polymer structure.

Regarding porous geopolymers, numerous techniques are available for producing them, such as chemical foaming (Pasupathy, Ramakrishnan and Sanjayan, 2021), the lyophilization technique (Minelli *et al.*, 2016), polymeric molding (Kovářík *et al.*, 2021), microwave heating (Onutai *et al.*, 2016), direct ink-printing (Franchin and Colombo, 2015), the mixed foam method (Hassan *et al.*, 2018), reactive emulsion (Medpelli *et al.*, 2015), extrusion (Okada *et al.*, 2011), and 3D printing (Panda, Paul and Tan, 2017; Lim, Panda and Pham, 2018; Chougan *et al.*, 2020; Muthukrishnan, Ramakrishnan and Sanjayan, 2020, 2021; Bong *et al.*, 2021).

In this context, in relation to preparing zeolite/polymer composites through the electrospinning process, polycaprolactone (PCL) is the most frequently utilized polymer. It is closely followed by-polyvinylpyrrolidone (PVP) and polylactic acid (PLA). In some instances, a combination of two polymers is employed. Table 2 provides an overview of various applications and compositions of electrospun zeolitic composites as reported in recent literature.

Table 2. Electrospun polymeric composites with zeolite fillers and their respective applications.

Zeolite (filler)	Polymeric (matrix)	Additive	Solvent (Electrospinnable base liquid)	Application	Reference
Zeolite	Polyvinyl alcohol (PVA)	Citric acid	Water	Ni^{2+} and Cd^{2+} removal from aqueous solution	(Rad *et al.*, 2014)
Zeolite-Y (600nm-1µm)	Polyvinylpyrrolidone (PVP)	-	Ethanol	Catalysis	(Anis and Hashaikeh, 2016)
Zeolite (<45µm)	Polyvinylidene fluoride (PVDF)	-	Dimethylformamide (DMF), acetone	Filtering and dehumidification	(Kang and Kang, 2016)
NaY zeolite (0.75µm)	PVP	-	Ethanol	Benzene adsorption	(Wu *et al.*, 2019)
Zeolite (1-3µm)	Polycaprolactone (PCL)	Silica (~17 µm)	Chloroform, butanol	Histamine-binding	(Alp-Erbay *et al.*, 2019)
Copper salt ion-exchange zeolite nanoparticles (~43.73nm)	Polylactic acid (PLA)	Cellulose nanofibers	Acetone, acetic acid, acetic anhydride, tartaric acid	Antimicrobial barrier	(Vergara-Figueroa *et al.*, 2020)
Zeolite (~2µm)	PCL, PLA	Nano-hydroxyapatite (nHA)	Dichloromethane (DCM): methanol	Dental tissue engineering	(Mohandesnezhad *et al.*, 2020)
Zeolite imidazole framework-8 (ZIF-8)	PLA	Titanium carbide (MXene)	DCM, ethanol	Bacterial infections	(Zhang *et al.*, 2021)
ZSM-5 zeolite (2078.79nm), beta Zeolite (842.06nm)	PVA, polyethersulfone (PES)	-	DMF, acetone	Creatinine adsorption	(Haghdoost *et al.*, 2021)

Zeolite	PS	-	DMF	Desalination	(Sihombing *et al.*, 2022)
HZSM-5 zeolite	PVP	Zirconium acetate	Acetic acid	Catalysis (dimethyl ether-to-olefins process)	(Cordero-Lanzac *et al.*, 2022)
Zeolite NaX	PVDF, Polyacrylonitrile (PAN), Polydopamine (PDA)	-	DMF, acetone	Adsorption/separation membranes in organic carbon interception, Ammonium recovery	(W. He *et al.*, 2023)
Zeolite Y (90 - 100nm)	PCL, Gelatin	Curcumin	Acetic acid, formic acid	Postsurgical glioblastoma treatment	(Jiang *et al.*, 2023)
Zeolitic-based metal-organic frameworks	Styrene acrylonitrile copolymer	Chitosan	Dimethyl sulfoxide	Pesticide residue analysis in food samples	(Pahang *et al.*, 2023)
ZSM-5 zeolite	PCL, polyethylene glycol	Dexamethasone, and ascorbic	DCM, methanol	Dexamethasone and and ascorbic acid delivery for bone regeneration	(Mofarrah *et al.*, 2023)

4.4 GEOPOLYMER IN ELECTROSPUN COMPOSITES

To the best of our knowledge, there is only one reported study in the literature which explores the utilization of electrospinning in the context of geopolymer development (Tang *et al.*, 2022). In this study, Tang et al. showed the feasibility of creating resilient geopolymer composites. They achieved this by combining the electrospinning process with the sol-gel method, resulting in the production of elastic nanofibers capable of withstanding high temperatures.

Electrospinning can be used to prepare geopolymer samples from a mixture of aluminiferous, siliceous, and phosphoric acid. In the study carried out by Tang et al. (2022) at first, a stabilizer solution (mixing boric acid, absolute ethanol, tetraethyl orthosilicate (TEOS), and deionized water) was mixed with aluminum nitrate nonahydrate under reflux. Then, PVA was added and continuously stirred until it was completely dissolved, forming a spinnable solution. The geopolymer solution was then suctioned into a syringe using a syringe needle. The solution was then fed at a controlled propulsion velocity of 1 mL/h, and electrospun with a voltage of 12 kV and receiving distance of 15 cm. After the spinning process, the nanofibers were collected by a rotating drum and very highly and continuously aligned in a single direction. The nanofibers had high tensile strength along the axial direction but extremely low strength limits in the radial direction. For this reason, the fibers were cut from the rotating drum collector and gathered as mats, layer by layer. Finally, the multi-layered mats were compacted in a hydraulic press at a pressure of 50–100 MPa to obtain an isotropic elastic nano geopolymer (Tang *et al.*, 2022). A schema of the procedure and final sample is presented in Figure 19.

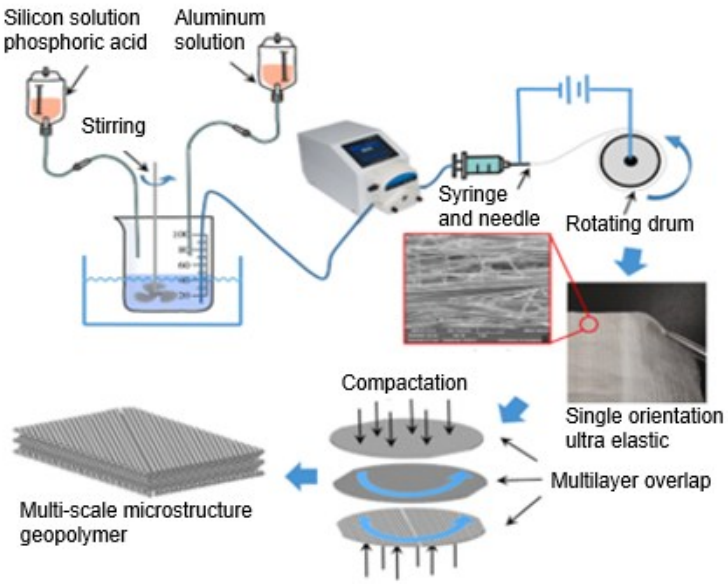

Figure 19. Schematic diagram of the electrospinning of geopolymer-based fibers (adapted from Tang et al., 2022). Copyright © 2022 Jiabo Tang, et al.

The electrospinning method created a lamellar-structured elastic geopolymer with a multi-scale microstructure (Figure 6). Some of the characteristics, like elemental composition, crystallinity, and oxide analysis, were analyzed. The electrospun geopolymer presented elemental composition peaks of Si, Al, and P, the Si:Al molar ratio was set as 1.5:1, and the diameter ratio of the nanofiber was around 500 nm. The crystallinity showed that the geopolymer is amorphous and the oxide analysis showed the characteristic peaks of aluminosilicates, polyphosphates, and silicophosphates (Tang *et al.*, 2022).

Finally, according to the authors, the advantages of this design were that the geopolymer retained its excellent mechanical properties and gained the benefits of unique thermal and corrosion stability. The multi-scaled, micro-structured geopolymer exhibited isotropic elasticity, demonstrated complete recovery from large deformations, and had high chemical and fire resistance properties since the electrospun nano-geopolymer displayed temperature-invariant super elasticity over 600 ºC.

4.5 POLYMER SELECTION IN ELECTROSPUN ZEOLITE COMPOSITES

This section will detail the preparation methods for a selection of samples listed in Table 1, with a focus on the rationale behind polymer choice. As mentioned above, diverse polymers have been employed to prepare zeolite-based composites through the

electrospinning process. This section will shed light on the specific polymer selections and their relevance to the manufacturing process.

Kang & Kang (2016) developed a zeolite/PVDF composite for application in filtration and dehumidification simultaneously using the electrospinning technique. To produce the composite, 12 wt% of PVDF powder (Mw ~531,000) was dissolved in dimethylformamide and acetone in a 3:7 volume ratio, then the zeolite powder (<45 μm) was added to the solution, which in this case was used as a desiccant material. Then, the zeolite/PVDF solutions were treated with ultrasonication to disperse the zeolite particles for 48 h at 35°C. PVDF was chosen as a polymer due to its outstanding thermal stability, mechanical strength, chemical resistance, piezoelectric property, and lower weight than other polymers, which are important characteristics for filter application. Moreover, the authors pointed out that electrospun PVDF nanofiber film shows improved physical properties, like tensile stress and tensile modulus, by thermal and oxygen plasma treatments.

According to Sihombing et al. (2022), polystyrene (PS) has several interesting characteristics. It is low cost, non-degradable, and has high mechanical strength, although the hydrophobic properties limit its application as a membrane for water treatment. This limitation still offers an advantage since water molecules can pass through the membrane when the breakthrough pressure is attained, moreover, the use of zeolite as a nanofiller can enhance the hydrophilicity of polystyrene membranes, forming a composite suitable for water filtration. Thus, they developed a novel composite membrane of PS integrated with natural zeolite particles for desalination purposes. To do so, first, 6 wt% of zeolite powder was dispersed in sulfuric acid and stirred at 350 rpm, and 70 °C for 4 h. The residue obtained was then washed until neutral pH was reached, and the material was dried at 105 °C for 1 h. The membrane was prepared by dissolving 4.7 g of PS in 20 ml of dimethylformamide and stirring at 350 rpm, 80 °C for 30 min. Finally, the zeolite microparticles were added to the solution.

Rad et al. (2014) produced a PVA/zeolite nanofibrous adsorbent for the removal of Ni^{2+} and Cd^{2+} from water. To prepare the solution, first, the solution containing 10% of PVA in DIW was refluxed at 80 °C for 4h, then the zeolite was added to the PVA solution. Lastly, citric acid was added to the solution at a weight of 10% of the total solution and mixed at 20 °C for 5h. In this case, PVA polymer was chosen due to its high potential for loading nanoparticles without compromising mechanical stability. PVA and

polyacrylamide have been the most used polymers to produce zeolite-based composite fibers, due to their low cost, low toxicity, good tensile strength, biocompatibility, and excellent hydrophilicity (Wu *et al.*, 2019).

Lastly, Haghdoost et al. (2021) produced a PES/PVP-zeolite core-shell composite nanofiber. To do so, they prepared two solutions, PVP/zeolite (shell) and PES (core). The PES solution was prepared by dissolving 25% (v/v) of PES flakes in DMF at room temperature for 3h. The PVP/zeolite solution was prepared by dissolving 10% PVP powder in acetone for 12h, then the zeolites (at 10 and 20 wt%) were directly added to the PVP solution and stirred at room temperature for 24h. Finally, the dispersions were sonicated for 1h before the electrospinning process.

Regarding the characteristics of the fluid for production by electrospinning, some important parameters need to be discussed, including viscosity, surface tension, contact angle, conductivity, and dielectric constant. Viscosity is an essential characteristic for producing fluids to be electrospun and the addition of polymer becomes imperative for this purpose since viscosity and surface tension are variables that depend on the selected polymer and its molecular weight, as well as the concentration ratio between solvent and polymer (Liu *et al.*, 2014; Kang and Kang, 2016). Although many studies highlight the importance of these characteristics for preparing fluids to be used in electrospinning, only a few present the results of analysis of these characteristics.

The PCL and PCL/zeolite 20% fluids prepared by Alp-Erbay et al. (2019) had a viscosity of 0.7548 Pa·s and 8.194 Pa·s, respectively, that is, when zeolite was added to the polymer, the viscosity increased significantly. In addition, they analyzed the surface tension and conductivity of the fluids and the PCL had a surface tension of 27.8 mN/m, which was reduced to 24.0 mN/m when adding zeolite. In terms of conductivity, zeolite had a minimal impact on the PCL solution's conductivity, with values in the 0.01-0.02 S/cm range.

Haghdoost et al. (2021) also analyzed these parameters for the produced samples, and for viscosity found 0.050, 0.075, 0.675, 0.070, and 0.620 Pa·s for the N0 (PES), NZ10, NZ20, NB10, and NB20, respectively. The surface tension and conductivity of the fluids were 36 mN/m and 29 μS/cm for the N0, 32 mN/m and 20.30 μS/cm for the NZ10, 22 mN/m and 37.2 μS/cm for the NZ20, 30 mN/m and 18.2 μS/cm for the NB10, and 27.7 mN/m and 35.8 μS/cm for the NB20. Moreover, they also analyzed the contact angle of

the fluid, and, as a result, the N0, NB20, and NZ20 had contact angles of 116.7º, 37.7º, and 32.5º, respectively.

These two studies were the only ones that carried out detailed analyses of fluid samples, however, some studies analyzed the contact angle. The Zeolite/PCDF fluid composite prepared by (Kang and Kang, 2016) had a contact angle of ~125º, the M2' produced by H. He et al. (2023) had a contact angle of 4.27º, and the PCL-PLA/Zeolite and PCL-PLA/nHA/Zeolite fluid samples prepared by Mohandesnezhad et al. (2020) had contact angles of 118 and 98º, respectively. Moreover, Sihombing et al. (2022) studied the conductivity of the PS/Zeolite sample with 10% zeolite, and the result was a conductivity of 478 $S \cdot cm^{-1}$.

Considering the scarcity of comprehensive analyses of the prepared solutions, the multitude of polymers employed, and the assortment of zeolite types utilized, conducting an extensive comparative assessment of these studies remains a challenge. Nevertheless, it is worth noting that certain studies have highlighted remarkable characteristics of these fluids.

According to Sreekumar et al. (2017), obtaining uniform electrospun fibers from biopolymers requires relatively high viscosities, but excessively high viscosities can result in low processability due to instabilities during processing. Since lower levels of surface tension may boost the processability of biopolymers, lower surface tension is often favored during electrospinning, because it requires less effort to separate the variety of molecules during the applied electric field (Geng, Kwon and Jang, 2005).

The conductivity of the solution greatly affects the electrospinning process and the fiber shape because the electrospinning solution repels, stretches, and forms the nanofibers. Therefore, by increasing the electrical conductivity of the solution as the jet becomes more strongly charged, a discernible decrease in the diameter of the nanofibers may be seen (Kim, Kirch and Mawst, 2010). Moreover, it has been noted that adding salt to the polymer solution raised the charge on the electrospinning jet's surface, and the electrical forces drove the jet to lengthen and create uniform fibers with a lower diameter (Tang *et al.*, 2022).

Unfortunately, it is not possible to make a deeper correlation regarding the synthesis with the properties of the materials due to the small number of studies available in the literature. However, although the properties of the solutions can help predict processability problems during electrospinning, it is typically challenging to explain the

influence of a single property without considering the impact of others and the target application field (Huang *et al.*, 2003; Alp-Erbay *et al.*, 2019).

4.6 ELECTROSPINNING PARAMETERS IN THE FABRICATION OF ZEOLITE COMPOSITE NANOFIBERS

As demonstrated in the preceding section, a wide array of polymers and materials can be incorporated into zeolites to craft composites suitable for a diverse range of applications. This section will review the electrospinning parameters employed, such as electric field strength, separation distance between the needle and collector, flow rate of the solution, voltage, fluid composition and solid concentration, and needle diameter. These parameters play a pivotal role in the manufacturing of these materials.

Figure 20 shows a typical electrospinning setup, with a straight plate, indicating some of the main processing components and factors, such as a syringe, distance, voltage, and collector. This setup was used by Anis & Hashaikeh (2016) to obtain zeolite-Y/PVP fibers. In this case, the electrospun material was collected on an aluminum foil, and after electrospinning, the material was dried at 80 °C for 6 h to remove moisture. The material was then calcined at 550 °C for 2 h to remove the polymeric phase.

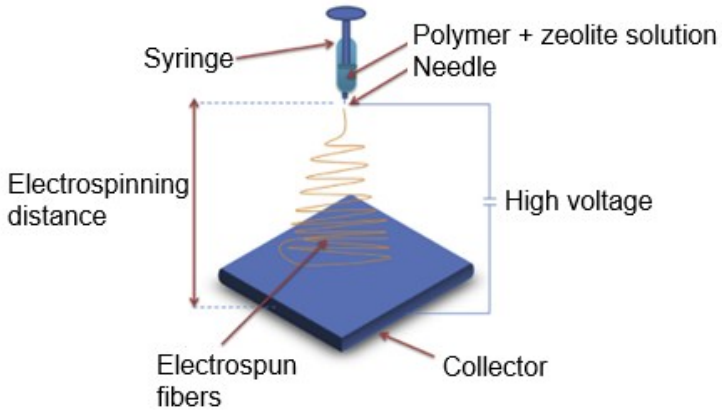

Figure 20. Schema of a generic electrospinning setup (Adapted from Anis et al. (2019)).

A scheme of the electrospinning device used by Sihombing et al. (2022), which has a rotatory drum as a collector, is presented in Figure 21. To electrospun the zeolite/PVDF composite, they placed the mixture of PS and zeolite in a syringe with a 0.8 mm needle at 10 cm from the collector, with a flow rate of the solution of 13 µL/min at a voltage of 15 kV.

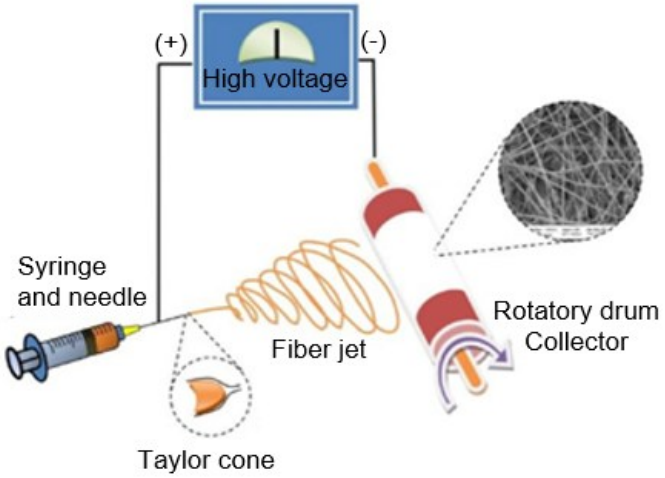

Figure 21. Illustration of the electrospinning device to produce a zeolite composite (Adapted from Sihombing et al., (2022)). Copyright © 2022 Yuan Alfinsyah Sihombing et al.

The distance between the needle and the collector is important for determining the nanofiber's morphology, since the deposition time, the evaporation rate, and the whipping or instability interval are dependent on this distance (Haider, Haider and Kang, 2018). According to Huang et al. (2003), when the distance between the needle and the collector is short, the spun fibers tend to stick to the collector and to each other, due to incomplete solvent evaporation. Table 3 illustrates a range of distances between the needle and the collector, spanning from 3 to 20 cm. Nevertheless, the most frequently utilized distances are consistently 10, 15, and 20 cm. While several studies omitted the specification of needle diameter, those that did provide this detail reported diameters within the range of 18 to 22 gauge. Notably, 20- and 21-gauge needles were the options most employed in the studies.

Concerning voltage, application of a high voltage from a power supply to the solution through a metallic needle induces a transformation of a spherical droplet into a characteristic Taylor cone shape. This electrical influence leads to the creation of ultrafine nanofibers, and the critical voltage required for this process varies depending on the specific polymer used (Haider, Haider and Kang, 2018). By increasing voltage, it is possible to form nanofibers with smaller diameters, due to the stretching of the polymer solution around the charge repulsion within the polymer jet (Sill and von Recum, 2008). An increase in the applied voltage beyond the critical value will result in the formation of beads or beaded nanofibers, which is attributed to the decrease in the size of the Taylor cone and increase in jet velocity for the same flow rate (Haider, Haider and Kang, 2018).

In the studies examined, the voltage applied ranged from 10 to 30 kV and 20 kV was the most frequently employed voltage among these studies, as highlighted in Table 2.

Finally, the flow rate of the fluid is a very important parameter, since it is directly related to the fiber size, and can influence the fiber's porosity and morphology (Sill and von Recum, 2008). Since the flow rate directly affects nanofiber formation, a minimum flow rate is preferred to maintain a balance between the expelled polymeric solution and the replacement of that solution with a new one during jet formation (Haider, Haider and Kang, 2018). Table 2 reveals a notable deviation from standardization in terms of the flow rate parameter when compared to the other parameters. The flow rates utilized range from 0.1 to 3 ml/h, with the most frequently employed flow rate being 0.5 ml/h. This flow rate is relatively low, aligning with findings from the study conducted by Haider et al. (2018).

Table 3. Electrospinning parameters for producing zeolite-based composites.

Composite	**Flow rate (mL/h)**	**Voltage (kV)**	**Distance (cm)***	**Needle (gauge)**	**Reference**
PVA/NaX	0.5	20	14	-	(Rad *et al.*, 2014)
Zeolite/PCDF	~3	10 – 12.5	3 – 20	-	(Kang and Kang, 2016)
Zeolite-Y fibers	0.5	10 – 28	10 – 15	20	(Anis and Hashaikeh, 2016)
Z-NaY/PVP (commercial)	0.5 – 3.5	20 – 25	15	20	(Wu *et al.*, 2019)
Z-NaY/PVP (synthesized)					
Zeolite/PCL	3	14	15	20	(Alp-Erbay *et al.*, 2019)
nZH-Cu/ CNF	0.1	24	20	-	(Vergara-Figueroa *et al.*, 2020)
Zeolite/PCL-PLA	2	20 – 25	15	18	(Mohandesnezhad *et al.*, 2020)
Zeolite/PCL-PLA/nHA					
MZ-8/PLA	1 – 2	20 – 30	15 – 20	-	(Zhang *et al.*, 2021)
NZ10	0.4 – 0.7	16	15	16 – 22	(Haghdoost *et al.*, 2021)
NZ20					
NB10					
NB20					
Zeolite/PS	~0.8	15	10	21	(Sihombing *et al.*, 2022)
FZ30(20%)	0.5	14	20	-	

FZ50(20%) FZ80(20%)					(Cordero-Lanzac *et al.*, 2022)
M2’	0.01 μm/min	20	10	21	(W. He *et al.*, 2023)
nZY/PG Curc@ nZY-PG	1	20	20	21	(Jiang *et al.*, 2023)
p(St-Co-AC)/Co-ZIF-67/C	0.6	18	10	-	(Pahang *et al.*, 2023)
ASC@ZSM-5/PCL-PEG/ DEX	1	25	20	22	(Mofarrah *et al.*, 2023)

* Distance between needle and collector

A zeolite/PVDF composite for simultaneous application in filtration and dehumidification was developed using the electrospinning technique by Kang & Kang (2016). The experimental electrospinning setup included a high-voltage source, a syringe pump, a metal needle, and a grounded collector. A syringe pump injected the composite into a metal needle, and a high-voltage source was connected to the tip of a metal needle and supplied the electrons to the composite. The tip-to-collector distance is one of the main variables in the electrospinning process that control the film morphology and porosity. A heat lamp was placed above the collector to speed evaporation of the solvents from the electrospun fibers.

Haghdoost et al. (2021) produced a core-shell PES/PVP-zeolite, the solutions were placed in~~to~~ a 5 mL polyethylene syringe capped with a 22 G (core-shell PES) and 16 G (PVP/zeolite) inner and outer needle, respectively. A 33 × 11 cm aluminum foil was used as a collector~~,~~ and the rate of the rotating collector was 100 rpm. After electrospinning, the fibers were placed in a desiccator for 24h, and thermal crosslinking was performed by placing the nanofibers in an oven at 200 °C for 1h. A schematic illustration of the electrospinning setup is presented in Figure 22.

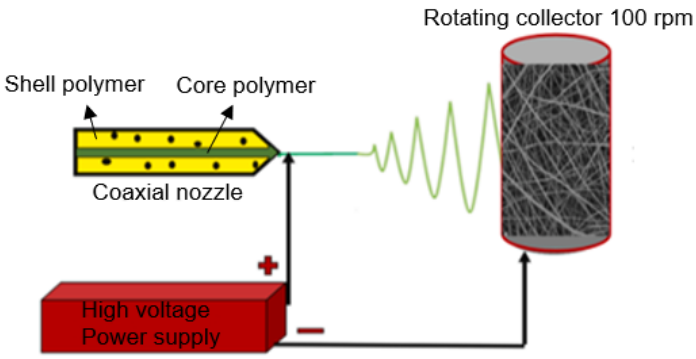

Figure 22. Schematic illustration of a core-shell electrospinning setup (adapted from Haghdoost et al., (2021)). Copyright © 2021 Fatemeh Haghdoost, et al.

S. Zhang et al. (2021) fabricated a MXene/ZIF-8/PLA membrane composite as an antibacterial nanofiber membrane by electrospinning. To do so, first a PLA solution was prepared using dichloromethane as a solvent, and the MXene/ZIF-8 suspension mixture was then added to the solution. As a result, the nanoparticles were encapsulated inside the fibrous membrane. Figure 23 displays the microstructure, offering a view of the encapsulated nanoparticles, along-with a photograph of the membrane.

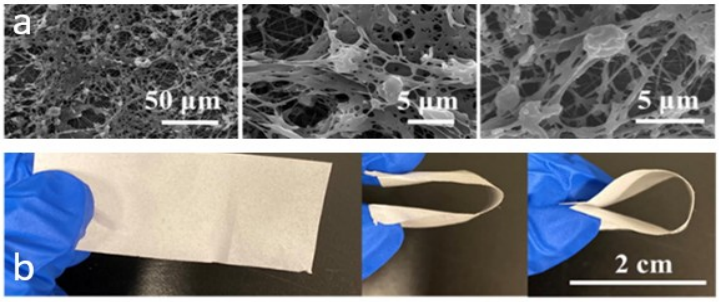

Figure 23. SEM images (a) and photographs (b) of a MZ-8/PLA membrane (adapted from S. Zhang et al., 2021)). Copyright © 2021 Siqi Zhang et al.

Table 4 presents some characteristics of the nanofibrous composites investigated in this review, such as size, specific surface area, and pore size, as well as a pore volume scan, and SEM images for enhanced visualization. The composition of the cited materials is presented in Table 2. However, it's worth noting that these characteristics do not appear to exhibit a clear correlation with each other.

In general, the diameter size of the fibers varies between ~50 nm and ~3µm, depending on the particle size of the zeolite. Some composites showed continuous fibers and others have small beads where the zeolite is encapsulated, as described by S. Zhang et al. (2021). Furthermore, there is no correspondence between the fiber's diameter and

surface area, being the surface area in the range 14.2 to 686 m^2/g. Although it did not present a pattern, some composites had porous characteristics, like those produced by H. He et al. (2023), Jiang et al. (2023), Mofarrah et al. (2023), and Wu et al. (2019), with pore sizes of 0.1 nm, 0.8 nm, 5.28 nm, and ~0.6 µm, respectively. Pore volumes of 0.06, 0.15, ~0.54, and ~0.24 cm^3/g were obtained in the composites prepared (Mofarrah et al., 2023; Cordero-Lanzac et al., 2022; Jiang et al., 2023; Pahang et al., 2023), respectively.

Table 4. Characteristics of the nanofibrous composites obtained.

Composite	**SEM images**[*©]	**Fiber diameter (nm)**	**Specific surface area (m^2/g)**	**Reference**
NaX /PVA	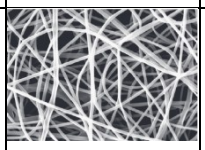	170	212	(Rad *et al.*, 2014)
Zeolite/PCDF	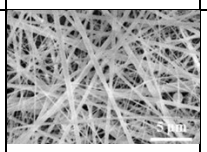	350-400	-	(Kang and Kang, 2016)
Zeolite-Y fibers	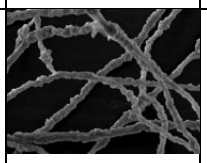	~3000	686	(Anis and Hashaikeh, 2016)
Z-NaY/PVP (commercial)	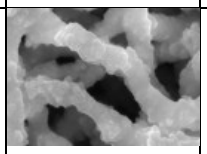	750	192	(Wu *et al.*, 2019)
Z-NaY/PVP (synthesized)	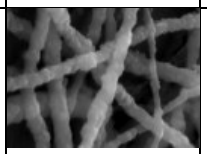	400	262	
Zeolite/PCL	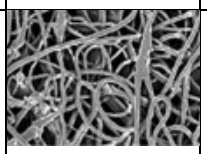	773	-	(Alp-Erbay *et al.*, 2019)
nZH-Cu/CNF		1700 – 2400	-	(Vergara-Figueroa *et al.*, 2020)
Zeolite/PCL-PLA	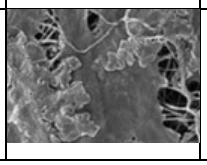	-	-	(Mohandesnezhad *et al.*, 2020)

Zeolite/PCL-PLA/nHA	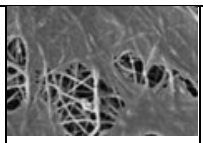	-	-	
MZ-8/PLA	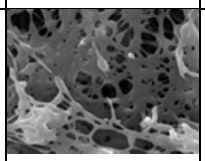	650	506	(Zhang *et al.*, 2021)
NZ10	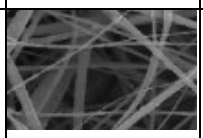	2078	330	(Haghdoost *et al.*, 2021)
NZ20	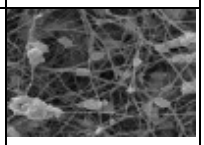			
NB10	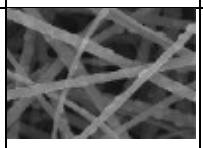	824	566	
NB20	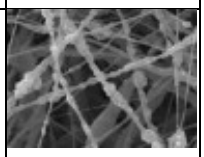			
Zeolite/PS	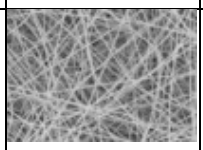	-	-	(Sihombing *et al.*, 2022)
FZ30(20%)	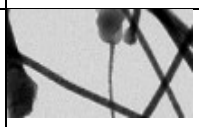	1240	421	(Cordero-Lanzac *et al.*, 2022)
M2’	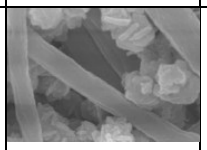	-	-	(W. He *et al.*, 2023)
nZY-PG	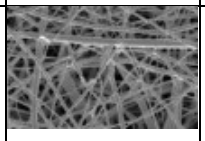	632	654	(Jiang *et al.*, 2023)
Curc@nZY-PG	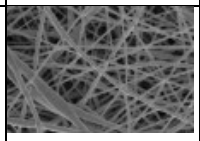	64		
p(St-Co-AC)/Co-ZIF-67/C	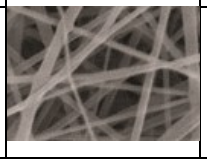	232.25 – 414.29	39.5	(Pahang *et al.*, 2023)

DEX/ASC@ZSM-5/PCL-PEG	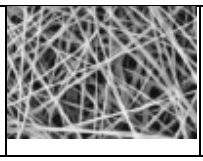	675	14.2	(Mofarrah *et al.*, 2023)

*All the images in this table are licensed for use by Elsevier and Copyright Clearance Center's RightsLink®

So, in terms of operational parameters, optimal conditions for producing nanofibers with desirable properties involve maintaining a distance of 10-20 cm between the needle and the collector, using a needle diameter within the range of 18-22 gauge, applying a high voltage of approximately 20kV, and adjusting the flow rate based on fluid viscosity.

4.7 APPLICATIONS, CHALLENGES AND LIMITATIONS

The wide array of applications for the materials generated in the studies examined in this review is notably diverse, complicating the direct comparison of their conclusions. Nevertheless, it is important to highlight that the outcomes of the studies that tested these samples had highly promising results.

Pahang et al. (2023) developed a method for extracting pesticide residues from foods, using a composite containing zeolitic-based metal-organic frameworks, chitosan, and, styrene-acrylonitrile copolymer, the composite was investigated in food samples including apples, tomatoes, honey, and milk and a pesticide recovery between 88.1–95.2 % was achieved, indicating that the fabricated composite is effective and promising for the pre-concentration of pesticides in various matrices.

Rad et al. (2014) tested the PVA/zeolite sample for the adsorption of Cd^{2+} and Ni^{2+} and found that the sample had a higher affinity for Cd^{2+} sorption than Ni^{2+} sorption. The best monolayer sorption capacities for Cd^{2+} and Ni^{2+} at 45 °C were 838.7 and 342.8 (mg g-1) at an equilibrium time of 60 min. Moreover, they also tested the reusability of the nanofibers, and the sample's capacity of adsorption did not change after five sorption-desorption cycles for both ions.

According to a study carried out by W. He et al. (2023), a sample produced using a straightforward approach can operate as a cost-effective functional membrane to simultaneously remove bovine serum albumin, and NH_4^+ contaminants with a high solution flow in wastewater treatment.

The ZrO_2/HZSM-5 composites produced by (Cordero-Lanzac et al. 2022) were tested as catalysts in the dimethyl ether-to-olefins (DTO) process. As a result, they

concluded that at a modest zeolite loading (5 wt%), at 400 °C, and a dimethyl ether partial pressure of 1 bar, the ZrO_2/HZSM-5 catalysts demonstrated remarkable activity in the DTO process, attaining a maximum selectivity to olefins of around 70%.

Haghdoost et al. (2021) produced an electrospun core-shell nanofiber sample for creatinine adsorption purposes, so to test the sample they removed creatinine from a solution and concluded that the removal of creatinine increased significantly with Beta zeolite and the highest adsorption potential of creatinine was obtained with the beta zeolite at a concentration of 20%. Moreover, by comparing the two types of zeolites that were tested, they showed that the zeolite particle size and surface area might be important factors in determining the functional impacts of core-shell nanofibers.

The biofilm samples produced by Vergara-Figueroa et al. (2020) showed antimicrobial activity against two types of bacteria, *S. Typhi* and *S. aureus*, in *in vitro* tests confirming that they can be used as an antimicrobial barrier. Moreover, their biodegradable features would help lower contamination from the buildup of plastic garbage.

The *in vivo* and *in vitro* experiments performed by S. Zhang et al. (2021) demonstrated that MZ-8/PLA can accelerate the healing of wounds infected with bacteria without evident resistance. A thorough analysis of its antibacterial abilities revealed that MZ-8 has bacterial inhibition rates of more than 99.0% against *Methicillin-resistant staphylococcus aureus* (MRSA) and *E. coli*. Additionally, MZ-8/PLA demonstrated strong photothermal and photodynamic therapy characteristics under near-infrared irradiation with bactericidal rates of up to 99.9% and 99.8% against *E. coli* and MRSA, respectively.

The samples produced by Alp-Erbay et al. (2019), electrospun zeolite-containing PCL films, indicated a high ability to bind histamine after in vitro tests by *S. aureus* and *S. Paratyphi A*, even at the lowest mineral content. They attributed the results to the porous-like surface characteristics of the samples and their high selectivity for the adsorption of polar and hydrophilic molecules.

Sihombing et al. (2022), who produced a PS/PNZ composite for desalination, tested the sample in artificial seawater and concluded that the sample with 30% zeolites had the best desalination results. The experiment demonstrates a strong potential for the future use of polystyrene/PNZ for desalination.

Jiang et al. (2023) investigated the potential of the integration of Curcumin into zeolite Y/PCL-gelatin composites for glioblastoma post-surgical tumor resection via in vitro anticancer assays. They discovered that the integration of curcumin not only demonstrated superior cytotoxicity, effective anti-migratory activity, and enhanced apoptosis induction against glioblastoma cells in the first 72h but also demonstrated sustained and prolonged release of medicinal curcumin that can ensure an acceptable concentration of curcumin within the cells for a relatively long period to completely eradicate the remaining cancer cells after surgical tumor resection.

Mofarrah et al. (2023) developed a zeolite (ZSM5)+PCL-PEG composite for the delivery of Dexamethasone (DEX) and ascorbic acid (ASC) to promote bone regeneration. The DEX/ASC@ZSM-5/PCL-PEG composite demonstrated successful continuous drug delivery over a 2-week period. Furthermore, the composite exhibited robust adhesion to human adipose-derived stem cells and elicited a positive impact on osteoblastic markers throughout an extended cell culture duration.

In general, the studies did not highlight the main challenges and limitations for zeolite-composite electrospinning production. However, Kang & Kang, (2016) related that although there are advantages of the superabsorbent polymers (SAPs) use as multi-functional filters produced with electrospinning, the synthesis has some limitations due to the complex processes, expensive equipment and material cost that are considered critical obstacles for the production.

Xue et al. (2019) pointed out that the simulation models related to the electrospinning process need to be optimized by considering all of the properties of the liquid used for electrospinning and processing parameters, to better elucidate the phenomenology of the electrified jets. Then, theoretical models should be realistic to predict the behavior of the electrified jet to produce well-controlled size, structure, and morphology.

Furthermore, they also commented on the large amount of solvents involved, which results in both economic and environmental concerns, hence, it is important to develop methods that use “green” solvents or even solvent-free systems, though this issue is more related to the polymer than the electrospinning itself, since in the study carried out by Rad et al. (2014) the solvent used was water. And finally, the challenge remains to produce nanofibers with diameters below 10 nm (Xue *et al.*, 2019).

Lastly, Table 5 presents a summary of the applications, results and conclusions of the studies that tested the production of electrospun material.

Table 5. Application, results, and conclusion of the electrospun materials

Composite	Application	Results	Conclusions	Reference
PVA/NaX	Ni^{2+} and Cd $^{2+}$ removal from aqueous solution	Monolayer sorption capacities for Cd^{2+} and Ni^{2+} were 838.7 and 342.8 (mg g-1).	The adsorption capacity of the composite did not change after 5 adsorption-desorption cycles, confirming the reusability of the material.	(Rad *et al.*, 2014)
Z-NaY/PVP (commercial)	Benzene adsorption	Benzene adsorption of 667 mg/g.	The significantly enhanced adsorption is due to the synergistic effect of the hierarchical structures configured with porous PVP and microporous zeolite.	(Wu *et al.*, 2019)
Z-NaY/PVP (synthesized)	Histamine-binding	The composite presented high ability to bind histamine, through in vitro tests by *S. aureus* and *S. Paratyphi A.*	Even at the lowest mineral content the material had excellent results, which can be related to the porous-like surface characteristics of the samples, and their high selectivity for the adsorption of polar and hydrophilic molecules.	(Alp-Erbay *et al.*, 2019)
Zeolite/PCL	Antimicrobial barrier	The in-vitro tests confirmed that it can be used as an antimicrobial barrier.	The biodegradable features can aid in lowering contamination issues brought on by the buildup of plastic garbage.	(Vergara-Figueroa *et al.*, 2020)
Zeolite/PCL-PLA	Bacterial infections	The material presented antibacterial abilities revealed that MZ-8 has bacterial inhibition rates of more than 99.0% against (MRSA) and *E. coli.*	The composite can accelerate the healing of wounds infected with bacteria without evident resistance.	(Zhang *et al.*, 2021)
Zeolite/PCL-PLA/nHA	Creatinine adsorption	The removal of creatinine increased significantly with Beta zeolite and the highest adsorption potential of creatinine was obtained with the beta zeolite in concentration of 20%.	The zeolite particle size and surface area might be important factors in determining the functional impacts of core-shell nanofibers.	(Haghdoost *et al.*, 2021)
MZ-8/PLA	Desalination	In artificial seawater the sample with 30% zeolites had the best results when desalinating	The experiment demonstrates that there is strong potential for the future use of polystyrene/PNZ in desalination.	(Sihombing *et al.*, 2022)
NZ10	Catalysis (dimethyl ether-to-olefins process)	Maximum selectivity to olefins of around 70%.	With modest zeolite loading the catalysts demonstrated significant activity.	(Cordero-Lanzac

				et al., 2022)
NZ20	Adsorption/separation membranes in organic carbon interception, Ammonium recovery	The maximum experimental adsorption capacity achieved was 27.02 mg/g, in the static adsorption process.	The sample produced can operate as a cost-effective functional membrane to remove bovine serum albumin, and NH_4^+ contaminants simultaneously with a high solution flow in wastewater treatment.	(W. He *et al.*, 2023)
NB10	Postsurgical glioblastoma treatment	The integration of curcumin demonstrated superior cytotoxicity, effective anti-migratory activity, and enhanced apoptosis induction against glioblastoma cells in the first 72h.	The material also presented a sustained and prolonged release of medicinal curcumin that can ensure an acceptable concentration of curcumin within the cells for a relatively long period to completely eradicate the remaining cancer cells after surgical tumor resection.	(Jiang *et al.*, 2023)
NB20	Pesticide residue analysis in food samples	Pesticide recovery between 88.1–95.2 %.	The composite is effective and can be promising for pre-concentration of pesticides in various matrices.	(Pahang *et al.*, 2023)
Zeolite/PS	Dexamethasone and and ascorbic acid delivery for bone regeneration	The composite delivered the drug continuously over 2 weeks.	The composite showed strong adhesion to the cell and proliferation for human adipose-derived stem cells and a favorable effect on osteoblastic markers throughout a long-term cell culture.	(Mofarrah *et al.*, 2023)

4.8 CONCLUDING REMARKS

Electrospinning has emerged as a highly promising technique for the fabrication of zeolite/polymer composite nanofibers, primarily due to its versatility and cost-effectiveness. The method allows the creation of composites with predefined porosity and surface area, offering control over the morphology of the resulting nanofibers. Several parameters, including component concentration, fluid viscosity, applied voltage, tip-to-collector distance, the needle, and solvent, significantly impact the final product. It's noteworthy that these parameters play a crucial role in the preparation of fluids for electrospinning, which is essential for the reproducibility of studies, although only a limited number of studies have presented these essential details. By mastering these parameters, it becomes feasible to tailor electrospun nanofibers to fulfill a wide range of functions.

Electrospun zeolite/polymer composite nanofibers have potential applications in various fields, encompassing filtration, dentistry, medicine, and catalysis. Consequently, these electrospun nanofibrous membranes and their composites not only hold great promise for various industrial applications but have also presented promising results. Given the diversity of applications, a comprehensive analysis of material performance across these applications remains challenging, preventing direct comparisons of results. Nevertheless, it is essential to recognize that these materials have proven to be efficient in their specific applications, highlighting the potential of electrospun nanofibers to address multifaceted challenges in various industries.

Electrospinning is a novel way to develop zeolite/polymer composite nanofibers with hierarchical porosity and depending on the operating conditions and type of polymer different materials can be produced. PVDF, PVP, polyvinyl alcohol, polycaprolactone, and polylactic acid are usually used, and other polymeric materials, such as polyurethane, poly(methyl methacrylate, PEG, could also be explored. The combination of different solid materials, such as zeolite and geopolymers enable the development of a series of innovative applications. Unfortunately, due to the considerably small number of studies related to the synthesis and application of zeolite/polymer and geopolymer/polymer composite materials found in the literature to the date, and the diversity of applications, it is not possible to generalize the best configuration to produce zeolite/polymer nanofiber, and further studies are encouraged to develop advanced materials for others potential applications, such as gas separation, gas and water filtration, catalyst support, etc.

5 GEOPOLYMERS, ZEOLITES, AND COMPOSITES IN CO_2 CAPTURE AND SEPARATION

This Chapter presents the theoretical background for the application of zeolite, geopolymer, and hybrid geopolymer/zeolite in gas adsorption.

5.1 ADSORPTION

Adsorption corresponds to a mass transfer process, where constituents of a fluid phase (gas, vapor, or liquid) spontaneously concentrate on a surface, usually a solid phase. Adsorption is considered a surface phenomenon because it occurs at interfaces, zones of separation between the phases of the fluid-solid system. In adsorption, two phases are distinguished: the adsorbent and the adsorbate (also known as the adsorbed substance). From a thermodynamic point of view, adsorption is a spontaneous process (Vaclavik, 2010).

In the adsorption process, either chemical adsorption (chemisorption) or physical adsorption (physisorption) may occur. In chemisorption, the force interaction between the adsorbent and adsorbate is strong and involves the formation of chemical bonds between the free valences of the solid and the adsorbate. This process involves the rearrangement of forces and is restricted to the first surface layer of the adsorbent. The chemisorption is localized, that is, the adsorbed molecules are fixed on the surface of the adsorbent (Silveira, 2021).

In physisorption, the interaction between the adsorbent and adsorbate is weak and does not present any change in the nature of the species involved. In this case, the van der Waals forces (attraction and repulsion) and electrostatics interactions, as polarization, dipole, and quadrupole, are involved. Thus, there is a change in the properties of the fluid phase around the adsorbent surface, and this region is studied as a thermodynamically different phase. This region is the interfacial layer, also known as the adsorbent surface, where fluid phase enrichment can take place (Silveira, 2021).

In adsorption, a decrease in the surface free energy of the system is usually observed. It is therefore a spontaneous process, that is, $\Delta G < 0$, and the adsorption is frequently an exothermic process (Ruthven, 1984).

Moreover, the degree of temperature changes that occur inside the adsorber during the adsorption and desorption phases of the processes is determined by the isosteric heat of adsorption (Sircar *et al.*, 1999; Seabra *et al.*, 2019), also known as enthalpy adsorption (ΔH_{ads}) (Nuhnen and Janiak, 2020). The portion of heat adsorbed by the adsorbent increases the particle

temperature, and this increase in temperature affects the adsorption kinetics of the adsorbent and the separation performance of the bed using the adsorbent (Park *et al.*, 2016). As a result, the isosteric heat is a crucial variable in adsorption processes and is also employed to learn more about the interactions between the adsorbate and the adsorbent.

The isosteric heat of adsorption is commonly calculated using the Clausius–Clapeyron equation (Equation 2) based on the isotherm data obtained at different temperatures, where ΔH_{ads} is the isosteric heat of adsorption (kJ/mol), R is the universal gas constant, T is the adsorption temperature (K), P is the adsorption pressure (bar), and n is the adsorbed gas amount (mmol/g).

$$\Delta H_{ads} = RT^2 \left(\frac{\partial lnP}{\partial T}\right)_n \quad (2)$$

For the development of an adsorption system and development of an adsorbent, it is essential to know some characteristics of this system, such as the adsorption rate, the amount adsorbed at a given time and equilibrium, the mechanisms involved in the adsorption process in question, among others (Chan et al., 2017).

According to kinetic laws, three main steps of mass transfer are present: (1) external diffusion, which involves the passage of the adsorbate through the resistance provided by the boundary layer around the adsorbent particles; (2) internal diffusion, which is related to the displacement of the adsorbate through the porous channels of the adsorbent; and (3) the adsorptive process of adsorbate into the adsorption sites (Pérez-Botella, Valencia and Rey, 2022). Moreover, the thermodynamic parameters, equilibrium constants and enthalpy of adsorption are also important.

.

5.1.1 Equilibrium of adsorption

The determination of the experimental isotherms is the first step in the study of a new adsorbent system, since through it, the adsorption equilibrium data are reported, therefore it is very important to understand the hole process. The accumulated data over the years allowed the establishment of a classification of isotherm shapes, with gives information about the textural

properties of the solid adsorbent material (Pérez-Botella, Valencia and Rey, 2022). The IUPAC classification is shown in Figure 24.

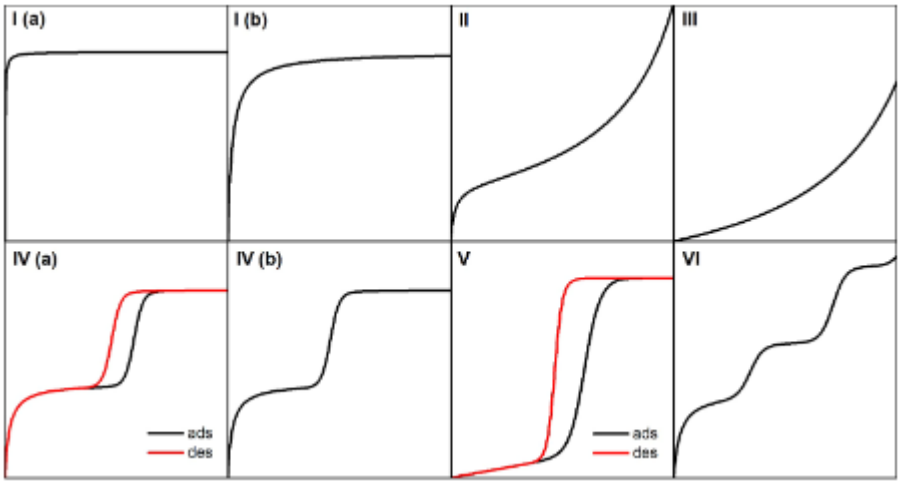

Figure 24. Isotherm types according to the IUPAC classification. The *x*-axis is related to the pressure, and the *y*-axis to the adsorbed amount. In the cases where there is a single black line, the adsorption and desorption are equal, and in the IV (a), and V isotherms there is a hysteresis phenomenon, where the black line represents the adsorption, and the red line represents the desorption (Pérez-Botella et al., 2022).

The isotherm represented by type I (a), and I (b) are the most common. Its configuration is characteristic of microporous adsorbents due to the size of the solid pores, which are not much larger than the molecular diameter of the adsorbate, like the zeolites. With these adsorbents, there is a saturation limit due to the complete filling of the pore by a single adsorbate molecule.

Type II isotherms are characterized by relatively weak adsorption on nonporous or microporous adsorbents, where multilayer adsorption and capillary condensation occur. Some materials present a mix of the Type I and Type II isotherms. The Type III isotherms also belong to nonporous or microporous adsorbents; however, in this case, the interaction with the adsorbent is very weak.

Type IV isotherm is typical of mesoporous solids. The IV (a) isotherm type presents a hysteresis loop which is related to the capillarity condensation in the pores and is given by solids in which the opening of the pore exceeds a certain value, depending on the nature of the adsorbate. The hysteresis refers to cases in which the adsorption and desorption have a different path in the isotherm plot. Type V isotherms are seen in microporous and mesoporous

adsorbents, in cases where the adsorbent-adsorbate interaction is weak, and at higher pressure a pore filling occurs, and the interactions overrule causing an increase in the adsorbed amount. The hysteresis is typical in this isotherm.

Finally, the VI isotherm type is given by highly uniform nonporous surfaces, in which the adsorption in layer by layer is perceptible.

There are many mathematical models of adsorption isotherms are reported in the literature to correlate equilibrium data with the different types of isotherms, as zeolites and geopolymers are the object of this study, they usually present the isotherm type I, and some of the most relevant models used to describe this type of isotherm are Langmuir, Freundlich, Henry, Sips, Toth, BET, and Redlich-Peterson models (Kyzas, Bikiaris and Mitropoulos, 2017; Khoramzadeh, Mofarahi and Lee, 2019; Voigt, 2019; Freire *et al.*, 2020; Freire, 2022).

In Equation 3, q_{eq} represents the adsorbate concentration in the solid phase in equilibrium with the fluid phase at a pressure P. In Equation 4, the parameter q_m is the maximum capacity of the monolayer, and K_{eq} is a adsorption equilibrium constant.

The isotherm model proposed by Henry (Equation 3) can be considered simple since represents a linear isotherm, where the adsorbed amount is proportional to the partial pressure of the fluid. This model is mainly applied to low pressure and concentrations of adsorbate, when increasing concentration, the interactions between adsorption sites and adsorbate increase, and saturation in the adsorbed phase occurs. In this case, "H" is the adsorption equilibrium constant, also known as Henry's constant (Pérez-Botella et al., 2022; Ayawei et al., 2017).

$$q_{eq} = H \cdot P \tag{2}$$

Langmuir's theory is based on kinetics in which the adsorption rate is equal to the desorption rate (Dantas, 2009). For a single adsorption site, the Langmuir model (Equation 4), considers that the entire surface of the adsorbent is homogeneous and has a defined number of sites with equivalent energy, the molecules do not interact with each other, and the adsorption occurs in monolayer, where each site can only accommodate a single adsorbate molecule. In this theory, is considered that the speed of adsorption is equal to the speed of desorption when the equilibrium is reached. This model can be applied in many cases, however, has some limitations, like when the system has high concentrations and pressures, in which

intermolecular forces cannot be disregarded (Pérez-Botella et al., 2022; Alafnan et al., 2021; Ayawei et al., 2017).

$$q_{eq} = \frac{q_m \cdot K_{eq} \cdot P}{1 + K_{eq} \cdot P} \tag{3}$$

The Toth model (Equation 5) is derived from the Langmuir models, presenting a different approach to simulate the energy distribution. This model accounts for surface heterogeneity using a parameter that modifies the shape of the isotherm, allowing for higher loading values at low pressure as compared to the Langmuir model. This is because a solid presenting a heterogeneous surface will have a larger capacity at low pressure than one with a homogeneous surface. (Pérez-Botella et al., 2022; Dantas, 2009).

$$q_{eq} = \frac{q_m \cdot K_{eq} \cdot P}{[1 + (K_{eq} \cdot P)^n]^{\frac{1}{n}}} \tag{4}$$

The Freundlich model (Equation 6) is one of the first empiric equations used to describe equilibrium data. This model describes the equilibrium in heterogeneous surfaces and considers that the heat of adsorption is exponentially given from the monolayer. (Ayawei et al., 2017; Ming and Hsu, 2013). In this equation $\frac{1}{n}$ is related to the adsorption intensity, the relative distribution of energy and the heterogeneity.

$$q_{eq} = K_{eq} \cdot P^{\frac{1}{n}} \tag{5}$$

The Sips isotherm model (Equation 6) is a combination of Langmuir and Freundlich models. It was developed aiming to predict heterogeneous adsorption systems and remove the limitation caused by the increasing adsorbate concentration encountered when utilizing the Freundlich isotherm model. It predicts monolayer adsorption at large concentrations, indicating the Langmuir isotherm. The model is a highly flexible gas adsorption equilibrium modeling with good fitness to the experimental data in both the low and high-pressure regions, though with a finite limit when the pressure is sufficiently high (Park *et al.*, 2016). So, this model is the most applied commonly model, because of its high accuracy (Khoramzadeh, Mofarahi and Lee, 2019). In the equation, n_S is the Sips isotherm exponent (−).

$$q_{eq} = \frac{q_m \cdot (K_{eq} \cdot P)^{\frac{1}{n}}}{[1 + (K_{eq} \cdot P)^n]^{\frac{1}{n}}} \quad (6)$$

Finally, the BET model (Equation 8) uses the same mechanism of the Langmuir model, nonetheless with some simplifications and suppositions to represent the adsorption in multilayers: i) each molecule of the first layer provides an adsorption site for subsequent layers; ii) molecules from the second layer onwards, which are in contact with other molecules, behave essentially like a saturated liquid; iii) the enthalpy of the first layer is the enthalpy of adsorption, and; iv) the enthalpy of subsequent layers is considered equal to the adsorbate's enthalpy of vaporization. In this model, P_s is the adsorbate saturation pressure at the system temperature. This model is often used to determine the specific area of porous solids through liquid nitrogen adsorption (Pérez-Botella et al., 2022; Dantas, 2009).

$$\frac{q_{eq}}{q_m} = \frac{K_{eq} \cdot \frac{P}{P_s}}{(1 - \frac{P}{P_s})\,(1 - \frac{P}{P_s} + \frac{K_{eq} \cdot P}{P_s})} \quad (7)$$

5.2 ADSORPTION IN A FIXED BED COLUMN

Fixed bed adsorption for gas separation and purification has gained widespread use in industrial applications due to its advantages of high capacity, ease of operation, and low energy consumption (Liu *et al.*, 2016). Up to now, most of the studies on CO_2 adsorption and desorption have been conducted using fixed bed or thermogravimetric analyzer (TGA) methods (Xu *et al.*, 2024).

The behavior in a fixed bed relies on mass transfer zones. This concept represents a macroscopic approximation, delineating the movement of the mass transfer zone during adsorption operations, where the mass transfer zone is defined as the section of the bed where the adsorbate from the feed solution transfers to the solid phase (adsorbent). This method applies to the system when there is a rapid formation of a stable mass transfer zone. These factors lead to the adsorption process being restricted, preferably to a small area of the bed, which soon after the process begins flows gradually and at a steady speed. The maximal

adsorption capacity of the adsorbent, the adsorptive concentration, and the operational flow rate influence this displacement. Monitoring the shape of the mass transfer zones is conducted by observing the concentration of the adsorbate at the outlet of the fixed bed column (Ruthven, 1984; Richardson and Harker, 2002; Dantas, 2009).

The analysis of fixed bed operation for sizing adsorption or ion exchange columns is based on the breakthrough curve of the adsorbent, which is graphically represented in Figure 25. The curvilinear behavior of the rupture curve delineates a region of the bed in which adsorption is occurring, the mass transfer zone. Thus, the shorter the length of the mass transfer zone, the closer the system is to ideality, indicating greater efficiency (Dantas, 2009). The breakthrough point (t_{Bp}) is defined as the moment when the solute is detected at the column outlet (Cc ≈ 5% Co), while the exhaustion time (t_E) occurs when the concentration Cd reaches 95% of the initial concentration. Under ideal conditions, i.e., in the absence of mass transfer resistances, the column response would resemble a step located at the stoichiometric time (t_{St}).

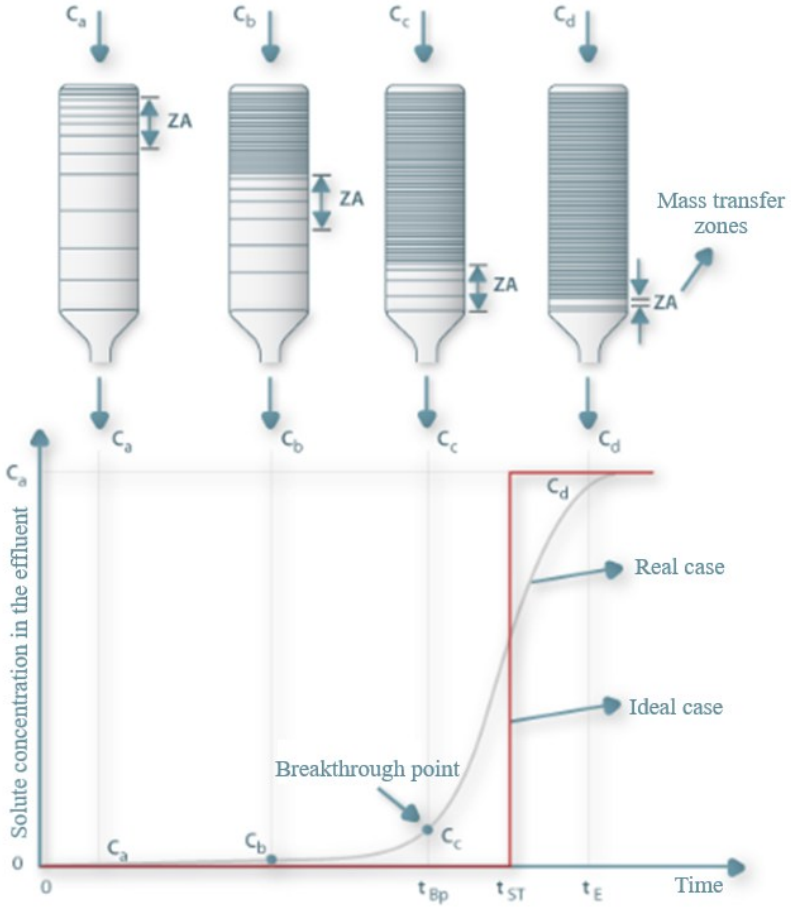

Figure 25. Graphic representation of a breakthrough curve. Adapted from (Ferreira et al., 2024)

5.3 ZEOLITE IN GAS ADSORPTION PROCESS

Zeolites are materials widely discussed in the literature as adsorbent materials, due to characteristics like microporosity and regular pore size, selectivity, large adsorption capacity, thermal stability, and relatively low-cost production. The studies made in 1840 by Damour, and in 1896 by Friedel, about the reversible adsorption of molecules by zeolites were the first to clarify the adsorption properties of this material (Pérez-Botella, Valencia and Rey, 2022).

Overall, there are studies about many types of zeolites, however, zeolites 3A, 4A, 5A, and 13X are the ones on which most adsorption studies have been carried out and the most used in industrial separations. The zeolites can differentiate between molecules smaller than the pore size and larger ones, due to their molecular sieving mechanism, thus being part of the so-called molecular sieve materials (Pérez-Botella, Valencia and Rey, 2022).

Khoramzadeh et al. (2019), realized a study for testing zeolite 13X, 4A, 5A, and beta type, for N_2 and CO_2 adsorption, in different temperatures and pressure, and as a result, they

have that the zeolite type A and 13X showed a good capability to separate de CO_2 over N_2, in lower pressures the zeolite 4A had the highest selectivity, and in higher pressures, the zeolite 13X showed the highest selectivity and adsorption capacity, followed by 5A, 4A, and beta. Lastly, they conclude that the zeolite 13X can be a promising adsorbent for practical applications in CO_2 adsorption.

Moreover, in a recent study realized by Najafi et al. (2023), where the adsorption capacity of CO_2, CH_4 and N_2 were analyzed on zeolite 13X and binder-based extrusion with 20% of inorganic binders (silica sol, pseudo-boehmite, bentonite, and attapulgite). As a result, the adsorption isotherm studies on binder-less zeolite 13X and extrudes with inorganic binders up to 100 kPa and 25ºC showed that the trend of CO_2 adsorption was 13X > B2 (pseudo-boehmite) > B3 (bentonite) > B4 (attapulgite) > B1 (silica) in which the adsorption capacity of binders increased by 6.97, 12.95, 16.94, and 21.76%, respectively, proving that the 13X zeolite type without binder is a promising adsorbent for applications in CO_2 adsorption.

In addition to the 3D-printed zeolite composite's adsorptive capacity values previously presented in section 3.2, Table 6 presents the adsorptive capacity of zeolites in studies reported in the literature. In all cases, the tests were carried out at a temperature between 25 and 30 °C at the pressure of 1 bar. It is possible to notice that the adsorption capacity of the zeolite in powder is higher than in monoliths or composites. Moreover, the zeolite 13X type samples presented higher adsorptive capacity than the 5A zeolite type.

Table 6. Comparison of the adsorption capacity of the Z13X and Z13X-composites samples with some research reported in the literature.

Sample	**CO_2 Adsorption capacity (mmol/g)***	**Reference**
13X (powder)	~5.01	Thakkar et al. (2016)
13X-R4	~4.49	
13X-Powder	4.04	Thakkar et al. (2018)
T-13X	1.83	
13X-AC	~5.50	Regufe et al. (2019)
Zeo-powder	~5.4	Mendes et al. (2021)
Zeo-3D	~4.2	
Zeo-AC-3D	~3	
Zeo-G-3D	~1.8	

50%13X-50%AC monolith	3.02	Pereira et al. (2022)
13X	6.02	(Najafi *et al.*, 2023)
Na13X	2.5	(Minelli *et al.*, 2016)
Na13X	3.5	(Minelli *et al.*, 2018)
13X	4.86	(Khoramzadeh, Mofarahi and Lee, 2019)

* Temperature between 25 °C and 30 °C and pressure at 1 bar.

5.4 APPLICATION OF GEOPOLYMERS IN GAS ADSORPTION PROCESS

The adsorption capacity of geopolymers is associated with their porous structure, the presence of negative charges in aluminum tetrahedra, as well as their mechanical stability, low cost, and high efficiency (Freire *et al.*, 2020), the intrinsic mesoporosity, high surface area (50-100 $m^2 \cdot g^{-1}$), and high compressive strength (20-90 MPa) make geopolymers potential candidates for industrial processes as solid adsorbents (Minelli *et al.*, 2016). Nevertheless, the use of geopolymers as adsorbent material for CO_2 capture or gas separation is recent.

Furthermore, preparing geopolymers for new applications can be more difficult using raw materials resulting from waste than using pure materials. This is due to impurities in the base materials, such as fly ash and red mud (Silveira, 2021). Therefore, clarifying the chemical method of geopolymer formation from industrial by-products is a challenge. Some researchers have developed materials that utilize geopolymers in the CO_2 capture process, achieving a significant adsorptive capacity of 1.7 mmol/g (Minelli *et al.*, 2018), and 1.9 mmol/g (Freire, 2022). Table 7 presents some geopolymer adsorption capacity values, with the respective precursors materials. The tests were carried out at temperatures between 25 and 30 °C at a pressure of 1 bar.

Table 7. Adsorption capacity of geopolymer samples reported in the literature.

Adsorbent	**Precursor materials**		**CO_2 adsorption (mmol/g)**	**Reference**
	Aluminosilicate source	**Alkaline activator**		
G10	Metakaolin, fumed silica	Potassium silicate	0.62	(Minelli *et al.*, 2016)
G13			0.58	
G23			0.57	
K-G_2	Metakaolin	Sodium hydroxide,	0.58	(Minelli *et al.*, 2018)
Na-$G_{1,2}$			1.7	

		potassium di-silicate		
GEO	Metakaolin, silica fume	Potassium hydroxide	0.19	(Chen *et al.*, 2020)
MCR-1	Metakaolin, calcined rice husk ash	Sodium hydroxide	0.80	(Freire *et al.*, 2020)
MF-1	Metakaolin, fly ash		0.78	
MR-1	Metakaolin, rice husk ash		0.69	
MFCR-1	Metakaolin, fly ash, calcined rice husk ash		0.63	
MFR-1	Metakaolin, rice husk ash, fly ash	Sodium silicate	0.68	
MF-2	Metakaolin, fly ash		0.64	
MPW	Metakaolin/Phosphate mining tailing	sodium hydroxide, sodium silicate	1.9	(Freire, 2022)

5.5 GEOPOLYMER/ZEOLITE COMPOSITES IN GAS ADSORPTION

Studies using geopolymer and zeolite composites for gas capture and separation are recent. Candamano et al. (2022), Minelli et al. (2018), and Papa et al. (2023), developed efficient geopolymer/zeolite composite for CO_2 capture and separation.

Minelli et al. (2018) demonstrated that combining a functional microporous zeolite with a mesoporous geopolymer matrix is an efficient strategy to improve CO_2 capture. In this case, they produced a hybrid material, where metakaolin was used as an aluminosilicate source for the geopolymerization along with Na13X zeolite powder, with an average particle size of 2 μm, which was used as filler. Na^+-based hydroxide and potassium di-silicate were used as alkali-activating solutions. The geopolymer matrices and composites were prepared following a mixing and curing protocol. Metakaolin was first mixed with the alkali silicate or hydroxide solution. Then, the zeolite was added to the geopolymer slurry and mechanically mixed. The mixtures were cast in silicone molds and cured for 24 h at 80 °C in closed molds and another 24 h at 80 °C in open molds. Pure gas (CO_2, N_2, and CH_4) adsorption capacity at 35 °C has been measured in the geopolymer zeolite composites. Three different composite samples were tested for CO_2 capacity and CO_2/N_2 and CO_2/CH_4 selectivity (at 1 bar).

A recent study by Candamano et al. (2022) highlights the preparation of rigid foams from geopolymer/zeolite-NaX/activated carbon composites and their application in CO_2 adsorption. The authors produced monoliths via geopolymerization followed by in situ conversion to NaX zeolite formation. The porosity was modified using hydrogen peroxide and albumin as porogenic agents (other porogenic agents could be used, such as powdered aluminum, silica, and surfactants derived from vegetable proteins and fatty acids), and the pastes were quickly transferred to Teflon molds. The hybrid was subject to hydrothermal treatment at 90ºC for 24 h in a Teflon-lined stainless-steel autoclave, in favor of the zeolite crystals growth embedded in the geopolymer matrix. A scheme of the overall reactions is presented in Figure 26.

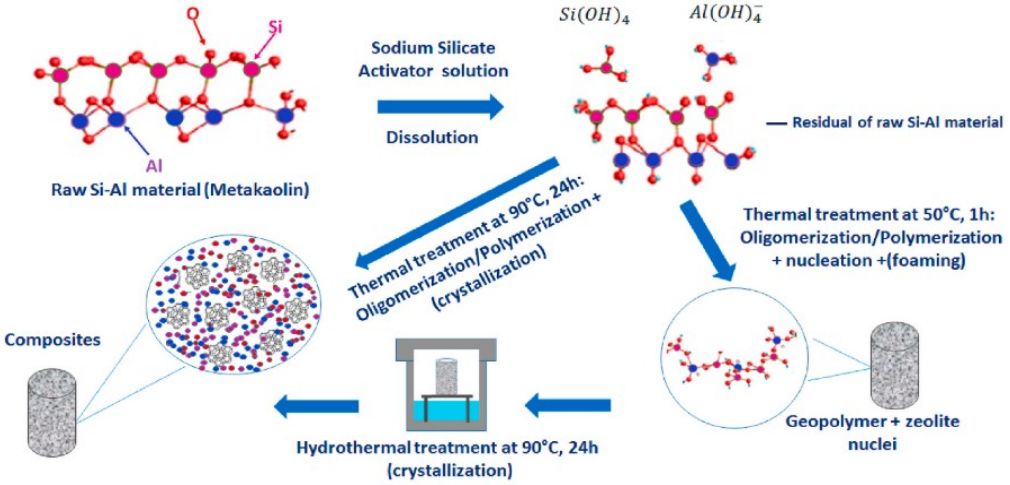

Figure 26. Scheme of the overall reactions for the preparation of rigid foams from geopolymer/zeolite-NaX/activated carbon composites (Candamano et al., 2022).

In this study, the CO_2 storage capacities of four prepared composites were analyzed: G-NaX (geopolymer/NaX zeolite), G-NaX-f (foamed geopolymer/NaX zeolite), G-NaX-AC (geopolymer/NaX zeolite/activated carbon), and G-NaX-AC-f (foamed geopolymer/NaX zeolite/activated carbon). The values of CO_2 storage capacities obtained were 3.4, 2.5, 2.7, and 2.8 mmol/g, for G-NaX-f, G-NaX, G-NaX-AC-f, and G-NaX-AC, respectively. In this regard, the study concludes that among the adsorbents tested, composite G-NaX-f offers the best overall CO_2 adsorption performance in terms of adsorption capacity, reversibility, and cyclability (Candamano *et al.*, 2022).

Table 8 presents the adsorption capacity value of the composites developed in the studies reported in the literature. The tests were carried out at between 25 and 30°C at 1 bar.

Table 8. Geopolymer and zeolite characteristics and CO_2 adsorption capacity.

Sample*	CO_2 adsorption capacity (mmol/g)	Reference
K-G_2-Z13X	2.50	(Minelli *et al.*, 2018)
Na-$G_{1.2}$-Z13X	1.60	
G-Z13X	2.5	(Candamano *et al.*, 2022)
Na-$G_{1,2}$-4A	2.60	(Papa *et al.*, 2023)
K-G_2-4A	0.47	
K-$G_{1,2}$-4A	0.03	

*2 or 1,2 is the geopolymer Si/Al molar ratio.

6 METHODOLOGY, RESULTS AND DISCUSSIONS

This section introduces the studies presented in Chapters 7–10, which are included in this thesis as a compilation of scientific articles. These chapters describe the development, characterization, and evaluation of geopolymer and geopolymer/zeolite-based materials for gas capture and separation applications.

Geopolymer materials based on metakaolin and phosphate mining tailings were synthesized using alkaline activation, and different curing conditions were evaluated in order to investigate their influence on the structural, chemical, and textural properties of the materials. The obtained materials were characterized using techniques such as XRF, XRD, SEM, FTIR, NMR, XPS, and surface area and porosity analyses.

Geopolymer/zeolite composites were also prepared by incorporating different amounts of zeolite 13X into the geopolymeric matrix, aiming to combine the structural stability of geopolymers with the high adsorption capacity of zeolites. In addition, different processing strategies were explored to obtain materials with controlled morphology. Electrospinning was used to produce fibrous membranes incorporating geopolymer, zeolite, and composite particles in a PVA matrix, while additive manufacturing through 3D printing was applied to produce geopolymer/zeolite monolithic structures with controlled geometry.

Overall, the results demonstrate that synthesis conditions, material composition, and processing methods influence the structural properties and adsorption behavior of the materials. The incorporation of zeolite increased the surface area and adsorption capacity for CO_2, while electrospinning and 3D printing enabled the fabrication of materials with different architectures for gas capture applications.

The methodologies, results, and discussion of these studies are presented in detail in Chapters 7–10, organized as three scientific articles that compose this section of the thesis.

7 INFLUENCE OF CURING TEMPERATURE ON THE SYNTHESIS OF A PHOSPHATE-WASTE BASED GEOPOLYMER FOR CO_2 CAPTURE AND SEPARATION

This section refers to an adaptation of the research paper entitled "Influence of Curing Temperature on the Synthesis of a Phosphate-Waste Based Geopolymer for CO_2 Capture and Separation"[2] published in "*ACS Applied Energy Materials*". This topic brings in the materials and procedures applied to prepare the geopolymeric materials, as well as their characterization, results and discussion.

7.1 MATERIALS AND METHODS

7.1.1 Materials

Kaolin was obtained from Caulisa Kaolin Industry (Pernambuco, Brazil), phosphate waste (PW) mining tailings, provided from a mine placed in Goiás (Brazil), sodium hydroxide (NaOH – micro-pearls with 98.5% purity) obtained from VWR Chemicals, and the sodium silicate solution (SS) – SiO_2/Na_2O (ratio SiO_2/Na_2O: 2.5) was purchased from Sigma-Aldrich.

7.1.2 Geopolymer Synthesis

The geopolymer was synthesized based on (Freire *et al.*, 2025), (Chen *et al.*, 2020), and (Minelli *et al.*, 2016) using metakaolin and phosphate waste as precursors, and a mix of sodium hydroxide (NaOH) and sodium silicate (Na_2SiO_3) as alkaline activator. A complete characterization of metakaolin and phosphate waste was carried out by Freire et al., 2024 and Freire et al., 2020. The chemical composition of metakaolin has predominantly silicon, at 54.3%, and iron oxides at 44.2% (Freire *et al.*, 2020), and the main chemical composition of PW is silicon, at approximately 49%, and iron oxides at 21% (Freire *et al.*, 2025).

[2] Schneider, M., Costa, D. G. da S., Rodríguez-Castellón, E., Guerrero-Pérez, M. O., Hotza, D., de Noni, A., & Moreira, R. de F. P. M. (2025). Influence of Curing Temperature on the Synthesis of a Phosphate-Waste-Based Geopolymer for CO_2 Capture and Separation. *ACS Applied Energy Materials*. https://doi.org/10.1021/acsaem.5c00426

For the synthesis, the kaolin was first calcinated at 900 ºC for 60 min to obtain the metakaolin. The choice of molar ratios for the geopolymer's synthesis was SiO_2:Al_2O_3 = 3.30; Na_2O:SiO_2 = 0.30; Na_2O:Al_2O_3 = 0.99; and H_2O:Na_2O = 12.00, based on a study developed by Davidovits et al. (1994), since it was already used for the synthesis of phosphate mining tailings-based geopolymer and it present interesting characteristics for CO_2 capture (Freire *et al.*, 2025). Then, the geopolymer was prepared by following six steps: i) mixing the two solid components (kaolin and PW); ii) preparation of the alkaline activator, mixing NaOH, SS, and deionized water (DIW) at 800 rpm for 10 min on a magnetic stirrer; iii) preparation of the suspension by adding the solids to the alkaline activator solution and mixing for 15 min at 1500 rpm, on a mechanical stirrer; iv) the geopolymeric slurry was molded into a cylindrical shape, using a 2×4 cm silicone mold; v) two samples were prepared and the curing process was carried out in an oven (VENTI-line VWR chemicals) at 80 °C and 65 °C, the latter covered with a high-temperature tape so that the water evaporates slowly; vi) after demolding, a part of the samples were submersed in DIW water to remove unreacted sodium ions, and the other part was left to cure without submersion, both samples were left at room temperature (25 ºC ± 2 ºC) for 30 days. Finally, the submersed material was dried in an oven at 100 °C for 24 h. The composition of the samples is presented in Table 9. The geopolymer samples cured at 65 ºC were named G65s and G65 for submersed cure and dry cure, respectively, as well as for the samples cured at 80 ºC, the sample with submersed cure was named G80s and the dry cured G80.

Table 9. Geopolymer formulation

Precursor material	**(wt%)**
Metakaolin	35
Phosphate waste	19
NaOH	11
Sodium silicate	13
Water	22

7.2 CHARACTERIZATION

All the characterizations were made at the Central Research Support Service (SCAI), at the University of Málaga.

The geopolymer samples were analyzed by X-ray fluorescence (XRF), to determine the chemical composition and the quantification of oxides, using Thermo Fisher Scientific

equipment. The density of the samples was evaluated using a pycnometer AccuPyc II1340 with helium, in a chamber with 1.0 cm^3 at 23.33 ºC with an equilibration rate of 0.0050 psig/min.

The crystalline structure and mineralogical composition of the samples were evaluated by X-ray powder diffraction (XRPD). To identify the crystalline phases present in the materials the X'pert HighScore plus software was used. To evaluate the chemical stability of the samples to CO_2 attack, the XRD analyses were performed before and after exposition to CO_2. The analysis was carried out using a PANanalytical Empyrean automated diffractometer. Powder patterns were recorded in the Bragg-Brentano reflection configuration using the PIXcel 3D detector with a step size of 0.017º (2θ). The powder patterns were recorded between 4 and 70º in 2θ with a total measuring time of 30 min.

Scanning electron microscopy (SEM) was employed to study the morphology and conduct chemical analysis of the materials. This technique allows for the identification of material components and provides detailed insights into the internal structure of the samples, including crystal structure, morphology, and stress state information. The equipment used was a FESEM Tescan Clara microscope, with a Leica EM ACE600 metallizer. The samples were coated with 4 nm of platinum, to make it more conductive for a better analysis.

The BET surface area (m^2/g) is an important parameter for the characterization of solids used for processes involving their surface, the kinetics of heterogeneous solid-fluid interaction processes directly depend on the specific area of this solid. The specific surface area, pore size, and total pore volume were obtained through nitrogen adsorption-desorption isotherms at -196 ºC using Micromeritics ASAP 2020 equipment.

For the micro-computed tomography (m-CT) analysis, the samples were scanned employing a SkyScan 2214 (Bruker) system, aiming to analyze the inner porosity of the materials. Projections were obtained using a W source filament and employing a 0.25- or 0.5-mm Al foil (for sample 3 or the other samples respectively) in front of the CDD3 detector to minimize the beam hardening artifact. This source was set to 45 or 95 kV and 130 or 86 µA (for sample 3 or the other samples respectively). The CCD3 detector with a physical pixel size of 17.427 µm was set in a middle position with a source-to-detector distance of 315.449 mm and a source-to-sample distance of 10.861 or 39.823 mm which yielded a voxel size of 0.6 µm for sample 3 or 2.2 µm for the other samples. All scans were acquired over 360° (0.15 or 0.2° rotation step) using an exposure time of 2.9 or 1.75 s for sample 3 or the other samples, respectively. This results in an overall recording time of 8.5 or 4.5 h per dataset (for sample 3

or the other samples, respectively). Image reconstruction was carried out using Bruker NRecon software (version 2.2.0.6) applying beam hardening correction.

Fourier-transform infrared spectroscopy (FTIR) was used to identify the functional groups and chemical bonds present on the surface of the samples. The analyses were performed on a spectrometer model 6800FV from Jasco Analitica. The measurements were made by total attenuated reflectance using the ATR ProOne accessory and making a blank in the air, without the need to disperse or treat the sample. For the acquisition of spectra, a standard spectral resolution of 4 cm^{-1} was used in the spectral range of 4000-400 cm^{-1}, as well as 64 accumulations per sample.

X-ray photoelectron spectroscopy (XPS) determined the samples' surface chemistry. The spectra were recorded on a physical electronic spectrometer (PHI Versa Probe II) using monochromatic Al Kα radiation (15 kV, 1486.6 eV), a dual beam charge neutralizer for analyzing the core-level signals of the elements of interest, and a hemispherical multichannel detector. The sample spectra were recorded with a constant pass energy value of 29.35 eV, 0.125 eV/step, and a beam diameter of 200 µm. The energy scale was calibrated using Cu $2p_{3/2}$, Ag $3d_{5/2}$, and Au $4f_{7/2}$ photoelectron lines at 932.7, 368.2, and 83.95 eV, respectively. Atomic concentration percentages of the characteristic elements were determined considering the corresponding area sensitivity factor for the different measured spectral regions. The Multipak 9.6 software was used for acquisition and data analysis. A Shirley-type background was subtracted from the signals. Recorded spectra were always fitted using Gaussian–Lorentzian curves to determine the binding energy of the different element core levels more accurately.

The thermal behavior of the samples and precursors was investigated by thermogravimetric analysis. A thermogravimetric analyzer Mettler Toledo model TGA/DSC 1 was used in a range from 30 to 900 ºC with an airflow of 50 ml/min, and heating velocity of 10 ºC, with 70 µl of alumina crucible and 10 mg of sample.

The ^{29}Si and ^{27}Al MAS-Nuclear magnetic resonance (NMR) analysis contribute to obtain information about the structure, chemical composition and purity, which can confirm the geopolymerization process, so the spectra were recorded using a high-definition nuclear magnetic resonance spectrometer, Bruker model AVIIIIHD 600, narrow bore with a magnetic field of 14.09 Tesla, at 156.4 MHz (Al frequency) and 119.2 MHz (Si frequency) with a probe 4 mm dual-resonance CPMAS using zirconia rotors at slew rates of 13KHz. Experiments with ^{27}Al were performed with proton decoupling (continuous wave sequence) by applying a single

pulse (π/18), an excitation pulse of 0.7 μs, and a relaxation delay of 1 s to obtain 1000 scans. Chemical shifts were referenced to an external 1 M of $Al(NO_3)_3$ solution. Experiments with ^{29}Si were also performed with proton decoupling (continuous wave sequence) by applying a single pulse (π/2), an excitation pulse of 8.5 μs, and a relaxation delay of 60 s to obtain 1000 scans. Chemical changes were referenced with an external solution of tetramethylsilane (TMS).

The adsorption equilibrium tests were carried out with the CO_2, CO, and H_2 gases at 30, 50, and 100 °C, with pressures between 0 and 760 mmHg, using a surface area and porosity analyzer, Micromeritics 3Flex model.

7.3 RESULTS AND DISCUSSION

7.3.1 Physico-Chemical Properties and Textural Characterization

The chemical composition of the geopolymer samples, analyzed through XRF, is presented in Table 10. As expected, the main components of the compositions are silica (SiO_2), alumina (Al_2O_3), sodium oxide (Na_2O), and iron oxide (Fe_2O_3). However, there is a considerable amount of titanium (TiO_2), calcium (CaO), and phosphorus (P_2O_5) oxides in the samples. The oxides in the geopolymer samples follow the analysis of precursors (metakaolin and phosphate mining tailings) carried out by (Freire *et al.*, 2025).

Regarding the curing temperature, the samples did not present a significant difference in composition. Finally, when comparing the submersed cured samples with the only dry cured ones, the amount of silica and aluminum oxides are very alike, however, sodium oxide is considerably higher for both dry cured samples, which can indicate the extraction of ions Na^+ not reacted throughout the submerse process.

Table 10. Total oxide composition and textural characterization of the samples.

	G65s	**G65**	**G80s**	**G80**
		Composition, wt%		
SiO_2	42.42±0.37	43.53±0.37	41.52±0.37	41.9±0.37
Al_2O_3	22.84±0.18	20.92±0.17	22.18±0.18	20.79±0.17
Na_2O	9.10±0.02	12.48±0.37	9.26±0.32	12.63±0.37
Fe_2O_3	7.40±0.09	6.93±0.18	7.27±0.18	6.77±0.18
TiO_2	3.07±0.05	2.96±0.02	3.06±0.02	2.83±0.02
CaO	1.74±0.03	1.73±0.09	1.82±0.09	1.60±0.09
P_2O_5	1.49±0.04	1.53±0.05	1.53±0.05	1.46±0.05

K_2O	0.38±0.01	0.37±0.03	0.36±0.03	0.36±0.03
MgO	0.36±0.00	0.27±0.03	0.32±0.03	0.25±0.03
MnO	0.33±0.00	0.30±0.01	0.29±0.00	0.29±0.00
CuO	0.04±0.00	0.03±0.00	0.03±0.00	0.03±0.00
Cl	0.02±0.00	0.02±0.00	0.01±0.00	0.01±0.00
ZnO	0.02±0.00	0.01±0.00	0.01±0.00	0.01±0.00
SO_3	-	-	-	0.01±0.00-
LOI	10.80	8.89	12.31	11.04
Textural characterization				
Density, (g/cm^3)	2.400±0.001	2.450±0.002	2.400±0.002	2.450±0.002
BET surface area (m^2/g)	301	187	337	154
Total pore volume (cm^3/g)	0.131	0.075	0.133	0.053
Pore size (Å)	55.89	52.68	61.81	64.25

The density, surface area, total pore volume and pore size of the samples are also shown in Table 10. The density of the samples was very similar comparing the samples; however, the submerged samples are little lower, with can be related to the dissolution of unreacted salt. The density of the samples increases as the surface area and total pore volume decrease, which is expected and agrees with the results obtained by Candamano et al. (2022) for zeolite and geopolymer composites.

Geopolymers have a zeolite-like structure, however, they do not present satisfying zeolitic capabilities in most cases, due to their limited porosity (Chen *et al.*, 2022). Herein, with the submerse cure process, the pore volume and specific surface area of the geopolymer are significantly higher than the samples without submersed cure (Table 10). Regarding the pore size, the sample cured at 65 °C is larger than the cured at 80 °C, and when comparing the submersed with the non-submersed ones, they are quite similar, showing that the submerse curing did not directly affect the pore size.

The presence of reacted or unreacted particles from the base materials, cracks, and pores are important factors that can affect mechanical and adsorption properties, as they contribute to the accessibility of the porous structure (Freire *et al.*, 2020). The BJH pore width distributions (Figure 27) of the G65s, G80s and G65 samples presented a significant broad peak in a range

of approximately 35-83 Å, 37- 81 Å, and 40- 73 Å, respectively, and the G80 sample presented a very low amount of pores in this range. This suggests that the geopolymer samples obtained in this study have mesoporous structures (Alothman, 2012; Thommes *et al.*, 2015; Wang *et al.*, 2025). Moreover, the presence of mesopores can be related to the associated with the occurrence of zeolitic phases (Freire, 2022), as shown in XRD (Figure 29), where the submersed samples presented more intense peaks.

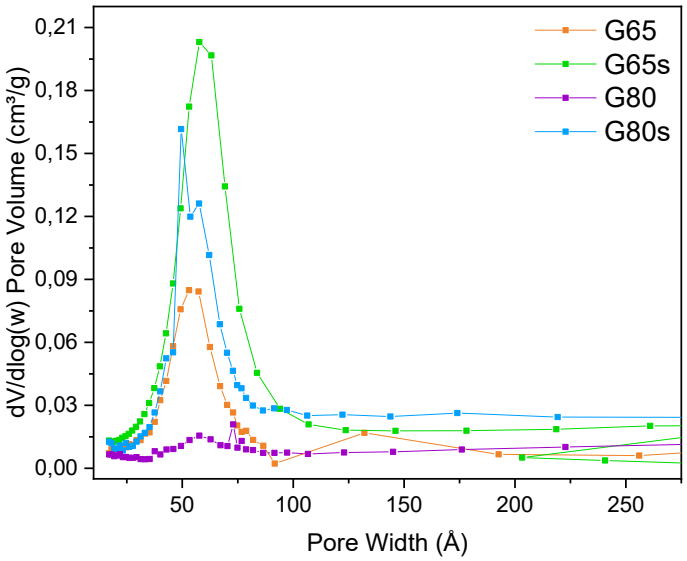

Figure 27. BJH pore distributions of the samples.

Open porosity (void space), closed porosity (pores, trapped bubbles), and total porosity, evaluated by mCT, are presented in Table 11. The sample G65s presented the highest open porosity, and the G80 the lowest. The volume of closed porosity is considerably similar for G65s and G80s, G65 and G80 presented greater closed porosity. However, it can be seen in Figure 28 that the black spots represent the pores closed. However, the number of pores on the G80 sample seems to be larger than the others, thus, this can be explained by the nano size of the pores, which is a size that the equipment is unable to recognize, due to the sensibility/precision of the equipment.

Table 11. Quantification of porosity using micro-CT analysis.

Sample	Open porosity (vol %)	Closed porosity (vol%)	Total porosity (vol%)
G65s	10.218	2.428	12.450
G65	1.550	4.893	6.367
G80s	1.477	2.300	3.743
G80	0.712	3.645	4.331

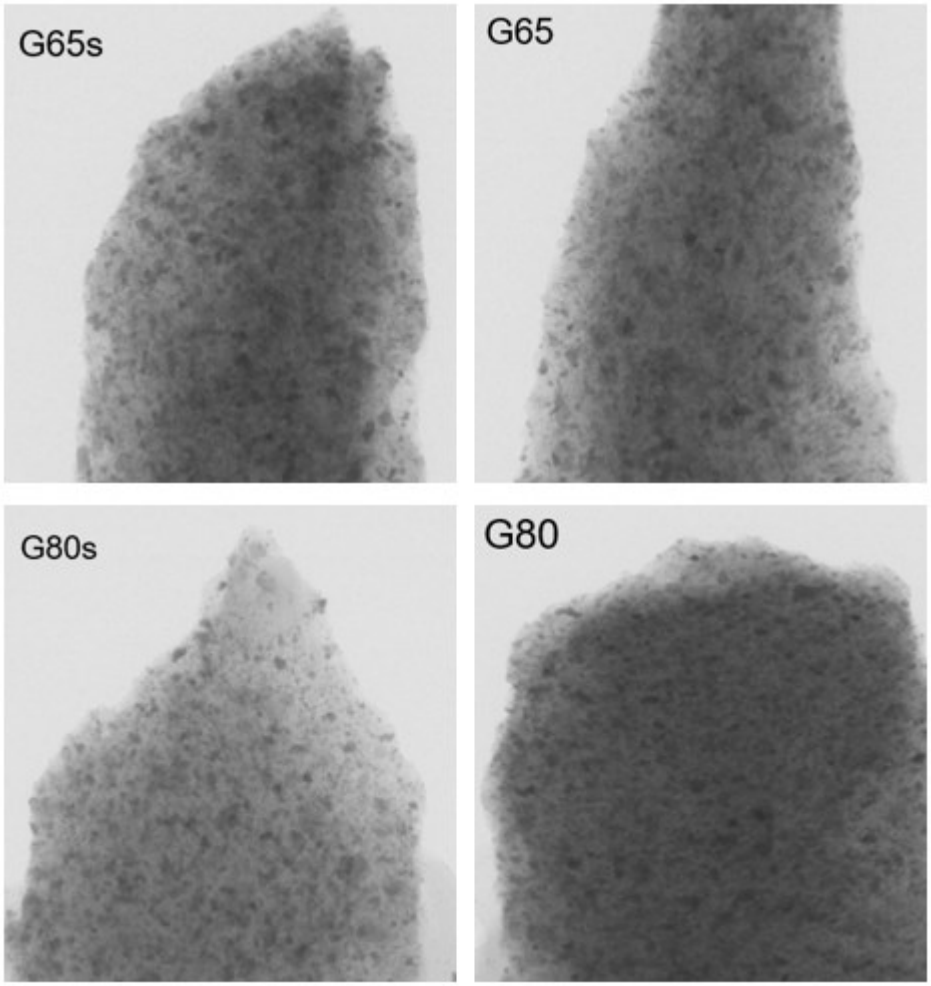

Figure 28. X-Ray Micro Computed Tomography of the geopolymer samples.

7.3.2 Mineralogical Composition, Crystallinity, and Morphology

The XRD patterns of the geopolymer samples are given in Figure 29. The presence of mineralogical phases in the geopolymers is reported in many studies, especially when there is a thermal cure in the synthesis process (Davidovits, 1994; Król, Minkiewicz and Mozgawa, 2016; He *et al.*, 2020).

For the precursors, the phosphate waste is crystalline, so the XRD patterns showed some crystalline phases, which are mainly composed by quartz (SiO_2 – ICSD-62405) at ~86%, and the remainder by anatase (TiO_2 – COD-9008215), vaterite ($CaCO_3$ – COD-9007475), magnetite ($FeO\text{-}Fe_2O_3$ – COD-9002329), and goethite (Fe_4O_8 – COD-9003077) (Freire *et al.*, 2025). And MK is mainly amorphous (~97%), however, two crystalline phases were identified, quartz (SiO_2- JCPDS-46-1045) and fluorite (CaF_2- JCPDS-35-0816) (Freire *et al.*, 2020).

Considering the precursors materials, during the curing process, different crystalline phases could be formed, even the geopolymers having identical formulations. However, in this case, the crystallography of the four samples is considerably identical, which means that the geopolymerization process occurred in the same way, independent from the cure temperature applied. In the diffractograms, a broad hump can be seen in the range from 15º to 40º, indicating the presence of amorphous aluminosilicate phases, which is expected, since the geopolymer is a predominantly amorphous material. Two crystalline phases were formed, alpha quartz (SiO_2 ICSD 062406) and faujasite ($Na_{5.12}Al_{52.35}Si_{139}O_{362.88}(OH)_{32}H_{39.594}$ ICSD 024867). In addition, some of the diffraction peaks were sharp and intense, indicating a high degree of crystallinity in these phases (Zhou *et al.*, 2013a).

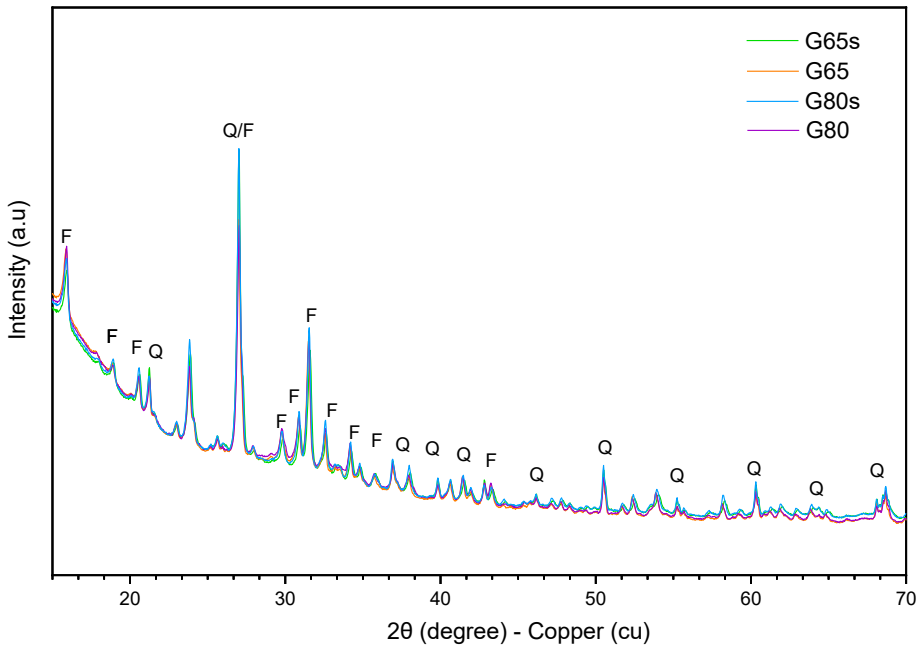

Figure 29. XRD patterns of the geopolymer samples, where Q is for quartz, and F is for faujasite.

The morphology of the microstructure of the samples is shown in Figures 30, 31, 32, and 33. Through these figures it is possible to notice the dense and homogeneous structure of the

samples, confirming the large amount of oligomers (Si-Al) in the reaction medium, which increases the degree of geopolymerization of the material (Kaze *et al.*, 2022). Unlike samples G65s and G80s, samples G65 and G80 are less compacted, which can be related to the dry curing, since without submersion, they have a high amount of salts present in the samples, as presented through XRF analysis, and higher density.

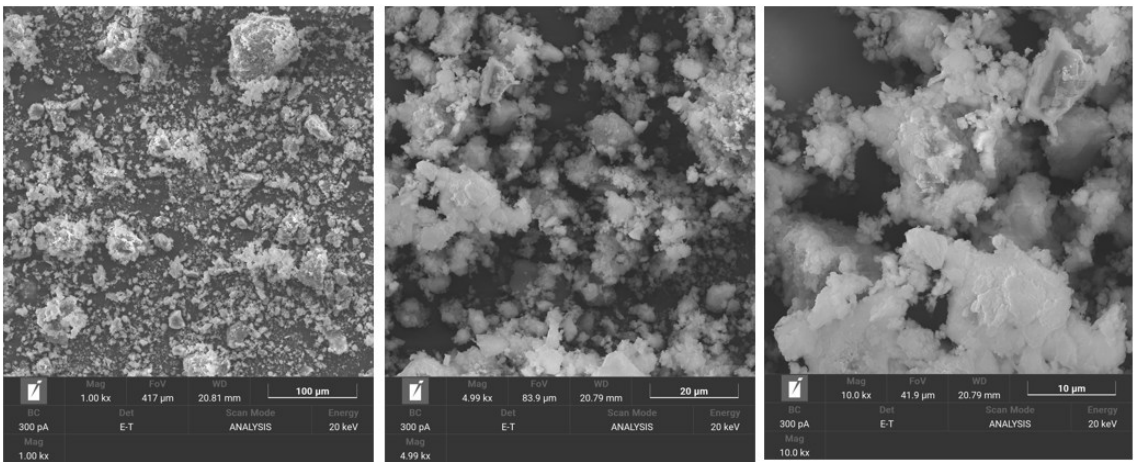

Figure 30. SEM images of the G65s sample.

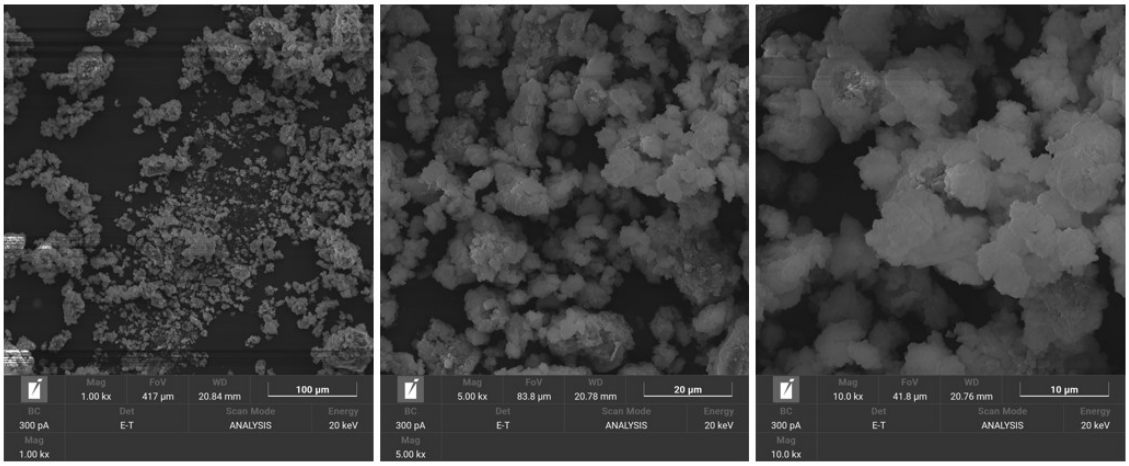

Figure 31. SEM images of the G65 sample.

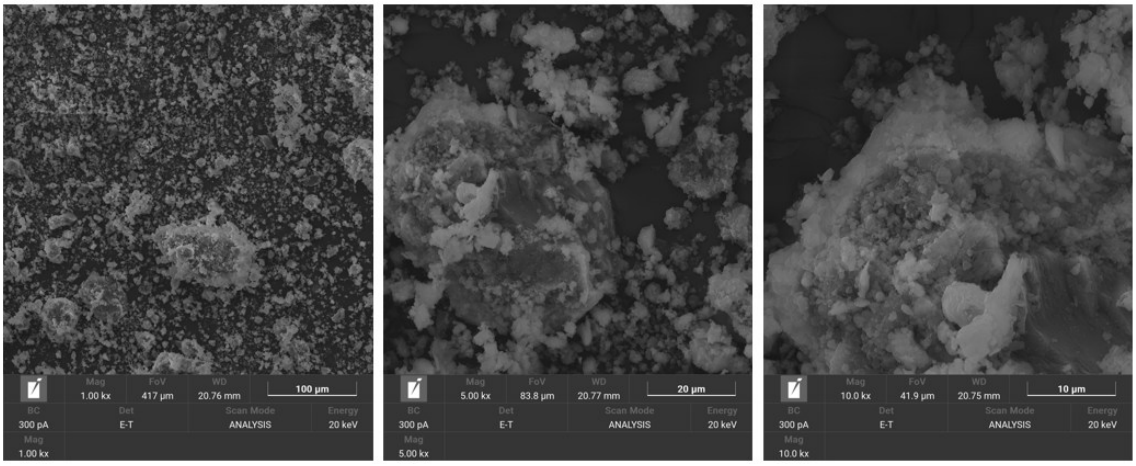

Figure 32. SEM images of the G80s sample.

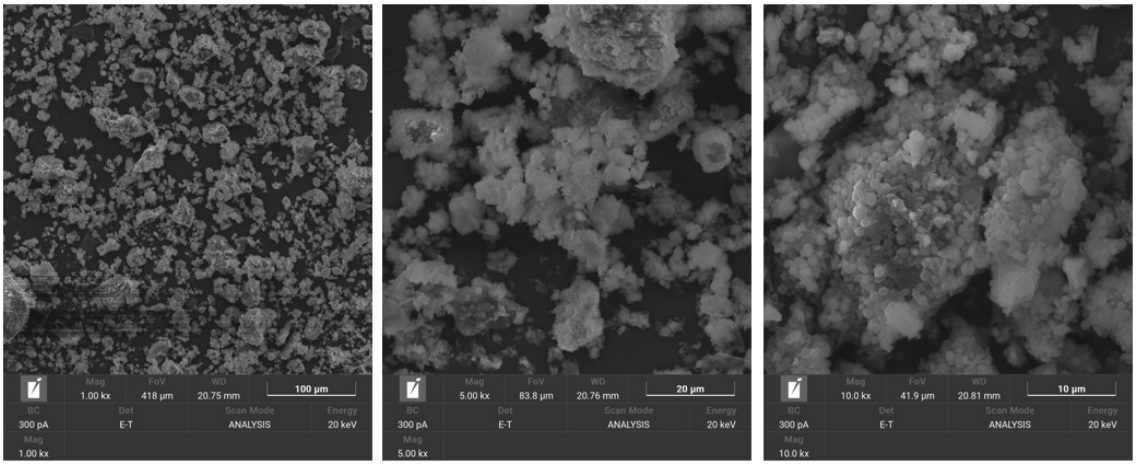

Figure 33. SEM images of the G80 sample.

7.3.3 Chemical Structure

The FTIR-ATR spectra for the samples are shown in Figure 34. The bands between the orange dash lines, in the region from 4000 to 2600 cm^{-1}, are attributed to the stretching vibrations of Si-OH, OH, and Si-OH-Al groups. The band between 1750 and 1650 cm^{-1}, red dash lines, is assigned to the bending vibration of the OH group (Król, Minkiewicz and Mozgawa, 2016; Kljajević *et al.*, 2017; Souza, 2021).

The bands in the region ~1500 to 1400 cm^{-1} represent the formation of carbonates, and in this case, their absence confirms that there are no carbonates in the samples, which is interesting, since the presence of carbonates can cause losses in the chemical and physical properties of the materials, mainly in geopolymers (Król et al., 2016; Rajini et al., 2021).

The bands between the black dash lines, in the 1300 to 900 cm^{-1} range, are characteristic of aluminosilicate materials, which correspond to the asymmetric stretching vibration of Si-O-

T type structures, where T is Si or Al (Kljajević *et al.*, 2017). The peak at ~1070 cm^{-1} represents the symmetric stretching vibration of the Si-O bonds and is identified in all sample spectra. The bands from 800 to 500 cm^{-1}, blue dash lines, are characteristic of symmetrical Si-O-Si group vibrations, and the bands between 730 and 554 cm^{-1} are correspondent to the vibrational bands of zeolitic materials, in this case, faujasite, zeolite 13X type (Jiménez, Lalangui, Guacho, Emperatriz Paucar, *et al.*, 2019).

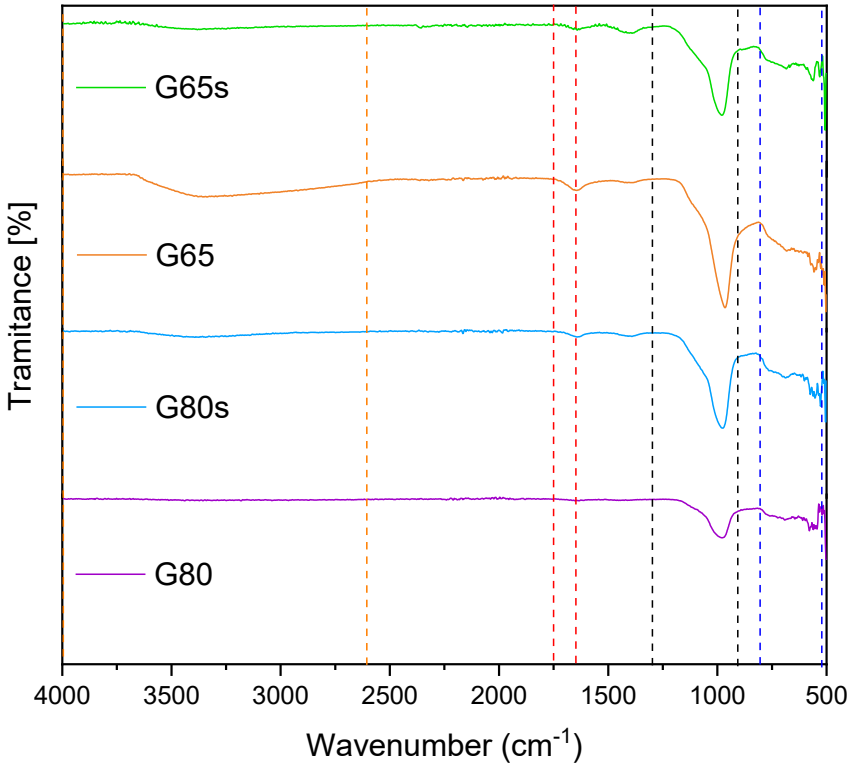

Figure 34. FTIR-ATR spectra of the samples.

7.3.4 Surface Chemistry

The XPS analysis was performed to know the chemical states and atomic composition of the surface of the sample's particles. The identification of the peaks was mainly based on the *Handbook of X-ray Photoelectron Spectroscopy* (Jolm F Moulder *et al.*, 1992). Overall, the sample spectra are very similar, changing mainly in the intensity of the peaks. The area of the peaks, atomic concentrations, and weight, obtained through the Multipak software are reported in Table 6, as expected the values are very similar for the submersed samples and the non-submersed samples.

The XPS spectra of the samples are shown in Figure 35 and the decomposed high resolution core level spectra are presented in Figures 36, 37, 38, and 39. The XPS quantification, atomic concentration, and weight of the samples are presented in Table 4, and the XPS quantification and area of the deconvoluted peaks of the samples are presented in Table 13, as expected, the values are very similar for the submersed samples and the not submersed samples.

For all samples, the positions of the peaks are quite similar, in the deconvolution spectra, the high resolution C 1*s* core level spectra were deconvoluted into four contributions, the contribution at 284.8 eV is correspondent to adventitious carbon (contamination), C-C, and/or C=C groups, at 286.3– 287.0 eV are related to the C-OH and C-O-C groups, the contribution at 288.4 - 289.4 eV is characteristic of the carbonate group, this group can also be assigned to the COOH or OH-C-OH bonds (Davydov *et al.*, 2014), and at the peak at 290.7 eV - 292.0 eV is correspondent to $\pi \rightarrow \pi^*$ satellite shake-up.

The O 1*s* spectra were deconvoluted in three contributions, at 529.9 - 530.5 eV is correspondent to lattice oxygen of the Na_2O group, the contribution at 531.5 eV to the O-H which can be assigned to water, and/or the carbonate$^-$ group, and the peak at 532.8 eV 532. 9 eV is related to Si-O groups.

The high-resolution Na 1*s* spectra present a single peak at 1071.6 - 1072.4 eV, which is characteristic of Na^+ in sodium aluminosilicate. Moreover, the Si 2*p* and Al 2*p* spectra have a single peak at 102.4- 102.6 and 74.2 - 74.4 eV, respectively, and these peaks are also characteristic of aluminosilicate. The submersed samples presented a small amount of iron, the peaks are at 711.0 eV and 711.1 eV, for G80s and G65s, respectively, which is assigned to the presence of Fe^{3+}.

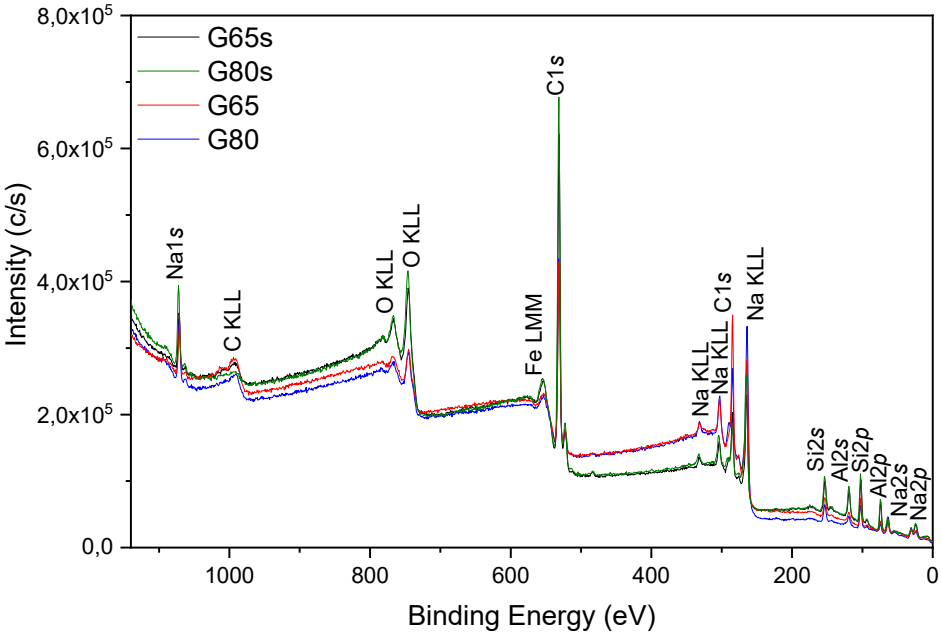

Figure 35. XPS survey spectra of the geopolymer samples.

Table 12. XPS quantification by atomic and weight concentration of the samples.

	G65s		G65		G80s		G80	
	Atomic (%)	**Weight (%)**	**Atomic (%)**	**Weight (%)**	**Atomic (%)**	**Weight (%)**	**Atomic (%)**	**Weight (%)**
C 1*s*	18.02	11.59	45.35	33.08	17.55	11.27	44.69	33.06
O 1*s*	50.66	43.41	33.00	32.06	50.63	43.29	35.30	34.79
Na 1*s*	6.66	8.21	5.71	7.98	7.17	8.81	6.91	9.79
Si 2*p*	13.07	19.66	10.79	18.41	12.89	19.35	8.48	14.68
Al 2*p*	11.26	16.28	5.11	8.38	11.54	16.65	4.62	7.68
Fe 2*p*3	0.16	0.48	-	-	0.15	0.45	-	-

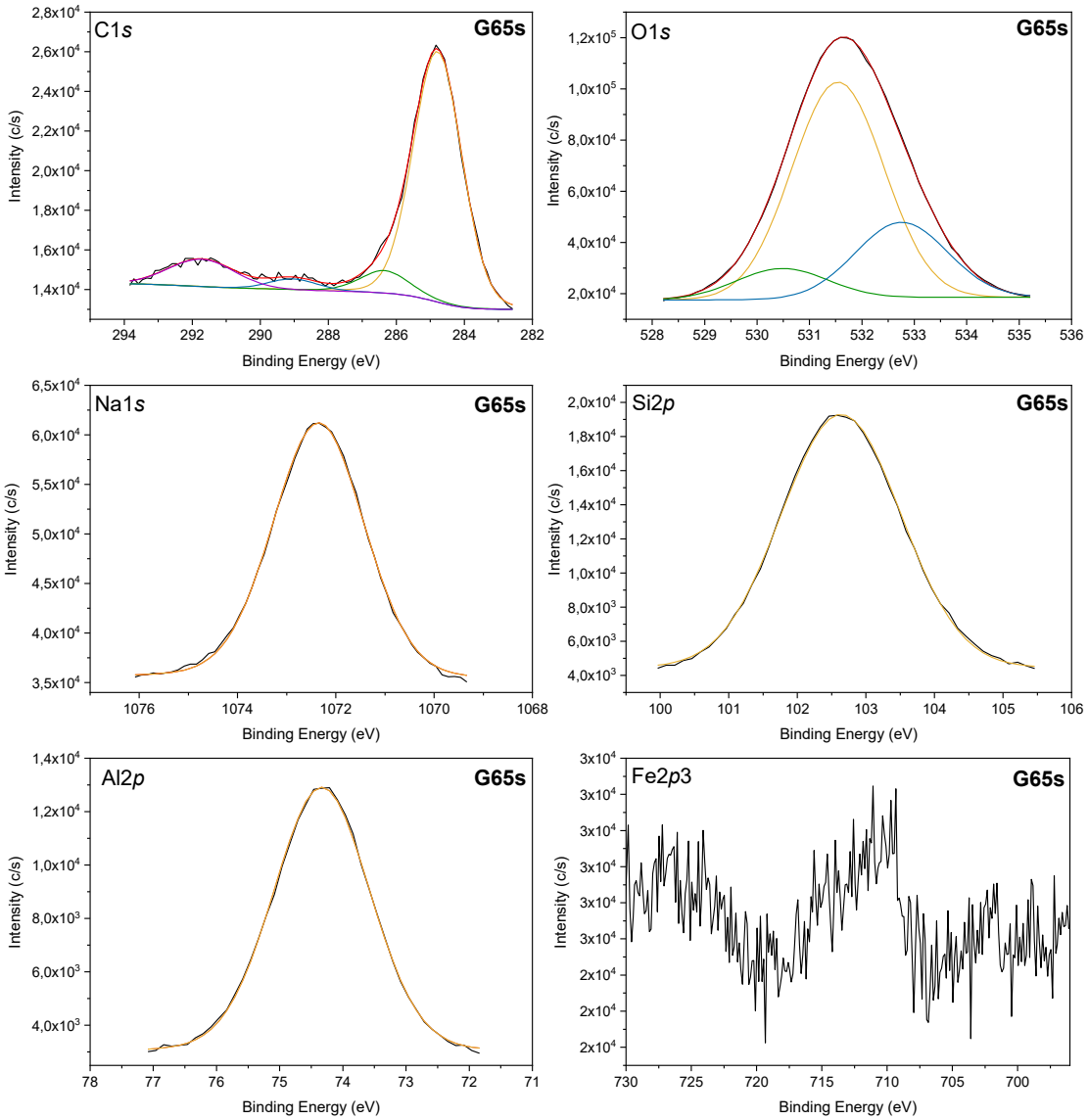

Figure 36. XPS decomposed atom electron orbitals spectra of the G65s sample.

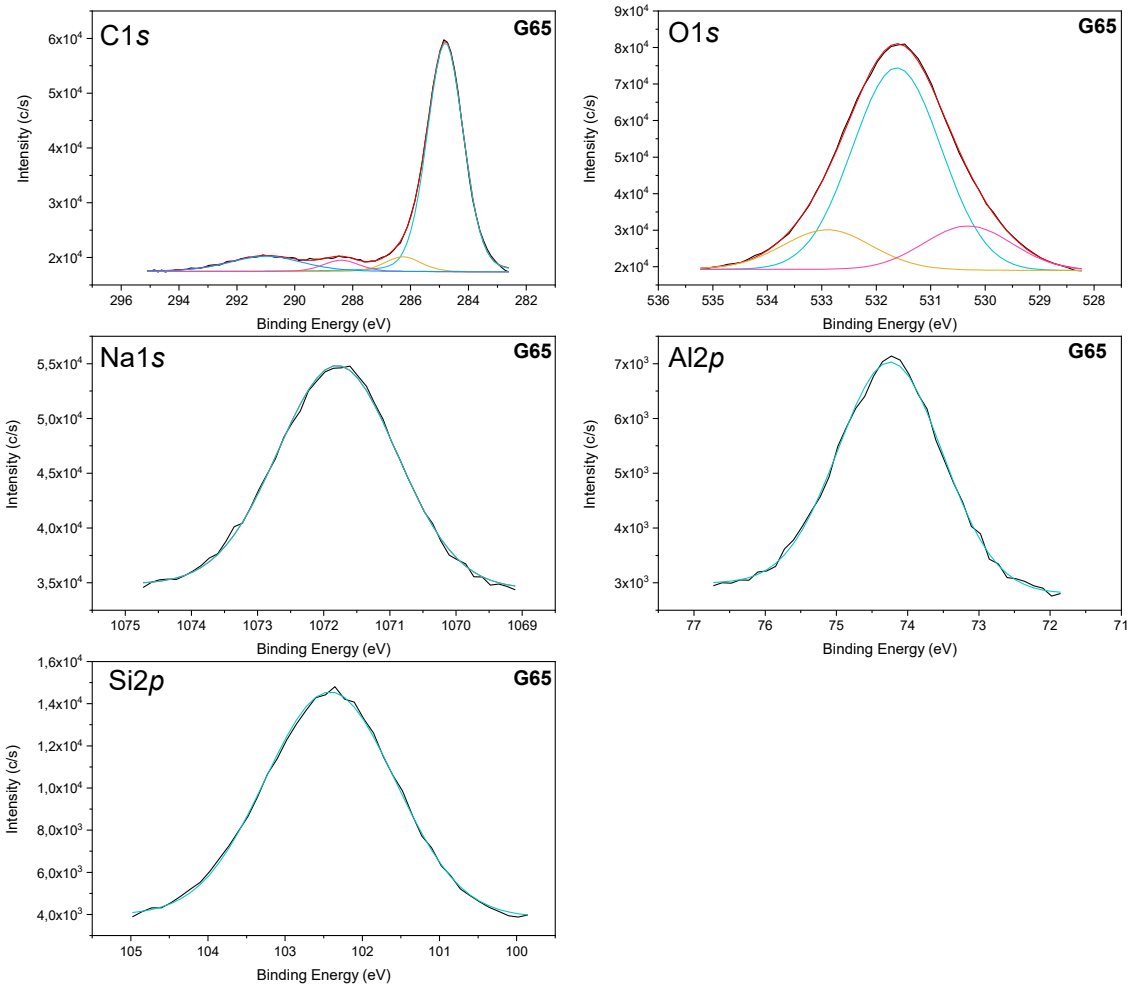

Figure 37. XPS decomposed atom electron orbitals spectra of the G65 sample.

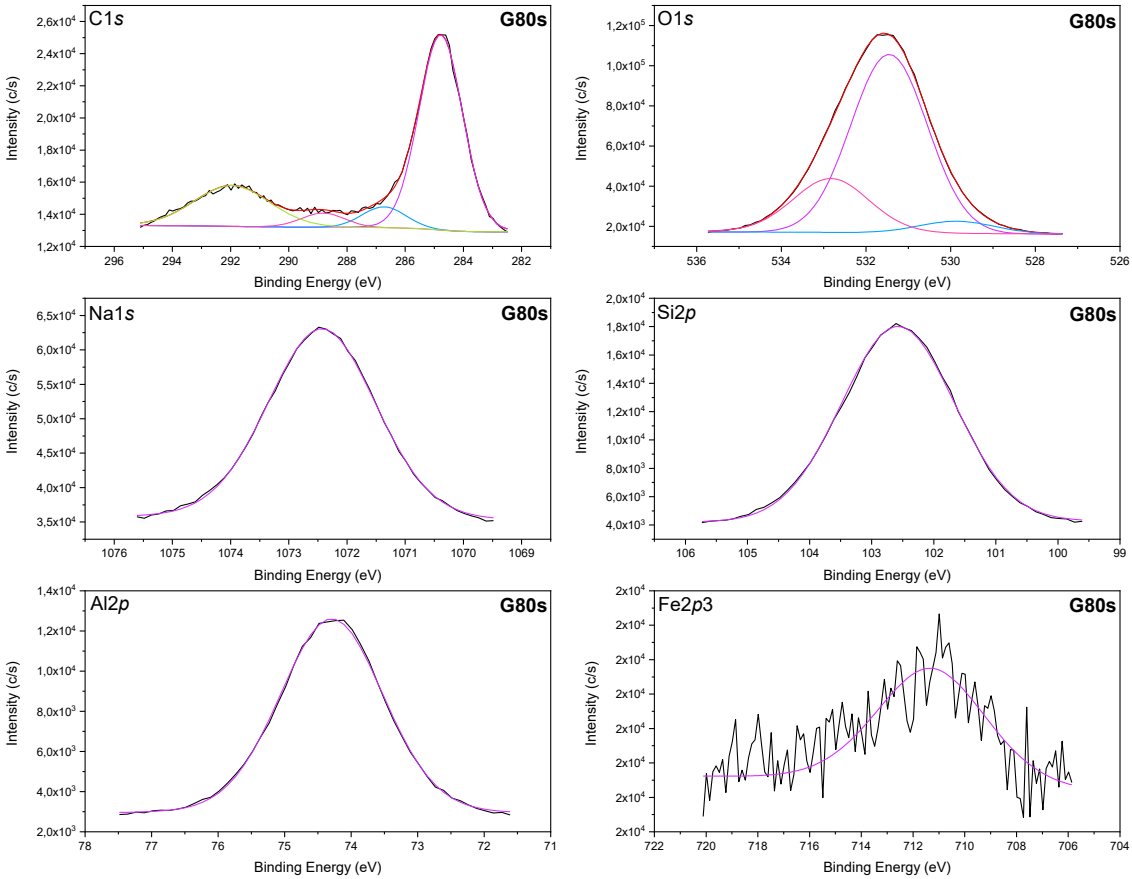

Figure 38. XPS decomposed atom electron orbitals spectra of the G80s sample.

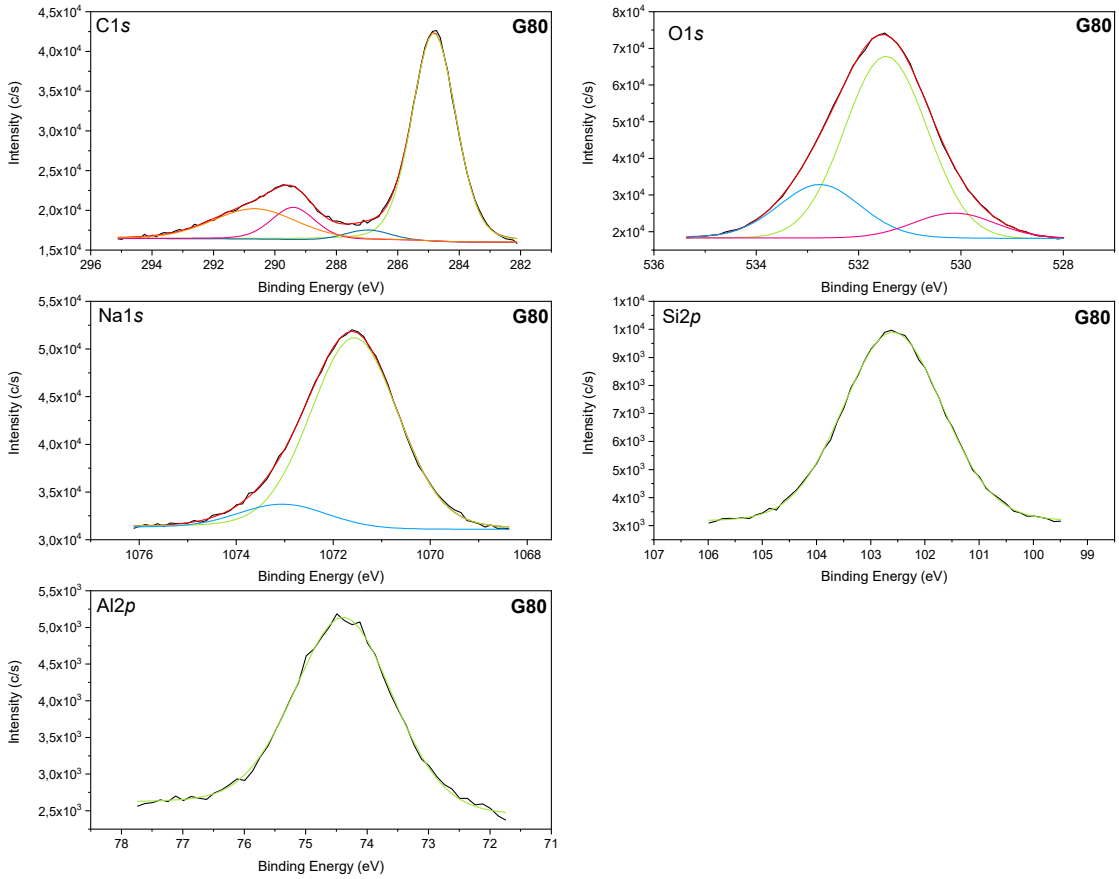

Figure 39. XPS decomposed atom electron orbitals spectra of the G80 sample.

Table 13. XPS quantification, area of the deconvoluted peaks of the samples.

	Area peaks (%)															
	G65s				G65				G80s				G80			
C 1*s*	284.8 eV 77.59	286.4 eV 7.57	289.0 eV 3.41	291.3 eV 11.44	284.8 eV 79.33	286.3 eV 5.40	288.4 eV 4.11	291.0 eV 11.16	284.8 eV 64.69	286.7 eV 6.83	288.8 eV 4.87	292.0 eV 23.60	284.8 eV 67.32	287.0 eV 3.03	289.4 eV 10.73	290.7eV 18.91
O 1*s*	530.5 eV 9.63	531.5 eV 67.05	532.8 eV 23.32	-	530.3 eV 15.41	531.6 eV 70.15	532.9 eV 14.44	-	529.9 eV 5.12	531.5 eV 71.97	532.8 eV 22.90	-	530.1 eV 9.67	531.5 eV 69.08	532.8 eV 21.25	-
Na 1*s*	1072.4 eV 100	-	-	-	1071.8 eV 100	-	-	-	1072.4 eV 100	-	-	-	1071.6 eV 100	-	-	-
Si 2*p*	102.6 eV 100	-	-	-	102.4 eV 100	-	-	-	102.6 eV 100	-	-	-	102.6 eV 100	-	-	-
Al 2*p*	74.3 eV 100	-	-	-	74.2 eV 100	-	-	-	74.3 eV 100	-	-	-	74.4 eV 100	-	-	-
Fe 2*p*3	711.1 eV 100	-	-	-	-	-	-	-	711.0 eV 100	-	-	-	-	-	-	-

7.3.5 Thermal behavior

The thermal behavior of the geopolymer samples is presented in Figure 40, which shows the thermogravimetric degradation and DTG curves. A significant decrease in the weight loss curves of the samples can be seen from room temperature to approximately 250 °C. The samples presented a mass loss of 13.85, 14.57, 14.83 and 13.03%, with the peaks at 123.5, 104.7, 125.6, and 109.1ºC, for the G65s, G65, G80s and G80 samples, respectively. This gradual decrease in the mass is related to the elimination of free and interstitial water in the sample (Kong, Sanjayan and Sagoe-Crentsil, 2007; Douiri *et al.*, 2016; Akarken and Cengiz, 2023). Moreover, the stable mass loss from 250 °C to approximately 680 °C can be explained by the release of chemically bound water and hydroxyl (OH) groups by dehydroxylation (Xu and van Deventer, 2003; Kong, Sanjayan and Sagoe-Crentsil, 2007; White *et al.*, 2010; Akarken and Cengiz, 2023).

Comparing the endothermic peaks with the porosity analysis, the two submersed samples (G65s and G80s) presented higher total pore volume than the no-submersed ones. This means that more space is available, and consequently, the interstitial water trapped in the pores requires a higher temperature to be removed (Douiri *et al.*, 2016). This increase in the temperature of the endothermic peak indicates a stronger binding between the water and the network in the geopolymer gel phase (Xu & van Deventer, 2003).

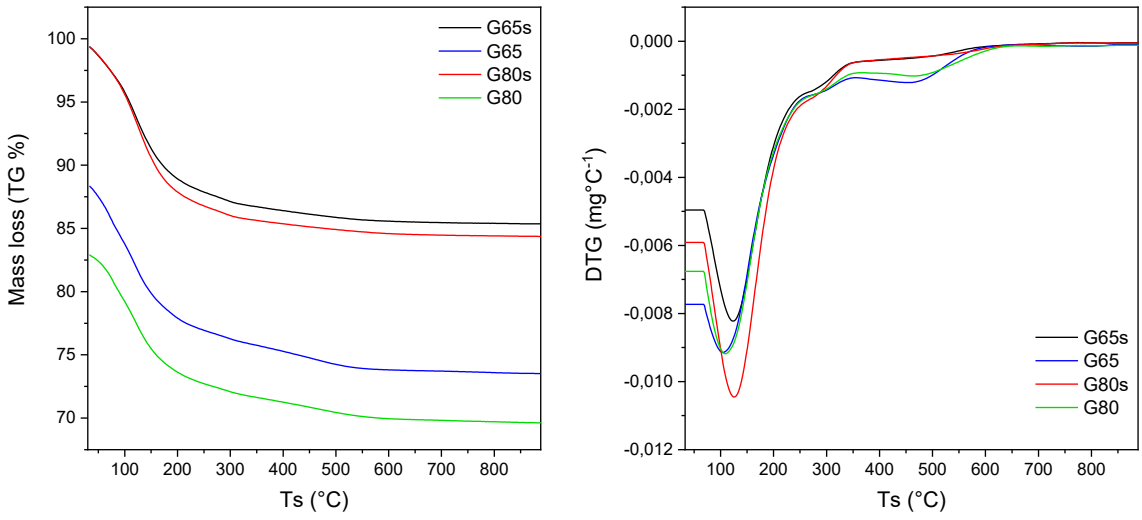

Figure 40. TG-DTG curves of the geopolymer samples.

Figure 41 shows the DSC thermogram of the samples. The samples presented small endothermic peaks located at 118.9, 124.1, 130.2 and 82.4 ºC, for the G65s, G65,

G80s, and G80 samples, respectively. This confirms the relationship to the removal of free and interstitial water contained in the geopolymers (Buchwald *et al.*, 2009; Douiri *et al.*, 2016).

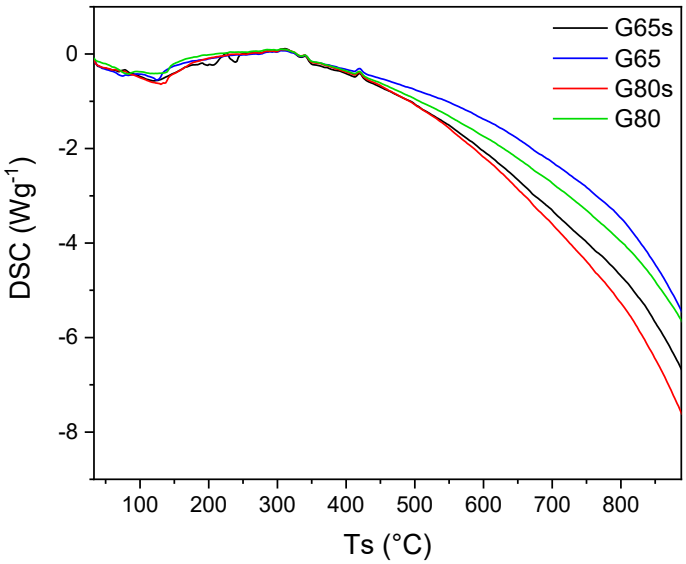

Figure 41. TG-DTG curves of the geopolymer samples.

7.3.6 Coordination of Si and Al

Solid-state NMR spectroscopy is an important analysis to investigate geopolymeric materials characteristics because it provides data regarding the coordination state of alumina units in the structure of precursor materials and geopolymers and, consequently, their reactivity (Freire *et al.*, 2020).

Figure 42 shows the ^{27}Al and ^{29}Si NMR spectra of all geopolymer samples, since they are very similar, only the intensity of the peaks changing. So, it can be observed that the ^{27}Al spectra present one sharp peak, at ~ 61 ppm, which corresponds to Al(IV), indicating the presence of tetrahedral aluminum in the sample, and two smaller peaks, at -10 ppm, and one at -21 ppm, which corresponds to Al(VI), octahedral aluminum. In this case, it can be related to zeolite (Bruker, 2012), since in the XRD analysis the samples presented some crystalline peaks, which were related to faujasite. The absence of octahedral and penta-coordinated aluminum sharp peaks confirms that the geopolymerization reaction is complete (Nasab, Golestanifard and MacKenzie, 2014; Petlitckaia *et al.*, 2020; Archez *et al.*, 2021; Revathi and Jeyalakshmi, 2021).

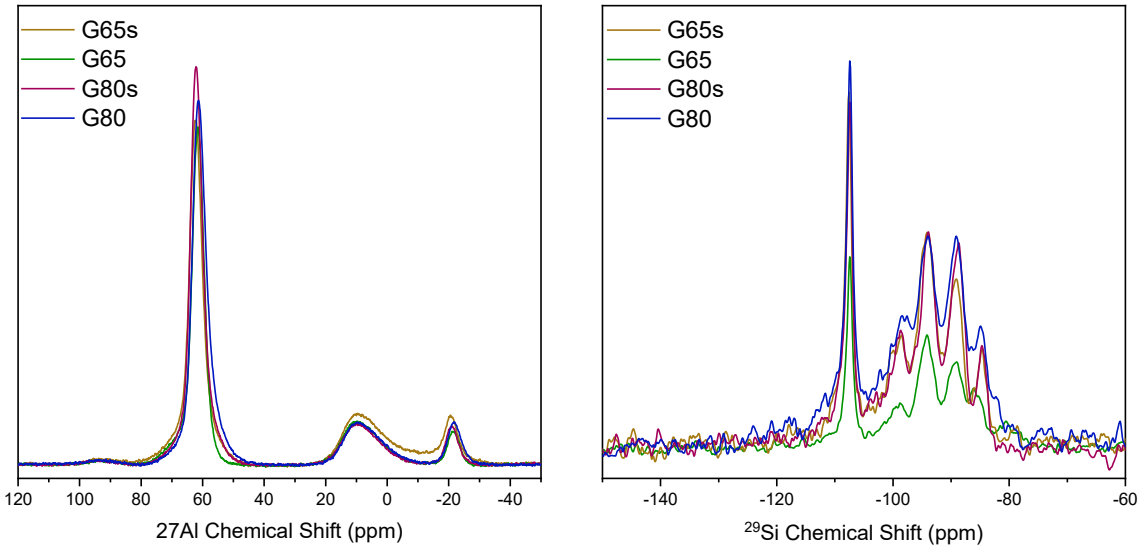

Figure 42. ^{27}Al and ^{29}Si NMR spectra of geopolymer samples.

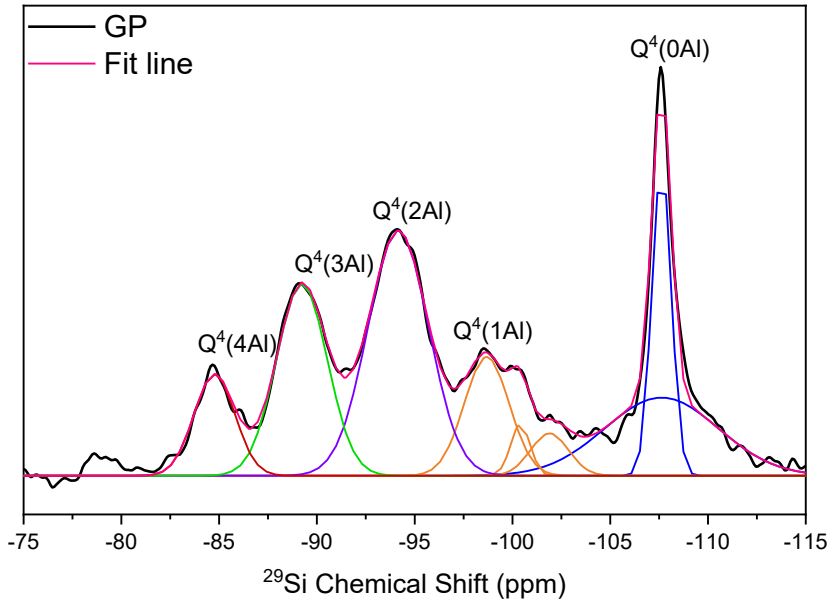

Figure 43. Deconvolution of the ^{29}Si NMR spectra of the G65s sample.

The ^{29}Si NMR spectra present five significant peaks, since they presented the same peaks, the G65s sample was chosen to be deconvolved, and the deconvolution is presented in Figure 43. The most intense peak at -107 ppm corresponds to the $Q^4$0Al silicon types. The peaks at approximately -99, -100, and -102 ppm correspond to the $Q^4$1Al unit. The peaks at -94, -89 and -85 ppm correspond to the $Q^4$2Al, $Q^4$3Al, and $Q^4$4Al units, respectively (Gore *et al.*, 2002; Greiser, Hunger and Jäger, 2016). As expected, the presence of peaks at approximately -107 ppm confirms the formation of aluminosilicate gels, alternating between silica and alumina tetrahedrons. Also, the

presence of a peak near -110 ppm can be assimilated to the presence of the unreacted crystalline phase of the precursor materials, and the use of sodium (Paiva *et al.*, 2018).

7.3.7 Adsorption-Desorption Equilibrium Isotherms

The capacity of a material to be adsorbent depends on many factors, like surface area, volume, density, pore size and volume, and connectivity between the pores (Freire, 2019). Since the physicochemical characteristics of the geopolymers synthesized in this study are very alike for the two types of curing (dry or submersed), the adsorption/desorption capacity of the samples for all gases is expected to be similar.

The CO_2, CO, and H_2 adsorption equilibrium isotherms were obtained at three different temperatures, 30, 50, and 100 °C, all with pressures between 0 and 760 mmHg. For the analysis of the experimental data, different mathematical models were applied (Langmuir, Freundlich, Sips, and Redlich Peterson) . However, the model that best fitted the experimental isotherms data was the Sips model. This model is a combination of the well-known Langmuir and Freundlich models, developed aiming to predict the heterogeneity of adsorptive systems. The parameters of the Sips equation are governed mainly by operating conditions, such as changes in pH, temperature, and solute concentration. (Voigt, 2019), and is the most applied model, because of its high accuracy (Khoramzadeh, Mofarahi and Lee, 2019).

The following Figure (44, 45, and 46) shows the isotherms with the respective suitable model. The CO_2 adsorption isotherms at the three studied temperatures of all samples present favorable shapes since the CO and H_2 isotherms are quite linear (Kyzas, Bikiaris and Mitropoulos, 2017). The parameters obtained by applying the models are presented in Table 15 at the end of the section.

Figure 44 presents the CO_2 adsorption isotherms carried out at 30 (A), 50 (B), and 100 °C (C). At 30 °C, the submersed samples presented a higher adsorption capacity than the no-submersed ones, reaching 2.25, 2.00, 1.43, and 0.88 mmol/g, for samples G80s, G65s, G65 and G80, respectively. The same happens for adsorption at 50 °C, the high gas adsorption, 1.85 mmol/g was obtained with sample G80s, followed by sample G65s, with an adsorption of 1.64 mmol/g, and samples G65 and G80 had an adsorption capacity of 0.93 and 0.60 mmol/g, respectively. And, it is well known and expressed in studies in the literature, the adsorption capacity decreases with increasing temperature, which reveals that the CO_2 capture occurs through physical adsorption, involving micropore structure

and surface area (Wei et al., 2012; Chang et al., 2020; Freire, José and Moreira, 2022; Freire et al., 2024), so, as expected, the adsorption at 100 °C presented the same pattern as that at 30 °C, however in a very small adsorbed amount, once again, the highest adsorption, of 1.11 mmol/g was achieved with sample G80s, followed by sample G65s, with an adsorption of 0.99 mmol/g, and samples G65 and G80 had an adsorption capacity of 0.70 and 0.46 mmol/g, respectively.

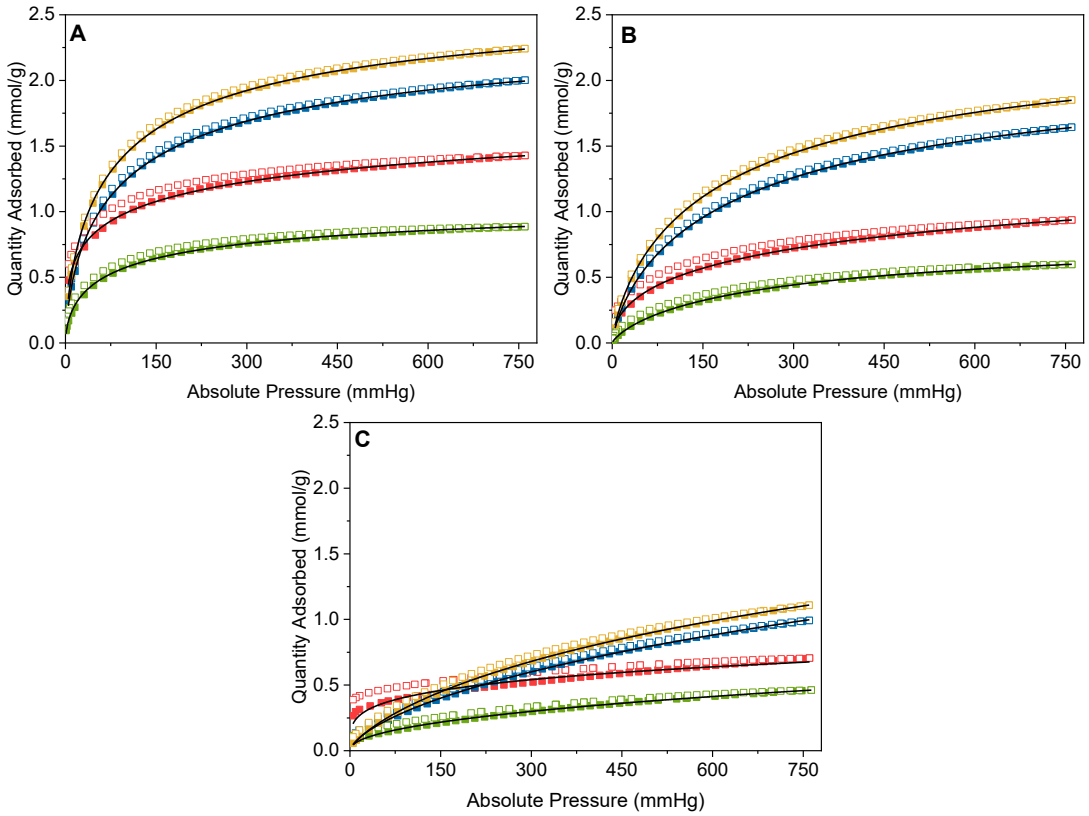

Figure 44. Adsorption (closed squares) and desorption (open squares) isotherms of **CO_2** on the G65s (blue), G65 (red), G80s (yellow), G80 (green), at 30 °C (A), 50 °C (B), and 100 °C (C), and the black line indicates the Sips isotherm model.

The degree of temperature changes that occur inside the adsorber during the adsorption and desorption phases of the processes is determined by the isosteric heat of adsorption (Sircar *et al.*, 1999; Seabra *et al.*, 2019). So, as an important parameter, the isotropic heat of adsorption was calculated using the Clausius–Clapeyron equation (Equation 2) based on the isotherm data obtained at the three temperatures. For this purpose, by plotting the values of lnP versus 1/T, the isosteric heats of adsorption were obtained from the slope. To date, no data geopolymers on isosteric heat for CO_2 adsorption have been found in the literature, therefore, zeolitic materials were used for comparison.

In the literature, the values of the isosteric heat for CO_2 adsorption in zeolite 4A type is 47.8 kJ·mol^{-1} (Romero-Pérez and Aguilar-Armenta, 2010), and ~43 kJ·mol^{-1} (Seabra *et al.*, 2019), in zeolite NaX and NaY types are 53.8 and 40.8 kJ·mol^{-1}, respectively (Kim and Kim, 2023), and about 37.20, 31.93, 30.19, and 25.08 kJ·mol^{-1} in zeolites 13X, 5A, 4A, and beta types, respectively (Khoramzadeh, Mofarahi and Lee, 2019). The isosteric heats of adsorption for CO_2 obtained in this study with the synthesized geopolymers were 38.49, 38.57, 30.34, and 38.76 kJ·mol^{-1} for the G65, G65s, G80, and G80s samples, thus, comparing the heats of adsorption of the samples with values reported in literature for zeolites, it can be concluded that the values in the present work are slightly lower for most of them, but very close to the ones obtained by (Khoramzadeh, Mofarahi and Lee, 2019).

Table 14 presents the CO_2 adsorption capacity of the geopolymers reported in the literature and the respective precursor materials. No studies were found that analyze the adsorption capacity at the same temperatures as those analyzed in this study for comparison. The geopolymers synthesized presented an adsorption capacity higher than most of the geopolymeric materials reported in the literature, and very close to others. Moreover, there is a wide range of materials reported in the literature for CO_2 adsorption, such as N-doped ordered mesoporous carbon, which reached an adsorption capacity of 1.4 mmol/g (Chang *et al.*, 2020), coconut shell-activated carbon with a maximum adsorption capacity of 3.61 mmol/g (Staudt *et al.*, 2024), polyethyleneimine-modified porous wood ceramics which reached an adsorption capacity of 3.06 mmol/g (Guo *et al.*, 2024) , and a foam geopolymer-zeolite X composite that presented a very high CO_2 adsorption capacity of 6.09 mmol/g (Han *et al.*, 2022).

Table 14. Comparison of the adsorption capacity of the samples with some geopolymer reported in the literature at 30-35ºC and 1 bar.

Adsorbent	Precursor materials		CO_2 adsorption (mmol/g)	Reference
	Aluminosilicate source	Alkaline activator		
G10	Metakaolin, fumed silica	Potassium silicate	0.62	(Minelli *et al.*, 2016)
G13			0.58	
G23			0.57	
K-G_2	Metakaolin	NaOH, potassium di-silicate	0.58	(Minelli *et al.*, 2018)
Na-$G_{1,2}$			1.95	
GEO	Metakaolin, silica fume	Potassium hydroxide	0.19	(Chen *et al.*, 2020)
MCR-1	Metakaolin, calcined rice husk ash	NaOH	0.80	(Freire *et al.*, 2020)
MF-1	Metakaolin, fly ash		0.78	
MR-1	Metakaolin, rice husk ash		0.69	
MFCR-1	Metakaolin, fly ash, calcined rice husk ash		0.63	
MFR-1	Metakaolin, rice husk ash, fly ash	Sodium silicate	0.68	
MF-2	Metakaolin, fly ash		0.64	
MPW	Metakaolin/Phosphate mining tailing	NaOH, sodium silicate	1.9	(Freire *et al.*, 2025)
TEPA-WPGS3	Fly ash	NaOH, sodium silicate	1.97	(Wang *et al.*, 2024)
G65s	Metakaolin/Phosphate mining tailing	NaOH, sodium silicate	2.00	This work
G65			1.42	
G80s			2.24	
G80			0.88	

Pressure: 1 bar = ~750 mmHg = ~ 1atm

Figure 45 shows the CO adsorption isotherms carried out at 30 °C (A), 50º (B), and 100 °C (C). The CO adsorption at 30 °C followed the same pattern as the CO_2 adsorption, however at a very low adsorption capacity, samples G65s and G80s had an adsorption capacity of 0.22 and 0.18 mmol/g, and samples G65 and G80 absorbed 0.05 and 0.06 mmol/g, respectively. However, for the CO adsorption at 50 °C the samples' adsorption did not have the same pattern, although the submersed samples showed higher adsorption. In this case, sample G65s presented the highest adsorption, of 0.14 mmol/g, followed by sample G80s with an adsorption capacity of 0.09 mmol/g. Samples G65 and G80 had an adsorption capacity of 0.02 and 0.03 mmol/g, respectively. For the CO adsorption at 100 °C, samples G80 and G80s did not present significant adsorption (below 0.001 mmol/g).

Samples G65s and G65 had an adsorption a little higher, but still very low, capacity of 0.03 and 0.01 mmol/g, respectively. Different from the other samples, the G80s sample, at 50 °C, presented a small hysteresis loop, this type of hysteresis is called H4, where the adsorption branch reflects a blend of isotherms Type I and II, characterized by presenting the main adsorption at low relative pressures (P/P_0), which is associated with micropore filling. The H4 hysteresis loops are usually observed in materials like zeolite crystals, specific mesoporous zeolites, and micro-mesoporous carbon structures (Thommes *et al.*, 2015; Dantas *et al.*, 2019; Pasabeyoglu *et al.*, 2024).

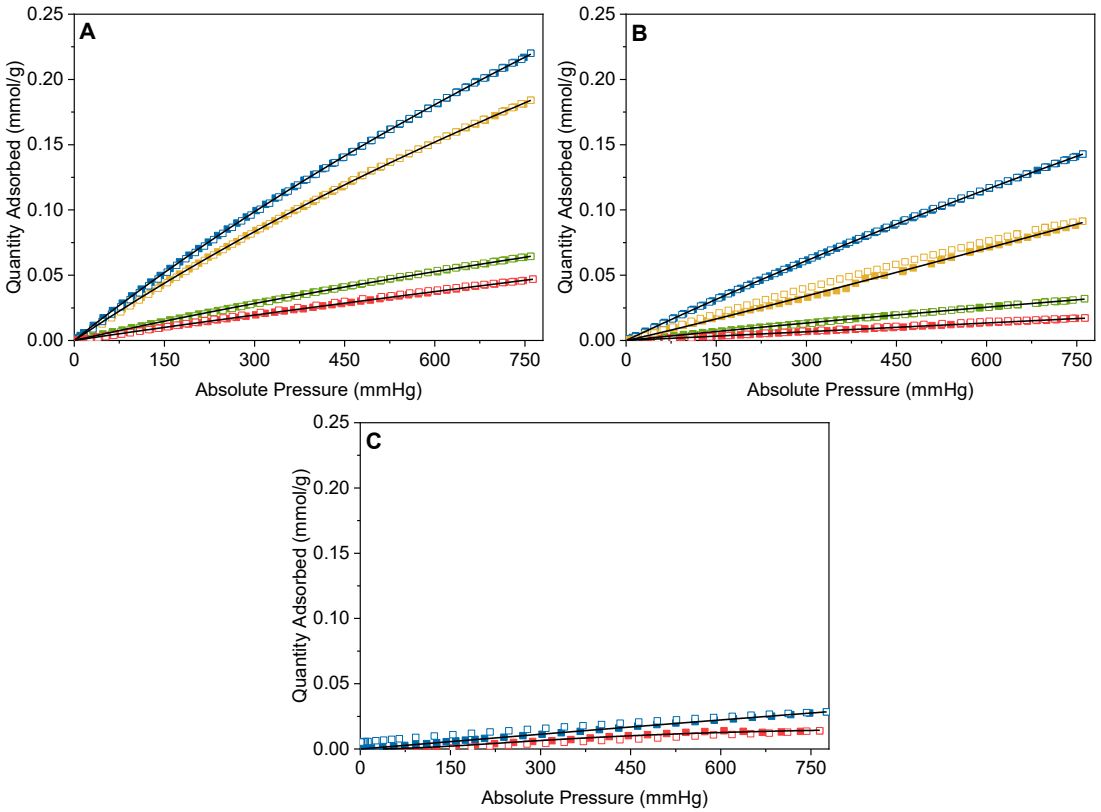

Figure 45. Adsorption (closed squares) and desorption (open squares) isotherms of **CO** on the G65s (blue), G65 (red), G80s (yellow), G80 (green), at 30 °C (A), 50 °C (B), and 100 °C (C), and the black line indicates the Sips isotherm model.

Finally, Figure 46 presents the H_2 adsorption capacity, at 30 °C, for this gas, all samples had a very low adsorption capacity, the adsorbed amount was 0.015 mmol/g for sample G65s, 0.008 with sample G80s, and 0.007 for samples G65 and G80. The adsorption capacity at 50 and 100 °C for the H_2 gas the samples presented an insignificant adsorbed amount, all being less than 0.006 mmol/g. The isotherms presented a wide hysteresis, which due to the very low adsorption was considered a pronounced behavior originating from the equipment.

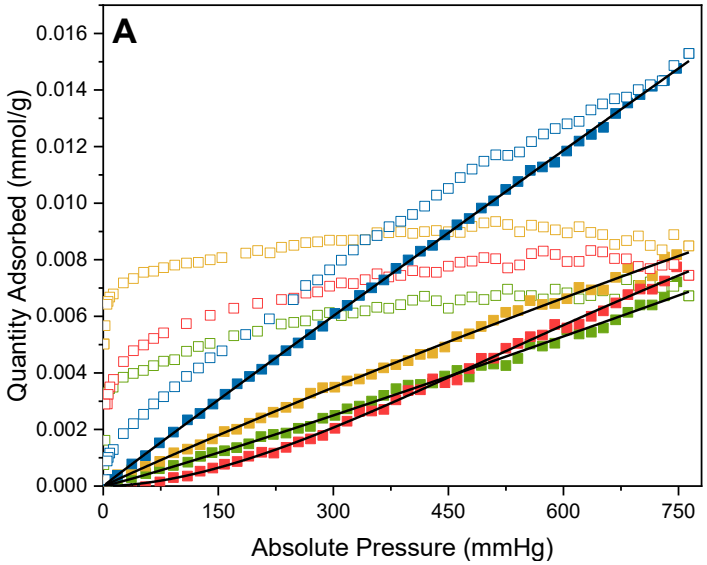

Figure 46. Adsorption (closed squares) and desorption (open squares) isotherms of **H_2** on the G65s (blue), G65 (red), G80s (yellow), G80 (green), at 30 °C, and the black line indicates the Sips isotherm model.

No studies were found in the literature that analyze the adsorption capacity of geopolymers for CO, and H_2. However, with a simple comparison with other solids, the values are significantly higher than those obtained in this study with geopolymers. Some studies analyze the adsorption capacity of these gases with zeolites, at different temperatures and pressures. (Cui, Xing, *et al.*, 2023) analyzed the CO adsorption capacity in zeolites at 25 °C with a pressure of approximately 750 mmHg, obtaining 1.13 mmol/g and 1.82 mmol/g for the NaX and CaA zeolites, respectively. Cui, Su, et al., (2023), analyzed the adsorption capacity of LiX, NaX, and KX zeolites, having an adsorption capacity of 0.97, 1.13, and 0.95 mmol/g, respectively, at 25 °C and pressure at 750mmHg. Kim & Kim, (2023) tested zeolites at 25 °C and a pressure of 750 mmH approximately for CO and H_2 with NaY and NaX zeolites, the NaY zeolite showed an adsorption capacity of 1.10 mmol/g for CO and 0.02 mmol/g for H_2, and the NaX zeolite had an adsorption of 1.12 and 0.02 mmol/g for CO and H_2, respectively. Shrotri et al., (2023) tested four different zeolites for H_2 adsorption at 30 °C and 7500mmHg, and as a result, the zeolites presented an adsorption capacity of 0.16, 0.21, 0.25, and 0.33 mmol/g for the Na-X, NH_4-X, Li-X, and Li-H-X zeolites, respectively. Streb & Mazzotti, (2021) tested the 13X zeolite for H_2 adsorption, obtaining an adsorption capacity of 0.22 mmol/g, at 25 °C and 7500 mmHg.

Table 15. Sips model parameters applied to the sample's equilibrium data.

Gas	Sample	Temp.	Sips Model				- ΔH ads (kJ·mol^{-1})
			K_S (mmHg)	q (mmol/g)	n_S	R^2	
CO_2	G65s	30 °C	0.043	2.517	0.676	0.999	-38.567
		50 °C	0.015	2.325	0.761	0.999	
		100 °C	0.003	4.872	0.652	0.999	
	G65	30 °C	0.131	2.307	0.379	0.999	-27.106
		50 °C	0.034	1.855	0.515	0.999	
		100 °C	2.167E-4	6.394	0.269	0.990	
	G80s	30 °C	0.048	2.758	0.682	0.999	-31.814
		50 °C	0.017	2.525	0.767	0.999	
		100 °C	0.004	3.125	0.734	0.999	
	G80	30 °C	0.065	1.159	0.590	0.999	-38.768
		50 °C	0.011	0.890	0.792	0.999	
		100 °C	6.596E-5	3.220	0.464	0.997	
CO	G65s	30 °C	3.227E-4	1.226	0.982	0.999	-19.347
		50 °C	1.867E-4	1.200	0.992	0.999	
		100 °C	9.811E-5	0.338	1.029	0.999	
	G65	30 °C	7.473E-5	1.048	0.970	0.999	-17.475
		50 °C	4.144E-6	5.166	1.007	0.999	
		100 °C	5.379E-6	0.018	2.022	0.987	
	G80s	30 °C	3.540E-4	0.887	0.996	0.999	-19.751
		50 °C	1.5523E-6	5.635	1.049	0.999	
	G80	30 °C	2.580E-4	0.418	0.989	0.999	-18.200
		50 °C	1.558E-4	0.314	0.991	0.999	
H_2	G65s	30 °C	7.633E-6	2.894	0.983	0.997	
	G6		4.357E-6	0.020	1.784	0.997	
	G80s		1.457E-4	0.091	0.984	0.997	
	G80		8.071E-7	6.402	1.083	0.996	

7.4 PARTIAL CONCLUSIONS

In this study, metakaolin-phosphate waste-based geopolymer samples with identical compositions were synthesized. However, part of the material was cured at 65 °C and another part at 80 °C. Additionally, some samples were subjected to a submerged curing process for 30 days. Aiming for use in CO_2 capture, the materials were examined by surface area, porosity, density, XRD, XRF, FITR-ATR, XPS, solid-state NMR, DLS, TG-DTG-DSC, and SEM. The solid-state NMR and FTIR analysis showed a large amount of reactive material in the four samples. Overall, the two submersed samples had very similar characteristics, as well as the two samples without submersed cure.

The CO_2 adsorption capacity obtained through the isotherms reached 2.24, 2.00, 1.42, and 0.88 mmol/g at 30 °C, for samples G80s, G65s, G65, and G80, respectively, and this capacity decreased as the temperature increased. The result obtained with the G80s sample represents a significant adsorption capacity, compared to results obtained in the literature, and is a promising material considering the easy preparation with low-cost materials. For the CO and H_2 adsorption, the samples presented a very low adsorption capacity, which is great and expected since the objective is to use the material for CO_2 capture.

These results confirm the importance of submerged curing during geopolymer synthesis. Regarding temperature, the geopolymer cured at 80 °C had greater adsorption than the sample cured at 65 °C. However, the characteristics of the two submersed samples are very similar. So, the only characteristic that seems to directly influence adsorption capacity is surface area and pore size, and for all samples, the adsorption capacity increased as surface area and pore size also increased.

8 SYNTHESIS AND CHARACTERIZATION OF GEOPOLYMER/ZEOLITE 13X COMPOSITE FOR CO_2 CAPTURE AND SEPARATION

This chapter describes the synthesis, characterization, and the evaluation of geopolymer/zeolite composites in CO_2 capture and separation. This section is an adaptation of the research paper entitled "Hierarchically porous composites containing mining tailings-based geopolymer and zeolite 13X: application for carbon dioxide sequestration", published in *Adsorption - Journal of the International Adsorption Society*[3].

8.1 MATERIALS AND METHODS

Kaolin was obtained from Caulisa (Pernambuco, Brazil); phosphate mining tailings waste (PW) was provided by a mine in Goiás (Brazil); sodium hydroxide (NaOH – micro-pearls with 98.5 % purity) was acquired from VWR Chemicals, sodium silicate solution (SS) – SiO_2/Na_2O (ratio SiO_2/Na_2O: 2.5) was purchased from Sigma-Aldrich, and the zeolite 13X type pellets from TradeShinli (China).

The geopolymer was synthesized based on Minelli et al. (2016), Chen et al. (2020), and Freire et al. (2024). Metakaolin and phosphate wastes were used as precursors and a mixture of sodium hydroxide and sodium silicate as alkaline activator. The addition of zeolite to the geopolymeric matrix was based on Minelli et al. (2018), and Papa et al. (2018, 2023).

For the synthesis, firstly, kaolin was calcined at 900 ºC for 60 min to obtain metakaolin. The choice of molar ratios for the geopolymer's synthesis was $SiO_2:Al_2O_3$ = 3.30; $Na_2O:SiO_2$ = 0.30; $Na_2O:Al_2O_3$ = 0.99; and $H_2O:Na_2O$ = 12.00, based on a study

[3] Schneider, M., Rodríguez-Castellón, E., Guerrero-Pérez, M. O., Hotza, D., de Noni Junior, A., & de Fátima Peralta Muniz Moreira, R. (2025). Hierarchically porous composites containing mining tailings-based geopolymer and zeolite 13X: application for carbon dioxide sequestration. *Adsorption*, *31*(1). https://doi.org/10.1007/s10450-024-00569-1

developed by Davidovits et al. (1994). The zeolite powder (Z13X) after drying at 120 °C for 24 h was mixed with DIW. In this way, it does not modify the geopolymerization reaction medium, since the pre-treatment prevents the subtraction of water from the alkaline solution. This avoids the exothermic reaction associated with the change from dehydrated to hydrated zeolite during geopolymerization (Papa *et al.*, 2018).

The composite was prepared following seven steps. First, kaolin and PW were mixed at 1500 rpm for 15 min on a mechanical stirrer, and while mixing the solid components, the alkaline solution was prepared by mixing the NaOH, sodium silicate (SS), and deionized water (DIW) at 800 rpm for 10 min on a magnetic stirrer. Then, the geopolymer slurry was prepared by adding the alkaline activator solution to the solid components and mixing for 15 min at 1500 rpm. While mixing, the zeolite was hydrated and then added to the slurry and mixed at 1000 rpm for 10 min more. After that, the composite slurry was molded into a cylindrical shape, using a 2 x 4 cm silicone mold, which was covered with high-temperature tape so that the water would slowly evaporate. The curing process was carried out in a laboratory oven (VENTI-line VWR chemicals) at 65 °C for 24 h (H-65). After curing, the material was de-molded, and the samples were submerged into DIW water at room temperature (25 ºC ± 2 ºC) for 36 days to remove unreacted sodium ions. Finally, the submersed material was dried in an oven at 100 °C for 24 h. After that, the samples were grounded using crucible pistil porcelain. Five different samples were prepared, and the compositions are described in Table 16.

Table 16. Composition of precursor materials and zeolite in the composite samples.

	Composition (wt%)						
Sample	**MK**	**PW**	**NaOH**	**SS**	**Water (slurry)**	**Z13x**	**Water (zeolite)**
GP	35.0	19.0	11.0	13.0	22.0	-	-
Z5	35.0	19.0	11.0	13.0	22.0	5	5
Z10	35.0	19.0	11.0	13.0	22.0	10	10
Z20	35.0	19.0	11.0	13.0	22.0	20	20
Z30	35.0	19.0	11.0	13.0	22.0	30	30

8.2 CHARACTERIZATION

The samples were analyzed by X-Ray Fluorescence (XRF) to determine the chemical composition and to quantify oxides, using a Thermo Fisher Scientific equipment. The density of the samples was evaluated using a pycnometer with helium gas, in a chamber with 1.0 cm^3 at 23 ºC with an equilibration rate of 0.0050 psig/min.

The crystalline structure and mineralogical composition of the samples were evaluated by X-ray powder diffraction (XRPD), to know the crystalline phases present in the materials the X'pert HighScore plus software was used. To evaluate the chemical stability of the samples to CO_2 attack, the XRD analyses were performed to investigate the samples before and after exposition to CO_2. The analysis was performed using a PANanalytical EMPYREAN automated diffractometer. Powder patterns were recorded in the Bragg-Brentano reflection configuration using the PIXcel 3D detector with a step size of 0.017 º (2θ). The powder patterns were recorded between 4 and 70 in 2θ with a total measuring time of 30 min.

Scanning electron microscopy (SEM) was used to study the morphology of materials and chemical analysis. It permits identification of the components of the material and the analysis of the inner structure of the samples, like the crystal structure, morphology, and stress state information. The equipment used was a FESEM TESCAN

CLARA microscope, with a LEICA EM ACE600 metallizer. The samples were coated with 4 nm of platinum, to make it more conductive for a better analysis.

The specific surface area, pore size, and total pore volume were determined through nitrogen adsorption-desorption isotherms at -196 ºC. The analysis was carried out using Micromeritics ASAP 2020 equipment.

For the micro-computed tomography (m-CT) analysis, the samples were scanned employing a SkyScan 2214 (Bruker) system. Projections were obtained using a W source filament and employing a 0.25 or 0.5 mm Al foil (for sample 3 or the other samples respectively) in front of the CDD3 detector to minimize the beam hardening artifact. This source was set to 45 or 95 kV and 130 or 86 µA (for sample 3 or the other samples respectively). The CCD3 detector with a physical pixel size of 17.427 µm was set in a middle position with a source-to-detector distance of 315.449 mm and a source-to-sample distance of 10.861 or 39.823 mm which yielded a voxel size of 0.6 µm for sample 3 or 2.2 µm for the other samples. All scans were acquired over 360° (0.15 or 0.2° rotation step) using an exposure time of 2.9 or 1.75 s for sample 3 or for the other samples, respectively. This results in an overall recording time of 8.5 or 4.5 h per dataset (for sample 3 or for the other samples, respectively). Image reconstruction was carried out using Bruker NRecon software (version 2.2.0.6) applying beam hardening correction.

Fourier-Transform Infrared Spectroscopy (FTIR) was used to identify the functional groups, and chemical bonds present on the surface of the samples. The analyses were performed on a spectrometer model 6800FV from Jasco Analitica. The measurements were made by total attenuated reflectance using the ATR ProOne accessory and making a blank in the air, without the need to disperse or treat the sample. For the acquisition of spectra, a standard spectral resolution of 4 cm-1 was used in the spectral range of 4000-400 cm^{-1}, as well as 64 accumulations per sample.

X-Ray Photoelectron Spectroscopy (XPS) determined the samples' surface chemistry. The spectra were recorded on a Physical Electronic spectrometer (PHI Versa Probe II) using monochromatic Al Kα radiation (15 kV, 1486.6 eV), a dual beam charge neutralizer for analyzing the core-level signals of the elements of interest, and a hemispherical multichannel detector. The sample spectra were recorded with a constant pass energy value of 29.35 eV, 0.125 eV/step, and a beam diameter of 200 μm. The energy scale was calibrated using Cu $2p_{3/2}$, Ag $3d_{5/2}$, and Au $4f_{7/2}$ photoelectron lines at 932.7, 368.2, and 83.95 eV, respectively. Atomic concentration percentages of the characteristic elements were determined considering the corresponding area sensitivity factor for the different measured spectral regions. The Multipak 9.6 software was used for acquisition and data analysis. A Shirley-type background was subtracted from the signals. Recorded spectra were always fitted using Gaussian–Lorentzian curves to determine the binding energy of the different element core levels more accurately.

The ^{29}Si and ^{27}Al NMR spectra were recorded using a High-Definition Nuclear Magnetic Resonance Spectrometer, Bruker model AVIIIIHD 600, narrow bore with a magnetic field of 14.09 Tesla, at 156.4 MHz (Al frequency) and 119.2 MHz (Si frequency) with a probe 4mm dual-resonance CPMAS using zirconia rotors at slew rates of 13KHz. Experiments with ^{27}Al were performed with proton decoupling (continuous wave sequence) by applying a single pulse (π/18), an excitation pulse of 0.7 μs, and a relaxation delay of 1 s to obtain 1000 scans. Chemical shifts were referenced to an external 1 M of $Al(NO_3)_3$ solution. Experiments with ^{29}Si were also performed with proton decoupling (continuous wave sequence) by applying a single pulse (π/2), an excitation pulse of 8.5 μs, and a relaxation delay of 60 s to obtain 1000 scans. Chemical changes were referenced with an external solution of tetramethylsilane (TMS).

Lastly, the adsorption equilibrium tests were carried out with the CO_2, CO, H_2, gases at 30-100 °C, and 0-760 mmHg. The analysis was performed using a surface area and porosity analyzer, Micromeritics ASAP 2020 model.

8.3 RESULTS AND DISCUSSION

8.3.1 Chemical Composition

The chemical composition of the composites, Z13X and GP samples, analyzed through XRF, are presented in Table 17. Silica (SiO_2), alumina (Al_2O_3), and sodium oxide (Na_2O) are the primary components of the compositions. However, there is a considerable amount of magnesium (MgO) and iron (Fe_2O_3) oxides in the Z13X sample, and iron (Fe_2O_3), titanium (TiO_2), calcium (CaO) and phosphate (P_2O_5) oxides in the GP sample. The oxides present in the GP sample are in accordance with the analysis of precursors (metakaolin and phosphate mining tailings) carried out by Freire et al. (2020), which belong to the same batch of those used in this work.

The composite samples, as expected, in the same way as the precursors, have a considerable amount of SiO_2, Al_2O_3, Na_2O, and Fe_2O_3.

Table 17. Total oxide composition of the Z13X, GP, and composite samples.

	Compound	Z13X	GP	Z5	Z10	Z20	Z30
wt%	SiO_2	42.41±0.37	42.42±0.37	37.75±0.54	37.62±0.54	39.23±0.54	39.85±0.54
	Al_2O_3	22.09±0.18	22.84±0.18	22.66±0.37	22.11±0.36	21.33±0.36	20.71±0.36
	Na_2O	13.09±0.37	9.10±0.02	16.75±0.20	16.85±0.20	15.53±0.19	15.09±0.19
	Fe_2O_3	1.05±0.07	7.40±0.09	3.98±0.16	3.87±0.16	3.38±0.15	3.24±0.14
	TiO_2	0.148±0.003	3.07±0.05	1.46±0.02	1.38±0.02	1.20±0.02	1.12±0.02
	CaO	0.194±0.014	1.74±0.03	0.699±0.06	0.702±0.06	0.585±0.050	0.586±0.05
	P_2O_5	0.211±0.009	1.49±1.49	0.386±0.013	0.395±0.013	0.337±0.011	0.333±0.011
	MgO	2.38±0.17	3.07±0.002	0.505±0.061	0.625±0.070	0.848±0.090	1.07±0.11
	K_2O	0.316±0.026	0.377±0.377	0.379±0.017	0.373±0.017	0.351±0.016	0.338±0.015
	MnO	0.0264±0.0017	0.328±0.004	0.148±0.006	0.141±0.005	0.119±0.005	0.116±0.004
	ZnO	0.0913±0.0026	0.0167±0.0023	0.0134±0.0004	0.0180±0.0005	0.0256±0.0005	0.0320±0.0007
	CuO	0.0122±0.0021	0.0370±0.0023	0.0121±0.0005	0.0111±0.0005	-	0.0104±0.0004
	Cl	0.0465±0.0045	0.0178±0.0046		-	-	-
	SO_3	0.0644±0.0052	-		-	-	-
	LOI	17.86	10.80	15.71	15.84	16.98	17.45

8.3.2 Textural Characterization

The surface area, pore volume, and size are important factors in the selection of an adsorbent. These characteristics are shown in Table 18.

The density of the samples (Table 18) is comparable and increases as the total pore volume decreases, which is expected and agrees with the results obtained by Candamano et al. (2022) for zeolite and geopolymer composites.

The pore size, total pore volume, and surface area of the Z13x are higher than for the GP, and the surface area increases as the zeolite content increases on the composite formulation (Table 18). The surface area of the GP sample obtained in this study was very similar to the one obtained by Freire (2024), which was used as a reference to prepare the geopolymer. The surface area values for geopolymer/zeolite are higher than the surface area obtained by (Minelli *et al.*, 2018), and (Candamano *et al.*, 2022), which were 211 and 343 m^2/g, respectively, and lower than the reported elsewhere (Han *et al.*, 2022), which was 579 m^2/g.

Table 18. Surface area, pore volume and size, and density of the samples.

Sample	Surface area (m^2/g)	Total pore volume (cm^3/g)	Average Pore size (Å)	Density (g/cm^3)
Z13x	550	0.1834	82.5	2.028±0.002
GP	301	0.1308	55.9	2.450±0.002
Z5	340	0.1534	57.1	2.368±0.001
Z10	345	0.1544	57.3	2.334±0.001
Z20	405	0.1479	55.1	2.426±0.001
Z30	438	0.1712	69.1	2.285±0.001

However, for the Z20 sample, the specific surface area increases like the other composites, but a decrease can be noted in total pore volume and pore size, reaching values close to the GP sample, which can also be seen through the BJH pore distribution

(Figure 47). This decrease can be related to the increase in density. This behavior is due to the complexities of the geopolymerization process involving zeolite, which is unable to fully understood (Panagiotopoulou *et al.*, 2007). The same situation applies to the Z5 and Z10 samples. When zeolite is added to the geopolymer, part of it is consumed in the geopolymerization process, while the remainder remains crystalline, and this dual role complicates the control of the final properties analysis (Papa *et al.*, 2018).

The geopolymer and composite samples presented a broad mesopore distribution centered with a dominant pore size at approximately 60 and 55 Å, respectively (Figure 47), suggesting a more uniform mesoporous structure than the zeolite sample (Pasabeyoglu *et al.*, 2024), which presented a little number of pores around 20 Å and a broad mesopore distribution from approximately 80 to 320 Å. The pore distribution of the zeolite is very similar to the porosity obtained by Kim et al., (2022) for zeolite 13X. So, the pore distribution suggests that the GP, Z13X, and the composites samples prepared in this study have mesoporous structures (Alothman, 2012; Thommes *et al.*, 2015; Wang *et al.*, 2025).

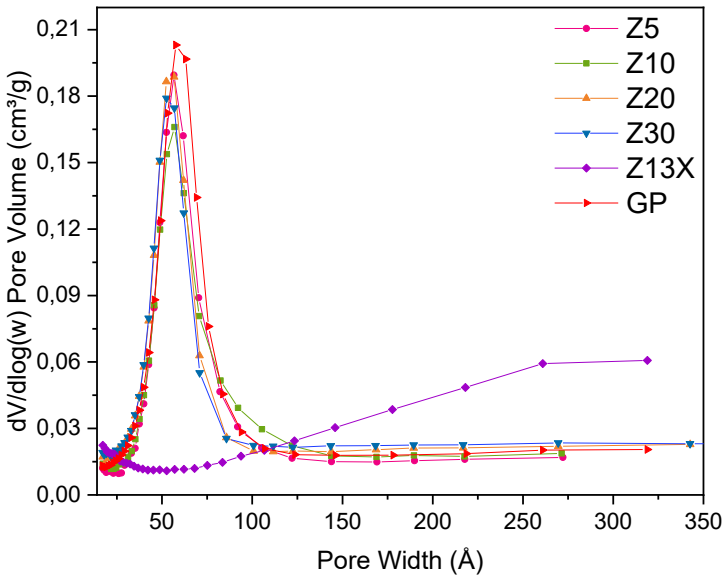

Figure 47. BJH pore distribution of the samples.

The open porosity (void space), closed porosity (pores, trapped bubbles), and the total porosity, evaluated by mCT, are presented in Table 19. The sample GP sample presented the higher open porosity and lower closed porosity. The volume of closed porosity is considerably similar for the GP, Z10, Z20, and Z30, and considerably higher for the Z5 and Z13X samples.

Table 19. Quantification of porosity using micro-CT analysis.

Sample	**Open porosity (vol %)**	**Closed porosity (vol%)**
Z13X	2.65	7.16
GP	10.22	2.43
Z5	4.44	4.68
Z10	9.04	2.57
Z20	0.89	2.48
Z30	0.83	2.62

However, it can be seen in Figure 48, where the black spots correspond to the closed porosity, that the zeolite has some fissures which may be considered as closed pores. No studies were found in the literature about mCT of geopolymer and zeolite composites. Nevertheless, the closed porosity of the samples agrees with the results obtained elsewhere (Kovářík *et al.*, 2021) for geopolymers. However, the open porosity is significantly lower, which is expected since the materials developed by them are geopolymer-based ceramic foams and the open porosity is visibly higher.

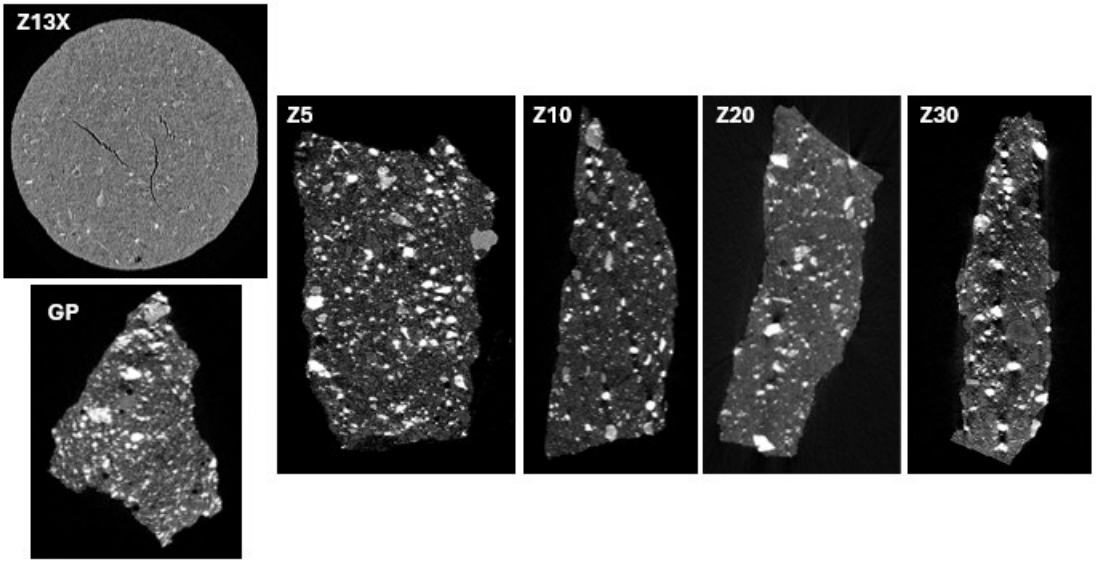

Figure 48. X-Ray Micro Computed Tomography of the samples.

8.3.3 Mineralogical Composition and Crystallinity

The XRD pattern of the commercial zeolite 13X and single geopolymer are given in Figure 49. The Z13X presented two crystalline phases, quartz (SiO_2 ICDD 01-086-1628), and Faujasite ($Na_2Al_2Si_{2.4}O_{8.8}{\cdot}6.7H_2O$ – ICDD 00-012-0246) as the main phase. As expected, the Z13X sample is crystalline, and the sharpness and intensity of the peaks indicate the high degree of crystallinity of the sample (Zhou *et al.*, 2013b). However, there is a slight elevation of the bottom of the diffractogram which indicates the presence of a small amount of amorphous material.

The geopolymer is mainly amorphous, as expected, but it presented some peaks in a very low intensity compared to the zeolite. Quartz (SiO_2 ICDD 01-086-1628), and Faujasite ($Na_2Al_2Si_{2.4}O_{8.8}{\cdot}6.7H_2O$ – ICDD 00-012-0246) were also identified. A crystalline phase in geopolymeric materials can be formed during the curing process in the synthesis. The presence of mineralogical phases in the geopolymers is reported in many studies, especially when there is a thermal cure involved in the synthesis process (Davidovits, 1994; Król, Minkiewicz and Mozgawa, 2016).

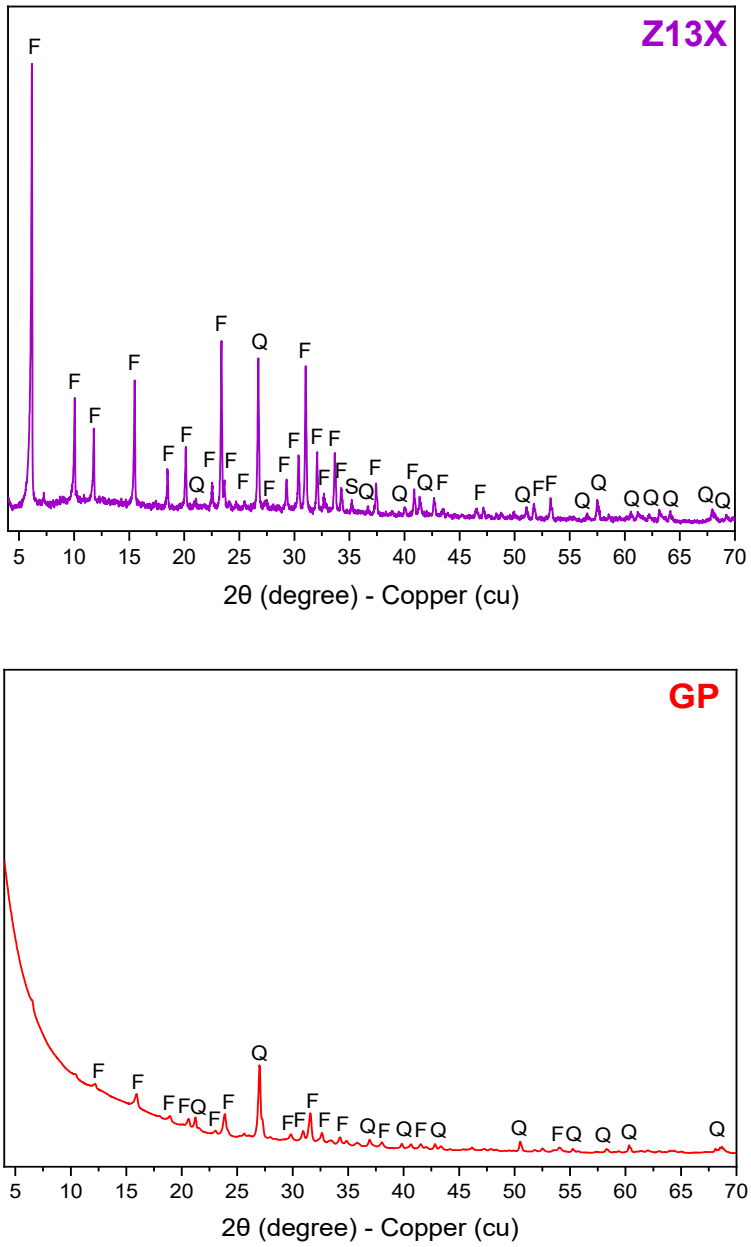

Figure 49. XRD patterns of the Z13X and GP samples, where Q is for quartz, and F is for faujasite.

The composites containing geopolymer and zeolite presented a significant crystallinity, and an XRD pattern very similar to the zeolite, as can be seen in Figure 50. The main difference is in the intensity of the peaks, also the composites presented an inferior number of peaks compared to the zeolite, which is expected since the base of the composites is the geopolymer, which is mainly amorphous. The peaks were identified as quartz (SiO_2 ICDD 01-086-1628), and faujasite ($Na_2Al_2Si_{2.4}O_{8.8}\cdot 6.7H_2O$ – ICDD 00-012-

0246), like the zeolite and geopolymer. Comparing the composites, it can be seen an increase in the intensity of the faujasite main peak at approximately 8º as increasing the amount of zeolite, and a decrease in the intensity of the main quartz peak at approximately 25º decrease for the Z5, Z10, and Z20 samples, and the intensity increases a little in the Z30 composite.

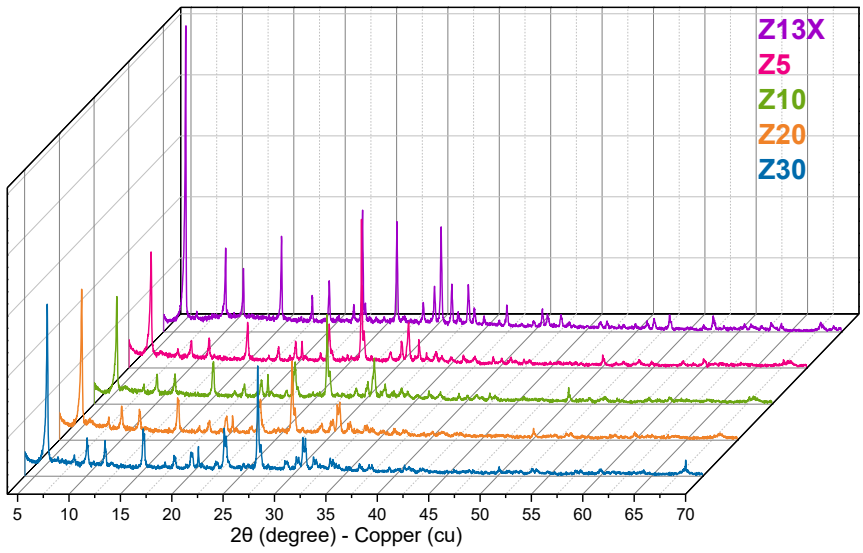

Figure 50. XRD pattern of the composite samples

8.3.4 Chemical Analysis and Morphology

The morphology of the microstructure of the Z13X and the GP samples are shown in Figure 51. The octahedral crystalline of the zeolite 13X particles can be observed in the images, also, some conglomerates can be seen. Through the microstructure of the GP sample, it is possible to notice the dense and homogeneous structure of the sample, confirming the large amount of oligomers (Si-Al) in the reaction medium, which increases de degree of geopolymerization of the material (Kaze *et al.*, 2022). Moreover, some ordered shapes can be seen in the figure, which can be considered a crystalline material, since the XRD analysis indicated a certain crystallinity in the sample.

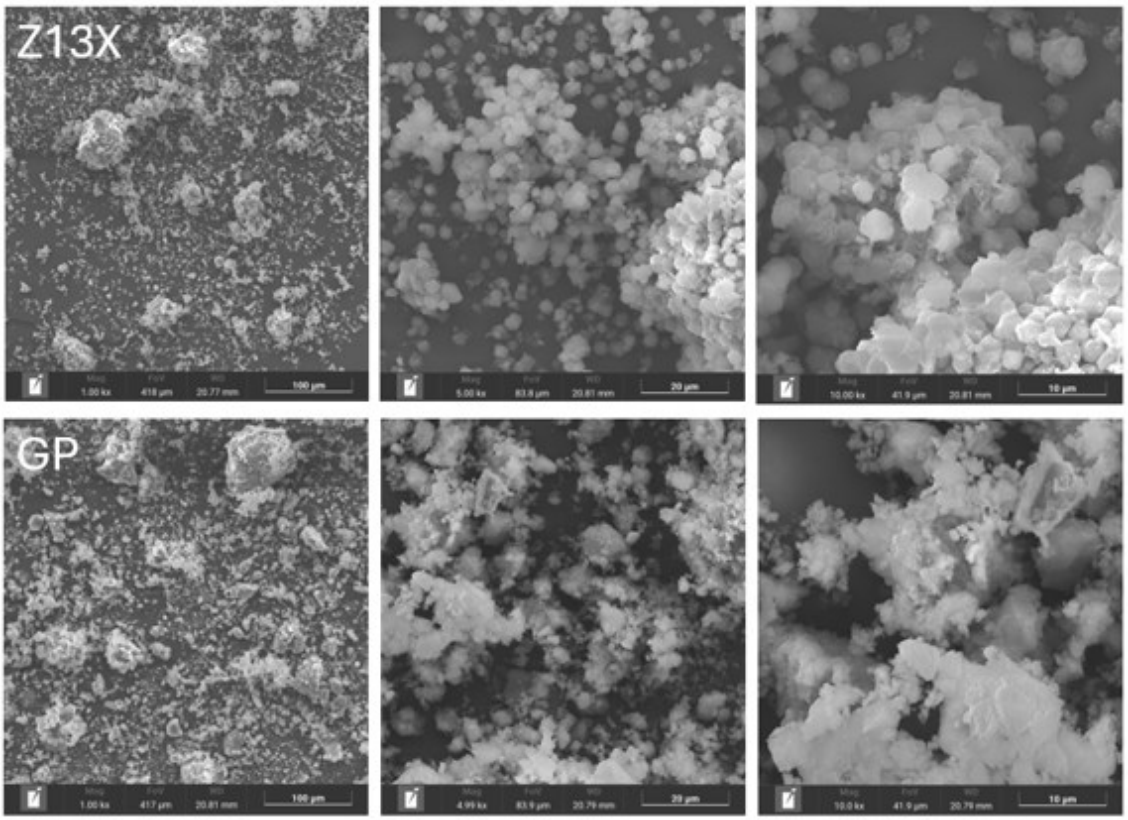

Figure 51. SEM images of the Z13X and GP samples.

The SEM images of the composite samples are reported in Figure 52. In the images it is possible to note the dense and homogeneous structure of the geopolymer, and when increasing the amount of zeolite on the composite sample it is possible to notice an increase in the crystalline materials on the sample, as expected due to the high crystallinity of the zeolite.

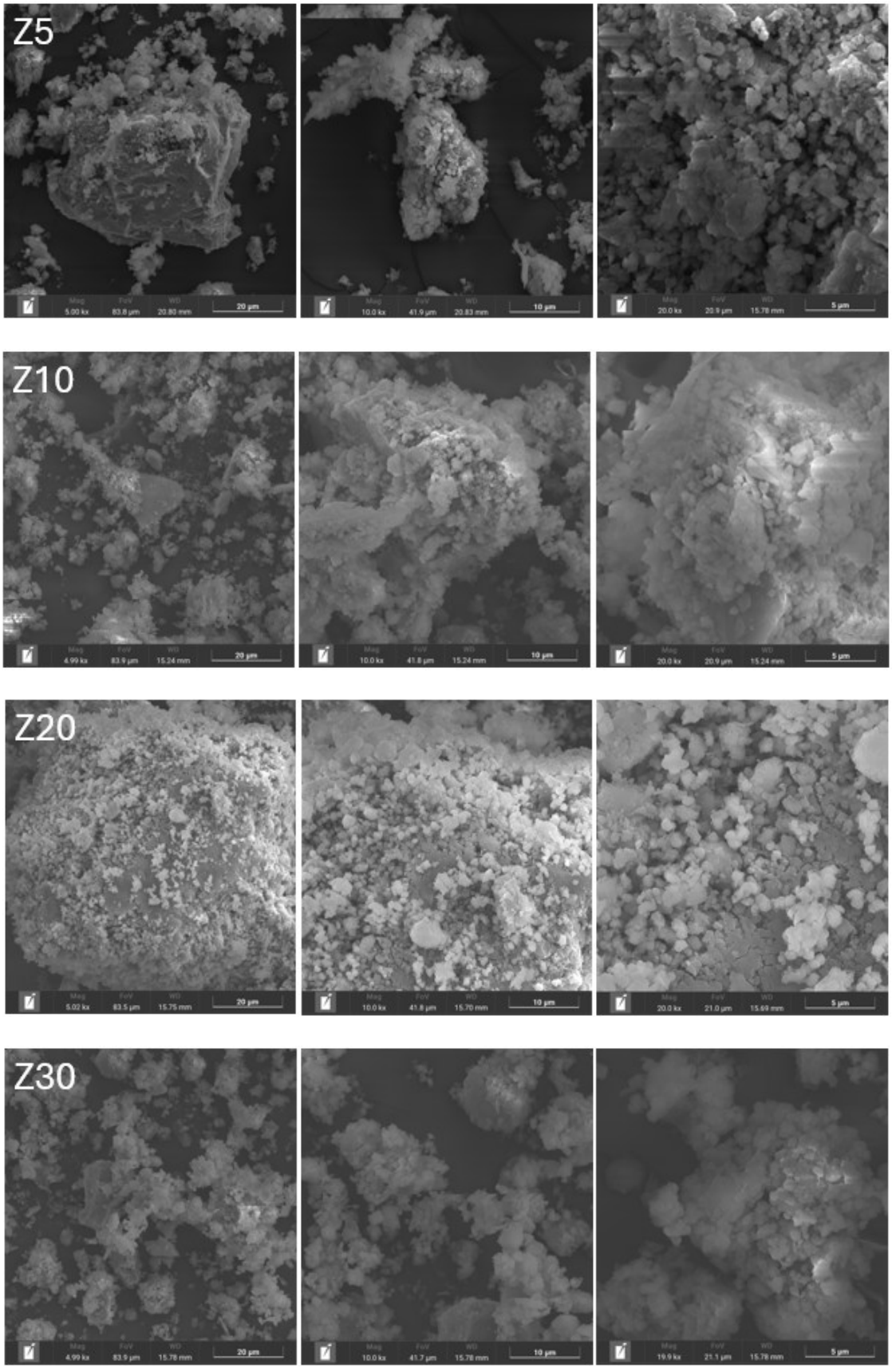

Figure 52. SEM images of the Z5, Z10, Z20, and Z30 composite samples.

The FTIR-ATR spectra for the Z13x, GP, and composite samples are shown in Figure 53. The spectra are very alike for all the samples, which is expected since they are aluminosilicates. The bands between the orange dash lines, at the region from 4000 to 2600 cm^{-1}, are attributed to the Si-OH, OH, and Si-OH-Al bands, and it is characterized by a stretching vibration. The bands at 3400 and 1640 cm^{-1} are referent to the stretching ν(OH) and bending δ(HOH) of the H_2O vibrations (Minelli *et al.*, 2018).

The low intensity of the bands around the 1400 cm^{-1} region of samples GP, Z5, Z10, and Z20 represent the formation of carbonates for Na^+-based materials. Samples Z31x and Z30 did not present these bands, which may be related to the fact that Z30 is the composite with the highest amount of zeolite (Minelli *et al.*, 2018) This is an important parameter to be analyze since the presence of carbonates on geopolymer samples can cause losses in the chemical and physical properties of the materials (Król, Minkiewicz and Mozgawa, 2016; Rajini, Narasimha Rao and Sashidhar, 2021).

The overlapping bands between 1200 and 400 cm^{-1} in the composite samples are due to the-crystalline and amorphous precursor structures of Z13X and the geopolymer, respectively (Minelli *et al.*, 2018). The bands between 1200 and 900 cm^{-1} are characteristics of aluminosilicate materials, which correspond to the asymmetric stretching vibration of Si-O-T type structures, where T is Si or Al (Kljajević *et al.*, 2017). Peaks at ~980 cm^{-1} represent the symmetric stretching vibration of Si-O bonds and are identified in all sample spectra (Papa *et al.*, 2023). The bands from 800 to 500 cm^{-1} are characteristic of symmetrical Si-O-Si vibrations, and the bands between 750 and 554 cm^{-1} correspond to the vibrational bands of zeolitic materials, in this case, the Faujasite, zeolite 13X type (Jiménez, Lalangui, Guacho, Paucar, *et al.*, 2019).

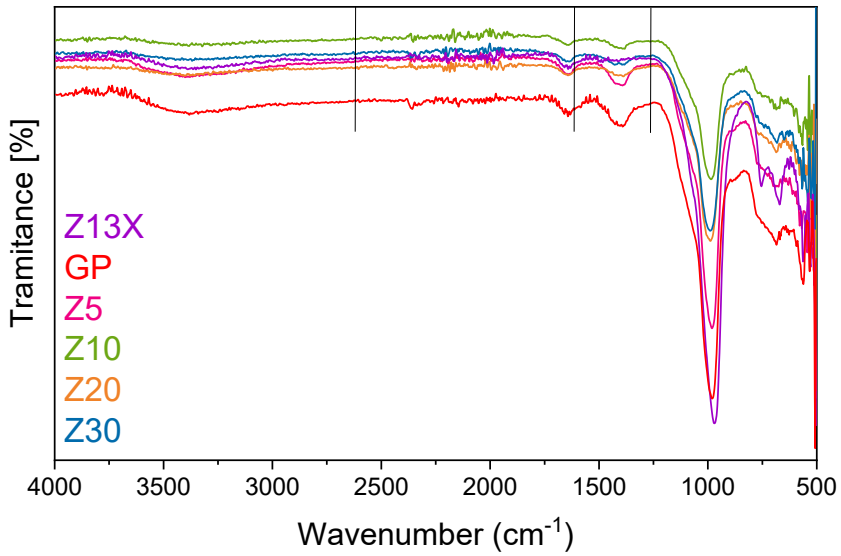

Figure 53. FTIR-ATR spectra of Z13X, GP, and composite samples.

The XPS analysis was performed to obtain the chemical states and atomic composition of the sample's particles' surface. The identification of the peaks was mainly based on the *Handbook of X-ray Photoelectron Spectroscopy*, Moulder et al. (1992) , and Wagner et al. (1979). Overall, the sample spectra are very similar, which is expected, since they all are aluminosilicates, changing mainly in the intensity of the peaks, atomic concentrations, and weight.

The XPS spectra of the Z13X sample are shown in Figure 54, and Figure 55 illustrates the XPS decomposed atom electron orbitals spectra. The high-resolution C 1*s* core level spectra was deconvoluted into four contributions, the contribution at 284.8 eV is assigned to adventitious carbon (contamination), C-C, and/or C=C groups, at 286.9 eV are related to the C-OH and C-O-C groups, the contribution at 289.3 eV is characteristic of the carbonate groups, and at the peak at 291.9 eV is attributed to $\pi \rightarrow \pi^*$ satellite shake-up. The O 1*s* spectra was deconvoluted in two contributions, the contribution at 531.7 eV is assigned to O-H groups, which can be assigned to water, and/or the C-OH group, and the contribution at 533.1 eV is related to the Si-O bonds

The high-resolution Na 1*s* spectra presents a peak at 1072.3 eV, which is characteristic of sodium aluminosilicate. Moreover, the high-resolution Si 2*p* and Al 2*p* spectra have peaks at 102.5 and 74.3 eV, respectively, and these peaks are also characteristic of aluminosilicate. The Mg *2p* has a maximum at 50.2 eV typical of Mg^{2+}. The Fe $2p_{3/2}$ *peak* was deconvoluted in three contribution, 710.6 eV corresponding to Fe(III), 713.8 eV to the $\pi \rightarrow \pi^*$ satellite shake-up, and at 724.7 eV to the FeO group. And finally, there is a little amount of Cl *2p* in the sample, the peak is at 199.0 eV which is assigned to Cl- group.

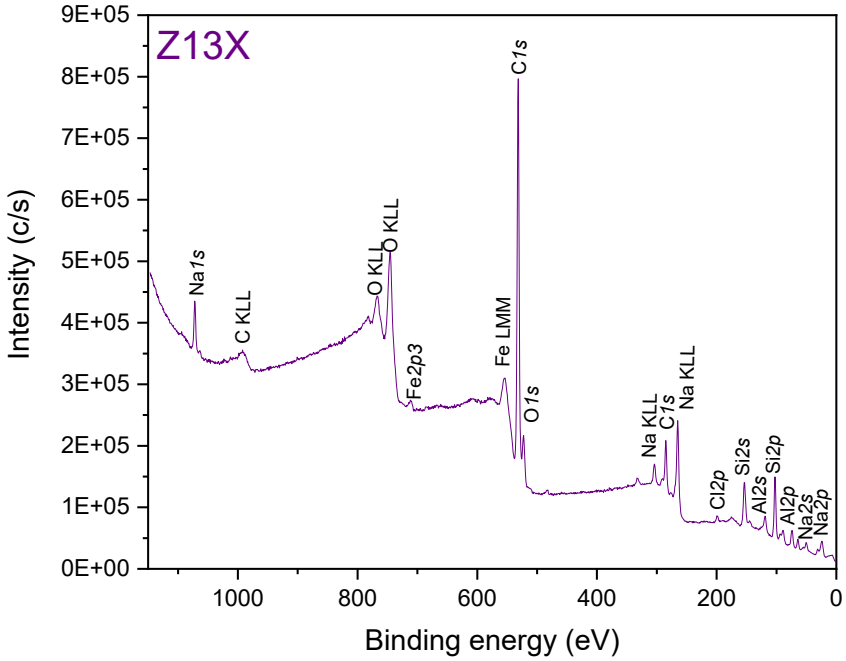

Figure 54. XPS spectra of the zeolite sample.

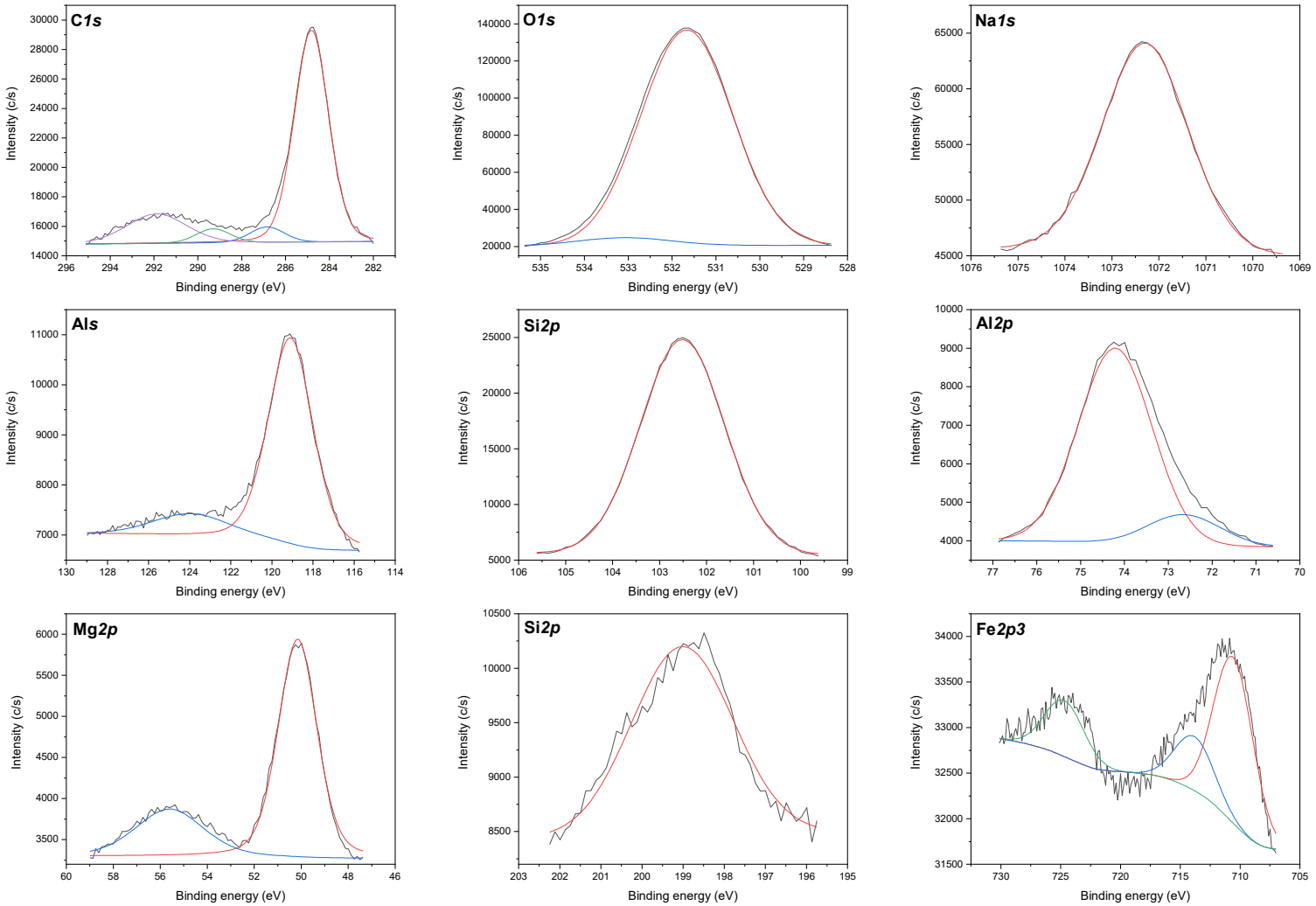

Figure 55. Deconvolution spectra of the zeolite sample.

The XPS spectra of the geopolymer sample are shown in Figure 56, and Figure 57 illustrates the XPS decomposed atom electron orbitals spectra. The high-resolution C 1*s* core level spectra were deconvoluted into four contributions. The contribution at 284.8 eV is assigned to adventitious carbon (contamination), C-C, and/or C=C groups, at 286.4 eV are related to the C-OH and C-O-C groups, the contribution at 289.0 eV is characteristic of the O-C=O and carbonate groups, and at the peak at 291.7 eV is correspondent to $\pi \rightarrow \pi^*$ satellite shake-up.

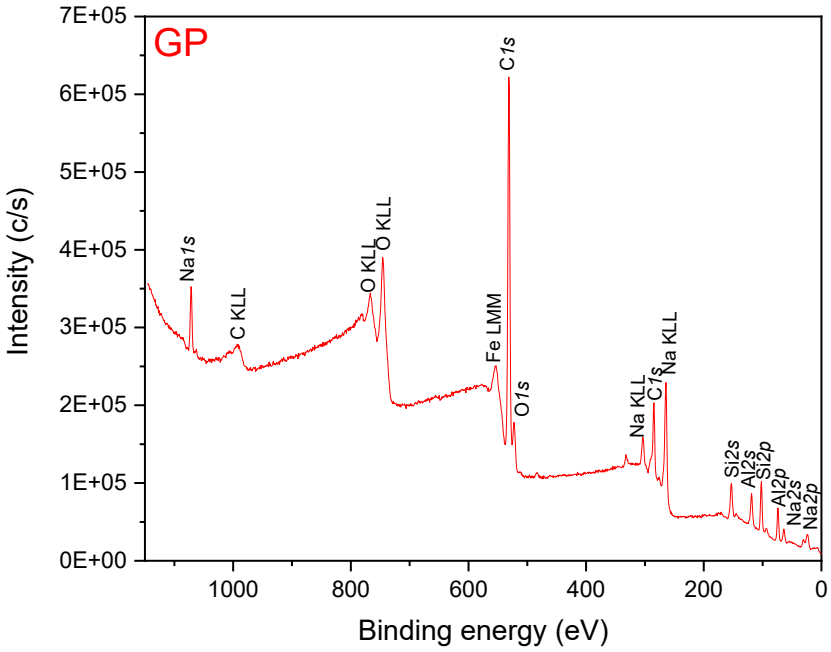

Figure 56. XPS spectra of the geopolymer sample.

The high-resolution O 1*s* spectra were deconvoluted in 3 contributions. The contribution at 530.5 eV is correspondent to the Na_2O (Auger) group, the peak at 531.5 eV to the O-H which can be assigned to water, and/or the C-OH group, and the contribution at 532.8 eV is related to the Si-O group. The Na 1*s* spectra present a peak at 1072.4 eV, which is characteristic of sodium aluminosilicate. Therefore, the Si 2*p* and Al 2*p* spectra have peaks at 102.6 and 74.3 eV, respectively, and these peaks are also

characteristic of aluminosilicate. Finally, there is a little amount of iron in the sample, the peak is at 711.1 eV which is assigned to Fe(III) group.

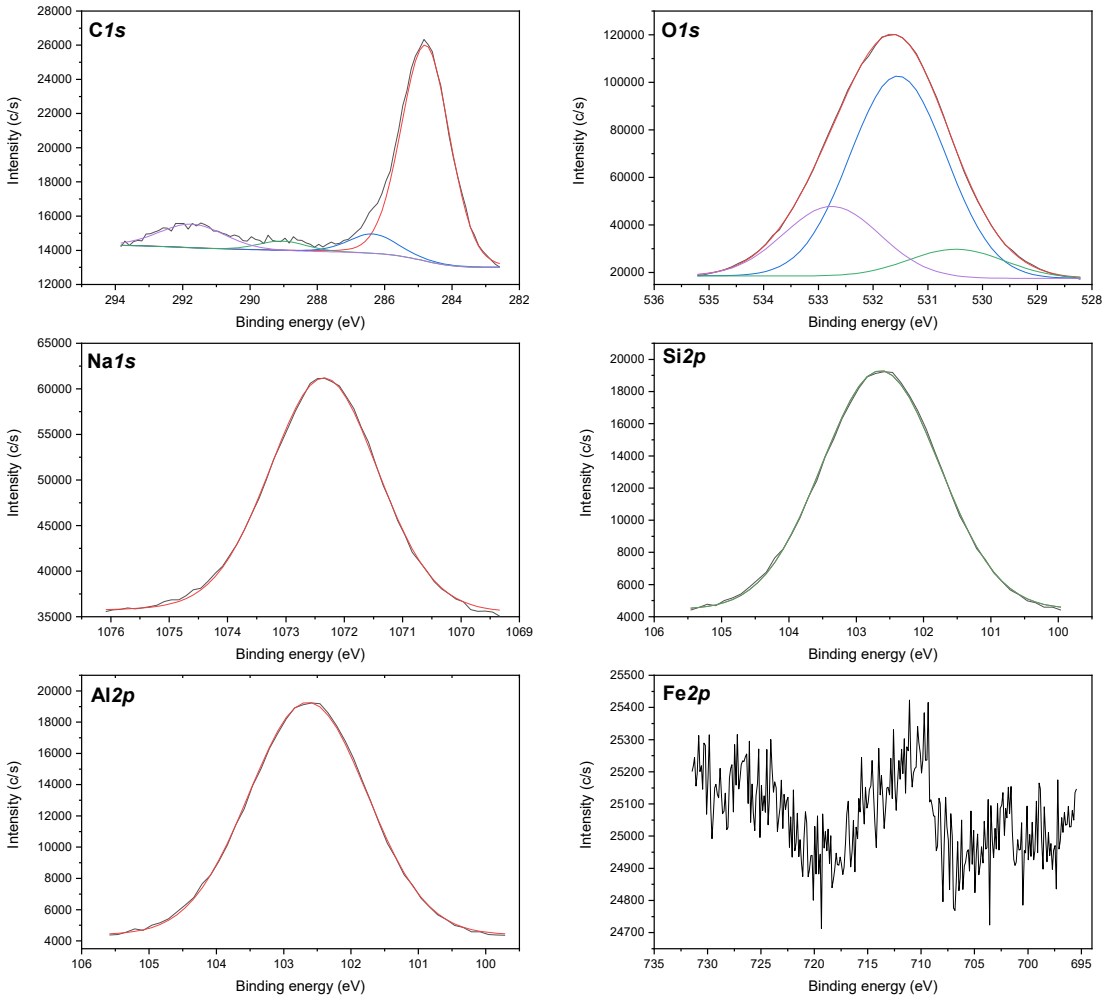

Figure 57. Deconvolution spectra of the geopolymer sample.

The XPS spectra of the composite samples are shown in Figure 58, and Figures 59. 60, 61, and 62 illustrates the XPS decomposed atom electron orbitals spectra. Overall, the four spectra are very similar. The difference in binding energy is very small, with the greatest variance being only 0.3 eV, affecting merely the intensity of the peaks.

The C 1*s* core level spectra of all samples were deconvoluted into three distinct contributions at high resolution: the contribution at ~284.8 eV is correspondent to

adventitious carbon (contamination), C-C, and/or C=C groups; at ~286.5 eV are related to the C-OH and C-O-C groups; and the peak at ~289.2 eV is characteristic of the carbonate group. The O 1*s* spectra were deconvoluted in two contributions: at 531.4 eV corresponds to the O-H that can be assigned to water, and/or the C-OH group; and the at 532.4 eV is related to the Si-O group.

The Na 1*s,* Si 2*p* and Al 2*p* spectra presented peaks at 1072.3 eV, 102.7 and 74.4 eV, respectively, which are characteristic of sodium aluminosilicate. The samples also presented an amount of Mg 1*s*, with peaks at ~1303.7 eV, related to the Mg-O group. Finally, samples Z20 and Z30 presented a small amount of Fe *2p*, which were deconvoluted in two contributions: at 711.4 and 712.0 eV, assigned to Fe(III) group; and at 723.9 and 725.2 eV, which are $\pi \rightarrow \pi^*$ satellites shake-up.

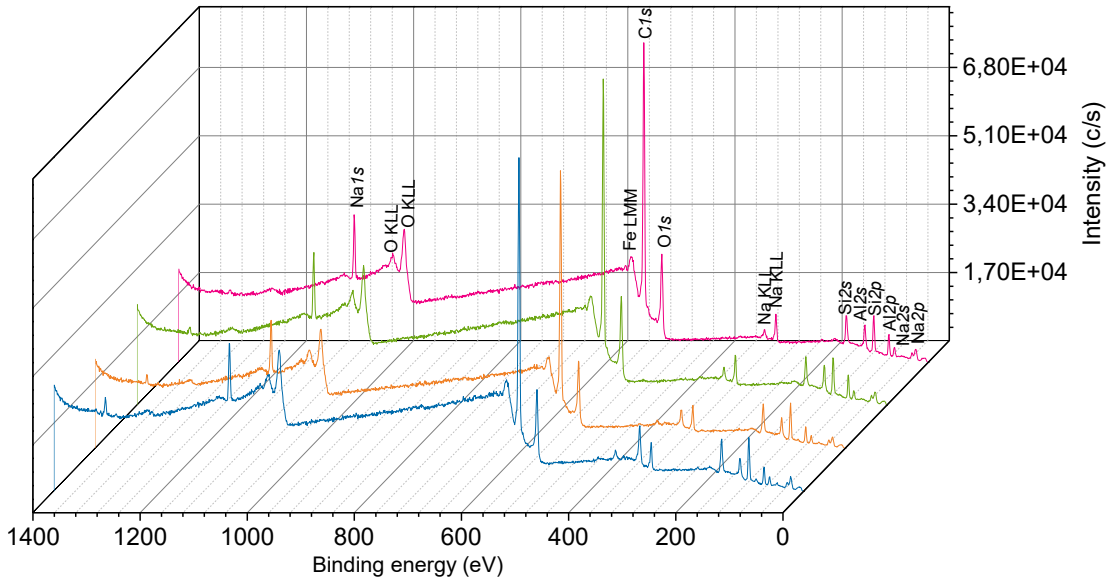

Figure 58. XPS spectra of the composite samples

The area of the peaks, atomic concentrations, and weight are reported in Table 20, and Table 21 are presented the quantification of the deconvoluted peaks.

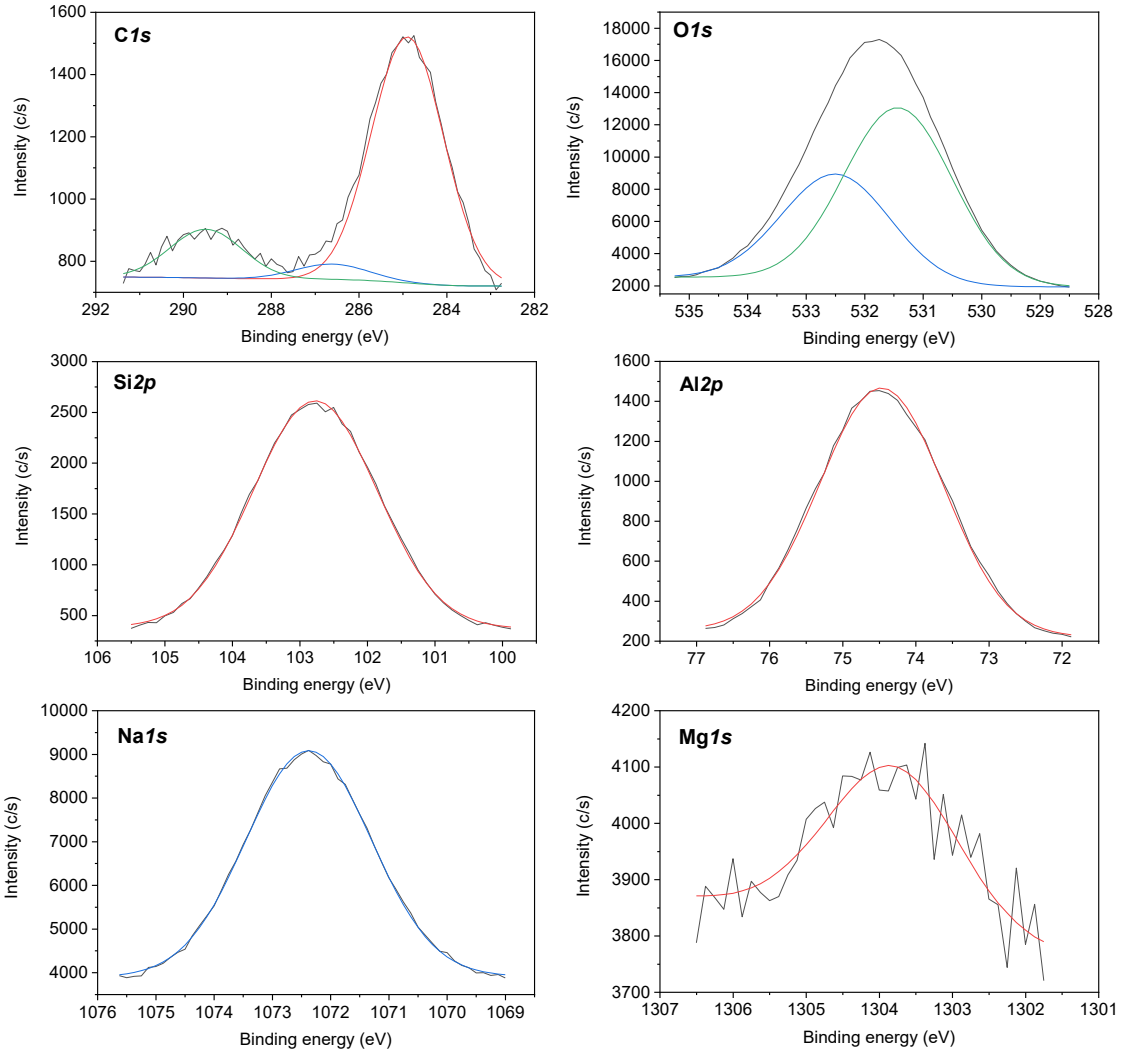

Figure 59. Deconvolution spectra of the Z5 sample.

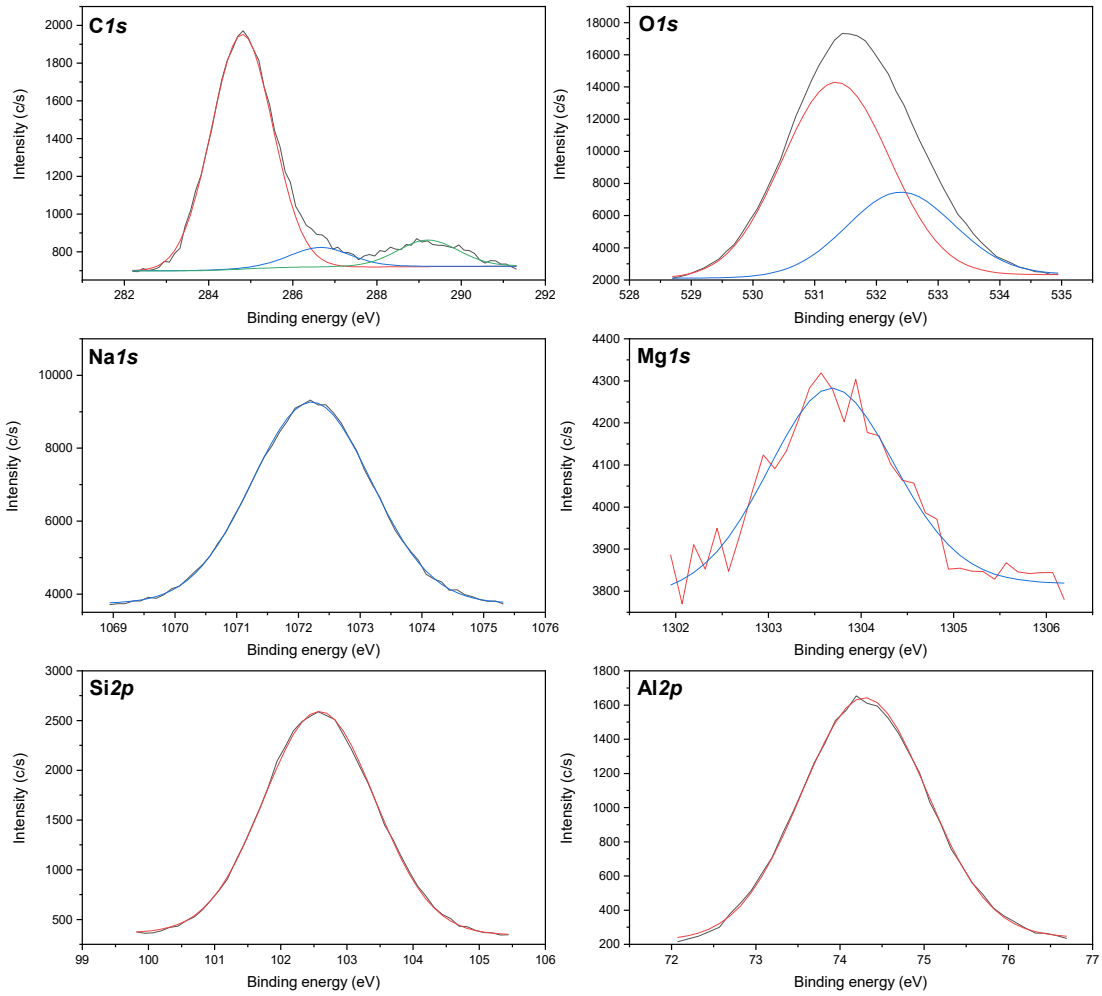

Figure 60. Deconvolution spectra of the Z10 sample.

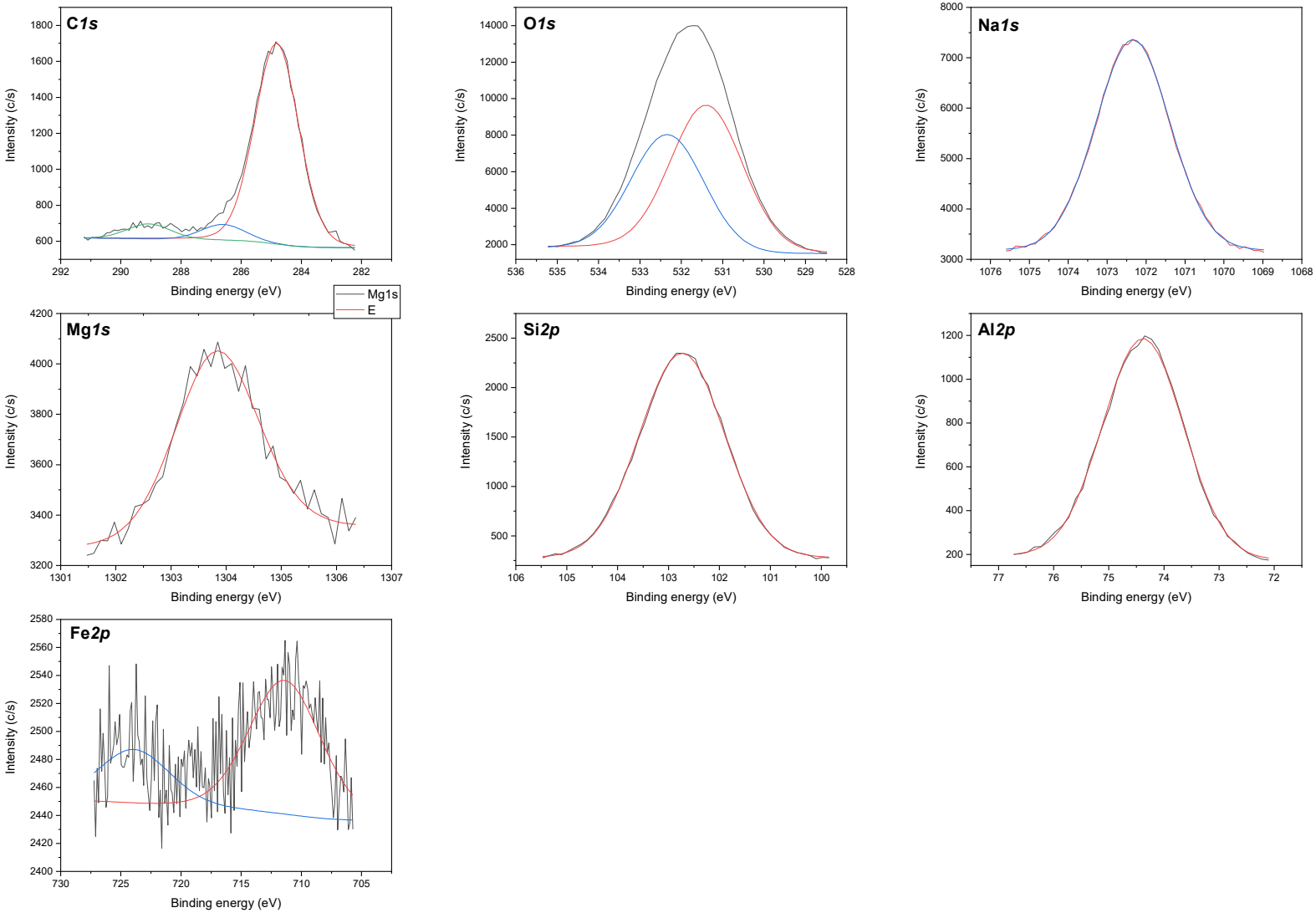

Figure 61. Deconvolution spectra of the Z20 sample.

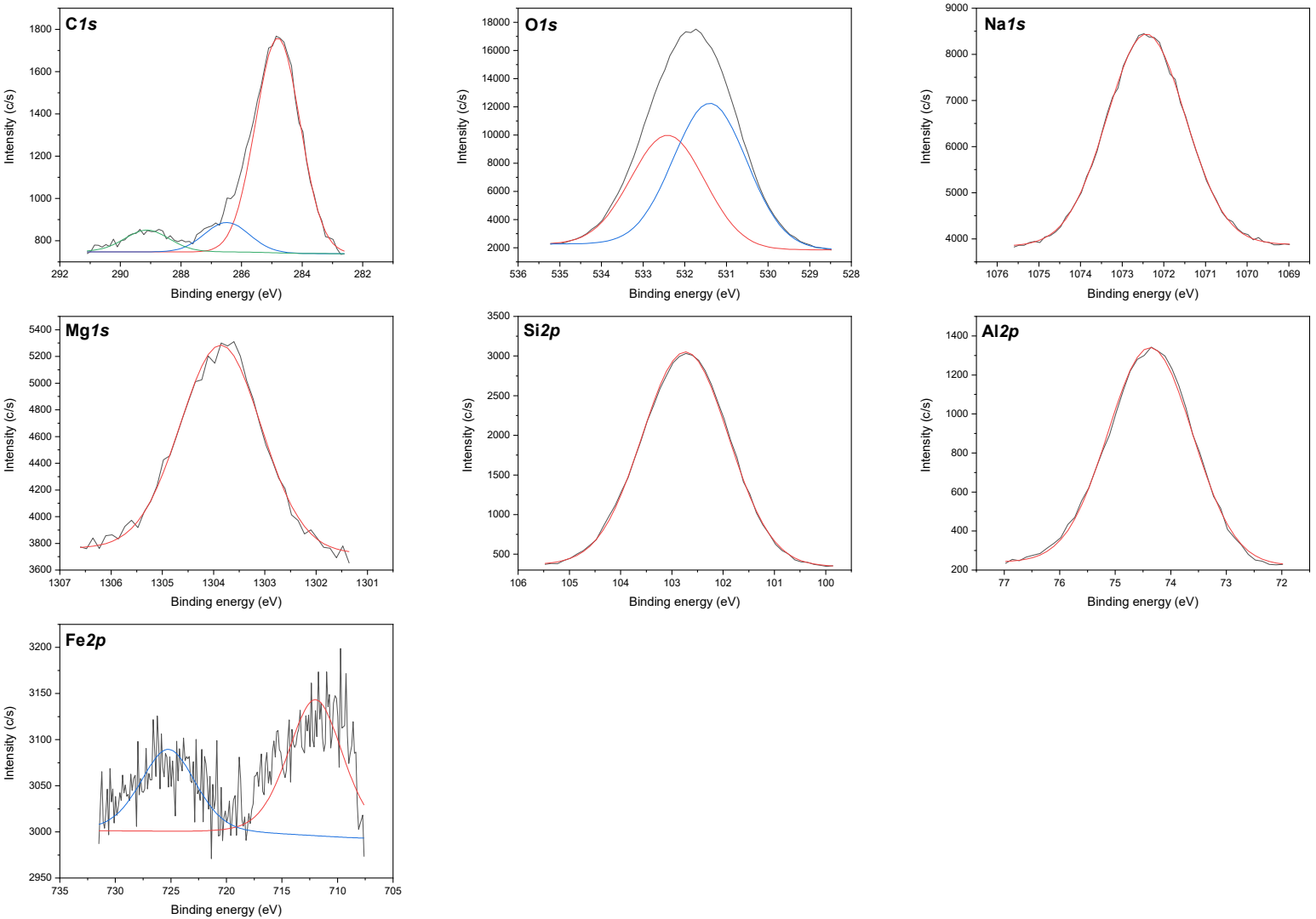

Figure 62. Deconvolution spectra of the Z20 sample.

Table 20. XPS quantification, atomic concentration, and weight of the samples.

	GP		Z13X		Z5		Z10		Z20		Z30	
	Atomic c. (%)	**Weight (%)**	**Atomic c. (%)**	**Weight (%)**	**Atomic c. (%)**	**Weight (%)**	**Atomic c. (%)**	**Weight (%)**	**Atomic c. (%)**	**Weight (%)**	**Atomic c. (%)**	**Weight (%)**
C *1s*	18.02	11.59	15.10	9.14	7.10	4.41	9.70	6.08	10.47	6.51	7.53	4.67
O *1s*	50.66	43.41	44.63	35.99	57.07	48.29	54.69	45.65	53.60	44.40	57.21	47.23
Na *1s*	6.66	8.21	4.11	4.77	11.89	14.16	11.86	14.23	10.97	13.06	9.67	111.47
Al *2s*			7.95	10.81								
Mg *1s*					0.60	0.76	0.81	1.03	1.68	2.11	.69	.37
Si 2*p*	13.07	19.66	14.48	20.50	13.49	13.76	12.77	18.71	14.26	20.73	4.40	0.87
Al *2p*	11.26	16.28	6.18	8.40	9.85	19.63	10.15	14.29	8.65	12.08	.13	1.32
Mg *2p*			6.42	7.86								
Fe *2p*	0.16	0.48	1.33	1.33					0.38	1.10	.37	.08
Cl *2p*			1.19	1.19								

Table 21. XPS quantification of the deconvoluted peaks.

	Area peaks (%)																	
	GP				Z13X				Z5			Z10			Z20			Z30	
C1s	284.8 eV 77.59	286.4 eV 7.57	289.0 eV 3.41	291.3 eV 11.44	284.8 eV 72.24	286.9 eV 5.31	289.3 eV 4.82	291.9 eV 17.62	284.9 eV 79.33	286.6 eV 4.95	289.5 eV 15.72	284.8 eV 82.60	286.6 eV 7.61	289.2 eV 9.79	284.8 eV 86.80	286.6 eV 6.75	289.1 eV 6.45	284.8 eV 80.09	289.1 eV 8.54
O1s	530.5 eV 9.63	531.5 eV 67.05	532.8 eV 23.32	-	531.6 eV 96.37	533.1 eV 3.63	-	-	531.4 eV 62.40	532.5 eV 37.60	-	531.3 eV 69.63	532.4 eV 30.37		531.4 eV 56.80	532.3 eV 43.20		532.4 eV 56.88	
Na*1s*	1072.6 eV 100	-	-	-	1072.3 eV 100	-	-	-	1072.8 eV 100	-	-	1072.2 eV 100	-		1072.3 eV 100	-		1072.4 eV 100	
Al*2s*	-	-	-	-	119.1 eV	123.9 eV	-	-			-								

					83.92	16.08										
Mg1*s*									1303.8 eV 100			1303.7 eV 100		1303.8 eV 100		1303.8 eV 100
Si2*p*	102.4 eV 100	-	-	-	102.5 eV 100	-	-	-	102.7 eV 100	-	-	102.6 eV 100	-	102.7 eV 100		102.7 eV 100
Al2*p*	74.3 eV 100	-	-	-	72.7 eV 13.83	74.2 eV 86.17	-	-	74.5 eV 100		-	74.3 eV 100		74.4 eV 100		74.4 eV 100
Mg2*p*	-	-	-	-	50.2 eV 72.08	55.6 eV 27.92	-	-								
Fe2*p*	711.1 eV 100	-	-	-	710.6 eV 60.09	713.8 eV 19.59	724.7 eV 20.32	-						711.4 eV 70.83	723.9 eV 29.17	713.0 722.2

									eV 32.09 67.91
Cl2*p*	-	-	-	-	199.0 eV 100	-	-	-	

Nuclear magnetic resonance (NMR) spectroscopy was used to investigate the structural units of the samples and the porous structure. The solid-state NMR spectroscopy is an important analysis to investigate geopolymeric materials characteristics because it provides data regarding the coordination status of the alumina units in the structure of the precursor materials and geopolymers, and consequently, its reactivity (Freire *et al.*, 2020).

Figure 63 shows the ^{27}Al NMR spectra of the samples, where it can be observed that the ^{27}Al NMR spectra of the samples, where it can be observed that the ^{27}Al spectra present only peak for the zeolite, at approximately 62 ppm, which corresponds to the presence of tetrahedral aluminum Al(IV) on the sample (Freire *et al.*, 2025). However, slightly different from the zeolite sample, the geopolymer and composite samples are very alike, having two smaller peaks at ~9 ppm, and ~ -20 ppm, which correspond to Al(VI), octahedral aluminum. In this case, for the geopolymer, the characteristics can be related to the zeolite, since the XRD analysis showed that the samples exhibited some crystalline peaks associated with faujasite. The absence of octahedral and penta-coordinated aluminum sharp peaks confirms that the geopolymerization is complete (Nasab, Golestanifard and MacKenzie, 2014; Petlitckaia *et al.*, 2020; Archez *et al.*, 2021; Revathi and Jeyalakshmi, 2021).

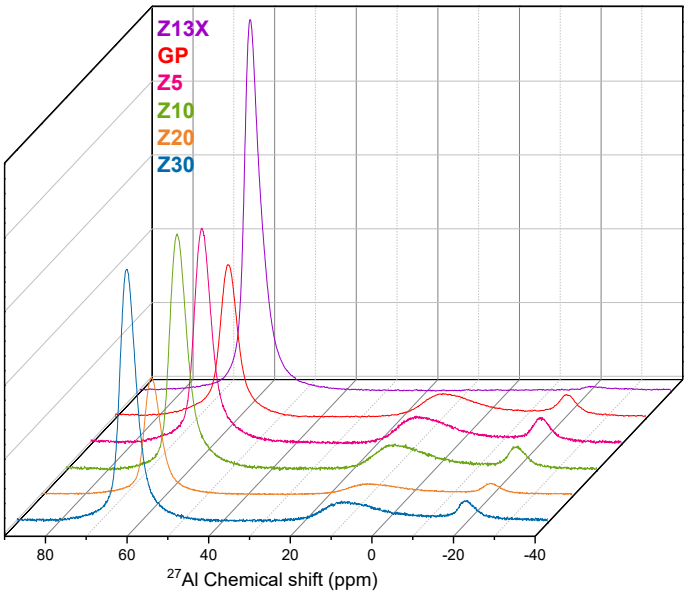

Figure 63. ^{27}Al NMR spectra of the samples.

Figure 64 shows the ^{29}Si NMR spectra of the samples. For all samples the ^{29}Si spectra presents 5 significant peaks. Again, the composites were very similar to the geopolymer, which was expected, since they are mostly geopolymer. In sample Z13X, it is possible to identify the chemical shifts of the different framework silicon Q^4 environments, Q^4(0Al) at -102 ppm, Q^4(1Al) at -98 ppm, Q^4(2Al) at -94 ppm, Q^4(3Al) at -89 ppm, and Q^4(4 Al) at -85 ppm (Gore *et al.*, 2002; Greiser, Hunger and Jäger, 2016). The same peaks can be observed in both geopolymer and composite samples. However, unlike zeolite, the most intense peaks correspond to the Q^4(0Al) silicon types. The peaks present in all samples confirm the presence of aluminosilicate, alternating between silica and alumina tetrahedra (Gore *et al.*, 2002; Nasab, Golestanifard and MacKenzie, 2014; Greiser, Hunger and Jäger, 2016; Gao, Yu and Brouwers, 2017; Paiva *et al.*, 2018).

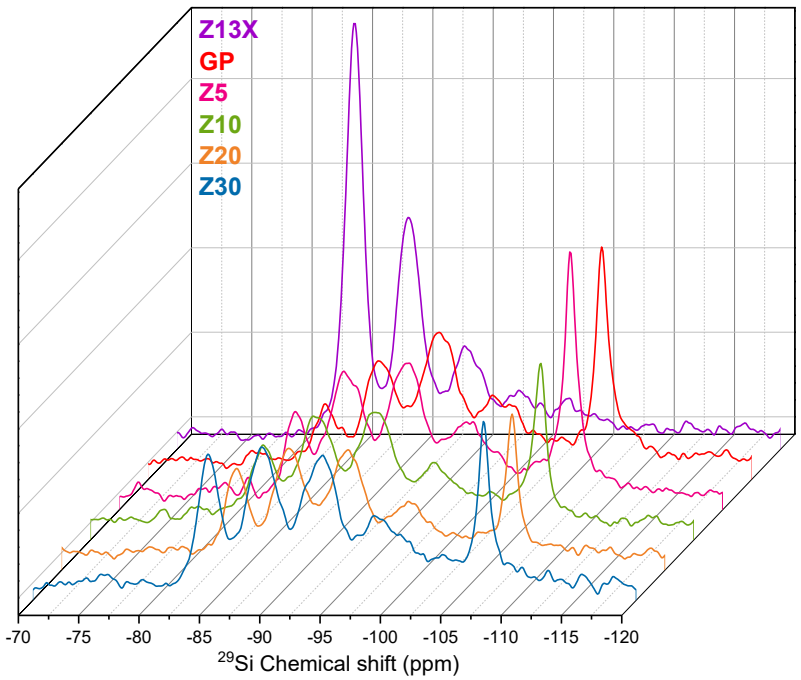

Figure 64. ^{29}Si NMR spectra of the samples.

8.3.5 Adsorption-Desorption Equilibrium Isotherms

The suitability of a material to be used as an adsorbent depends on many factors, like the characteristics mentioned. It is well known that zeolites have a high CO_2 adsorption capacity (Hauchhum and Mahanta, 2014; Minelli *et al.*, 2016; Khoramzadeh, Mofarahi and Lee, 2019; Karimi, Rodrigues and Silva, 2021; Papa *et al.*, 2023). Although the use of geopolymers in gas separation and capture is recent (Minelli *et al.*, 2016, 2018; Freire *et al.*, 2020; Freire, José and de Fátima Peralta Muniz Moreira, 2022; Papa *et al.*, 2023), there are already studies that report their adsorption capacity. In this study, it is expected that the adsorption/desorption capacity of the samples for the CO_2 will increase with the addition of more zeolite to the samples.

The CO_2, CO, and H_2 adsorption equilibrium isotherms were obtained at 30, 50, and 100 °C, with pressures between 0 and 760 mmHg. Different models (Langmuir, Freundlich, Temkin, Sips, Temkin, and Redlich Peterson) were applied for the analysis

of the experimental data. The models that best fit the experimental data were Sips and Freundlich models. The Sips model is a combination of the Langmuir and Freundlich models, aiming to predict the heterogeneity of adsorptive systems (Voigt, 2019). It is one of the most applied models due to its high accuracy (Khoramzadeh, Mofarahi and Lee, 2019).

Figures 65 and 66 present the CO_2 and CO adsorption isotherms carried out at 30, 50, and 100 ºC, with the respective model. Figure 67 presents the H_2 adsorption isotherm carried out at 30 ºC, according to the Freundlich model. The CO_2 adsorption isotherms at the three temperatures of all samples presented favorable shapes. For the CO and H_2 adsorption, the isotherms are quite linear (Kyzas, Bikiaris and Mitropoulos, 2017). In the CO isotherm, at 50 and 100 °C, the Z13X sample presented a small H4 type hysteresis loop, which is characteristic of a blend of isotherms Type I and II, characterized by presenting the main adsorption at low relative pressures (P/P_0), which is associated with micropore filling. The H4 hysteresis loops are usually observed as zeolitic materials (Thommes *et al.*, 2015; Dantas *et al.*, 2019; Pasabeyoglu *et al.*, 2024). And the H_2 isotherms presented a wide hysteresis, which due to the very low adsorption was considered a pronounced behavior originating from the equipment. The parameters of the Sips and Freundlich models are presented in Table 22, along with the exothermic parameters.

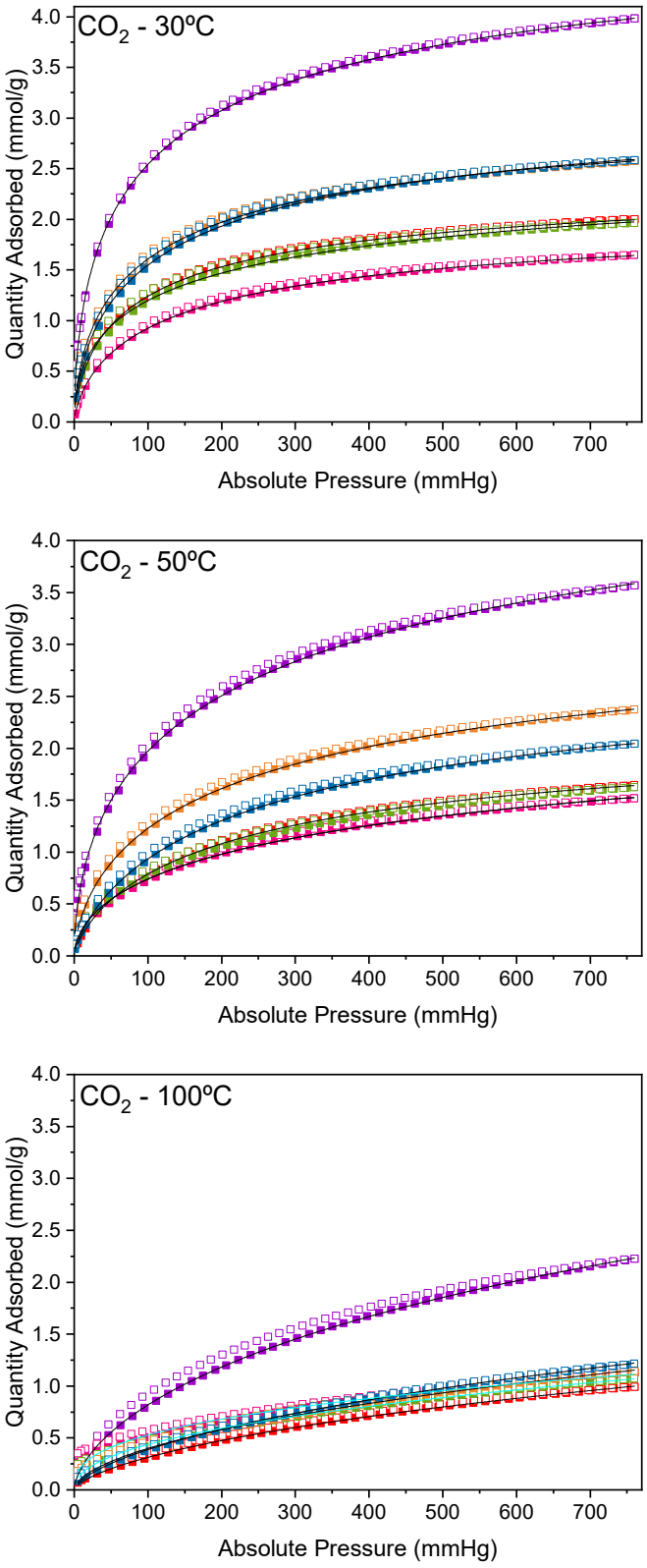

Figure 65. Adsorption (closed squares) and desorption (open squares) isotherms of **CO_2** on the Z13X (purple), GP (red), Z5 (pink), Z10 (green), Z20 (orange), and Z30 (blue) samples, at 30 ºC, 50 ºC, and 100 °C. The black line indicates the Sips isotherm model and the cyan indicates the Freundlich isotherm model (100 ºC).

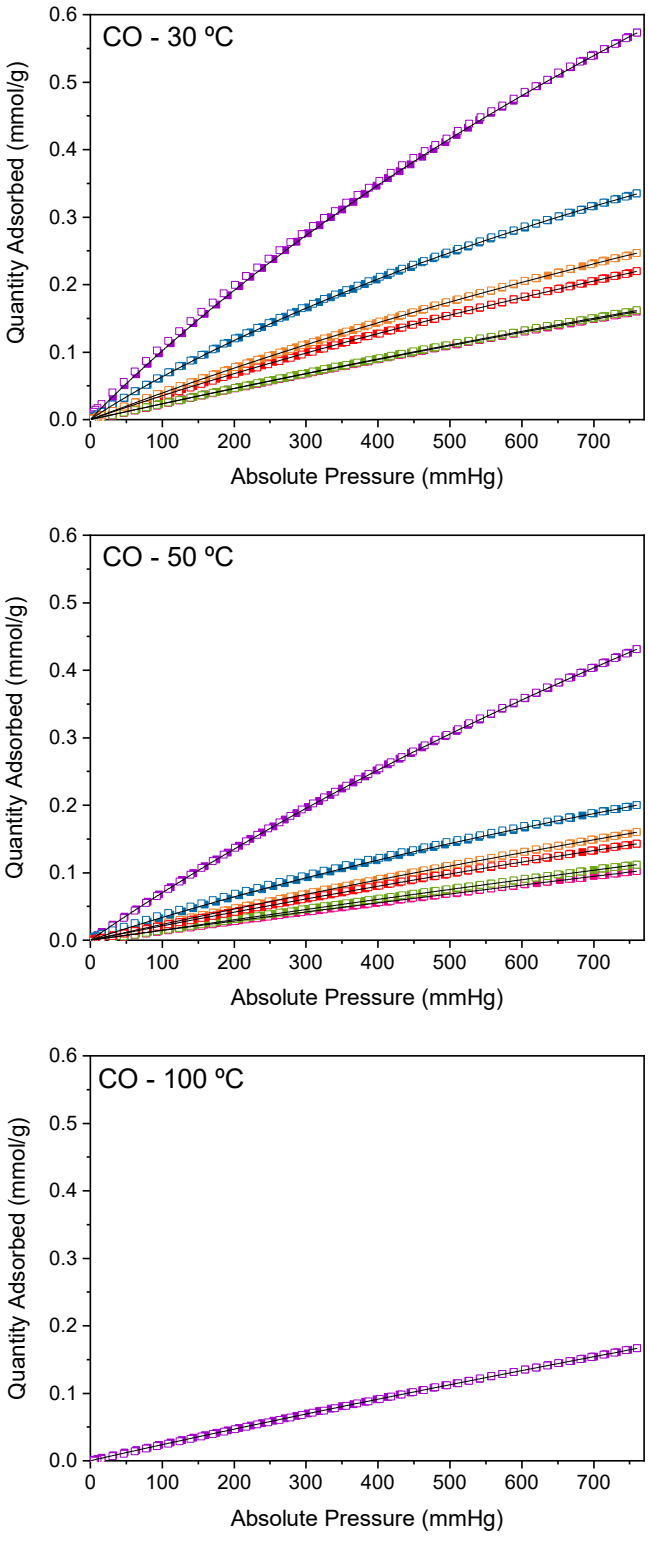

Figure 66. Adsorption (closed squares) and desorption (open squares) isotherms of **CO** on the Z13X (purple), GP (red), Z5 (pink), Z10 (green), Z20 (orange), and Z30 (blue) samples, at 30 ºC, 50 ºC, and 100 °C. The black line indicates the Sips isotherm model.

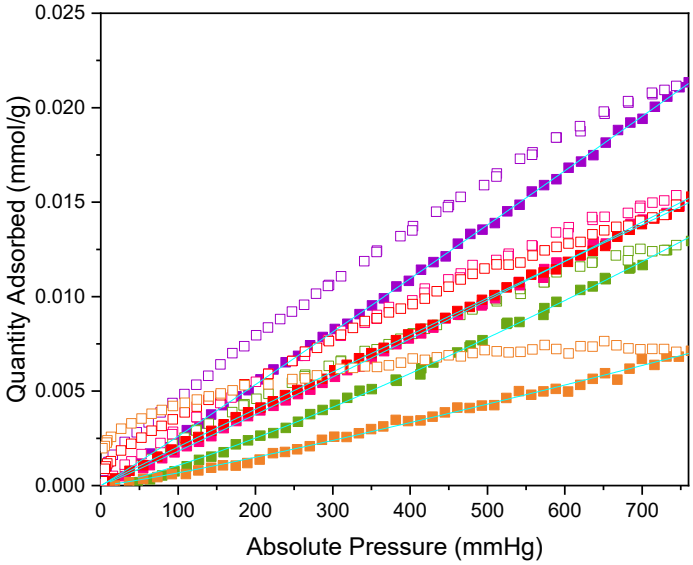

Figure 67. Adsorption (closed squares) and desorption (open squares) isotherms of **H_2** on the Z13X (purple), GP (red), Z5 (pink), Z10 (green), Z20 (orange), and Z30 (blue) samples, at 30 ºC. The black line indicates the Freundlich isotherm models.

The isosteric heat of adsorption determines the extent of temperature changes that take place inside the adsorbent during the adsorption and desorption phases of the processes (Sircar *et al.*, 1999; Seabra *et al.*, 2019). Thus, based on the isotherm data acquired at the three temperatures, the Clausius–Clapeyron equation (Equation 2) was utilized to compute the isotropic heat of adsorption. For this, the isosteric temperatures of adsorption were determined from the slope by plotting the values of lnP vs 1/T. Zeolitic materials were utilized as a comparison since there is currently no information in the literature regarding geopolymer and geopolymer/zeolite composites and isosteric heat for CO_2 adsorption.

The isosteric heat for CO_2 adsorption in zeolite 4A type obtained by Romero-Pérez and Aguilar-Armenta (2010) is 47.8 kJ·mol^{-1}; Seabra et al. (2019) reached ~43 kJ·mol^{-1} in zeolite 4A, Kim and Kim (2023) obtained 53.8 and 40.8 kJ·mol^{-1} with zeolite NaX and NaY types, respectively; and Khoramzadeh et al. (2019) reached about 37.20, 31.93, 30.19, and 25.08 kJ·mol^{-1} in zeolites 13X, 5A, 4A, and beta types, respectively.

The isosteric heats of adsorption for CO_2 obtained in this study were 31.99, 39.43, 18.09, 27.59, 39,31, and 34.18 $kJ \cdot mol^{-1}$ for the Z13X, GP, Z5, Z10, Z20, and Z30 samples, respectively. Thus, when comparing the heats of adsorption of the samples with values reported in the literature for zeolites, the values in the present work are slightly lower for most of them, yet they are very close to the ones obtained elsewhere (Khoramzadeh, Mofarahi and Lee, 2019).

Table 22. Sips and Freundlich models parameters applied to the sample's equilibrium data.

Gas	Sample	Temp.	Sips model				Freundlich model			- ΔH ads (kJ·mol^{-1})
			K_S (mmHg)	q (mmol/g)	n_S	R^2	K_F (mmHg)	n_F	R^2	
CO_2	Z13X	30 °C	0.0628	5.3315	0.5808	0.999				-44.650
		50 °C	0.0386	5.8534	0.5595	0.999				
		100 °C	0.0073	7.4014	0.6143	0.999				
	GP	30 °C	0.0433	2.5166	0.6758	0.999				-36.731
		50 °C	0.0154	2.3251	0.7612	0.999				
		100 °C	0.0034	4.8721	0.6515	0.999				
	Z5	30 °C	0.0285	2.1667	0.7083	0.999				-18.620
		50 °C	0.0240	3.0327	0.5640	0.999				
		100 °C					0.0977	2.7256	0.992	
	Z10	30 °C	0.0583	2.9629	0.5331	0.998				-36.964
		50 °C	0.0226	2.9075	0.6078	0.999				
		100 °C					0.0569	2.2615	0.997	
	Z20	30 °C	0.0507	3.3653	0.6281	0.999				-40.712
		50 °C	0.0266	3.6637	0.6392	0.999				
		100 °C	0.0031	9.8775	0.5646	0.999				
	Z30	30 °C	0.0414	3.4518	0.6462	00.999				-40.832
		50 °C	0.0136	3.0433	0.7564	0.999				
		100 °C	0.0035	6.0532	0.6434	0.999				
CO	Z13X	30 °C	5.3094E-4	2.3200	0.9687	0.999				-19.789
		50 °C	2.5384E-4	2.1885	0.9861	0.999				
		100 °C	1.0445E-4	2.4741	0.9854	0.999				

	GP	30 °C	3.2269E-4	1.2257	0.9823	0.999				-19.621
		50 °C	1.8660E-4	1.2001	0.9925	0.999				
	Z5	30 °C	1.7448E-4	1.3724	0.9989	0.999				-15.662
		50 °C	3.0258E -5	5.4640	0.9718	0.999				
	Z10	30 °C	1.7879E-4	1.2623	1.0116	0.999				-15.619
		50 °C	1.1889E -4	1.0539	1.0412	0.999				
	Z20	30 °C	3.3294E-4	1.2297	0.9987	0.999				-17,967
		50 °C	1.8271E -4	1.2418	1.0053	0.999				
	Z30	30 °C	6.9371E-4	1.1752	0.9576	0.999				-25.941
		50 °C	4.2222E-4	0.8997	0.9824	0.999				
H_2	Z13X						2.2236E-5	0.9665	0.999	x
	GP						2.2404E-5	1.0120	0.999	
	Z5						1.4716E-5	0.9558	0.999	
	Z10						3.5734E-6	0.8081	0.998	
	Z20						3.3115E-6	0.8666	0.994	

It is observed that the adsorption of CO_2, CO, and H_2 decreases as the temperature increases, in a behavior typical of exothermic adsorption (Kim and Kim, 2023). The CO adsorption capacity was very low compared to CO_2 adsorption. At 30 ºC it reached 0.57, 0.33, 0.25, 0.22, 0.16, and 0.16 mmol/g at 750 mmHg, with samples Z13X, Z30, Z20, GP, Z10, and Z5, respectively. For H_2 adsorption capacity, at 30 °C, all samples had a very low adsorption capacity: 0.021, 0.016, 0.015, 0.013, and 0.007 mmol/g for Z13X, Z5, GP, Z10, and Z20, respectively. The adsorption capacity of sample Z30 presented an insignificant amount of adsorbed, near to 0.001 mmol/g. The same happened with the adsorption capacities of all samples at 50 and 100 °C.

No studies were found in the literature that analyze the adsorption capacity of geopolymer/zeolite composites for CO, and H_2. For a simple comparison, some studies analyze the adsorption capacity of these gases with zeolites, at 25 ºC and 1 bar. Cui, Xing, et al. 2023 analyzed the CO adsorption capacity in NaX and CaA zeolites obtaining 1.13 and 1.82 mmol/g, respectively. Cui and Su et al. (2023) measured the adsorption capacity of LiX, NaX, and KX zeolites as 0.97, 1.13, and 0.95 mmol/g, respectively. Kim and Kim (2023) tested zeolites for CO and H_2 with NaY and NaX zeolites and found an adsorption capacity of 1.10 and 1.12 mmol/g for CO, respectively. Both samples presented an adsorption of 0.02 mmol/g for H_2. Shrotri et al. (2023) tested four different zeolites for H_2 adsorption at 30 °C, which reached adsorption capacities of 0.16, 0.21, 0.25, and 0.33 mmol/g for Na-X, NH_4-X, Li-X, and Li-H-X zeolites, respectively. In the present study, at 30 ºC, samples Z13X, GP, Z5, and Z10 presented an adsorption capacity similar to those reported in the literature for H_2 adsorption. However, samples Z20 and Z30 presented lower adsorption capacity. For CO adsorption, all samples presented an adsorption capacity lower than that reported in the literature.

Table 23 presents the CO_2 adsorptive capacity of some geopolymer, zeolite, and composites reported in the literature. No studies were found that analyze the adsorption capacity at the same temperatures analyzed in this study for comparison. Therefore, studies with temperatures close to those applied in this study were selected. Overall, the geopolymers synthesized presented a higher adsorption capacity than the geopolymeric materials reported in the literature. The zeolite sample presented a high adsorption capacity compared to most studies, and the Z20 and Z30 composites presented a similar adsorption capacity; samples Z5 and Z10 presented lower capacity at 30ºC.

Table 23. Adsorption capacity of the synthesized geopolymer samples with some geopolymers reported in the literature (Pressure 1 bar = ~1atm = ~750 mmHg).

	Adsorbent	**T (°C)**	**CO_2 adsorption (mmol/g)**	**Reference**
Zeolite	Z-Na4A		2.90	Papa et al. (2023)
	Z-A4	25	3.16	Hauchhum & Mahanta (2014)
	Z-Na13X	35	2.50	Minelli et al. (2016)
	Na13X	35	3.5	Minelli et al. (2018)
	Z-A4 BF	30	4.12	Karimi et al. (2021)
	Z-13X	35	4.86	Khoramzadeh et al. (2019)
	Z-LiX	25	0.97	Cui, Su, et al. (2023)
	Z-NaX		1.13	
	Z-KX		0.95	
	NaY	25	5.60	(Kim and Kim, 2023)
	NaX	25	4.60	
	Z13X	**30**	**3.98**	**This work**
Geopolymer	G10	35	0.62	Minelli et al. (2016)
	G13	35	0.58	
	G23	35	0.57	
	K-G_2	35	0.58	Minelli et al. (2018)
	Na-$G_{1,2}$	35	1.95	
	MCR-1	35	0.80	Freire et al. (2020)
	MF-1	35	0.78	
	MR-1	35	0.69	

	MFCR-1	35	0.63	
	MFR-1	35	0.68	
	MF-2	35	0.64	
	MPW	35	1.90	(Freire *et al.*, 2025)
	GP	**30**	**2.00**	**This work**
Composite	G-NaX	25	2.50	(Candamano *et al.*, 2022)
	K-G_2-Z	35	2.50	(Minelli *et al.*, 2018)
	Na-$G_{1,2}$-Z		1.60	
	Na-$G_{1,2}$-4A	35	2.60	(Papa *et al.*, 2023)
	K-G_2-4A		0.47	
	FGZ	25	6.09	(Han *et al.*, 2022)
	Z5	**30**	**1.65**	**This work**
	Z10		**1.96**	
	Z20		**2.57**	
	Z30		**2.58**	

8.4 PARTIAL CONCLUSIONS

In this study, low-cost metakaolin-phosphate waste-based geopolymer samples were synthesized to prepare geopolymer/zeolite 13X composites. By this manner, an accessible starting material has been used with a simple and low-cost synthesis method with is easily scale up.

The CO_2 adsorption capacity obtained through the isotherms reached 3.98, 2.57, 2.57, 2.00, 1.96, and 1.65 mmol/g at 30 °C, for samples Z13X, Z30, Z20, GP, Z10, and Z5, respectively. This capacity decreases as the temperature increases. For the adsorption of CO and H_2, the samples presented a very low adsorption capacity, which is beneficial and expected since the material is intended for the CO_2 capture and separation. These results confirm that composites with zeolite and geopolymer phosphate mining tailing-based can be used for CO_2 capture and separation. This approach is environmentally friendly and cost-effective, as the geopolymer can be synthesized from specific wastes, such as kaolin and phosphate mining tailings, which were used in this study.

The synthesized geopolymer presented a higher adsorption capacity than most of the studies found in the literature. The composite samples with the higher amount of zeolite presented the best results, which is expected since the zeolite has a higher adsorption capacity than the geopolymer. The characteristics of the composite samples are quite similar; however, the only characteristic that seems to influence the adsorption capacity is the surface area, which increases with the addition of more zeolite.

9 INNOVATIVE ELECTROSPUN GEOPOLYMER/ZEOLITE/PVA COMPOSITE

This chapter describes the preparation and characterization of geopolymer/zeolite/PVA composite prepared in this study.

9.1 MATERIALS AND METHODS

9.1.1 Materials

Polyvinyl alcohol (99% hydrolyzed, Mw 145,000 g/mol) was purchased from Sigma-Aldrich, the zeolite 13X type was provided from Trade/Shanli. The geopolymer and composites were selected from the works presented in the previous sections. The geopolymer was the G65s, the same used to prepare the composites, and the composites were Z20 and Z30, as they had a greater CO_2 adsorption capacity.

9.1.1.1 Solution composite preparation

First, the zeolite 13X (Z13X) pellets were powdered using a high-energy ball mill (Mixer/Mill 8000 SPEX SamplePrep).

The preparation of the fluid was based on the studies carried out by Asiri et al. (2021), who produced electrospun membranes using PVA with molecular weight of 145,000, Méndez-Ares et al. (2021) and Rad et al. (2014), who fabricated zeolite/PVA composites, by Kang & Kang (2016) that prepared a geopolymer membrane using electrospinning, and by Hong et al. (2022) who prepared PVA membranes incorporated with amine-modified silica nanoparticles for CO_2 capture.

The polyvinyl alcohol (PVA) was used due its increasingly use as a support for adsorbent membranes applied to gas capture (Hong *et al.*, 2021; Méndez-Ares *et al.*, 2021; Haleem *et al.*, 2022; Vatanpour *et al.*, 2023), fixed and mobile carriers have been developed to improve the transport of CO_2 (Hong *et al.*, 2021, 2022). PVA is not only environmentally friend but also shows low toxicity, high tensile strength, excellent flexibility, can impart some viscoelasticity to the zeolite/geopolymer paste (Khalil, Hashaikeh and Hilal, 2021), and is a low-cost polymer, and which makes it a promising support material for adsorption application in gas capture and separation (Méndez-Ares *et al.*, 2021; Hong *et al.*, 2022).

Aiming to prepare the ideal solution to produce the electrospun membrane, some tests were made: i) PVA at 8, 10, and 12%, ii) zeolite at 4, 2, and 1%; iii) ethanol at 0, 5, 10, and 20%; iv) the solution was prepared in a beaker and a closed bottle; v) with and without water-bath; vi) changing the addition order, first the PVA, then the zeolite, the reverse, and adding the two at the same time; vii) adding the PVA/zeolite first in ethanol than adding the deionized water, and reverse; viii) the temperature was tested at 80, 100, 120, 130, and 150 ºC, and; ix) under fast and slow magnetic stirring. With these tests, it was possible to find the best way to the ideal solution to produce the membranes.

So, the final solution was prepared by mixing ethanol with 8 wt% of PVA and 1wt% of the powder (zeolite, geopolymer, or the composites Z20 and Z30) under slow magnetic stirring at 80 ºC for 20 min, then deionized water was added and fast stirred at 130 °C for 2 h. Then, the heat was turned off, and the solution was stirred to cool down.

9.1.1.2 Electrospinning

To electrospin the nanofibers, an equipment developed by Calzado-Delgado et al. (2022) was used. It features rapid, independent, and precise x–y–z movements for large-area depositions of electrospun fibers, direct writing, or assembly of fibers into sub-millimeter and micron-sized patterns, and printing of 3D micro and nanostructures. However, it was used without movement. The experimental setup consists of a high-voltage source, a syringe pump, a metal needle, and a ground collector.

The preparation of the nanofiber through electrospinning was based on the studies conducted by Rad et al. (2014) and Asiri et al. (2021). The prepared solution was loaded into a 10 mL plastic syringe equipped with a syringe needle. The sample electrospun was performed in a room temperature environment, with a 14 cm distance between the needle and the collector, and initially with a voltage of 20 kV and a feeding rate of 0.5 mL/h, as in the basis references. However, considering the differences in the electrospinning equipment, these parameters do not work well, so aiming to use the lower voltage as possible the parameters were tested with a range of 10 to 16 cm distance between the needle and the collector, with a voltage between 5 and 8 kV, a feeding rate in a range of 0.10 to 0.40 mL/h, and needles with 21. 22, 25, and 27 G. The best performance was achieved with a voltage of 8 kV and a feeding rate of 0.13 mL/h. These are good parameters to be applied since a strong electric field and fast writing speed give nanofibers of narrow diameter (Calzado-Delgado, Guerrero-Pérez and Yeung, 2022a).

The electrospun membranes were named MZ (zeolite/PVA), MGP (geopolymer/PVA), MZ20 (geopolymer/zeolite20%/PVA), and MZ30 (geopolymer/zeolite30%/PVA). Figure 68 shows an image of the equipment with needle

and flashlight and a micro camera picture of the needle and fibers. And Figure 69 presents an image of the MGP, MZ20 and MZ30 membranes.

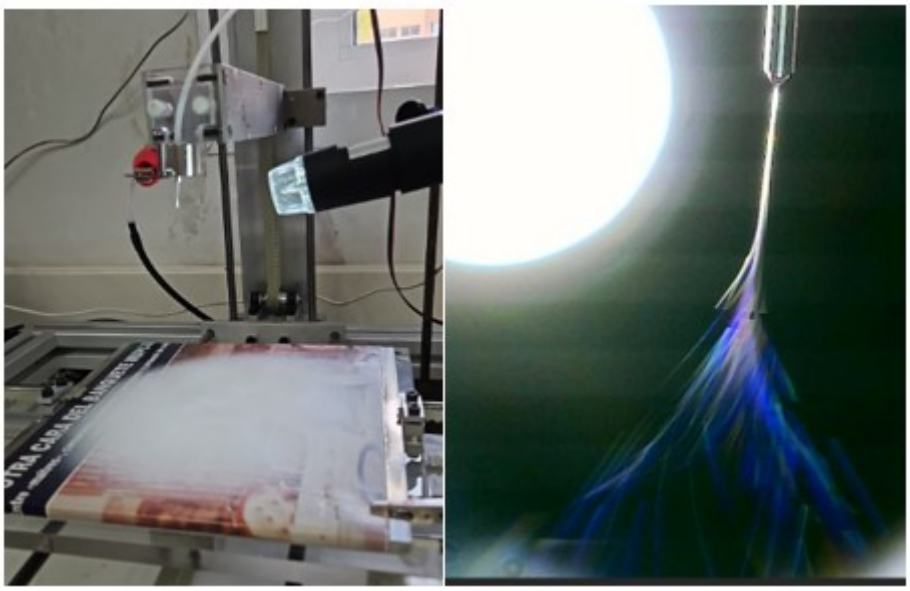

Figure 68. Images of the equipment and a picture of the microcamera while electrospinning.

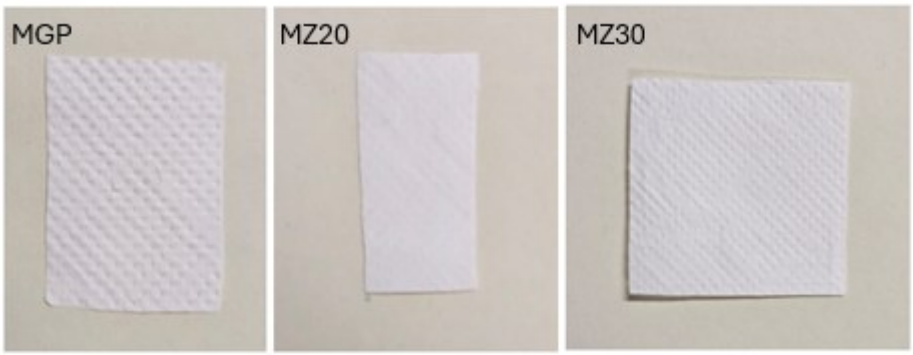

Figure 69. Image of the MGP, MZ20 and MZ30 membranes.

9.1.2 Characterization

9.1.2.1 Mineralogical composition and morphology

Scanning electron microscopy (SEM) associated with Energy-Dispersive Spectrometry (EDS) was used to study the morphology of materials and the chemical analysis. In this way, it is possible to identify the components of the material and to

analyze the inner structure of the samples, like the crystal structure, morphology, and stress state information. The equipment used was a FESEM TESCAN CLARA microscope, with a LEICA EM ACE600 metallizer. The samples were coated with 4nm of platinum, to make it more conductive for a better analysis.

9.1.2.2 Textural properties

The BET surface area (m^2/g) as an important parameter for the characterization of solids used for processes involving their surface was used to identify the textural properties of the samples. The kinetics of all heterogeneous "solid-fluid" interaction processes directly depend on the specific area of this solid. Several methods describe procedures for determining this characteristic; however, different methodologies can provide different values. The specific surface area, pore size, and total pore volume were obtained through nitrogen adsorption-desorption isotherms at -196 ºC, the analysis was carried out using Micromeritics ASAP 2020 equipment.

9.1.2.3 Chemical structure

Fourier-Transform Infrared Spectroscopy (FTIR) was used to identify the functional groups, and chemical bonds present on the surface of the samples. The analyses were performed on a spectrometer model 6800FV from Jasco Analitica. The measurements were made by total attenuated reflectance using the ATR ProOne accessory and making a blank in the air, without the need to disperse or treat the sample. For the acquisition of spectra, a standard spectral resolution of 4 cm^{-1} was used in the spectral range of 4000-400 cm^{-1}, as well as 64 accumulations per sample.

9.1.2.4 Surface chemistry characterization

X-ray photoelectron spectroscopy (XPS) was applied to determine the samples' surface chemistry. The spectra were recorded on a Physical Electronic spectrometer (PHI Versa Probe II) using monochromatic Al Kα radiation (15 kV, 1486.6 eV), a dual beam charge neutralizer for analyzing the core-level signals of the elements of interest, and a hemispherical multichannel detector. The sample spectra were recorded with a constant pass energy value of 29.35 eV, 0.125 eV/step, and a beam diameter of 200 μm. The energy scale was calibrated using Cu $2p_{3/2}$, Ag $3d_{5/2}$, and Au $4f_{7/2}$ photoelectron lines at 932.7, 368.2, and 83.95 eV, respectively. Atomic concentration percentages of the characteristic elements were determined considering the corresponding area sensitivity factor for the different measured spectral regions. The Multipak software was used for acquisition and data analysis. A Shirley-type background was subtracted from the signals. Recorded spectra were always fitted using Gaussian–Lorentzian curves to determine the binding energy of the different element core levels more accurately.

9.1.2.5 Adsorption Equilibrium Isotherms

The adsorption equilibrium tests were carried out with the CO_2, CO, H_2, gases at 30°C, with pressure between 0 and 760 mmHg. The analysis was performed using a Surface Area and Porosity Analyzer, Micromeritics ASAP 2020 model.

9.2 RESULTS AND DISCUSSION

9.2.1 Chemical analysis, morphology, and textural properties

The morphology of the microstructure of the MZ and MGP samples are shown in Figure 70. In the MGP and MZ it is noticeable the small particles where the zeolite and geopolymer are encapsulated inside the fibrous membrane evenly without conglomeration as well as membranes prepared by Zhang et al. (2021), also, the difference between zeolite and geopolymer is visible, the geopolymer has very amorphous particles, while the zeolite presented uniform and longer particles. Figure 71 presents the SEM images of the MZ20 and MZ30 samples. MZ20 presented a pattern like the MZ and MGP samples, although there are considerably more particles, and it is possible to see some agglomerates, while MZ30 sample presented many agglomerates along with the particles.

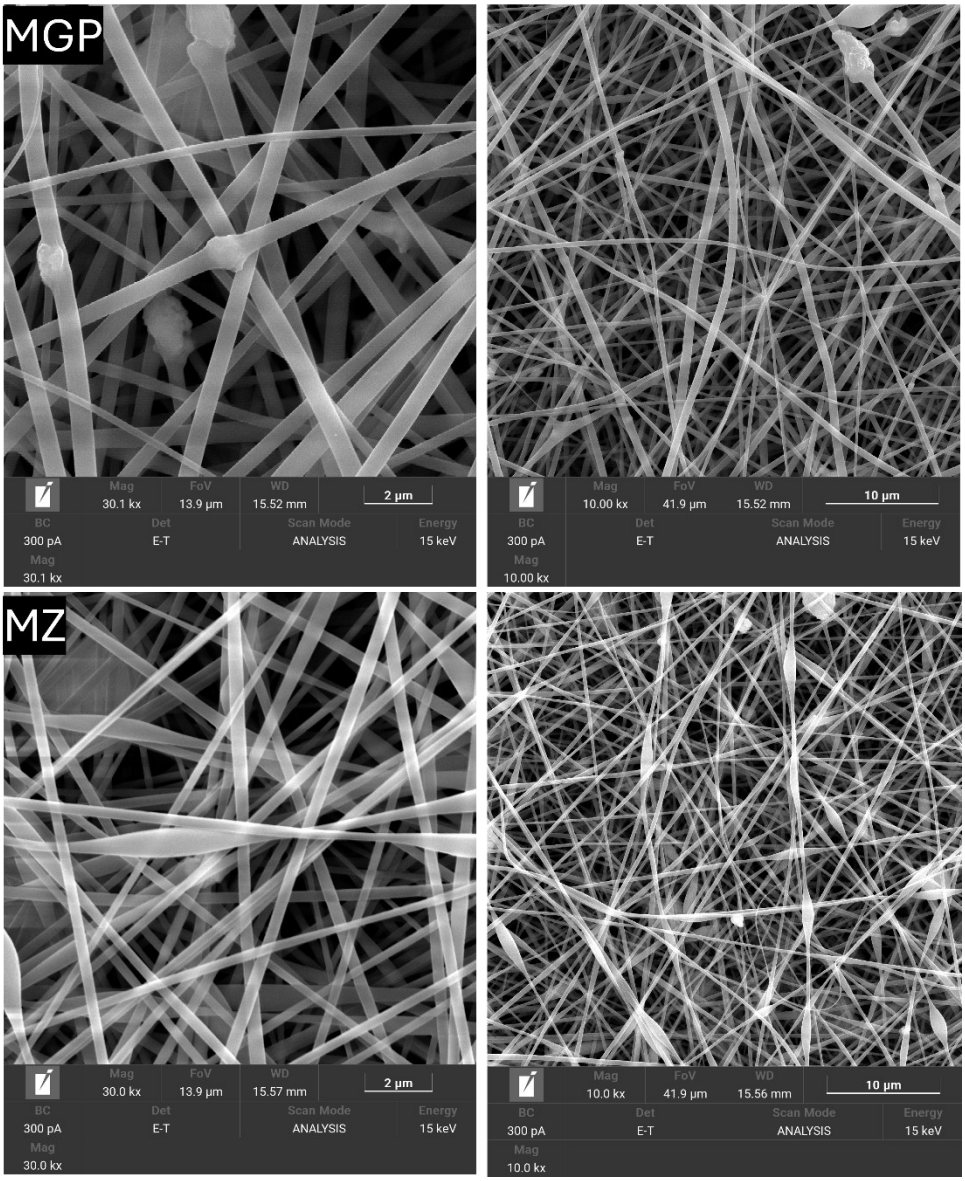

Figure 70. SEM images of the MGP, and MZ sample

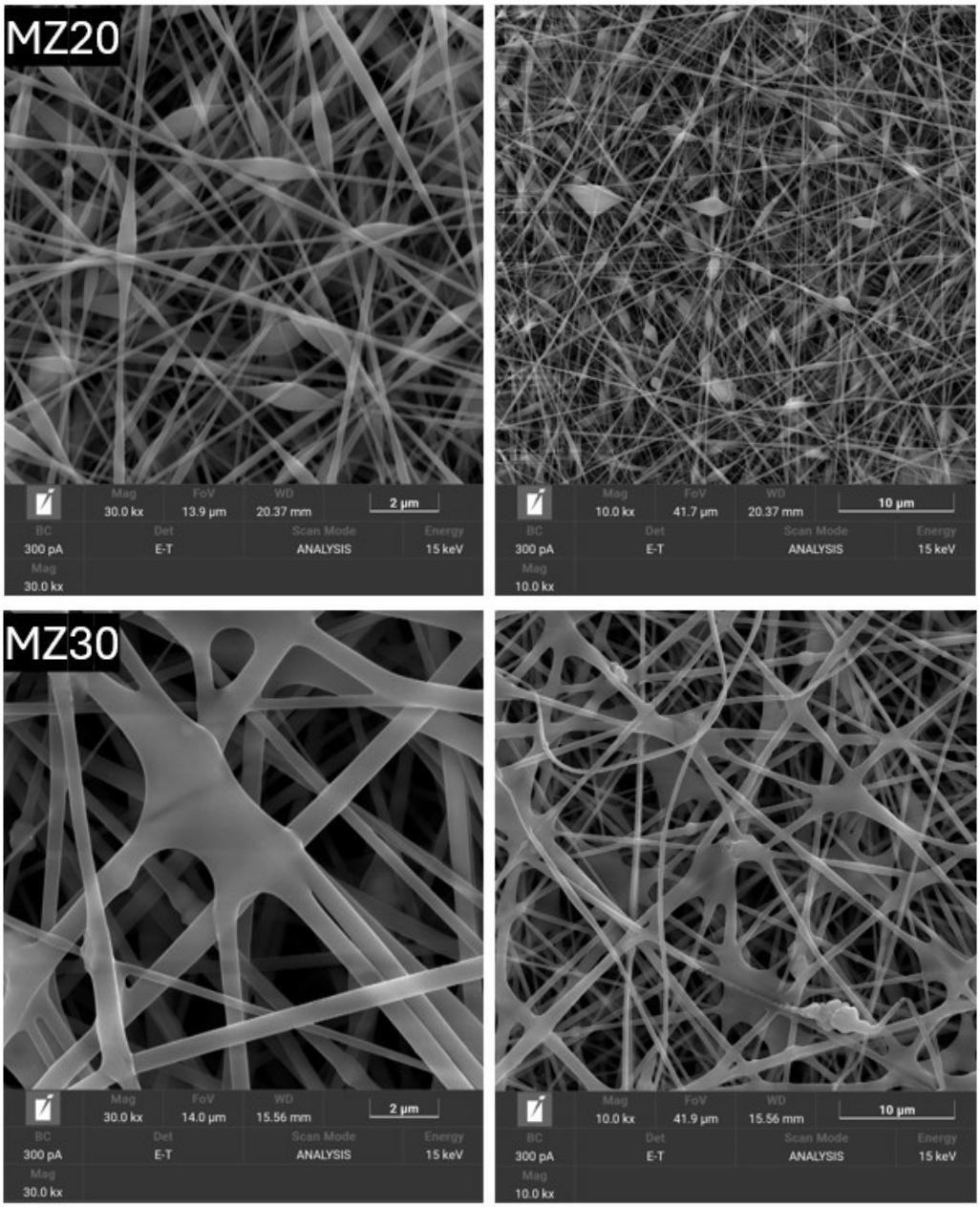

Figure 71. SEM images of the MZ20 and MZ30 sample

The chemical analysis (EDS) of the zeolite, geopolymer and composite samples are presented in Table 24. For each sample, three distinct regions were analyzed, and the reported values correspond to the average composition.

Table 24. Chemical analysis of the samples

Sample	C	O	Al	Si	Total (wt %)
MGP	73.81	25.54	0.21	0.45	100
MZ	75.23	23.62	0.39	0.76	100
MZ20	73.52	25.78	0.23	0.47	100
MZ30	74.19	25.32	0.15	0.35	100

The surface area, pore volume, and pore size are important factors in the selection of an adsorbent, so these characteristics are shown in Table 25, along with the fiber diameter, calculated using ImageJ software. The average fiber diameter was determined by measuring 10 beads from the SEM images.

The surface area of the MZ sample is lower, although, in the composites membranes, it increases as the amount of zeolite on the composite is increasing, therefore the MZ30 sample presented a higher surface area. The total pore volume and pore size did not present a pattern, also, the zeolite presented the lower total pore volume, though the MZ20 sample presented higher value than the MZ30 sample. The MZ30 presented the lower pore size, followed by the MGP sample, the MZ and MZ20 presented a considerably higher pore size than the other samples.

The surface area of the samples is very low compared to some zeolitic electrospun membranes presented in the literature, and to date, no studies on geopolymer/zeolite/PVA composites have been found for better comparison (Schneider *et al.*, 2024). The diameter of the sample's fibers is considerably higher than the reported values, which is in a nanometric range, with some studies reaching a maximum of 1.24 and 2.08 μm (Schneider *et al.*, 2024).

Table 25. BET Surface area, pore volume and size of the samples.

Sample	BET Surface area (m^2/g)	Total pore volume (cm^3/g)	Pore diameter (Å)	Diameter (µm)	Particles diameter (µm)
MZ	2.4	0.003	47.8	28.81	88.26
MGP	11.6	0.007	33.1	44.41	127.81
MZ20	17.4	0.013	49.3	12.81	56.97
MZ30	24.3	0.012	24.4	40.52	93.57

The BJH pore width distributions (Figure 72) of the MGP, MZ20 and MZ30 samples presented a broad mesopore distribution centered with a dominant pore size at approximately 25 and 100 Å. For the MZ, the pore distribution is similar to the porosity reported by Kim et al. (2022) for zeolite 13X, also, the sample presented a very low pore distribution, suggesting an uniform porosity, which a little number of pores around 25 Å and a broad mesopore distribution from approximately 70 to 230 Å. Overall, the samples prepared in this study exhibit mesoporous structures, as supported by findings from Alothman (2012), Thommes et al. (2015), and Wang et al. (2025).

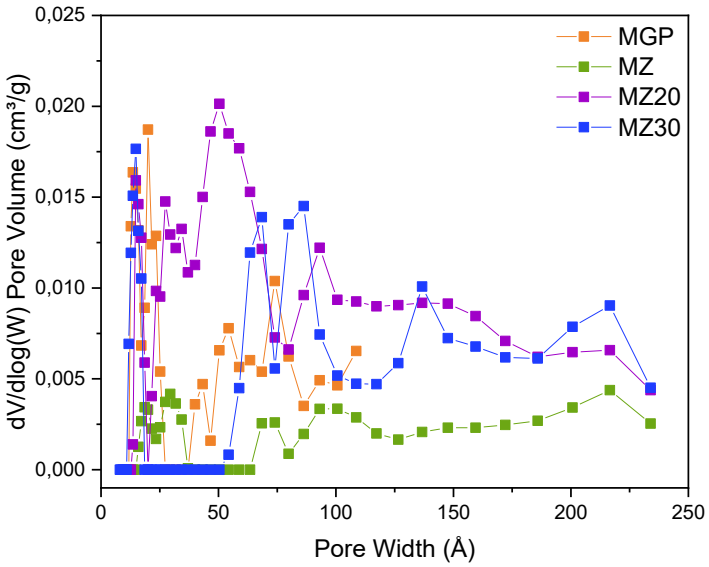

Figure 72. BJH pore width distributions of the samples.

9.2.2 Chemical structure

FTIR spectra of the samples are presented in Figure 73 along with their respective assignments. As expected, the spectra are very alike for all the samples and the bands correspond to the most characteristic bands of PVA. Large bands observed between 3550 and 3200 cm^{-1} are related to the O–H stretching from the intermolecular and intramolecular hydrogen bonds. The vibrational band observed between 2840 and 3000 cm^{-1} refers to the stretching C–H from alkyl groups. Furthermore, the peak at 1600–1700 cm^{-1} corresponds to the C=O stretching of the acetate group of the PVA.

The bands around 1600, 1400, 1300, 1100, and 850 are related to the (C–H)–CH_2, OH–C–OH, C–O–C, (C–O)–C–OH, and C–C vibrational modes, respectively (Mansur *et al.*, 2008; Ji *et al.*, 2022). The bands from 800 to 500 cm^{-1}, can be related to symmetrical Si-O-Si group vibrations, and the bands between 750 and 554 cm^{-1} correspondent with vibrational bands of zeolitic materials (Jiménez, Lalangui, Guacho, Paucar, *et al.*, 2019). However, the amount of aluminosilicates in the sample is very low, as shown by the EDS chemical analysis.

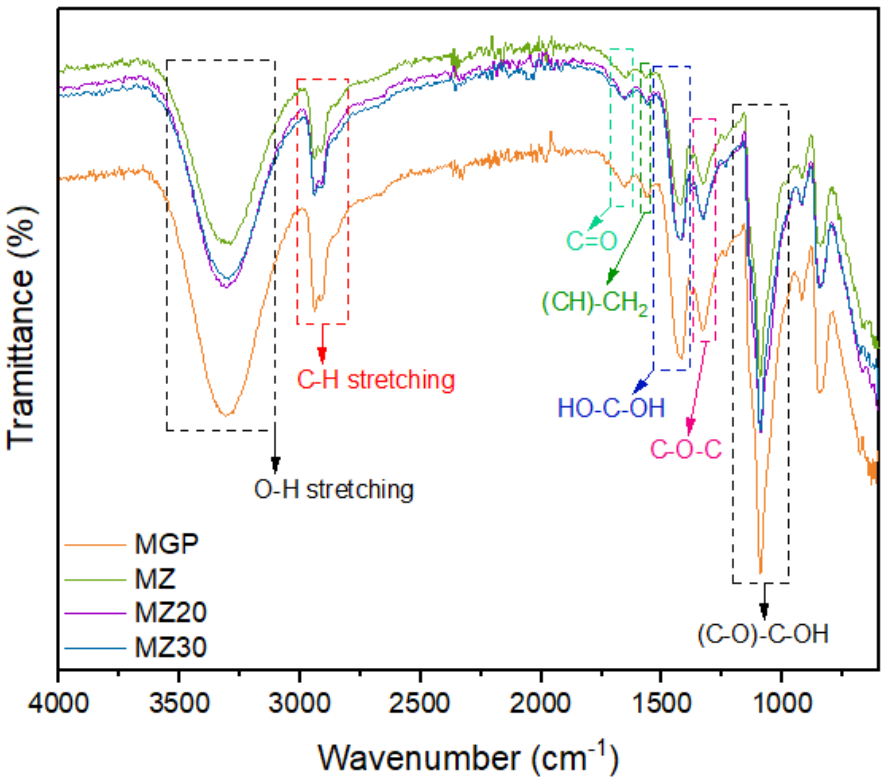

Figure 73. FTIR-ATR spectra of the samples.

9.2.3 Surface Chemistry

The XPS analysis was performed to obtain the chemical states and atomic composition of the sample's particles' surface. The identification of the peaks was based on the *Handbook of X-ray Photoelectron Spectroscopy* (Moulder et al., 1992; Wagner et al., 1979). The XPS spectra of the samples are presented in Figure 74. The sample spectra in terms of binding energy are the same, slightly differing in the intensity of the peaks, atomic concentrations, and weight, as reported in Table 26. The samples did not present aluminosilicates in their surface, which was expected, since the concentration on the samples is very low and covered by PDMS, and the EDS analysis shows low amounts of Si and Al.

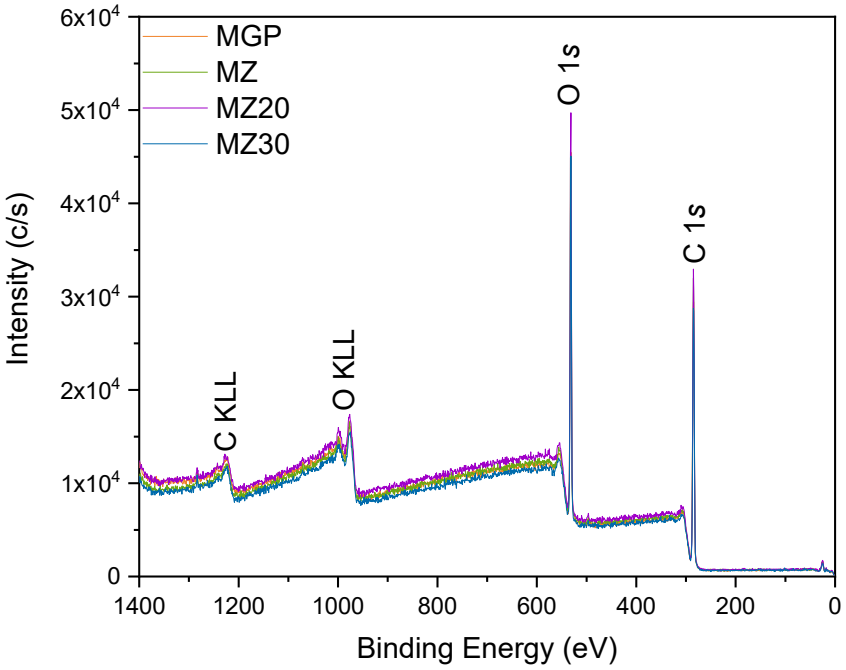

Figure 74. XPS survey spectra of the samples.

Table 26. XPS quantification, atomic concentration, and weight of the samples.

	MGP		MZ		MZ20		MZ30	
	Atomic c. (%)	**Weight (%)**	**Atomic c. (%)**	**Weight (%)**	**Atomic c. (%)**	**Weight (%)**	**Atomic c. (%)**	**Weight (%)**
C	64.49	57.69	65.24	58.49	64.39	57.58	64.55	35.45
O	35.51	42.31	34.76	41.51	35.61	42.42	57.75	42.25

9.2.4 CO_2, CO, and H_2 Adsorption-desorption Equilibrium Isotherms

The capacity of a material to adsorb depends on many factors, like surface area, volume, density, pore size and volume, and connectivity between the pores (Freire, 2019). The CO_2, CO, and H_2 adsorption equilibrium isotherms were at 30 °C with pressure between 0 and 760 mmHg. Different mathematical models (Langmuir, Freundlich, Temkin, Sips, and Redlich Peterson) were applied for the analysis of the experimental data, however, the model that best fitted to the experimental isotherms data was the Freundlich model, which is one of the first empiric equations used to describe equilibrium

data. This model describes the equilibrium in heterogeneous surfaces and considers that the heat of adsorption is exponentially given from the monolayer (Ming and Hsu, 2013; Ayawei, Ebelegi and Wankasi, 2017).

The following Figures (75 and 76) show the isotherms with the Freundlich isotherm model. The adsorption isotherms for all samples and gas are quite linear (Kyzas, Bikiaris and Mitropoulos, 2017). The CO_2 and H_2 adsorption presented high hysteresis, which can occur due to the formation of carbonates on the surface or a pronounced behavior originating from the equipment, since the adsorption was very low. The parameters obtained when applying the Freundlich model, which is represented by Equation 6, are presented in Table 28 at the end of the section.

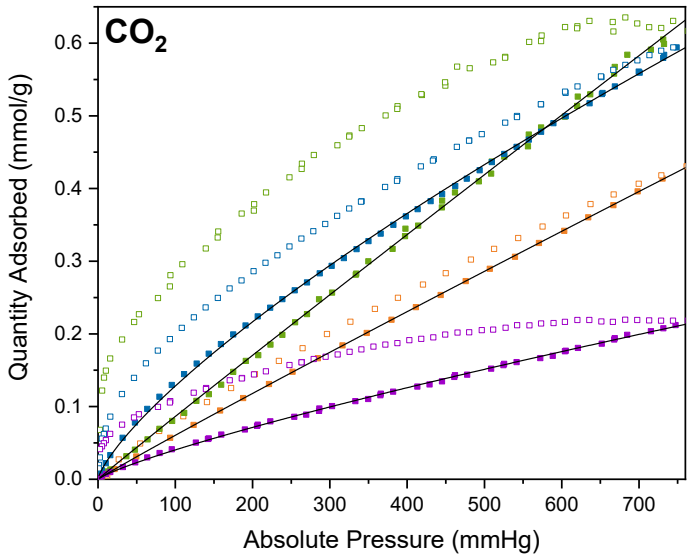

Figure 75. Adsorption isotherms of **CO_2** on the samples, which are indicated by colors, MGP is orange, MZ is green, MZ20 is purple, and MZ30 is blue, the closed squares are for adsorption and the open ones for desorption isotherms, and the black line indicates the Freundlich isotherm model.

To date, no studies have been found in the literature that prepared zeolite/geopolymer/PVA composites using the electrospinning technique and tested its applicability in CO_2 adsorption and separation. Table 27 presents a relation of some of

the adsorptive capacities of geopolymers, zeolites, and composites reported in the literature. No studies evaluating the adsorption capacity at the same temperature as used in this study were found for comparison; however, some studies have been conducted at 35 °C.

The adsorption capacity of the MZ and MGP samples was lower than compared to most studies on zeolite and geopolymer, and for composites. Although the adsorption capacity was also very low, Papa et al. (2023) achieved close results with one sample and lower with another. The low adsorption capacity can be justified by the low surface area, due to the very low concentration of zeolite, geopolymer, or composite in the samples, since these are the materials capable of adsorbing gases. In addition, these materials were encapsulated by the PVA, that is, they are not on the surface of the sample. Consequently, they do not have contact with the gases.

Table 27. CO_2 Adsorption capacity reported in the literature (Pressure: 1 bar = ~750 mmHg = ~ 1atm).

	Adsorbent	**T (°C)**	**CO_2 adsorption (mmol/g)**	**Reference**
Zeolite	Z-Na4A		2.90	Papa et al. (2023)
	Z-A4	25	3.16	Hauchhum & Mahanta (2014)
	Z-Na13X	35	2.50	Minelli et al. (2016)
	Na13X	35	3.5	Minelli et al. (2018)
	Z-LiX	25	0.97	Cui, Su, et al. (2023)
	Z-NaX		1.13	
	Z-KX		0.95	
	MZ	**30**	**0.62**	**This work**
Geopolymer	G10	35	0.62	Minelli et al. (2016)
	G13	35	0.58	
	G23	35	0.57	
	K-G_2	35	0.58	Minelli et al. (2018)
	Na-$G_{1,2}$	35	1.95	
	MCR-1	35	0.80	Freire et al. (2020)
	MF-1	35	0.78	
	MR-1	35	0.69	

	MFCR-1	35	0.63	
	MFR-1	35	0.68	
	MF-2	35	0.64	
	MGP	**30**	**0.43**	**This work**
Composite	G-NaX	25	2.50	(Candamano et al. 2022)
	K-G_2-Z	35	2.50	(Minelli et al. 2018)
	Na-$G_{1,2}$-Z		1.60	
	Na-$G_{1,2}$-4A	35	2.60	(Papa et al. 2023)
	K-G_2-4A		0.47	
	K-$G_{1,2}$-4A		0.03	
	MZ20	**30**	**0.21**	**This work**
	MZ30		**0.62**	

The CO and H_2 adsorption capacities were lower than the CO_2 adsorption. The MGP and MZ20 presented an adsorption of 0.05 mmol/g, and the MZ30 an adsorption of 0.08 mmol/g for both gases, the MZ did not present significant adsorption capacity for the CO, and for the H_2 gas the adsorption capacity was 0.16 mmol/g. For all adsorption evaluations, the best value was achieved at 760 mmHg.

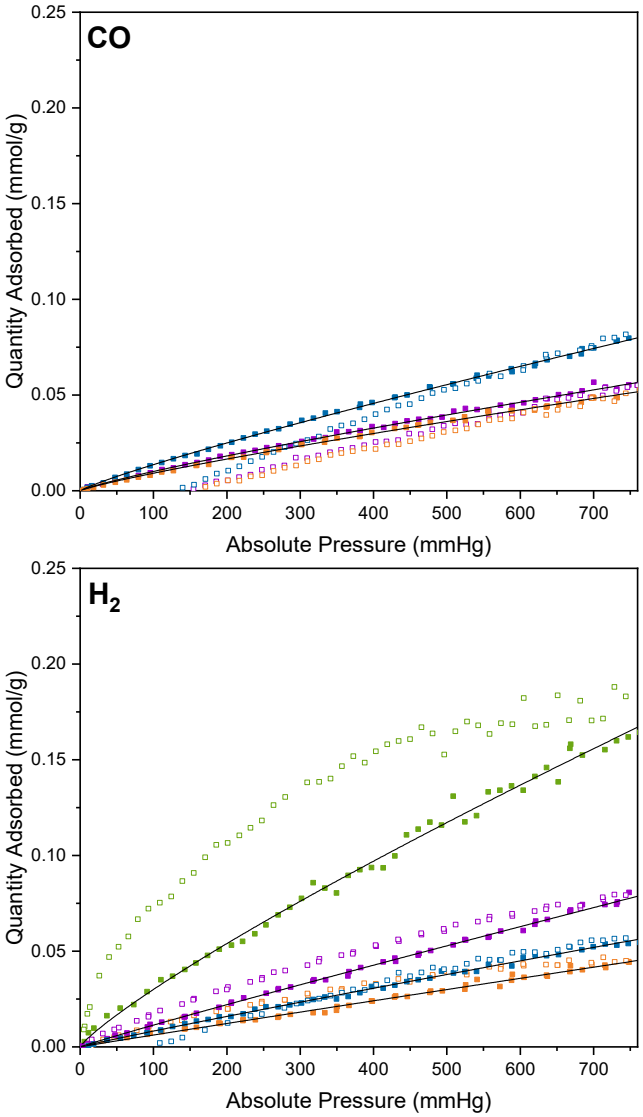

Figure 76. Adsorption isotherms of **CO** and **H_2** on the samples, which are indicated by colors, MGP is orange, MZ is green, MZ20 is purple, and MZ30 is blue, the closed squares are for adsorption and the open ones for desorption isotherms, and the black line indicates the Freundlich isotherm model.

Some studies that examine the CO and H_2 adsorption capacity of zeolites were found in the literature. However, no studies were found about the adsorption using geopolymer and zeolite/geopolymer/PVA composites.

Cui, Xing, et al. (2023) examined the CO adsorption capacity of zeolites at 25 ºC and found that the NaX and CaA zeolites had adsorption capacities of 1.13 mmol/g and 1.82 mmol/g, respectively. Cui, Su, et al. (2023) examined the zeolite LiX, NaX, and

KX's adsorption capacities, which were 0.97, 1.13, and 0.95 mmol/g, respectively. The experiments were carried out at a temperature of 25ºC, and the values are considerably higher than the obtained in this study.

Additionally, Shrotri et al. (2023) evaluated four distinct zeolites for H_2 adsorption at 30 ºC, and the results showed that the zeolites' respective adsorption capacities for the Na-X, NH4-X, Li-X, and Li-H-X zeolites were 0.16, 0.21, 0.25, and 0.33 mmol/g. The MZ sample of the present study had the same adsorption capacity as the Na-X sample, and the MGP, MZ20 and MZ30 had a significantly lower adsorption capacity. Moreover, when zeolites were tested for CO and H_2 adsorption at 25 °C, Kim & Kim (2023) found that the zeolite NaY had an adsorption capacity of 1.10 mmol/g for CO and 0.02 for H_2, while the zeolite NaX had an adsorption of 1.12 and 0.02 for CO and H_2, respectively. The value obtained for the CO was more than the obtained in this study and lower than this study for the H_2 adsorption.

Table 28. Freundlich model parameters applied to the sample's equilibrium data.

Gas	**Sample**	**Freundlich Model**		
		K_F (mmHg)	**n**	**R^2**
CO_2	MGP	7.088×10^{-4}	1.035	0.999
	MZ	9.437×10^{-4}	1.019	0.999
	MZ20	9.258×10^{-4}	1.219	0.999
	MZ30	0.396×10^{-3}	1.324	0.999
CO	**MGP**	**1.798** $\times 10^{-4}$	**1.172**	**0.998**
	MZ20	**2.015** $\times 10^{-4}$	**1.177**	**0.998**
	MZ30	**2.473** $\times 10^{-4}$	**1.148**	**0.999**

H_2	MGP	6.856×10^{-4}	1.022	0.994
	MZ	6.101×10^{-4}	1.182	0.994
	MZ20	1.066×10^{-4}	1.058	0.996
	MZ30	1.414×10^{-4}	1.049	0.998

9.3 PARTIAL CONCLUSIONS

In this study, polymeric mats were developed with PVA and geopolymer, zeolite, or geopolymer/zeolite composite by applying the electrospinning technique. The geopolymer samples were synthesized using metakaolin-phosphate waste, and the solutions were prepared by mixing ethanol 8 wt% of PVA with 1wt% of the powder (zeolite, geopolymer, Z20 or Z30)

The samples were examined by some characterization techniques, such as surface area, porosity, FITR-ATR, XPS, and SEM. The FTIR analysis did not show considerably reactive material in all the samples, and the XPS did not show the presence of the solid components in the samples, which can be justified by the low concentration of these in the samples. Overall, the samples presented very similar characteristics.

The CO_2 adsorption capacity obtained through the isotherms reached 0.62, 0.43, 0.21, and 0.62 mmol/g at 30°C, for the MZ, MGP, MZ20, and MZ30 samples, respectively. For CO and H_2 adsorption the samples presented a very low adsorption capacity, which is expected, since the objective is to use the material for CO_2 capture.

Results showing a low adsorption capacity were expected, considering that the concentration of zeolite, geopolymer and composite in the samples is very low compared to the amount commonly used in CO_2 adsorption. However, it was the highest concentration accepted by the equipment using the presented synthesis methodology. Therefore, for application in gas capture and separation, more studies need to be developed, and the methodology improved.

10 PHOSPHATE-WASTE BASED GEOPOLYMER/ZEOLITE 13X COMPOSITES MANUFACTURED BY 3D PRINTING FOR GAS CAPTURE AND SEPARATION

This section refers to part of the manuscript entitled "Phosphate-waste based geopolymer/zeolite 13x composites manufactured by 3D printing for gas capture and separation" that will be submitted for publishing. This topic brings in the materials and procedures applied to prepare the materials, as well as their characterization results and discussion.

10.1 MATERIALS AND METHODS

Kaolin was obtained from Caulisa (Pernambuco, Brazil); phosphate mining tailings waste (PW) was provided by a mine in Goiás (Brazil); sodium hydroxide (NaOH – micro-pearls with 97 % purity) was acquired from Neon, sodium silicate solution (SS) – SiO_2/Na_2O (ratio SiO_2/Na_2O: 2.5) and the zeolite 13X type (particle size ~2 μm) were purchased from Sigma-Aldrich.

The geopolymer was synthesized based on Freire et al. (2024) and previous work Schneider et al. (2025). Metakaolin and phosphate wastes were used as precursors and a mixture of sodium hydroxide and sodium silicate as alkaline activators. The addition of zeolite to the geopolymeric matrix was based on Minelli et al. (2018), and Papa et al. (2018, 2023).

For the synthesis, firstly, kaolin was calcined at 900 ºC for 60 min to obtain metakaolin. The choice of molar ratios for the geopolymer's synthesis was $SiO_2:Al_2O_3 = 3.30$; $Na_2O:SiO_2 = 0.30$; $Na_2O:Al_2O_3 = 0.99$; and $H_2O:Na_2O = 12.00$, based on a study developed by Davidovits et al. (1994).

The composites were prepared as follows. First, kaolin and PW were mixed at 1500 rpm for 15 min on a mechanical stirrer, and while mixing the solid components, the alkaline solution was prepared by mixing the NaOH, sodium silicate (SS), and deionized water (DIW) at 800

rpm for 10 min on a magnetic stirrer. Then, the geopolymer slurry was prepared by adding the alkaline activator solution to the solid components and mixing for 30 min at 1500 rpm. Then, the amount of zeolite was added to the slurry and mixed at 1000 rpm for 30 min more. The Free CAD and Slicer systems were used to design the samples, which were the dimensions of 4,5 x 2 x 1, and the extrusion was carried out using a noodle with diameter of 1.6 mm.

After printing, the composites were placed in a watch glass and closed with a high temperature tape so that the water would slowly evaporate. The curing process was carried out in a laboratory oven at 80 °C for 24 h. After curing, the samples were submerged into DIW at room temperature (25 ºC ± 2 ºC) for 30 days to remove unreacted sodium ions. Finally, the submersed material was dried in an oven at 100 °C for 24 h. Then, the samples were sanded to obtain the necessary dimensions of 4 cm x 0.4 cm for analysis. Three different samples were prepared, and the compositions are described in Table 29.

Table 29. Composition of precursor materials and zeolite in the composite samples.

	Composition (wt %)					
Sample	**MK**	**PW**	**NaOH**	**SS**	**Water**	**Z13x**
C5	35.0	19.0	11.0	13.0	22.0	5
C20	35.0	19.0	11.0	13.0	22.0	20
C40	35.0	19.0	11.0	13.0	22.0	40

10.2 CHARACTERIZATION

The crystalline structure and mineralogical composition of the samples were evaluated by X-ray powder diffraction (XRPD), to know the crystalline phases present in the materials the X'pert HighScore plus software was used. To evaluate the chemical stability of the samples to CO_2 attack, the XRD analyses were performed to investigate the samples before and after exposition to CO_2. The analysis was performed using a PANanalytical EMPYREAN automated

diffractometer. Powder patterns were recorded in the Bragg-Brentano reflection configuration using the PIXcel 3D detector with a step size of 0.017 º (2θ). The powder patterns were recorded between 4 and 70 in 2θ with a total measuring time of 30 min.

The specific surface area, pore size, and total pore volume were determined through nitrogen adsorption-desorption isotherms at -196 ºC. The analysis was carried out using Micromeritics ASAP 2020 equipment.

Scanning electron microscopy (SEM) was used to study the morphology of materials and to determine the chemical analysis. It permits the identification of the components of the material and the analysis of the inner structure of the samples, like the crystal structure, morphology, and stress state information. The equipment used was a FESEM TESCAN CLARA microscope, with a LEICA EM ACE600 metallizer. The samples were coated with 4 nm of platinum, to make it more conductive for a better analysis.

X-Ray Fluorescence (XRF) was used to determine the chemical composition and to quantify oxides, using a Thermo Fisher Scientific equipment. The density of the samples was evaluated using a pycnometer with helium gas, in a chamber with 1.0 cm^3 at 23 ºC with an equilibration rate of 0.0050 psig/min.

Fourier-Transform Infrared Spectroscopy (FTIR) was used to identify the functional groups and chemical bonds present on the surface of the samples. The analysis was performed on a spectrometer model 6800FV from Jasco Analitica. The measurements were made by total attenuated reflectance using the ATR ProOne accessory and making a blank in the air, without the need to disperse or treat the sample. For the acquisition of spectra, a standard spectral resolution of 4 cm-1 was used in the spectral range of 4000-400 cm^{-1}, as well as 64 accumulations per sample.

For the 3D X-ray micro-computed tomography (m-CT) analysis, the samples were scanned employing a SkyScan 2214 (Bruker) system. Projections were obtained using a W source filament and a CDD3 detector. This source was set to 80 kV and 110 μA. The CCD3 detector was set with a source-to-detector distance of 315.449 mm and a source-to-sample distance of 36.204 mm which yielded a voxel size of 2. All scans were acquired over 360° (0.2° rotation step) using an exposure time of 1.8 s. From the micro-CT measurement, a series of projections were obtained, which were used for the 3D reconstruction of the sample, which were carried out using post-alignment to reduce sample movement and a 40% correction for beam hardening, and the porosity analysis of the samples was performed using the CTAn software (Bruker).

The ^{29}Si and ^{27}Al MAS-NMR spectra were recorded using a High-Definition Nuclear Magnetic Resonance Spectrometer, Bruker model AVIIIIHD 600, narrow bore with a magnetic field of 14.09 Tesla, at 156.4 MHz (Al frequency) and 119.2 MHz (Si frequency) with a probe 4mm dual-resonance CPMAS using zirconia rotors at slew rates of 13KHz. Experiments with ^{27}Al were performed with proton decoupling (continuous wave sequence) by applying a single pulse ($\pi/18$), an excitation pulse of 0.7 μs, and a relaxation delay of 1 s to obtain 1000 scans. Chemical shifts were referenced to an external 1 M of $Al(NO_3)_3$ solution. Experiments with ^{29}Si were also performed with proton decoupling (continuous wave sequence) by applying a single pulse ($\pi/2$), an excitation pulse of 8.5 μs, and a relaxation delay of 60 s to obtain 1000 scans. Chemical changes were referenced with an external solution of tetramethylsilane (TMS).

X-Ray Photoelectron Spectroscopy (XPS) determined the samples' surface chemistry. The spectra were recorded on a Physical Electronic spectrometer (PHI Versa Probe II) using monochromatic Al Kα radiation (15 kV, 1486.6 eV), a dual beam charge neutralizer for analyzing the core-level signals of the elements of interest, and a hemispherical multichannel

detector. The sample spectra were recorded with a constant pass energy value of 29.35 eV, 0.125 eV/step, and a beam diameter of 200 µm. The energy scale was calibrated using Cu $2p_{3/2}$, Ag $3d_{5/2}$, and Au $4f_{7/2}$ photoelectron lines at 932.7, 368.2, and 83.95 eV, respectively. Atomic concentration percentages of the characteristic elements were determined considering the corresponding area sensitivity factor for the different measured spectral regions. The Multipak 9.6 software was used for acquisition and data analysis. A Shirley-type background was subtracted from the signals. Recorded spectra were always fitted using Gaussian–Lorentzian curves to determine the binding energy of the different element core levels more accurately.

10.3 RESULTS AND DISCUSSION

10.3.1 Chemical Composition

The chemical composition of the composites, analyzed through XRF (Table 30) presented Silica (SiO_2), alumina (Al_2O_3) and sodium oxide (Na_2O) as main components. However, there is a considerable amount of iron (Fe_2O_3) and titanium (TiO_2) oxide, and a small amount of calcium (CaO) and phosphate (P_2O_5) oxides. The oxides present in the samples are in accordance with the precursors analysis (metakaolin and phosphate mining tailings) carried out by Freire et al. (2020), which belong to the same batch of those used in this work.

Table 30. Total oxide composition (wt %)of samples Z13X, GP, and composites

Compound	C5	C20	C40
SiO_2	40.99±0.37	39.75±0.37	39.46±0.37
Al_2O_3	21.17±0.17	22.42±0.18	23.17±0.18
Na_2O	11.85±0.36	12.09±0.36	12.95±0.37
Fe_2O_3	8.70±0.20	7.12±0.18	5.69±0.16
TiO_2	3.56±0.03	2.94±0.02	2.30 ±0.02
CaO	1.01±0.07	0.82±0.06	0.62±0.04

P_2O_5	1.06±0.04	0.93±0.04	0.74±0.03
MgO	0.30±0.03	0.23±0.03	0.15±0.03
K_2O	0.45±0.04	0.38±0.03	0.31±0.02
MnO	0.34±0.01	0.28±0.01	0.22±0.01
ZnO	0.01±0.01	-	-
CuO	0.04±0.01	0.38±0.01	0.37±0.01
ZrO_2	0.30±0.01	0.25±0.01	0.19±0.01
Nb_2O_5	0.20±0.01	0.15±0.01	0.15±0.01
Nd_2O_3	0.07±0.01	0.06±0.01	0.11±0.01
NiO	0.03±0.01	0.02±0.01	0.02±0.01
V_2O_5	0.02±0.01	0.02±0.01	0.02±0.01
Cl	0.02±0.01	0.03±0.01	0.03±0.01
SO_3	0.02±0.01	-	-
Cr_2O_3	0.01±0.01	0.01±0.01	-
LOI	9.55	12.11	13.57

10.3.2 Surface area, Porosity and density

There are some important characteristics for adsorbent materials, like density, surface area, and pore volume (Table 31). The total pore volume and surface area of C40 are higher than those of C20 and C5, and the surface area increases as the zeolite content in the formulation increases. The surface area values for geopolymer/zeolite are very close to the ones obtained by Minelli et al. (2018), and Candamano et al. (2022), which were 211 and 343 m^2/g, respectively, and lower than those reported by Han et al. (2022), which was 579 m^2/g. The density of the samples (Table 31) is comparable and decreases as the surface area volume increases, which is expected and agrees with the results obtained by Candamano et al. (2022) for zeolite/geopolymer composites.

However, for the C20 sample, the specific surface area increases like the other composites, but a decrease can be noted in total pore volume and pore size. This decrease is

related to the increase in density. The same pattern occurs with the powder geopolymer/ zeolite composites developed in a previous work Schneider et al. (2025), and his behavior can be explained by the complexities of the geopolymerization process when involving the addiction of zeolite, which cannot be fully understood, as the exact mechanism involves four main stages, where two of them are challenging to control or analyze. (Panagiotopoulou *et al.*, 2007).

Table 31. Surface area, pore volume and size, density, and quantification of porosity using micro-CT analysis.

	C5	**C20**	**C40**
Langmuir surface area (m^2/g)	53	203	384
Total pore volume (cm^3/g)	0.017	0.063	0.118
BJH pore size (Å)	118.9	35.0	78.5
Density (g/cm^3)	2.38	2.27	2.18
Open porosity (vol %)	1.03	0.76	0.31
Closed porosity (vol %)	2.96	3.60	2.29

Open porosity (void space), closed porosity (pores, trapped bubbles) and total porosity, evaluated by mCT, are presented in Table 31. And in Figure 77, the reconstruction (left), reconstitution with pores (center), and porosity (right) of the C5 (a), C20 (b), and C40 (c) samples are presented. The C40 sample presented low open porosity and closed porosity. The higher volume of open porosity and closed was obtained with the C20 and C5 composites, respectively. The composite C5 has higher total pore volume compared to the other samples, while the C20 and C40 seem to have less and larger pores (Figure 1 a, b, c (right)). To date, no studies were found in the literature about mCT of geopolymer and zeolite composites, except for a previous work, so comparing these composites samples with the ones produced in a preview study (geopolymer composites with 5, 20 and 30% of zeolite) (Schneider *et al.*, 2025), they exhibit the same pattern, increasing the closed porosity and decreasing the open porosity.

Moreover, the closed porosity of the samples is like the ones obtained by Kovářík et al. (2021) for geopolymers. However, the open porosity is much lower, as expected, given that their materials are geopolymer-based ceramic foams, which have visibly higher open porosity.

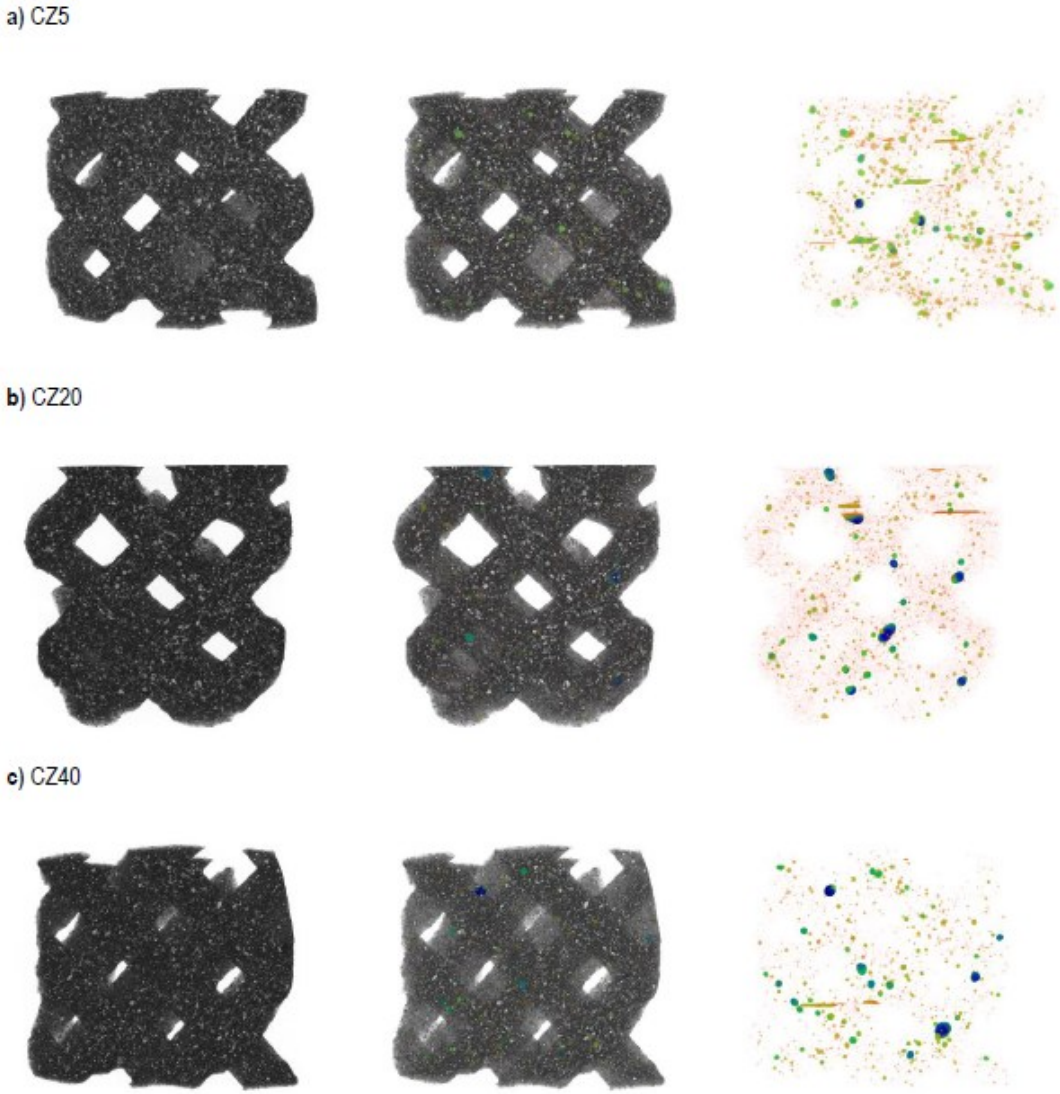

Figure 77. 3D reconstruction (left), visualization with pores (center), and porosity (right) of the C5 (a), C20 (b), and C40 (c) samples.

10.3.3 Mineralogical Composition and Crystallinity

The composites containing geopolymer and zeolite presented high crystallinity even though the composite with lower amount of zeolite (Figure 78). The peaks were identified as quartz (SiO_2 ICDD 01-086-1628), and Faujasite ($Na_2Al_2Si_{2.4}O_{8.8}\cdot 6.7H_2O$ – ICDD 00-012-

0246). The main difference is in the intensity of the peaks. An increase in the intensity of the main Faujasite peak can be observed by approximately 8º as the amount of zeolite increases, which is expected since the base of the composites is the geopolymer, which is mainly amorphous.

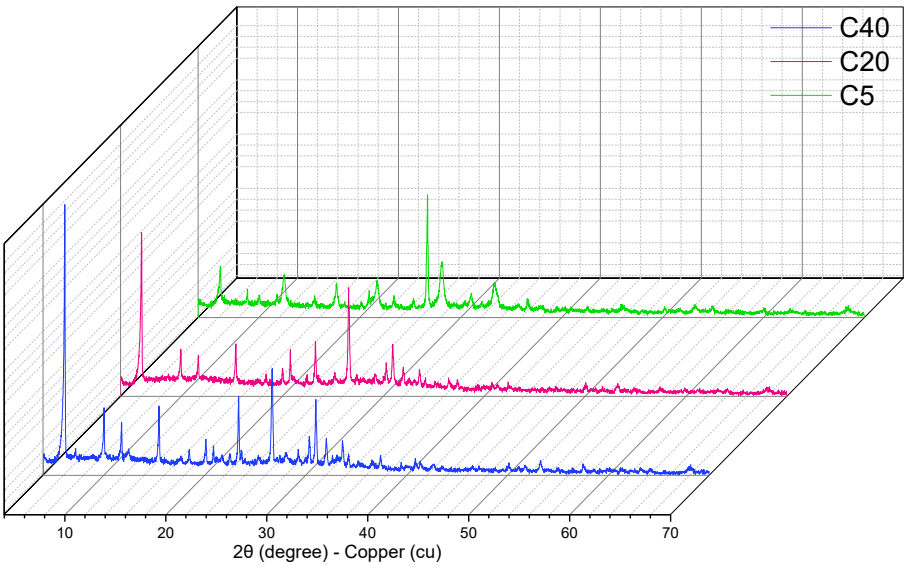

Figure 78. XRD pattern of the composite samples

10.3.4 Chemical Analysis and Morphology

Through the SEM images of the composite samples (Figure 79, 80 and 81), it is possible to note the dense, homogeneous and amorphous structure of the geopolymer, and by increasing the amount of zeolite in the composite it is possible to notice an increase in the crystalline materials on the sample. Different from the C20 and C40 samples, the C5 sample presented some cracks, which may be related to the fact that the image was taken from the area where the material was sliced, and in the surface of the samples .

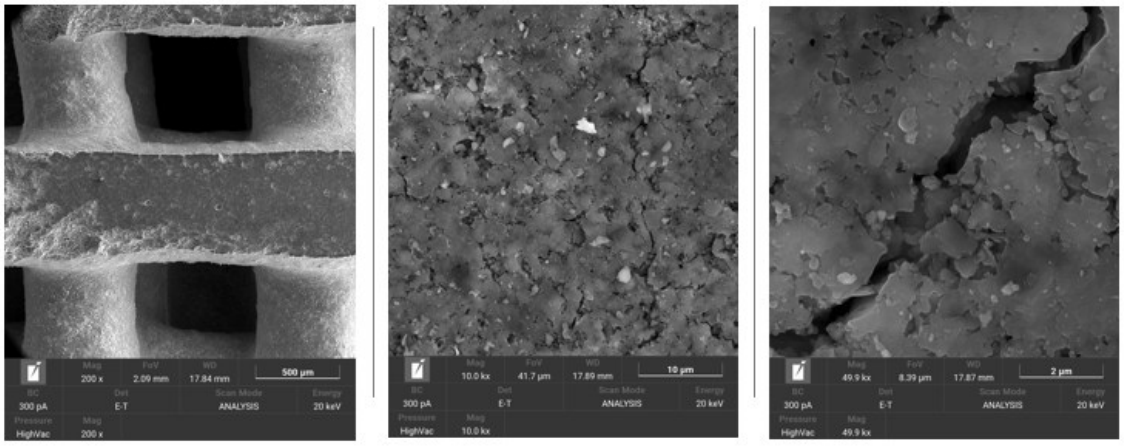

Figure 79. SEM images of the C5 sample.

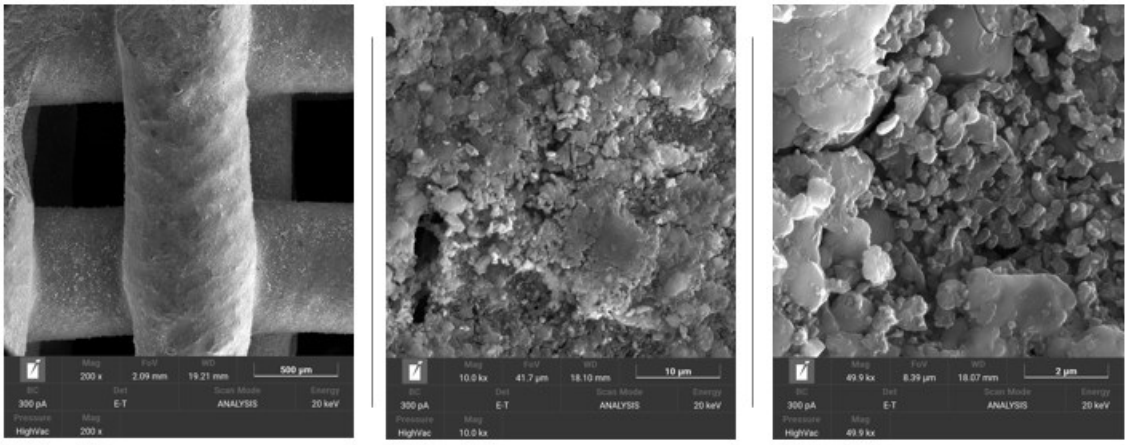

Figure 80. SEM images of the C20 sample.

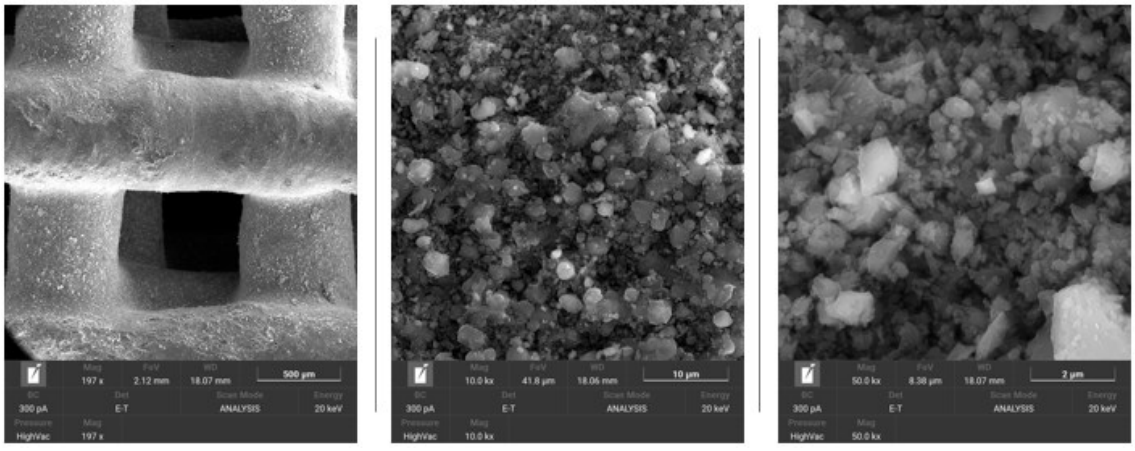

Figure 81. SEM images of the C40 sample.

Nuclear magnetic resonance (NMR) spectroscopy was employed to examine both the structural units of the samples and their porous characteristics. Solid-state NMR spectroscopy

is a valuable method for analyzing geopolymeric materials, as it supplies information about the coordination state of alumina units within the structure of precursor materials and geopolymers, which consequently indicates their reactivity (Freire et al., 2020). The ^{27}Al MAS-NMR spectra of the samples (Figure 83), are very similar. All the samples presented a peak at approximately 63 ppm, which corresponds to the presence of tetrahedral aluminum Al(IV) on the sample (Freire *et al.*, 2025), and a small peak at ~ -20 ppm, which correspond to Al(VI), octahedral aluminum. These peaks can be related to the zeolite, since the XRD analysis showed that the samples exhibited crystalline peaks associated with Faujasite. The absence of sharp octahedral and penta-coordinated aluminum peaks confirms that the geopolymerization process is complete (Nasab, Golestanifard and MacKenzie, 2014; Petlitckaia *et al.*, 2020; Archez *et al.*, 2021; Revathi and Jeyalakshmi, 2021).

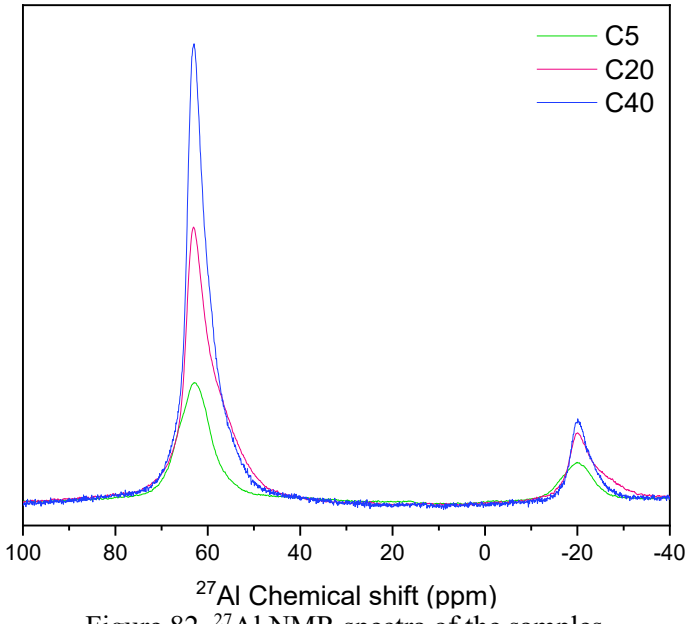

Figure 82. ^{27}Al NMR spectra of the samples.

For all samples the ^{29}Si spectra presents 5 significant peaks (Figure 84). The composites were very similar, differing in the intensity of the peaks as the concentration of zeolite increases. Through the spectra, it is possible to identify the chemical shifts of the different framework

silicon Q^4 environments, Q^4(0Al) at -107 ppm, Q^4(1Al) at -98 ppm, Q^4(2Al) at -94 ppm, Q^4(3Al) at -89 ppm, Q^4(4 Al) at -84 ppm (Gore *et al.*, 2002; Greiser, Hunger and Jäger, 2016). The presence of these peaks on the samples confirms the presence of aluminosilicate, by alternating between silica and alumina tetrahedra (Gore *et al.*, 2002; Nasab, Golestanifard and MacKenzie, 2014; Greiser, Hunger and Jäger, 2016; Gao, Yu and Brouwers, 2017; Paiva *et al.*, 2018).

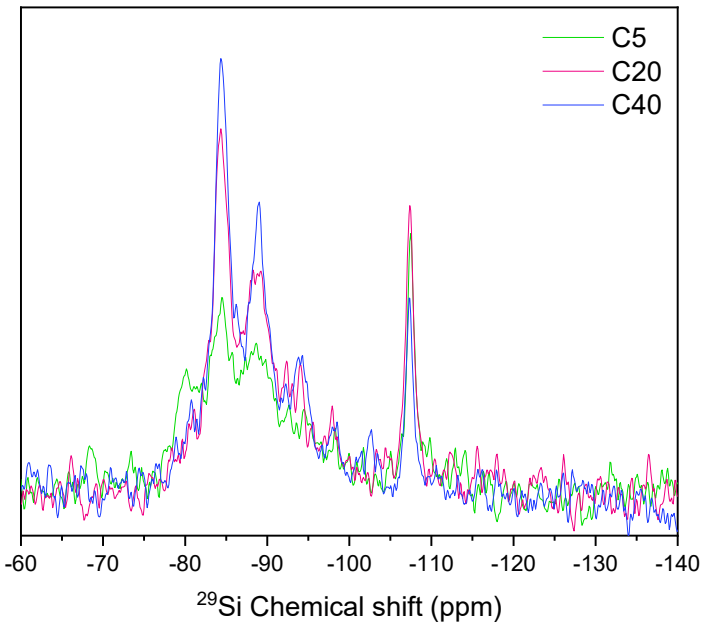

Figure 83. 29Si NMR spectra of the samples.

The FTIR-ATR analysis (Figure 85) confirms the presence of characteristic bands related to aluminosilicate materials in the samples. The bands between the region from 4000 to 2600 cm^{-1}, are attributed to the Si-OH, OH and Si-OH-Al bands, and are characterized by a stretching vibration. The bands at 3400 and 1640 cm^{-1} refer to the stretching ν(OH) and bending δ(HOH) of H_2O vibrations (Minelli *et al.*, 2018).

The overlapping bands between 1200 and 400 cm^{-1} are due to the crystalline and amorphous precursor structures of Z13X and the geopolymer, respectively (Minelli *et al.*,

2018). The bands between 1200 and 900 cm^{-1} are characteristics of aluminosilicate materials, which correspond to the asymmetric stretching vibration of Si-O-T type structures, where T is Si or Al (Kljajević *et al.*, 2017). Peaks at ~980 cm^{-1} represent the symmetric stretching vibration of Si-O bonds and are identified in all sample spectra (Papa *et al.*, 2023). The bands from 800 to 500 cm^{-1} is characteristic of symmetrical Si-O-Si vibrations, and the bands between 750 and 554 cm^{-1} correspond to the vibrational bands of zeolitic materials, in this case, the Faujasite, zeolite 13X type (Jiménez, Lalangui, Guacho, Paucar, *et al.*, 2019).

The absence of bands around the 1400 cm^{-1} region of samples confirms that there is no formation of carbonates for Na^{+}-based materials. This is an important parameter to analyze since the presence of carbonates on geopolymer samples can cause losses in the chemical and physical properties of the materials (Król, Minkiewicz and Mozgawa, 2016; Rajini, Narasimha Rao and Sashidhar, 2021).

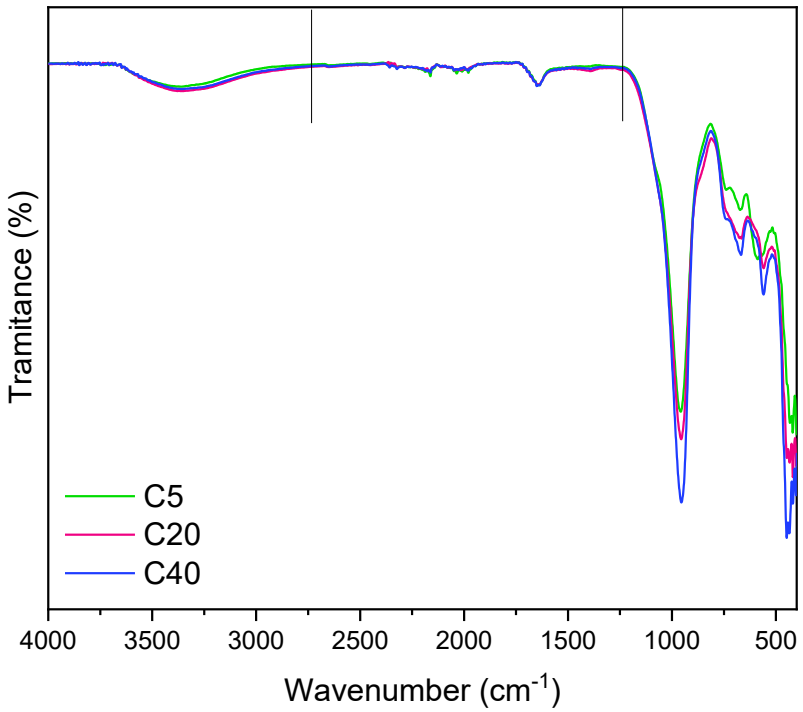

Figure 84. FTIR-ART spectra of the samples.

The XPS analysis was performed to determine the chemical states and atomic composition of the sample's particles' surface. The peak identification was mainly based on the Moulder et al. (1992) , and Wagner et al. (1979). Generally, the sample spectra are very similar, since they all are aluminosilicates, with variations mainly in peak intensity, atomic concentrations, and weight.

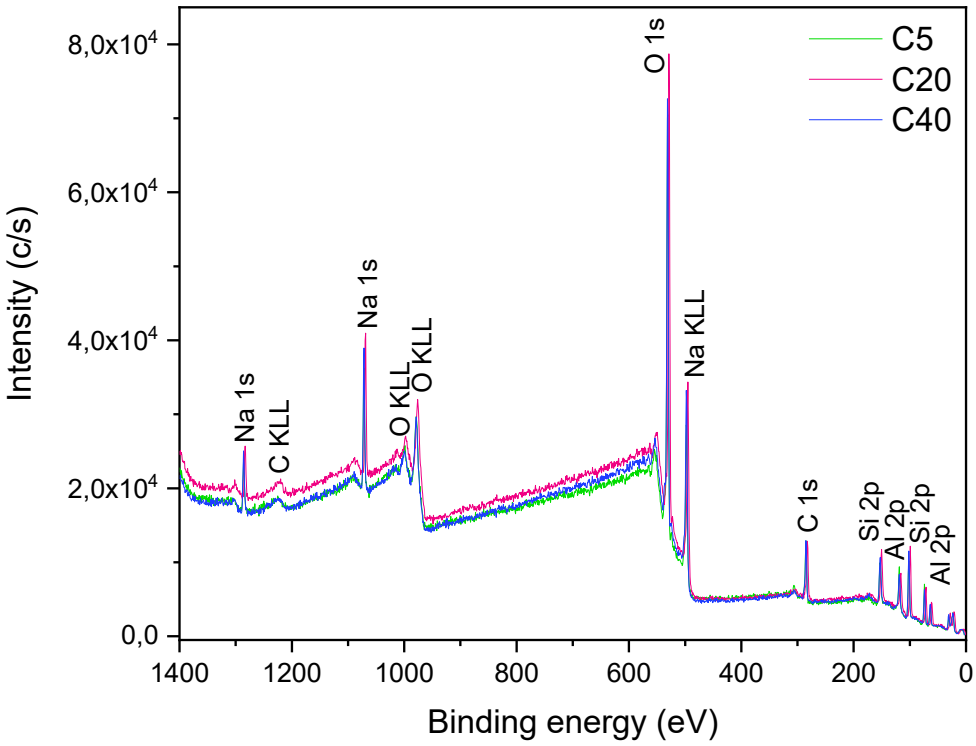

Figure 85. XPS spectra of the composite samples

The XPS spectra of the composite samples are presented in Figure 86, with Figures 87, 88, 89, and 90 showing the decomposed atom electron orbitals spectra. In general, the four spectra are highly similar. The binding energy differences are minimal, with the largest variation being just 0.3 eV.

The C 1*s* core level spectra of all samples were deconvoluted into three distinct contributions at high resolution: the contribution at ~284.8 eV, which is correspondent to

adventitious carbon (contamination), C-C, and/or C=C groups; the contribution at ~286.3 eV is related to the C-OH and C-O-C groups; and the contribution at ~288.7 eV is characteristic of the carbonate group.

The O 1*s* spectra were deconvoluted in two contributions: at 531.1 eV corresponds to the O-H that can be assigned to water, and/or the C-OH group; and the at 532.4 eV is related to the Si-O group. Finally, the Na 1*s,* Si 2*p* and Al 2*p* spectra presented peaks at 1072.0 eV, 102.1 and 74.1 eV, respectively, which are characteristic of sodium aluminosilicate. The area of the peaks, atomic concentrations, and weight are reported in Table 32 and in Table 33 are presented the quantification of the deconvoluted peaks from the high-resolution spectra.

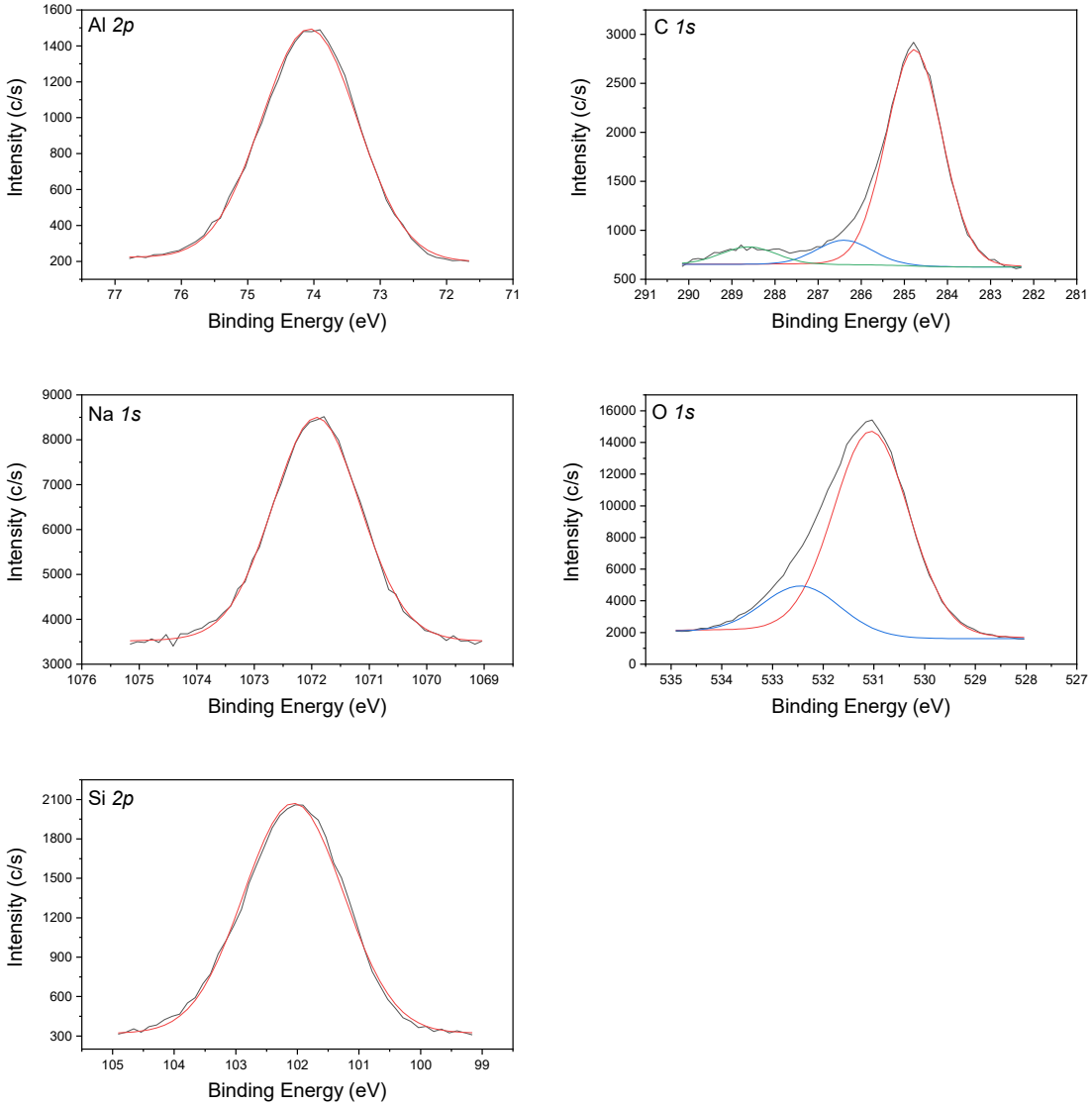

Figure 86. Deconvolution spectra of the C5 sample.

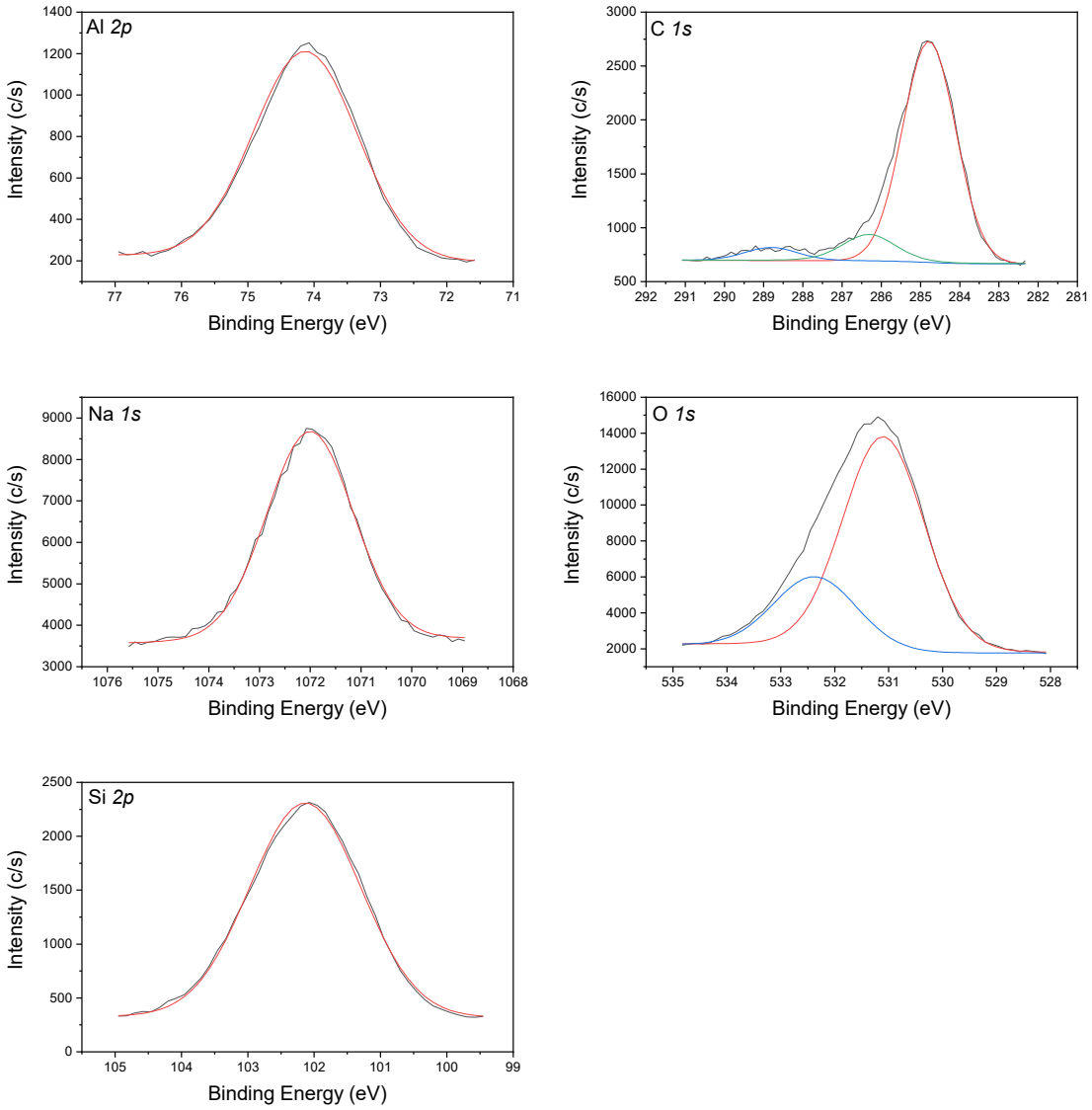

Figure 87. Deconvolution spectra of the C20 sample.

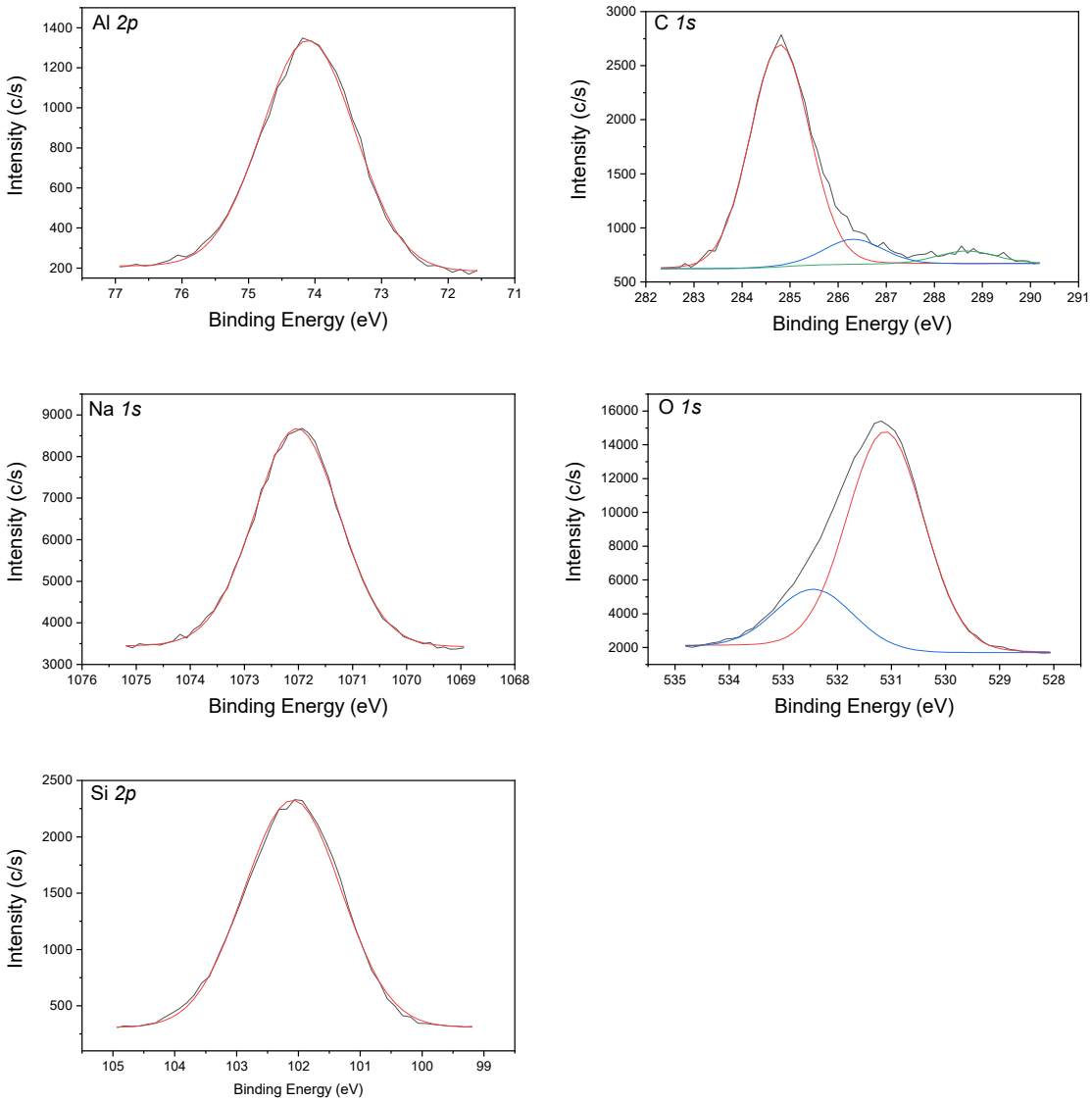

Figure 88. Deconvolution spectra of the C40 sample.

Table 32. XPS high resolution spectra quantification, atomic concentration, and weight of the samples.

	C5		**C20**		**C40**	
	Atomic c. (%)	**Weight (%)**	**Atomic c. (%)**	**Weight (%)**	**Atomic c. (%)**	**Weight (%)**
C *1s*	17.80	11.57	16.68	10.76	16.02	10.29
O *1s*	50.53	43.73	50.51	43.39	50.67	43.32
Na *1s*	10.07	12.52	11.36	14.03	11.21	13.76
Si *2p*	11.17	16.96	12.53	18.90	12.79	19.20
Al *2p*	10.43	15.21	8.92	12.93	9.31	13.42

Table 33. XPS quantification of the deconvoluted peaks.

	C5			C20			C40		
C 1*s*	284.8 eV 83.42	286.4 eV 9.68	288.6 eV 6.87	284.8 eV 83.81	286.4 eV 10.99	288.6 eV 5.20	284.8 eV 84.85	286.3 eV 10.02	288.7 eV 5.13
O 1*s*	531.1 eV 82.12	532.4 eV 17.88	-	531.1 eV 75.89	532.4 eV 24.11	-	531.1 eV 79.51	532.4 eV 20.49	-
Na 1*s*	1071.9 eV 100	-	-	1072.0 eV 100	-	-	1072.0 eV 100	-	-
Si 2*p*	102.1 eV 100	-	-	102.1 eV 100	-	-	102.1 eV 100	-	-
Al 2*p*	74.1 eV 100		-	74.1 eV 100		-	74.1 eV 100		-

10.4 PARTIAL CONCLUSIONS

The 3D-printed geopolymer/zeolite 13X composites presented a stable structure with porous materials suitable for CO_2 capture. Porosity analysis showed that total pore volume and surface area increased with zeolite content, while open porosity decreased, indicating a denser microstructure at higher loadings. SEM images confirmed the successful incorporation of zeolite into the geopolymer matrix, with more defined crystalline phases appearing as zeolite content increased.

Moreover, XPS analysis revealed consistent chemical composition across samples and confirmed the presence of sodium aluminosilicate bonds, with minimal carbonate formation, suggesting good chemical stability. Among the evaluated properties, the surface area was identified as the main factor influencing adsorption capacity, increasing proportionally with the zeolite content.

Overall, the combination of additive manufacturing, sustainable raw materials, and favorable adsorption properties positions these geopolymer/zeolite composites as promising candidates for efficient, low-cost, and eco-friendly CO_2 separation technologies.

11 FINAL REMARKS AND PERSPECTIVES

Zeolites have been extensively studied in CO_2 separation due to their crystalline and microporous structures, high surface area, thermal stability, and adsorption selectivity. Geopolymeric materials have gained relevant research interest in recent years, for application in gas capture, mainly due to their low-cost and eco-friendly synthesis and properties like mechanical and chemical resistance and thermal stability. Moreover, recent studies about the production of geopolymer/zeolite composites presented successful results for CO_2 capture and separation.

Curing temperature and method were shown to significantly influence the performance of phosphate waste-based geopolymers. Submerged curing led to higher reactivity and CO_2 adsorption capacity, and curing at 80 °C resulted in better performance than curing at 65 °C. These findings emphasize the relevance of both thermal conditions and post-curing treatments in improving the efficiency of geopolymers for gas capture applications. The four samples had a significant amount of reactive material, as revealed by the FTIR and NMR analyses. Overall, the two submersed samples had very similar characteristics, as well as the two without the submersed cure samples. However, for the G80s, G65s, G65, and G80 samples, the CO_2 adsorption capacity determined by the isotherms was 2.24, 2.00, 1.42, and 0.88 mmol/g at 30 °C, respectively, and this capacity decreased as the temperature increased. The results support the significance of the submerged cure during the synthesis of the geopolymer. In terms of temperature, the geopolymer cured at 80 ºC had a higher adsorption than the sample cured at 65 ºC, although both submerged samples had very similar properties.

Geopolymer/zeolite composite samples were also synthesized to evaluate their potential for CO_2 capture. These samples were analyzed using a variety of characterization methods and the samples showed a lot of similarities in their overall characteristics. The composite samples with higher zeolite content presented the best results, which was expected since the zeolite indeed have higher adsorption capacity than the geopolymer. The characteristics of the composite samples are very alike. However, the only characteristic that seems to influence directly the adsorption capacity is the surface area, since it increases as the amount of zeolite. For the Z13X, Z30, Z20, GP, Z10, and Z5 samples, the CO_2 adsorption capacity determined by the equilibrium isotherms was 3.98, 2.57, 2.57, 2.00, 1.96, and 1.65 mmol/g at 30 °C, respectively. As expected, the materials showed negligible adsorption for CO and H_2,

reinforcing their selectivity for CO_2 and highlighting the viability of these composites as low-cost, sustainable materials for carbon capture.

In further development, electrospinning was explored as a technique for producing polymer-based membranes with embedded zeolite and geopolymer particles. So, four polymeric membranes were developed applying the electrospinning technique. The samples were characterized by surface area, porosity, FITR-ATR, XPS, and SEM. Overall, the samples presented very similar characteristics. The FTIR and XPS analysis did not show considerably reactive material in all the samples which can be justified by the low concentration of aluminosilicates on the sample. The CO_2 adsorption capacity obtained through the isotherms reached 0.62, 0.43, 0.21, and 0.62 mmol/g at 30°C, for the MZ, MGP, MZ20, and MZ30 samples, respectively. Results showing a low adsorption capacity were expected, considering that the concentration of zeolite, geopolymer, and composite in the samples is very low compared to the amount commonly used in CO_2 adsorption. However, it was the highest concentration accepted by the equipment using the presented synthesis methodology. Therefore, for application in gas capture and separation, more studies need to be developed, and the methodology improved.

Lastly, 3D-printed geopolymer/zeolite 13X composites exhibited stable structures with interconnected porosity suitable for CO_2 adsorption. Porosity measurements showed that total pore volume and surface area increased with zeolite content, while open porosity decreased, suggesting a denser microstructure at higher zeolite loadings. SEM imaging confirmed successful zeolite incorporation, with more prominent crystalline features appearing as the zeolite content increases. XPS analysis revealed consistent chemical composition across the samples, indicating good chemical stability. Among all analyzed properties, surface area emerged as the main factor influencing CO_2 uptake. These findings demonstrate the potential of combining additive manufacturing with sustainable raw materials to create efficient, eco-friendly, and cost-effective materials for CO_2 separation technologies.

Overall, this study reinforces the suitability of geopolymer and zeolite-based materials for CO_2 capture and separation applications. The results demonstrate that adjusting synthesis parameters such as curing temperature, composition, and the use of additive manufacturing methods like 3D printing can enhance material performance. The use of accessible and low-cost raw materials, along with favorable adsorption and structural properties, makes these composites strong candidates for developing sustainable and scalable carbon capture technologies. Further investigation and refinement of these systems could improve their efficiency and expand their potential in practical applications.

12 REFERENCES

Ahmed, R. *et al.* (2020) 'Recent advances in carbon-based renewable adsorbent for selective carbon dioxide capture and separation-A review', *Journal of Cleaner Production*. Elsevier Ltd. Available at: https://doi.org/10.1016/j.jclepro.2019.118409.

Akarken, G. and Cengiz, U. (2023) 'Fabrication and characterization of metakaolin-based fiber reinforced fire resistant geopolymer', *Applied Clay Science*, 232. Available at: https://doi.org/10.1016/j.clay.2022.106786.

Akhtar, F. *et al.* (2014) 'Structuring adsorbents and catalysts by processing of porous powders', *Journal of the European Ceramic Society*, 34(7), pp. 1643–1666. Available at: https://doi.org/10.1016/j.jeurceramsoc.2014.01.008.

Alothman, Z.A. (2012) 'A review: Fundamental aspects of silicate mesoporous materials', *Materials*, pp. 2874–2902. Available at: https://doi.org/10.3390/ma5122874.

Alp-Erbay, E. *et al.* (2019) 'The impact of electrospun films of poly(ε-caprolactone) filled with nanostructured zeolite and silica microparticles on in vitro histamine formation by Staphylococcus aureus and Salmonella Paratyphi A', *Food Packaging and Shelf Life*, 22. Available at: https://doi.org/10.1016/j.fpsl.2019.100414.

Anis, S.F. *et al.* (2016) 'A review on the fabrication of zeolite and mesoporous inorganic nanofibers formation for catalytic applications', *Microporous and Mesoporous Materials*. Elsevier B.V., pp. 176–192. Available at: https://doi.org/10.1016/j.micromeso.2016.08.043.

Anis, S.F. and Hashaikeh, R. (2016) 'Electrospun zeolite-Y fibers: Fabrication and morphology analysis', *Microporous and Mesoporous Materials*, 233, pp. 78–86. Available at: https://doi.org/10.1016/j.micromeso.2015.11.022.

Anis, S.F., Hashaikeh, R. and Hilal, N. (2019) 'Flux and salt rejection enhancement of polyvinyl(alcohol) reverse osmosis membranes using nano-zeolite', *Desalination*, 470. Available at: https://doi.org/10.1016/j.desal.2019.114104.

Archez, J. *et al.* (2021) 'Geopolymer local network evolution under time and temperature', *Journal of Non-Crystalline Solids*, 566. Available at: https://doi.org/10.1016/j.jnoncrysol.2021.120870.

Asiri, A. *et al.* (2021) 'Epidermal and fibroblast growth factors incorporated polyvinyl alcohol electrospun nanofibers as biological dressing scaffold', *Scientific Reports*, 11(1). Available at: https://doi.org/10.1038/s41598-021-85149-x.

Assi, L.N. *et al.* (2020) 'Review of availability of source materials for geopolymer/sustainable concrete', *Journal of Cleaner Production*, 263, p. 121477. Available at: https://doi.org/10.1016/j.jclepro.2020.121477.

Ayawei, N., Ebelegi, A.N. and Wankasi, D. (2017) 'Modelling and Interpretation of Adsorption Isotherms', *Journal of Chemistry*. Hindawi Limited. Available at: https://doi.org/10.1155/2017/3039817.

Bahi, A. *et al.* (2017) 'Membranes based on electrospun lignin-zeolite composite nanofibers', *Separation and Purification Technology*, 187, pp. 207–213. Available at: https://doi.org/10.1016/j.seppur.2017.06.015.

Bedarf, P. *et al.* (2021) 'Foam 3D printing for construction: A review of applications, materials, and processes', *Automation in Construction*, 130, p. 103861. Available at: https://doi.org/10.1016/j.autcon.2021.103861.

Bong, S.H. *et al.* (2021) 'Ambient temperature cured "just-add-water" geopolymer for 3D concrete printing applications', *Cement and Concrete Composites*, 121, p. 104060. Available at: https://doi.org/10.1016/j.cemconcomp.2021.104060.

Bruker (2012) 'NMR Frequencies vs. Bruker Field Strengths'. Bruker.

Buchwald, A. *et al.* (2009) 'Geopolymeric binders with different fine fillers - Phase transformations at high temperatures', *Applied Clay Science*, 46(2), pp. 190–195. Available at: https://doi.org/10.1016/j.clay.2009.08.002.

Byrappa, K. and Yoshimura, M. (2013) 'Hydrothermal Synthesis and Growth of Zeolites', *Handbook of Hydrothermal Technology*, pp. 269–347. Available at: https://doi.org/10.1016/B978-0-12-375090-7.00006-2.

Calzado-Delgado, M., Guerrero-Pérez, M.O. and Yeung, K.L. (2022a) 'A new versatile x–y–z electrospinning equipment for nanofiber synthesis in both far and near field', *Scientific Reports*, 12(1). Available at: https://doi.org/10.1038/s41598-022-08310-0.

Calzado-Delgado, M., Guerrero-Pérez, M.O. and Yeung, K.L. (2022b) 'Dissolvable Topical Formulations for Burst and Constant Delivery of Vitamin C', *ACS Omega* [Preprint]. Available at: https://doi.org/10.1021/acsomega.2c06738.

Candamano, S. *et al.* (2022) 'Preparation of foamed and unfoamed geopolymer/NaX zeolite/activated carbon composites for CO2 adsorption', *Journal of Cleaner Production*, 330. Available at: https://doi.org/10.1016/j.jclepro.2021.129843.

Chan, W.H. *et al.* (2017) 'The development of low cost adsorbents from clay and waste materials: a review', *Journal of Material Cycles and Waste Management*, 19(1), pp. 1–14. Available at: https://doi.org/10.1007/s10163-015-0396-5.

Chang, R.W. *et al.* (2020) 'Enhanced cyclic CO2/N2 separation performance stability on chemically modified N-doped ordered mesoporous carbon', *Catalysis Today*, 356, pp. 88–94. Available at: https://doi.org/10.1016/j.cattod.2019.08.004.

Chaves Lima, R. *et al.* (2019) *Environmentally Friendly Zeolites:Synthesis and Source Materials*. Springer Cham (Engineering Materials). Available at: https://doi.org/10.1007/978-3-030-19970-8.

Chen, H. *et al.* (2020) 'Novel activated carbon route to low-cost geopolymer based porous composite with high mechanical resistance and enhanced CO2 capacity', *Microporous and Mesoporous Materials*, 305. Available at: https://doi.org/10.1016/j.micromeso.2020.110282.

Chen, H. *et al.* (2022) 'Robust structure regulation of geopolymer as novel efficient amine support to prepare high-efficiency CO2 capture solid sorbent', *Chemical Engineering Journal*, 427. Available at: https://doi.org/10.1016/j.cej.2021.131577.

Chougan, M. *et al.* (2020) 'The influence of nano-additives in strengthening mechanical performance of 3D printed multi-binder geopolymer composites', *Construction and Building Materials*, 250, p. 118928. Available at: https://doi.org/10.1016/j.conbuildmat.2020.118928.

Cooley, J.F. (1902) 'Apparatus for electrically dispersing fluids.' United States.

Cordero-Lanzac, T. *et al.* (2022) 'Binderless ZrO2/HZSM-5 fibrillar composites by electrospinning as catalysts for the dimethyl ether-to-olefins process', *Microporous and Mesoporous Materials*, 342. Available at: https://doi.org/10.1016/j.micromeso.2022.112102.

Couck, S. *et al.* (2017) 'CO2, CH4 and N2 separation with a 3DFD-printed ZSM-5 monolith', *Chemical Engineering Journal*, 308, pp. 719–726. Available at: https://doi.org/10.1016/j.cej.2016.09.046.

Cui, Y., Su, W., *et al.* (2023) 'Experimental and simulation evaluation of CO2/CO separation under different component ratios in blast furnace gas on zeolites', *Chemical Engineering Journal*, 472. Available at: https://doi.org/10.1016/j.cej.2023.144579.

Cui, Y., Xing, Y., *et al.* (2023) 'Insights into the adsorption performance and separation mechanisms for CO2 and CO on NaX and CaA zeolites by experiments and simulation', *Fuel*, 337. Available at: https://doi.org/10.1016/j.fuel.2022.127179.

Cundy, C.S. and Cox, P.A. (2005) 'The hydrothermal synthesis of zeolites: Precursors, intermediates and reaction mechanism', *Microporous and Mesoporous Materials*, 82(1–2), pp. 1–78. Available at: https://doi.org/10.1016/j.micromeso.2005.02.016.

Damideh, V. *et al.* (2020) 'Study of ozone concentration from CO2 decomposition in a water cooled coaxial dielectric barrier discharge', *Vacuum*, 177, p. 109370. Available at: https://doi.org/10.1016/j.vacuum.2020.109370.

Dantas, S. *et al.* (2019) 'Phase Behavior and Capillary Condensation Hysteresis of Carbon Dioxide in Mesopores', *Langmuir*, 35(35), pp. 11291–11298. Available at: https://doi.org/10.1021/acs.langmuir.9b01748.

Dantas, T.L.P. (2009) 'Separação de dióxido de carbono por adsorção a partir de misturas sintéticas do tipo gás de exaustão.', pp. 1–172.

Davidovits, J. (1994) 'Geopolymers: Man-made rock geosynthesis and the resulting development of very early high strength cement', *Journal of Materials Education*, 16(2 & 3), pp. 91–139. Available at: https://www.researchgate.net/publication/303244566_Geopolymers_Man-made_rock_geosynthesis_and_the_resulting_development_of_very_early_high_strength_cement (Accessed: 22 November 2023).

Davydov, V. *et al.* (2014) 'Solid state synthesis of carbon-encapsulated iron carbide nanoparticles and their interaction with living cells †'. Available at: https://doi.org/10.1039/c3ta21599g.

Douiri, H. *et al.* (2016) 'Water molecular dynamics of metakaolin and phosphoric acid-based geopolymers investigated by impedance spectroscopy and DSC/TGA', *Journal of Non-Crystalline Solids*, 445–446, pp. 95–101. Available at: https://doi.org/10.1016/j.jnoncrysol.2016.05.013.

Etxeberria-Benavides, M. *et al.* (2020) 'PBI mixed matrix hollow fiber membrane: Influence of ZIF-8 filler over H2/CO2 separation performance at high temperature and

pressure', *Separation and Purification Technology*, 237. Available at: https://doi.org/10.1016/j.seppur.2019.116347.

Ferreira, A. *et al.* (no date) *Portal Laboratórios Virtuais de Processos Químicos - Separações e Operações Unitárias*, *Unidersidade de Coimbra - Departamento de Engenharia Química*. Available at: http://labvirtual.eq.uc.pt/siteJoomla/index.php?Itemid=450#4 (Accessed: 23 June 2024).

Fong, H., Chun, I. and Reneker, D.H. (1999) 'Beaded nanofibers formed during electrospinning', *Polymer*, 40(16), pp. 4585–4592. Available at: https://doi.org/10.1016/S0032-3861(99)00068-3.

Formhals, A. (1934) 'Process and apparatus for preparing artificial threads'. United States.

Formhals, A. (1944) 'Method and apparatus for spinning'. United States.

Franchin, G. and Colombo, P. (2015) 'Porous geopolymer components through inverse replica of 3D printed sacrificial templates', *Journal of Ceramic Science and Technology*, 6(2), pp. 105–112. Available at: https://doi.org/10.4416/JCST2014-00057.

Freire, A.L. (2019) *Application of Geopolymers in CO2 Adsorption at Low Temperature*. Dissertation. Federal University of Santa Catarina.

Freire, A.L. *et al.* (2020) 'Geopolymers produced with fly ash and rice husk ash applied to CO2 capture', *Journal of Cleaner Production*, 273. Available at: https://doi.org/10.1016/j.jclepro.2020.122917.

Freire, A.L. (2022) *Synthesis, Characterization and Application of Geopolymers based on Phosphate Mining Tailings in Carbon Capture Sequestration*. Qualification project. Federal University of Santa Catarina.

Freire, A.L. *et al.* (2025) 'Synthesis and characterization of geopolymers based on phosphate mining tailings and its application for carbon dioxide and nitrogen adsorption', *Ceramics International*, 51(7), pp. 8396–8407. Available at: https://doi.org/10.1016/j.ceramint.2024.12.270.

Freire, A.L., José, H.J. and de Fátima Peralta Muniz Moreira, R. (2022) 'Potential applications for geopolymers in carbon capture and storage', *International Journal of Greenhouse Gas Control*, 118(May). Available at: https://doi.org/10.1016/j.ijggc.2022.103687.

Frontera, P. *et al.* (2013) 'Ferrierite zeolitic thin-layer on cordierite honeycomb support by clear solutions', *Materials Letters*, 104, pp. 72–75. Available at: https://doi.org/10.1016/j.matlet.2013.03.138.

Fu, B., Zhou, X. and Wang, Y. (2016) 'High-rate performance electrospun Na0.44MnO2 nanofibers as cathode material for sodium-ion batteries', *Journal of Power Sources*, 310, pp. 102–108. Available at: https://doi.org/10.1016/j.jpowsour.2016.01.101.

Gao, X., Yu, Q.L. and Brouwers, H.J.H. (2017) 'Apply 29Si, 27Al MAS NMR and selective dissolution in identifying the reaction degree of alkali activated slag-fly ash composites', *Ceramics International*, 43(15), pp. 12408–12419. Available at: https://doi.org/10.1016/j.ceramint.2017.06.108.

Geng, X., Kwon, O.H. and Jang, J. (2005) 'Electrospinning of chitosan dissolved in concentrated acetic acid solution', *Biomaterials*, 26(27), pp. 5427–5432. Available at: https://doi.org/10.1016/j.biomaterials.2005.01.066.

Guerrero-Pérez, M. O. (2024). Perspectives and State of the Art of Membrane Separation Technology as a Key Element in the Development of Hydrogen Economy. Membranes, 14(11), 228. https://doi.org/10.3390/membranes14110228.

Gore, K.U. *et al.* (2002) '29Si and 27Al MAS/3Q-MAS NMR studies of high silica USY zeolites', *Journal of Physical Chemistry B*, 106(23), pp. 6115–6120. Available at: https://doi.org/10.1021/jp0143241.

Greiser, S., Hunger, M. and Jäger, C. (2016) '29Si{27Al} TRAPDOR MAS NMR to distinguish Qn(mAl) sites in aluminosilicates. Test case: Faujasite-type zeolites', *Solid State Nuclear Magnetic Resonance*, 79, pp. 6–10. Available at: https://doi.org/10.1016/j.ssnmr.2016.10.004.

Guerrero-Pérez, M.O. (2021) 'Research Progress on the Applications of Electrospun Nanofibers in Catalysis', *Catalysts*, 12(1), p. 9. Available at: https://doi.org/10.3390/catal12010009.

Guo, X. *et al.* (2024) 'Polyethyleneimine modified porous wood ceramics for efficient and high-capacity adsorption of CO2 in simulated gases', *Journal of Environmental Chemical Engineering*, 12(2). Available at: https://doi.org/10.1016/j.jece.2024.112081.

Haghdoost, F. *et al.* (2021) 'Preparation and characterization of electrospun polyethersulfone/polyvinylpyrrolidone-zeolite core–shell composite nanofibers for creatinine

adsorption', *Separation and Purification Technology*, 257. Available at: https://doi.org/10.1016/j.seppur.2020.117881.

Haider, A., Haider, S. and Kang, I.K. (2018) 'A comprehensive review summarizing the effect of electrospinning parameters and potential applications of nanofibers in biomedical and biotechnology', *Arabian Journal of Chemistry*. Elsevier B.V., pp. 1165–1188. Available at: https://doi.org/10.1016/j.arabjc.2015.11.015.

Haleem, N. *et al.* (2022) 'Development of poly vinyl alcohol (PVA) based biochar nanofibers for carbon dioxide (CO2) adsorption', *Renewable and Sustainable Energy Reviews*, 157. Available at: https://doi.org/10.1016/j.rser.2021.112019.

Han, L. *et al.* (2022) 'In-situ synthesis of zeolite X in foam geopolymer as a CO2 adsorbent', *Journal of Cleaner Production*, 372. Available at: https://doi.org/10.1016/j.jclepro.2022.133591.

Hassan, H.S. *et al.* (2018) 'Fabrication and characterization of thermally-insulating coconut ash-based geopolymer foam', *Waste Management*, 80, pp. 235–240. Available at: https://doi.org/10.1016/j.wasman.2018.09.022.

Hauchhum, L. and Mahanta, P. (2014) 'Carbon dioxide adsorption on zeolites and activated carbon by pressure swing adsorption in a fixed bed', *International Journal of Energy and Environmental Engineering*, 5(4), pp. 349–356. Available at: https://doi.org/10.1007/s40095-014-0131-3.

He, H. *et al.* (2023) 'Fabrication of a flexible and efficient electromagnetic wave absorber based on reduced graphene oxide/Fe7Co3 filled into polydimethylsiloxane', *Synthetic Metals*, 293, p. 117296. Available at: https://doi.org/10.1016/j.synthmet.2023.117296.

He, P.Y. *et al.* (2020) 'Low-cost and facile synthesis of geopolymer-zeolite composite membrane for chromium(VI) separation from aqueous solution', *Journal of Hazardous Materials*, 392, p. 122359. Available at: https://doi.org/10.1016/J.JHAZMAT.2020.122359.

He, W. *et al.* (2023) 'Anchoring nano-zeolite NaX particles on polydopamine-modified PVDF/PAN electrospun membranes for enhancing interception, adsorption and antifouling performance', *Colloids and Surfaces A: Physicochemical and Engineering Aspects*, 670. Available at: https://doi.org/10.1016/j.colsurfa.2023.131587.

Henke, K. and Treml, S. (2013) 'Wood based bulk material in 3D printing processes for applications in construction', *European Journal of Wood and Wood Products*, 71(1), pp. 139–141. Available at: https://doi.org/10.1007/s00107-012-0658-z.

Hodhod, Osama.A., Alharthy, Samiha.E. and Bakr, Shreen.M. (2020) 'Physical and mechanical properties for metakaolin geopolymer bricks', *Construction and Building Materials*, 265, p. 120217. Available at: https://doi.org/10.1016/j.conbuildmat.2020.120217.

Hohman, M.M. *et al.* (2001) 'Electrospinning and electrically forced jets. I. Stability theory', *Physics of Fluids*, 13(8), pp. 2201–2220. Available at: https://doi.org/10.1063/1.1383791.

Hong, C.H. *et al.* (2021) 'Progress in polyvinyl alcohol membranes with facilitated transport properties for carbon capture', *Journal of Environmental Chemical Engineering*. Elsevier Ltd. Available at: https://doi.org/10.1016/j.jece.2021.106783.

Hong, C.H. *et al.* (2022) 'Polyvinyl alcohol membrane incorporated with amine-modified silica nanoparticles and ionic liquid for facilitated transport of CO2', *International Journal of Greenhouse Gas Control*, 120. Available at: https://doi.org/10.1016/j.ijggc.2022.103774.

Hu, Y. *et al.* (2023) 'Self-intensified synergy of a versatile biomimetic nanozyme and doxorubicin on electrospun fibers to inhibit postsurgical tumor recurrence and metastasis', *Biomaterials*, 293. Available at: https://doi.org/10.1016/j.biomaterials.2022.121942.

Huang, Z.M. *et al.* (2003) 'A review on polymer nanofibers by electrospinning and their applications in nanocomposites', *Composites Science and Technology*, 63(15), pp. 2223–2253. Available at: https://doi.org/10.1016/S0266-3538(03)00178-7.

Idrissi, H. *et al.* (2021) 'Sustainable use of phosphate waste rocks: From characterization to potential applications', *Materials Chemistry and Physics*, 260, p. 124119. Available at: https://doi.org/10.1016/j.matchemphys.2020.124119.

Izquierdo, M. *et al.* (2010) 'The role of open and closed curing conditions on the leaching properties of fly ash-slag-based geopolymers', *Journal of Hazardous Materials*, 176(1–3), pp. 623–628. Available at: https://doi.org/10.1016/j.jhazmat.2009.11.075.

Ji, W. *et al.* (2022) 'Development of Flexible Plasticized Ion Conducting Polymer Blend Electrolytes Based on Polyvinyl Alcohol (PVA): Chitosan (CS) with High Ion Transport Parameters Close to Gel Based Electrolytes'. Available at: https://doi.org/10.3390/gels.

Jiang, B. *et al.* (2023) 'Potentiation of Curcumin-loaded zeolite Y nanoparticles/PCL-gelatin electrospun nanofibers for postsurgical glioblastoma treatment', *Journal of Drug Delivery Science and Technology*, 80. Available at: https://doi.org/10.1016/j.jddst.2022.104105.

Jiménez, E., Lalangui, S., Guacho, E., Emperatriz Paucar, A., *et al.* (2019) 'Nanotechnological characterization of allofanite and faujasite (Y-faujasite) catalysts and comparing with a commercial FCC catalyst (X-zeolite)', *AIMS Materials Science*, 6(6), pp. 911–943. Available at: https://doi.org/10.3934/matersci.2019.6.911.

Jiménez, E., Lalangui, S., Guacho, E., Paucar, A.E., *et al.* (2019) 'Nanotechnological characterization of allofanite and faujasite (Y-faujasite) catalysts and comparing with a commercial FCC catalyst (X-zeolite)', *AIMS Materials Science*, 6(6), pp. 911–943. Available at: https://doi.org/10.3934/matersci.2019.6.911.

Jin, H. *et al.* (2022) '3D printed geopolymer adsorption sieve for removal of methylene blue and adsorption mechanism', *Colloids and Surfaces A: Physicochemical and Engineering Aspects*, 648(May), p. 129235. Available at: https://doi.org/10.1016/j.colsurfa.2022.129235.

Kang, D.H. and Kang, H.W. (2016) 'Surface energy characteristics of zeolite embedded PVDF nanofiber films with electrospinning process', *Applied Surface Science*, 387, pp. 82–88. Available at: https://doi.org/10.1016/j.apsusc.2016.06.096.

Karimi, M., Rodrigues, A.E. and Silva, J.A.C. (2021) 'Designing a simple volumetric apparatus for measuring gas adsorption equilibria and kinetics of sorption. Application and validation for CO2, CH4 and N2 adsorption in binder-free beads of 4A zeolite', *Chemical Engineering Journal*, 425. Available at: https://doi.org/10.1016/j.cej.2021.130538.

Kazancoglu, Y., Ozbiltekin-Pala, M. and Ozkan-Ozen, Y.D. (2021) 'Prediction and evaluation of greenhouse gas emissions for sustainable road transport within Europe', *Sustainable Cities and Society*, 70. Available at: https://doi.org/10.1016/j.scs.2021.102924.

Kaze, C.R. *et al.* (2022) 'Influence of mineralogy and activator type on the rheology behaviour and setting time of laterite based geopolymer paste', *Cement and Concrete Composites*, 126. Available at: https://doi.org/10.1016/j.cemconcomp.2021.104345.

Khalil, A., Hashaikeh, R. and Hilal, N. (2021) '3D printed zeolite-Y for removing heavy metals from water', *Journal of Water Process Engineering*, 42(May), p. 102187. Available at: https://doi.org/10.1016/j.jwpe.2021.102187.

Khoramzadeh, E., Mofarahi, M. and Lee, C.H. (2019) 'Equilibrium Adsorption Study of CO2 and N2 on Synthesized Zeolites 13X, 4A, 5A, and Beta', *Journal of Chemical and Engineering Data*, 64(12), pp. 5648–5664. Available at: https://doi.org/10.1021/acs.jced.9b00690.

Kim, J. *et al.* (2022) 'Comprehensive evaluation of 3A, 4A, 5A, and 13X zeolites for selective 1-octene adsorption over n-octane', *Journal of Industrial and Engineering Chemistry*, 110, pp. 274–285. Available at: https://doi.org/10.1016/j.jiec.2022.03.003.

Kim, K.H. and Kim, M.H. (2023) 'Adsorption of CO2, CO, H2, and N2 on Zeolites, Activated Carbons, and Metal-Organic Frameworks with Different Surface Nonuniformities', *Sustainability (Switzerland)*, 15(15). Available at: https://doi.org/10.3390/su151511574.

Kim, S., Kirch, J. and Mawst, L. (2010) 'Highly strained InAs quantum wells on InP substrates for mid-IR emission', *Journal of Crystal Growth*, 312(8), pp. 1388–1390. Available at: https://doi.org/10.1016/j.jcrysgro.2009.12.003.

Kljajević, L.M. *et al.* (2017) 'Structural and chemical properties of thermally treated geopolymer samples', *Ceramics International*, 43(9), pp. 6700–6708. Available at: https://doi.org/10.1016/j.ceramint.2017.02.066.

Komnitsas, K.A. (2011) 'Potential of geopolymer technology towards green buildings and sustainable cities', *Procedia Engineering*, 21, pp. 1023–1032. Available at: https://doi.org/10.1016/j.proeng.2011.11.2108.

Kong, D.L.Y., Sanjayan, J.G. and Sagoe-Crentsil, K. (2007) 'Comparative performance of geopolymers made with metakaolin and fly ash after exposure to elevated temperatures', *Cement and Concrete Research*, 37(12), pp. 1583–1589. Available at: https://doi.org/10.1016/j.cemconres.2007.08.021.

Kovářík, T. *et al.* (2021) 'Cellular ceramic foam derived from potassium-based geopolymer composite: Thermal, mechanical and structural properties', *Materials and Design*, 198. Available at: https://doi.org/10.1016/j.matdes.2020.109355.

Król, M., Minkiewicz, J. and Mozgawa, W. (2016) 'IR spectroscopy studies of zeolites in geopolymeric materials derived from kaolinite', *Journal of Molecular Structure*, 1126, pp. 200–206. Available at: https://doi.org/10.1016/j.molstruc.2016.02.027.

Kyzas, G.Z., Bikiaris, D.N. and Mitropoulos, A.C. (2017) 'Chitosan adsorbents for dye removal: a review', *Polymer International*, 66(12), pp. 1800–1811. Available at: https://doi.org/10.1002/pi.5467.

Labonnote, N. *et al.* (2016) 'Additive construction: State-of-the-art, challenges and opportunities', *Automation in Construction*, 72, pp. 347–366. Available at: https://doi.org/10.1016/j.autcon.2016.08.026.

Li, Z., Wang, L. and Ma, G. (2020) 'Mechanical improvement of continuous steel microcable reinforced geopolymer composites for 3D printing subjected to different loading conditions', *Composites Part B: Engineering*, 187(September 2019), p. 107796. Available at: https://doi.org/10.1016/j.compositesb.2020.107796.

Lim, J.H., Panda, B. and Pham, Q.C. (2018) 'Improving flexural characteristics of 3D printed geopolymer composites with in-process steel cable reinforcement', *Construction and Building Materials*, 178, pp. 32–41. Available at: https://doi.org/10.1016/j.conbuildmat.2018.05.010.

Liu, J. *et al.* (2021) 'Fabrication of advanced polydimethylsiloxane-based functional materials: Bulk modifications and surface functionalizations', *Chemical Engineering Journal*. Elsevier B.V. Available at: https://doi.org/10.1016/j.cej.2020.127262.

Liu, Jia *et al.* (2014) 'Hierarchical macro-meso-microporous ZSM-5 zeolite hollow fibers with highly efficient catalytic cracking capability', *Scientific Reports*, 4. Available at: https://doi.org/10.1038/srep07276.

Liu, P. *et al.* (2016) 'Adsorption separation for high purity propane from liquefied petroleum gas in a fixed bed by removal of alkanes', *Separation and Purification Technology*, 158, pp. 1–8. Available at: https://doi.org/10.1016/j.seppur.2015.12.003.

Luna, F.J. and Schuchardt, U. (2001) 'Modificação de zeólitas para uso em catálise', *Quimica Nova*, 24(6), pp. 885–892. Available at: https://doi.org/10.1590/S0100-40422001000600027.

Luz, A.B. (1995) 'Zeólitas: propriedades e usos industriais', in F.F. Lins (ed.) *Série Tecnologia Mineral*. CETEM/CNPq, p. 35. Available at: http://mineralis.cetem.gov.br:8080/bitstream/cetem/132/1/stm-68.pdf.

Mabroum, S. *et al.* (2020) 'Elaboration of geopolymers based on clays by-products from phosphate mines for construction applications', *Journal of Cleaner Production*, 261, p. 121317. Available at: https://doi.org/10.1016/j.jclepro.2020.121317.

Mansur, H.S. *et al.* (2008) 'FTIR spectroscopy characterization of poly (vinyl alcohol) hydrogel with different hydrolysis degree and chemically crosslinked with glutaraldehyde', *Materials Science and Engineering C*, 28(4), pp. 539–548. Available at: https://doi.org/10.1016/j.msec.2007.10.088.

Mastropietro, T.F. *et al.* (2016) 'Crystallization and assembling of FAU nanozeolites on porous ceramic supports for zeolite membrane synthesis', *Microporous and Mesoporous Materials*, 228, pp. 141–146. Available at: https://doi.org/10.1016/j.micromeso.2016.03.037.

Medpelli, D. *et al.* (2015) 'Iron oxide-modified nanoporous geopolymers for arsenic removal from ground water', *Resource-Efficient Technologies*, 1(1), pp. 19–27. Available at: https://doi.org/10.1016/j.reffit.2015.06.007.

Mendes, D.N.D.L. *et al.* (2021) '3D-printed hybrid zeolitic/carbonaceous electrically conductive adsorbent structures', *Chemical Engineering Research and Design*, 174, pp. 442–453. Available at: https://doi.org/10.1016/j.cherd.2021.08.020.

Méndez-Ares, R. *et al.* (2021) 'Membranas poliméricas cargadas con zeolita para su futuro empleo en la adsorción de gases contaminantes', *Revista Cubana de Química*, 33(2), pp. 257–278. Available at: http://scielo.sld.cu/scielo.php?script=sci_arttext&pid=S2224-54212021000200069 (Accessed: 15 June 2023).

Minelli, M. *et al.* (2016) 'Geopolymers as solid adsorbent for CO2 capture', *Chemical Engineering Science*, 148, pp. 267–274. Available at: https://doi.org/10.1016/j.ces.2016.04.013.

Minelli, M. *et al.* (2018) 'Characterization of novel geopolymer – Zeolite composites as solid adsorbents for CO2 capture', *Chemical Engineering Journal*, 341, pp. 505–515. Available at: https://doi.org/10.1016/j.cej.2018.02.050.

Ming, Z.J. and Hsu, L.Y. (2013) 'Networking scalable parallelism, integrity in knowledge economy - Civilization from shuyuans toward ubiquitous university cities', in *Proceeding of the 2013 'Suzhou-Silicon Valley-Beijing' International Innovation Conference: Technology Innovation and Diasporas in a Global Era, SIIC 2013*, pp. 310–315. Available at: https://doi.org/10.1109/SIIC.2013.6624206.

Mintova, S. *et al.* (2016) *Verified syntheses of zeolitic materials*. Synthesis Commission of the International Zeolite Association.

Mofarrah, M. *et al.* (2023) 'Fabricating ZSM-5 zeolite/ polycaprolactone nano-fibers co-loaded with dexamethasone and ascorbic acid: Potential application in osteogenic differentiation of human adipose-derived stem cells', *Journal of Drug Delivery Science and Technology*, 79. Available at: https://doi.org/10.1016/j.jddst.2022.103999.

Mohandesnezhad, S. *et al.* (2020) 'In vitro evaluation of Zeolite-nHA blended PCL/PLA nanofibers for dental tissue engineering', *Materials Chemistry and Physics*, 252. Available at: https://doi.org/10.1016/j.matchemphys.2020.123152.

Morton, W.J. (1902) 'Method of dispersing fluids.' United States.

Moukannaa, S. *et al.* (2018) 'Recycling of phosphate mine tailings for the production of geopolymers', *Journal of Cleaner Production*, 185, pp. 891–903. Available at: https://doi.org/10.1016/j.jclepro.2018.03.094.

Moukannaa, S. *et al.* (2019) 'Alkaline fused phosphate mine tailings for geopolymer mortar synthesis: Thermal stability, mechanical and microstructural properties', *Journal of Non-Crystalline Solids*, 511, pp. 76–85. Available at: https://doi.org/10.1016/j.jnoncrysol.2018.12.031.

Moulder, Jolm F *et al.* (1992) *Handbook of X-ray Photoelectron Spectroscopy A: Reference Book of Standard Spectra for Identification and Interpretation of XPS Data*. Edited by J. Chastain. Minnesota: Perkin-Elmer Corporation.

Moulder, John F *et al.* (1992) *Handbook of X-ray Photoelectron Spectroscopy: A Reference Book of Standard Spectra for Identification and Interpretation of XPS Data*. Edited by J. Chastain. Perkin-Elmer Corporation - Physical Electronics Division.

Muthukrishnan, S., Ramakrishnan, S. and Sanjayan, J. (2020) 'Effect of microwave heating on interlayer bonding and buildability of geopolymer 3D concrete printing', *Construction and Building Materials*, 265, p. 120786. Available at: https://doi.org/10.1016/j.conbuildmat.2020.120786.

Muthukrishnan, S., Ramakrishnan, S. and Sanjayan, J. (2021) 'Effect of alkali reactions on the rheology of one-part 3D printable geopolymer concrete', *Cement and Concrete Composites*, 116(December 2020), p. 103899. Available at: https://doi.org/10.1016/j.cemconcomp.2020.103899.

Najafi, A.M. *et al.* (2023) 'Effect of binder on CO2, CH4, and N2 adsorption behavior, structural properties, and diffusion coefficients on extruded zeolite 13X', *Chemosphere*, 324. Available at: https://doi.org/10.1016/j.chemosphere.2023.138275.

Nasab, G.M., Golestanifard, F. and MacKenzie, K.J.D. (2014) 'The effect of the SiO2/Na2O ratio in the structural modification of metakaolin-based geopolymers studied by XRD, FTIR and MAS-NMR', *Journal of Ceramic Science and Technology*, 5(3), pp. 185–191. Available at: https://doi.org/10.4416/JCST2014-00007.

Nollet, J.A. (1748) 'Part of a letter from Abbè Nollet, of the Royal Academy of Science at Paris, and F. R. S. to Martin Folkes Esq; President of the same, concerning electricity', *Philosophical Transactions of the Royal Society of London*, 45(486), pp. 187–194. Available at: https://doi.org/10.1098/rstl.1748.0018.

Nuhnen, A. and Janiak, C. (2020) 'A practical guide to calculate the isosteric heat/enthalpy of adsorption: Via adsorption isotherms in metal-organic frameworks, MOFs', *Dalton Transactions*. Royal Society of Chemistry, pp. 10295–10307. Available at: https://doi.org/10.1039/d0dt01784a.

Okada, K. *et al.* (2011) 'Capillary rise properties of porous geopolymers prepared by an extrusion method using polylactic acid (PLA) fibers as the pore formers', *Journal of the European Ceramic Society*, 31(4), pp. 461–467. Available at: https://doi.org/10.1016/j.jeurceramsoc.2010.10.035.

Oliveira, M.R. *et al.* (2023) 'Microwave-Assisted Synthesis of Zeolite A from Metakaolinite for CO2 Adsorption', *International Journal of Molecular Sciences*, 24(18), p. 14040. Available at: https://doi.org/10.3390/ijms241814040.

Onutai, S. *et al.* (2016) 'Fast microwave syntheses of fly ash based porous geopolymers in the presence of high alkali concentration', *Ceramics International*, 42(8), pp. 9866–9874. Available at: https://doi.org/10.1016/j.ceramint.2016.03.086.

Pahang, F. *et al.* (2023) 'Electrospun poly(ST-Co-AC)/Co-ZIF-67@Chitosan composite nanofibers as a sorbent with superior reusability for pesticide residues analysis in food samples', *Microchemical Journal*, 188. Available at: https://doi.org/10.1016/j.microc.2023.108476.

Paiva, M.D.M. *et al.* (2018) 'A geopolymer cementing system for oil wells subject to steam injection', *Journal of Petroleum Science and Engineering*, 169, pp. 748–759. Available at: https://doi.org/10.1016/j.petrol.2018.06.022.

Panagiotopoulou, C. *et al.* (2007) 'Dissolution of aluminosilicate minerals and by-products in alkaline media', *Journal of Materials Science*, 42(9), pp. 2967–2973. Available at: https://doi.org/10.1007/s10853-006-0531-8.

Panda, B. *et al.* (2017) 'Additive manufacturing of geopolymer for sustainable built environment', *Journal of Cleaner Production*, 167, pp. 281–288. Available at: https://doi.org/10.1016/j.jclepro.2017.08.165.

Panda, B., Paul, S.C. and Tan, M.J. (2017) 'Anisotropic mechanical performance of 3D printed fiber reinforced sustainable construction material', *Materials Letters*, 209, pp. 146–149. Available at: https://doi.org/10.1016/j.matlet.2017.07.123.

Paolini, A., Kollmannsberger, S. and Rank, E. (2019) 'Additive manufacturing in construction: A review on processes, applications, and digital planning methods', *Additive Manufacturing*, 30(September), p. 100894. Available at: https://doi.org/10.1016/j.addma.2019.100894.

Papa, E. *et al.* (2016) 'Insights into the macroporosity of freeze-cast hierarchical geopolymers', *RSC Advances*, 6(29), pp. 24635–24644. Available at: https://doi.org/10.1039/c6ra02232d.

Papa, E. *et al.* (2018) 'Zeolite-geopolymer composite materials: Production and characterization', *Journal of Cleaner Production*, 171, pp. 76–84. Available at: https://doi.org/10.1016/j.jclepro.2017.09.270.

Papa, E. *et al.* (2021) 'CO2 adsorption at intermediate and low temperature by geopolymer-hydrotalcite composites', *Open Ceramics*, 5(December 2020), p. 100048. Available at: https://doi.org/10.1016/j.oceram.2020.100048.

Papa, E. *et al.* (2023) 'Metakaolin-based geopolymer – Zeolite NaA composites as CO2 adsorbents', *Applied Clay Science*, 237. Available at: https://doi.org/10.1016/j.clay.2023.106900.

Park, Y. *et al.* (2016) 'Adsorption equilibria and kinetics of six pure gases on pelletized zeolite 13X up to 1.0 MPa: CO2, CO, N2, CH4, Ar and H2', *Chemical Engineering Journal*, 292, pp. 348–365. Available at: https://doi.org/10.1016/j.cej.2016.02.046.

Pasabeyoglu, P. *et al.* (2024) 'Solar-driven calcination of clays for sustainable zeolite production: CO2 capture performance at ambient conditions', *Journal of Cleaner Production*, 477. Available at: https://doi.org/10.1016/j.jclepro.2024.143838.

Pasupathy, K., Ramakrishnan, S. and Sanjayan, J. (2021) 'Formulating eco-friendly geopolymer foam concrete by alkali-activation of ground brick waste', *Journal of Cleaner Production*, 325, p. 129180. Available at: https://doi.org/10.1016/j.jclepro.2021.129180.

Pereira, A. *et al.* (2022) 'Evaluation of the potential of a 3D-printed hybrid zeolite 13X/activated carbon material for CO2/N2 separation using electric swing adsorption', *Chemical Engineering Journal*, 450. Available at: https://doi.org/10.1016/j.cej.2022.138197.

Pérez-Botella, E., Valencia, S. and Rey, F. (2022) 'Zeolites in Adsorption Processes: State of the Art and Future Prospects', *Chemical Reviews*. American Chemical Society, pp. 17647–17695. Available at: https://doi.org/10.1021/acs.chemrev.2c00140.

Petlitckaia, S. *et al.* (2020) 'Effect of kaolin and argillite mixtures on the dielectric properties of geopolymers', *Open Ceramics*, 4. Available at: https://doi.org/10.1016/j.oceram.2020.100035.

Pinto, A.T. (2006) 'Introdução ao Estudo dos Geopolimeros', *universidade de Trás-os-montes e Alto Douro*, 28(4), p. 423.

Rad, L.R. *et al.* (2014) 'Removal of Ni2+ and Cd2+ ions from aqueous solutions using electrospun PVA/zeolite nanofibrous adsorbent', *Chemical Engineering Journal*, 256, pp. 119–127. Available at: https://doi.org/10.1016/j.cej.2014.06.066.

Rahmani-Manglano, N.E. *et al.* (2024) 'Oxidative stability and oxygen permeability of oil-loaded capsules produced by spray-drying or electrospraying measured by electron spin resonance', *Food Chemistry*, 430. Available at: https://doi.org/10.1016/j.foodchem.2023.136894.

Rajini, B., Narasimha Rao, A. V. and Sashidhar, C. (2021) 'Micro-level studies of fly ash and GGBS -based geopolymer concrete using Fourier transform Infra-Red', in *Materials Today: Proceedings*. Elsevier Ltd, pp. 586–589. Available at: https://doi.org/10.1016/j.matpr.2020.11.291.

Rasaki, S.A. *et al.* (2019) 'Geopolymer for use in heavy metals adsorption, and advanced oxidative processes: A critical review', *Journal of Cleaner Production*, 213, pp. 42–58. Available at: https://doi.org/10.1016/j.jclepro.2018.12.145.

Rayleigh, Lord (1882) 'On the equilibrium of liquid conducting masses charged with electricity', *The London, Edinburgh, and Dublin Philosophical Magazine and Journal of Science*, 14(87), pp. 184–186. Available at: https://doi.org/10.1080/14786448208628425.

Regufe, M.J. *et al.* (2019) 'Electrical conductive 3D-printed monolith adsorbent for CO2 capture', *Microporous and Mesoporous Materials*, 278, pp. 403–413. Available at: https://doi.org/10.1016/j.micromeso.2019.01.009.

Reneker, D.H. *et al.* (2000) 'Bending instability of electrically charged liquid jets of polymer solutions in electrospinning', *Journal of Applied Physics*, 87(9), pp. 4531–4547. Available at: https://doi.org/10.1063/1.373532.

Revathi, T. and Jeyalakshmi, R. (2021) 'Fly ash–GGBS geopolymer in boron environment: A study on rheology and microstructure by ATR FT-IR and MAS NMR', *Construction and Building Materials*, 267. Available at: https://doi.org/10.1016/j.conbuildmat.2020.120965.

Richardson, J.F. and Harker, J.H. (2002) *Coulson and Richardson's CHEMICAL ENGINEERING - Particle Technology and Separation Processes*. Fifth edition. Edited by J.R. Backhurst. Elsevier Science.

Romero-Pérez, A. and Aguilar-Armenta, G. (2010) 'Adsorption kinetics and equilibria of carbon dioxide, ethylene, and ethane on 4A(CECA) zeolite', *Journal of Chemical and Engineering Data*, 55(9), pp. 3625–3630. Available at: https://doi.org/10.1021/je100215c.

De Rossi, A. *et al.* (2018) 'Waste-based geopolymeric mortars with very high moisture buffering capacity', *Construction and Building Materials*, 191, pp. 39–46. Available at: https://doi.org/10.1016/j.conbuildmat.2018.09.201.

De Rossi, A. *et al.* (2020) 'Study of cure conditions effect on the properties of wood biomass fly ash geopolymers', *Journal of Materials Research and Technology*, 9(4), pp. 7518–7528. Available at: https://doi.org/10.1016/J.JMRT.2020.05.047.

Rowles, M. and O'Connor, B. (2003) 'Chemical optimisation of the compressive strength of aluminosilicate geopolymers synthesised by sodium silicate activation of metakaolinite', *Journal of Materials Chemistry*, 13(5), pp. 1161–1165. Available at: https://doi.org/10.1039/b212629j.

Ruthven, D.M. (1984) *Principles of Adsorption and Adsorption Processes*. New York: John Wiley & Sons.

Schneider, M. *et al.* (2024) 'Advances in electrospun composite polymer/zeolite and geopolymer nanofibers: A comprehensive review', *Separation and Purification Technology*, 340, p. 126684. Available at: https://doi.org/10.1016/j.seppur.2024.126684.

Schneider, M. *et al.* (2025) 'Hierarchically porous composites containing mining tailings-based geopolymer and zeolite 13X: application for carbon dioxide sequestration', *Adsorption*, 31(1). Available at: https://doi.org/10.1007/s10450-024-00569-1.

Seabra, R. *et al.* (2019) 'Adsorption equilibrium and kinetics of carbon dioxide, methane and nitrogen on binderless zeolite 4A adsorbents', *Microporous and Mesoporous Materials*, 277, pp. 105–114. Available at: https://doi.org/10.1016/j.micromeso.2018.10.024.

Shan, X. *et al.* (2023) 'Solid-state electrochemiluminescence sensor based on the carbon fibers derived from ZIFs-containing electrospun fibers for chlorpyrifos detection', *Microchemical Journal*, 185. Available at: https://doi.org/10.1016/j.microc.2022.108221.

Shin, Y.M. *et al.* (2001) 'Electrospinning: A whipping fluid jet generates submicron polymer fibers', *Applied Physics Letters*, 78(8), pp. 1149–1151. Available at: https://doi.org/10.1063/1.1345798.

Shrotri, A.R. *et al.* (2023) 'Performance of Li exchange hierarchical X zeolite for CO2 adsorption and H2 separation', *Journal of Industrial and Engineering Chemistry* [Preprint]. Available at: https://doi.org/10.1016/j.jiec.2023.12.027.

Sihombing, Y.A. *et al.* (2022) 'Preparation, characterization, and desalination study of polystyrene membrane integrated with zeolite using the electrospinning method', *Heliyon*, 8(8). Available at: https://doi.org/10.1016/j.heliyon.2022.e10113.

Sill, T.J. and von Recum, H.A. (2008) 'Electrospinning: Applications in drug delivery and tissue engineering', *Biomaterials*, pp. 1989–2006. Available at: https://doi.org/10.1016/j.biomaterials.2008.01.011.

Silva, B.A. da *et al.* (2021) 'Electrospinning of cellulose using ionic liquids: An overview on processing and applications', *European Polymer Journal*. Elsevier Ltd. Available at: https://doi.org/10.1016/j.eurpolymj.2021.110283.

Silveira, A.R. Da (2021) *Desenvolvimento de materiais compósitos geopolímero-zeólita derivados de resíduos industriais para adsorção de CO2*. Federal University of Santa Catarina.

Singh, N.B. and Middendorf, B. (2020) 'Geopolymers as an alternative to Portland cement: An overview', *Construction and Building Materials*, 237, p. 117455. Available at: https://doi.org/10.1016/j.conbuildmat.2019.117455.

Sircar, S. *et al.* (1999) 'Isosteric Heat of Adsorption: Theory and Experiment', *Journal of Physical Chemistry B*, 103(31), pp. 6539–6546. Available at: https://doi.org/10.1021/jp9903817.

Souza, G.S. (2021) *Desenvolvimento de compósito zeólita Na-LTA/polidimetilsiloxano aplicado para separação CO2/N2 por adsorção.* . Federal University of Santa Catarina.

Sreekumar, S. *et al.* (2017) 'Preparation and optimization of submicron chitosan capsules by water-based electrospraying for food and bioactive packaging applications', *Food*

Additives and Contaminants - Part A Chemistry, Analysis, Control, Exposure and Risk Assessment, 34(10), pp. 1795–1806. Available at: https://doi.org/10.1080/19440049.2017.1347284.

Staudt, J. *et al.* (2024) 'Evaluation of the CH4/CO2 separation by adsorption on coconut shell activated carbon: Impact of the gas moisture on equilibrium selectivity and adsorption capacity', *Heliyon*, 10(9). Available at: https://doi.org/10.1016/j.heliyon.2024.e30368.

Streb, A. and Mazzotti, M. (2021) 'Adsorption for efficient low carbon hydrogen production: part 1—adsorption equilibrium and breakthrough studies for H2/CO2/CH4 on zeolite 13X', *Adsorption*, 27(4), pp. 541–558. Available at: https://doi.org/10.1007/s10450-021-00306-y.

Su, S., Ma, H. and Chuan, X. (2016) 'Hydrothermal synthesis of zeolite A from K-feldspar and its crystallization mechanism', *Advanced Powder Technology*, 27(1), pp. 139–144. Available at: https://doi.org/10.1016/j.apt.2015.11.011.

Tang, J. *et al.* (2022) 'Elastic geopolymer based on nanotechnology: Synthesis, characterization, properties, and applications', *Ceramics International*, 48(5), pp. 5965–5971. Available at: https://doi.org/10.1016/j.ceramint.2021.11.070.

Taylor, G.I. (1964) 'Disintegration of water drops in an electric field', *Proceedings of the Royal Society of London. Series A. Mathematical and Physical Sciences*, 280(1382), pp. 383–397. Available at: https://doi.org/10.1098/rspa.1964.0151.

Taylor, G.I. (1966) 'The force exerted by an electric field on a long cylindrical conductor', *Proceedings of the Royal Society of London. Series A. Mathematical and Physical Sciences*, 291(1425), pp. 145–158. Available at: https://doi.org/10.1098/rspa.1966.0085.

Taylor, G.I. (1969) 'Electrically driven jets', *Proceedings of the Royal Society of London. A. Mathematical and Physical Sciences*, 313(1515), pp. 453–475. Available at: https://doi.org/10.1098/rspa.1969.0205.

Thakkar, H. *et al.* (2016) '3D-Printed Zeolite Monoliths for CO2 Removal from Enclosed Environments', *ACS Applied Materials and Interfaces*, 8(41), pp. 27753–27761. Available at: https://doi.org/10.1021/acsami.6b09647.

Thakkar, H. *et al.* (2018) 'Development of 3D-printed polymer-zeolite composite monoliths for gas separation', *Chemical Engineering Journal*, 348(February), pp. 109–116. Available at: https://doi.org/10.1016/j.cej.2018.04.178.

Thommes, M. *et al.* (2015) 'Physisorption of gases, with special reference to the evaluation of surface area and pore size distribution (IUPAC Technical Report)', *Pure and Applied Chemistry*, 87(9–10), pp. 1051–1069. Available at: https://doi.org/10.1515/pac-2014-1117.

Torgal, F.P. and Jalali, S. (2010) *Ligantes obtidos por activação alcalina*, *Engenharia Civil*. Available at: http://hdl.handle.net/1822/12749.

Vaclavik, F.D. (2010) 'Avaliação e otimização do uso de zeólitas no tratamento terciário de efluentes liquidos industrias', p. 71.

Vatanpour, V. *et al.* (2023) 'Polyvinyl alcohol-based separation membranes: a comprehensive review on fabrication techniques, applications and future prospective', *Materials Today Chemistry*. Elsevier Ltd. Available at: https://doi.org/10.1016/j.mtchem.2023.101381.

Vergara-Figueroa, J. *et al.* (2020) 'Dual electrospinning of a nanocomposites biofilm: Potential use as an antimicrobial barrier', *Materials Today Communications*, 25. Available at: https://doi.org/10.1016/j.mtcomm.2020.101671.

Voigt, C.L. (org) (2019) *A Produção do Conhecimento na Engenharia Química*. Atena Editora. Available at: https://doi.org/10.22533/at.ed.475190611.

Wagner, C.D. *et al.* (1979) *Handbook of X-ray photoelectron spectroscopy*. Edited by G.E. Muilenberg. Minnesota: Perkin-Elmer Corporation.

Wan, Q., Rao, F. and Song, S. (2017) 'Reexamining calcination of kaolinite for the synthesis of metakaolin geopolymers - roles of dehydroxylation and recrystallization', *Journal of Non-Crystalline Solids*, 460, pp. 74–80. Available at: https://doi.org/10.1016/j.jnoncrysol.2017.01.024.

Wang, Y. *et al.* (2024) 'A novel amine functionalized porous geopolymer spheres from municipal solid waste incineration fly ash for CO2 capture', *Journal of Environmental Management*, 349. Available at: https://doi.org/10.1016/j.jenvman.2023.119540.

Wang, Y. *et al.* (2025) 'Synthesis of geopolymer-zeolite composite from municipal solid waste incineration fly ash and their performance for CO2 adsorption', *Separation and Purification Technology*, 354. Available at: https://doi.org/10.1016/j.seppur.2024.129114.

Wei, H. *et al.* (2012) 'Granular bamboo-derived activated carbon for high CO2 adsorption: The dominant role of narrow micropores', *ChemSusChem*, 5(12), pp. 2354–2360. Available at: https://doi.org/10.1002/cssc.201200570.

White, C.E. *et al.* (2010) 'The effects of temperature on the local structure of metakaolin-based geopolymer binder: A neutron pair distribution function investigation', *Journal of the American Ceramic Society*, 93(10), pp. 3486–3492. Available at: https://doi.org/10.1111/j.1551-2916.2010.03906.x.

Wong, W.C. *et al.* (2001) 'Effects of synthesis parameters on the zeolite membrane morphology', *Journal of Membrane Science*, 193(2), pp. 141–161. Available at: https://doi.org/10.1016/S0376-7388(01)00454-9.

Wu, X. *et al.* (2019) 'Hierarchically structured PVP porous fibers derived from the embedding of NaY zeolite synergize the adsorption of benzene', *Composites Part B: Engineering*, 179. Available at: https://doi.org/10.1016/j.compositesb.2019.107542.

Xu, C. *et al.* (2024) 'Probing the differences in CO2 adsorption/desorption behaviors of solid amine sorbents in fixed and fluidized beds', *Separation and Purification Technology*, 343. Available at: https://doi.org/10.1016/j.seppur.2024.127171.

Xu, H. and van Deventer, J.S.J. (2003) 'The effect of alkali metals on the formation of geopolymeric gels from alkali-feldspars', *Colloids and Surfaces A: Physicochemical and Engineering Aspects*, 216(1–3), pp. 27–44. Available at: https://doi.org/10.1016/S0927-7757(02)00499-5.

Xue, J. *et al.* (2019) 'Electrospinning and electrospun nanofibers: Methods, materials, and applications', *Chemical Reviews*. American Chemical Society, pp. 5298–5415. Available at: https://doi.org/10.1021/acs.chemrev.8b00593.

Yarin, A.L., Koombhongse, S. and Reneker, D.H. (2001a) 'Bending instability in electrospinning of nanofibers', *Journal of Applied Physics*, 89(5), pp. 3018–3026. Available at: https://doi.org/10.1063/1.1333035.

Yarin, A.L., Koombhongse, S. and Reneker, D.H. (2001b) 'Taylor cone and jetting from liquid droplets in electrospinning of nanofibers', *Journal of Applied Physics*, 90(9), pp. 4836–4846. Available at: https://doi.org/10.1063/1.1408260.

Zailan, S.N. *et al.* (2016) 'Self-cleaning geopolymer concrete - A review', in *IOP Conference Series: Materials Science and Engineering*. Institute of Physics Publishing. Available at: https://doi.org/10.1088/1757-899X/133/1/012026.

Zhang, Q. *et al.* (2016) 'Synthesis of novel cobalt-containing polysilazane nanofibers with fluorescence by electrospinning', *Polymers*, 8(10). Available at: https://doi.org/10.3390/polym8100350.

Zhang, S. *et al.* (2021) 'Titanium carbide/zeolite imidazole framework-8/polylactic acid electrospun membrane for near-infrared regulated photothermal/photodynamic therapy of drug-resistant bacterial infections', *Journal of Colloid and Interface Science*, 599, pp. 390–403. Available at: https://doi.org/10.1016/j.jcis.2021.04.109.

Zhang, Z. *et al.* (2014) 'Fly ash-based geopolymers: The relationship between composition, pore structure and efflorescence', *Cement and Concrete Research*, 64, pp. 30–41. Available at: https://doi.org/10.1016/j.cemconres.2014.06.004.

Zhong, H. and Zhang, M. (2022) '3D printing geopolymers: A review', *Cement and Concrete Composites*, 128, p. 104455. Available at: https://doi.org/10.1016/j.cemconcomp.2022.104455.

Zhou, C. *et al.* (2013a) 'Characteristics and evaluation of synthetic 13X zeolite from Yunnan's natural halloysite', *Journal of Porous Materials*, 20(4), pp. 587–594. Available at: https://doi.org/10.1007/s10934-012-9631-9.

Zhou, C. *et al.* (2013b) 'Characteristics and evaluation of synthetic 13X zeolite from Yunnan's natural halloysite', *Journal of Porous Materials*, 20(4), pp. 587–594. Available at: https://doi.org/10.1007/s10934-012-9631-9.

Zibouche, F. *et al.* (2009) 'Geopolymers from Algerian metakaolin. Influence of secondary minerals', *Applied Clay Science*, 43(3–4), pp. 453–458. Available at: https://doi.org/10.1016/j.clay.2008.11.001.

Zribi, M., Samet, B. and Baklouti, S. (2019) 'Effect of curing temperature on the synthesis, structure and mechanical properties of phosphate-based geopolymers', *Journal of Non-Crystalline Solids*, 511, pp. 62–67. Available at: https://doi.org/10.1016/j.jnoncrysol.2019.01.032.